# CONNECTING PROTEIN STRUCTURE AND DYNAMICS ON BIOMATERIALS WITH THE FOREIGN BODY RESPONSE

by

David Faulón Marruecos

B.S., University of Barcelona, Catalonia (Spain), 2014

M.S., University of Colorado, 2016

A thesis submitted to the

Faculty of the Graduate School of the

University of Colorado at Boulder in partial fulfillment

of the requirement for the degree of

Doctor of Philosophy

Department of Chemical and Biological Engineering

2018

This thesis entitled:

Connecting Protein Structure and Dynamics on Biomaterials with the Foreign Body Response

written by David Faulón Marruecos

has been approved for the Department of Chemical and Biological Engineering

_____

Joel L. Kaar, Committee Chair

_____

Daniel K. Schwartz, Committee Member

Date _____

The final copy of this thesis has been examined by the signatories, and we find that both the content and the form meet acceptable presentation standards of scholarly work in the above mentioned discipline.

Faulón Marruecos, David (Ph.D., Chemical and Biological Engineering)

**Connecting Protein Structure and Dynamics on Biomaterials with the Foreign Body Response**

Thesis directed by Dr. Joel L. Kaar and Dr. Daniel K. Schwartz

## Abstract

The harsh environment of the foreign body response (FBR) has the potential to negatively impact the implantations of biomaterials in the body. The FBR is initiated by inflammatory cells that recognize the material as foreign through surface-adsorbed proteins. When proteins interact with surfaces, they can unfold and expose epitopes that may be recognized by immune cells and trigger a series of reactions. Importantly, the presentation of unfolded proteins is directly influenced by the highly dynamic and heterogeneous behavior of proteins in near-surface environments, as well as by the physicochemical features of the underlying surface. Such behavior is the result of transient unfolding and refolding, rapid exchange of folded and unfolded protein molecules between the surface and the bulk solution, intermittent interfacial diffusion, and protein-protein associations. While these interfacial processes are likely involved in the FBR, both their characterization and respective roles in the FBR have been ignored due to the lack of experimental techniques to directly observe individual molecular processes.

The work presented here aims to address this lack of fundamental understanding by applying novel single-molecule (SM) methods, which are uniquely sensitive to interfacial dynamics as well as protein and surface heterogeneities, to investigate the mechanisms that lead to the FBR. Specifically, we focused on tuning surface functionalization to reveal the connection between material properties, protein adsorption and stabilization, and ultimately cell response.

Total internal reflection fluorescence microscopy (TIRFM) was combined with Förster resonance energy transfer (FRET) to independently dissect individual molecular processes, such as adsorption, desorption, diffusion, folding, unfolding, and binding. The studies were performed using recombinant fibronectin (FN) as a model protein, which was site-specifically labeled to undergo FRET. First, the effect of poly(ethylene glycol) (PEG) grafting density on protein adsorption and stabilization was studied. Furthermore, mapping accumulated probe trajectories (MAPT) with an environmentally sensitive molecule was used as a tool to identify local changes in brush hydrophobicity. Secondly, in order to understand the connection between surface properties, FN conformation (ligand), and integrins (cell receptors), a three-color FRET method was developed to track both protein conformation and ligand-receptor binding as a function of surface chemistry. Finally, the extent to which the addition of a zwitterionic polymer (poly(sulfobetaine)) to PEG can improve the stability of FN was explored. Altogether, the results obtained from these studies will shed light on the rational design of materials to mediate cell signaling in physiological and synthetic environments.

*To my parents, Toni and Manoli, and my brother, Javier*

# Acknowledgements

I am extremely grateful for having had the opportunity to meet so many amazing scientists, engineers, staff, and coworkers during my PhD. First, I would like to thank my advisors Joel Kaar and Daniel Schwartz, for all of their support during this journey and for making this thesis possible. Joel's passion for science has inspired and given me the motivation and strength to fight for my goals and overcome any challenge. His endless patience and dedication to listen and advise helped me learn many valuable skills as both a scientist and a person. Dan has also provided invaluable guidance during these years with his constant intellectual challenges that forced me to think critically. Thank you Dan for always setting high expectations and believing in me, even when I thought I was not capable. Again, thank you both for mentoring me and making my experience as your research assistant fun, enriching, and fulfilling.

I would like to thank my committee members Ted Randolph, Kristi Anseth, and Corey Neu for their support and helpful insights. Also, the faculty and staff in the department of Chemical and Biological Engineering at the University of Colorado excelled at creating a friendly, collaborative environment, encouraging great research. I would like to thank Dominique deVangel in particular for all the incredible help he has provided as the department's graduate advisor. I must thank Rob Davis and Pere Balsells for their generosity and giving me the opportunity to start my PhD at CU Boulder with the Balsells Fellowship. My project was also funded by grants from the National Institute of Health, the Army Research Office, the Department of Energy, and the University of Colorado startup fund to Joel, which I am thankful for.

I would like to acknowledge the moral support and intellectual help of all former and current members of the Kaar and Schwartz labs whom I had the luck to meet and work closely.

Thank you, Núria, for everything you taught me in the lab when I first joined, and for your great friendship. Erik and Kelsey, thank you for your patience transferring your knowledge to the next generations. Thank you Joe, James, and Garrett for making the office a fun place and helping me with anything I needed. Sam, thank you for being not only a friend, but also an inspiration in life. Alaksh, Andres, Becca, Louis, and Sally: a warm thank you to all of you. Also, thank you to Mark Kastantin, Daniel Kienle, and Nathaniel Nelson for your expertise in single-molecule and teaching me amazing things! The knowledge I have gained during group meetings, gatherings, and informal conversations has made me a better scientist and led to the completion of this thesis.

It has been really complicated for me to be far away from home, but luckily I found wonderful individuals in Colorado who turned this place into a second home. Xavi and Sarah, thank you for being the best roommates I have ever had, for being my family in Boulder, and for showing me how to be a better human being. Davis and Logan, I would have never imagined I could learn so many outdoor activities, but you two taught me all of them. Thank you for always being there when I needed it, for the fun camping trips, and for being incredible friends. A very special thank you to Toni, the person who has been the foundation of my PhD. We started this adventure together, and we finished it together. You helped me grow, reminded me every day that I could accomplish this, and always stood by my side. This thesis would have not been possible without you. A big thank you also to my friends Cam, Shruthi, Milly, Stanley, and Rocío.

The most special of my acknowledgements go to my grandparents, my parents, and my brother. It has been very tough to be far away from you, but your constant and unconditional love kept me going day by day. This thesis is dedicated to you for all the efforts you had to make so that I could get to this point. Finally, I would like to thank Jake, for being there for me when I was

stressed, for his eternal patience, for his positive energy, and for making every experience we live together an incredible, unforgettable adventure. “T’estimo.”

# Table of Contents

# List of Tables

# List of Figures

# Chapter I: Introduction

*Impact of Surface Interactions on Protein Conformation*

David Faulón Marruecos, Daniel K. Schwartz, and Joel L. Kaar

(Published November, 2018: Current Opinion in Colloid & Interface Science, 38, 45-55)

## 1.1 Protein Structure at Interfaces

### 1.1.1 Abstract

Understanding the behavior of proteins at material interfaces has become increasingly important as the intersection between the biological and synthetic worlds continues to grow. By inducing changes in protein structure, interactions with materials may lead to a loss of function and/or biological activity, as well as undesirable cellular interactions *in vivo*, including the foreign body reaction to implantable materials. Despite extensive research, the understanding of the mechanisms that lead to protein conformational changes on surfaces remains incomplete. Here, we highlight recent advances in understanding and controlling protein conformation on the surface of synthetic materials, including nanomaterials, polymer films and brushes, metal coatings and particles, and graphitic materials. We also review developments in the use of biophysical and computational methods for characterizing the structure of proteins at solution-solid interfaces. These approaches have provided important new insights into the physico-chemical factors that control protein conformation in near-surface environments, which represents a critical step towards the rational design of biotic-abiotic interfaces in biomedical and biotechnological applications.

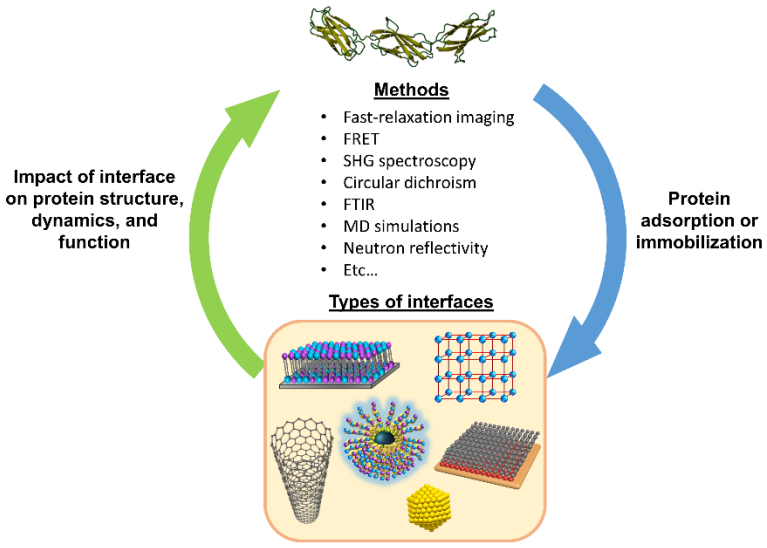


**Figure 1. 1.** Graphical abstract summarizing the different types of methods and interfaces covered in this section in order to elucidate the correlation between surface properties and protein structure.

### 1.1.2 Introduction

The interaction of proteins, including enzymes, with synthetic materials is a ubiquitous, yet poorly understood phenomenon that affects nearly every area of biotechnology. As synthetic materials and proteins/enzymes are increasingly combined, or used in conjunction, the significance of such interactions has been magnified. Proteins and enzymes are inherently delicate molecules with a natural propensity to denature on many surfaces. The biological function of most proteins and enzymes is lost upon unfolding, which constitutes one of the single largest barriers and causes of failure of many biotechnological solutions to global challenges in healthcare, sustainability, and environmental remediation. For example, the reduction in activity of enzymes due to interfacial interactions has hindered the utility and thus adoption of immobilized enzyme biocatalysts in industrial processes, including the transformation of toxic waste materials[1-3]. Such interactions have similarly prevented the clinical translation of biomaterials for tissue engineering and

regenerative medicine where the utility of such materials *in vivo* is hindered by the adsorption and subsequent unfolding of serum proteins on the surface of the material. In this case, the unfolding of surface-adsorbed proteins results in the presentation of damage-associated molecular patterns (i.e., DAMPs), which may elicit the activation of macrophages, leading to adverse immunological responses that obstruct the integration of the material with native host tissues[4-6]. Furthermore, surface-induced denaturation of vaccines and therapeutic proteins during storage in pre-filled syringes and vials, which may stem from the interaction of proteins and antibodies with the walls of the container as well as adjuvant particles, can lead to aggregation. The injection of the aggregated form of such drugs may also have dire outcomes, including reduced efficacy of the drug, anaphylactic shock, and even, in severe cases, patient mortality[7-9].

While the impact of synthetic materials on protein conformation has been studied extensively, the mechanisms that underlie surface-induced unfolding as well as the physico-chemical factors associated with protein denaturation on surfaces have yet to be fully elucidated. These phenomena have been investigated using a plethora of conventional biophysical and structure determination methods, yielding qualitative correlations between surface and protein properties. However, when applied to interfacial systems (i.e., proteins in near-surface environments), many conventional methods for studying protein structure afford limited mechanistic understanding because they provide ensemble-averaged information, when in reality the interaction of proteins with surfaces may be highly heterogeneous. Such ensemble-averaging findings can be easily misinterpreted, potentially leading to oversimplications of the relevant mechanisms. Recent advances in biophysical methods, including the development of sophisticated dynamic single-molecule (SM) techniques as well as fast relaxation imaging and methods based on nonlinear optical spectroscopy and microscopy, have contributed important new insights.

Additionally, new mechanistic understanding has been enabled by advances in computational methods, including the development of appropriate force fields for molecular dynamic simulations of proteins in near-surface environments.

The goal of this review is to summarize recent findings on the impact of interfacial interactions on protein conformation from the application of conventional and novel methods. Notably, while there are numerous reviews on the topic of protein adsorption on material surfaces, there are relatively few reviews on the impact of materials on protein conformation. It is interesting to note that, although qualitative correlations between surface and protein properties exist in the recent literature, the observations in the literature are still highly case-specific (i.e., dependent on the protein, surface, and solution conditions). In this review, we specifically highlight findings from recent papers on the impact of a broad range of materials, including nanomaterials, polymer films and brushes, metal coatings and particles, and graphitic materials, on protein conformation.

### 1.1.3 Soft Material Interfaces

#### 1.1.3.1 Lipid Bilayers and Micelles

Because of their biomimetic nature, supported lipid bilayers and vesicles have received considerable attention as interfaces for the stabilization of proteins and enzymes. Recently, there have been a number of studies that have elucidated the impact of lipid composition and heterogeneity as well as the mechanical properties of lipid interfaces on protein stability. In a study by Findlay and Booth, the folding and stability of lactose permease in contact with lipid bilayers as a function of lateral pressure and charge of the bilayer was measured[10]. The lateral pressure and charge of the bilayer was varied by systematically changing the ratio of 1,2-dioleoyl-glycero-3-

phosphoglycerol (DOPG), L-α-1,2-dioleoylphosphatidylcholine (DOPC), and L-α-1,2-dioleoylphosphatidylethanolamine (DOPE). Using synchrotron radiation circular dichroism, it was shown that native structure of the enzyme was stabilized as the fraction of DOPE in the bilayer increased, which corresponded with an increase in lateral chain pressure in the bilayer. However, the addition of DOPE inhibited the re-folding of denatured lactose permease, and, furthermore, the addition of DOPG, which is negatively charged, resulted in mis-folding. Additionally, Chaparro and co-workers reported related effects in which the stability as well as activity of nitroreductase (NfsB) tethered to supported lipid bilayers was strongly dependent on the bilayer composition (**Figure 1.2 A** and **1.2 B**)[11]. Specifically, in this work, it was shown that mixing DOPG and DOPC in the bilayer dramatically increased the stability of NfsB in the near-bilayer environment. The increase in stability coincided with an increase in the rate of re-folding of the enzyme, suggesting that the mechanism of stabilization was due to a chaperone-like effect of the bilayer (**Figure 1.2 C**). Notably, with between 15-50% DOPG, the mean fraction of enzyme molecules that were folded was greater than 95%, indicating virtually all of enzyme retained its native structure. The effect of bilayer composition on NfsB stability was directly observed using methods that are uniquely sensitive to monitoring protein structure and dynamics (e.g., re-folding) at the solution-solid interface. Such methods included exploiting SM tracking with total internal reflection fluorescence (TIRF) microscopy in combination with Förster resonance energy transfer (FRET). In this approach, TIRF illumination was used to excite protein molecules labeled with a donor and acceptor fluorophore, which were monitored using two-color wide-field imaging. From statistical analysis of the emission intensities of the donor and acceptor fluorophore, the conformational state (i.e., folded or unfolded) of individual protein molecules was determined. While these findings

demonstrate that mixed lipid bilayers may actively re-fold enzymes, it remains to be determined if this mechanism of stabilization is universal to other proteins.

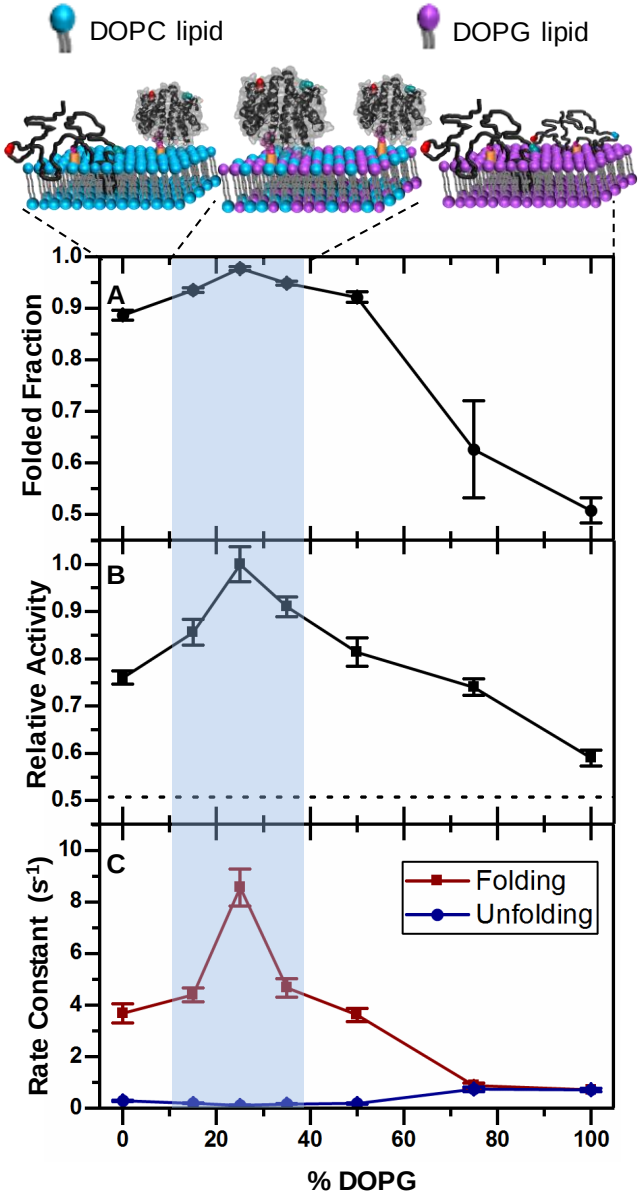

**Figure 1. 2.** Analysis of the impact of supported lipid bilayer composition on the structure, dynamics, and activity of immobilized NfsB, adapted from[11]. The structure and dynamics of the immobilized enzyme on the bilayer surface was characterized by SM-FRET using NfsB that was site-specifically labeled with donor and acceptor fluorophores. NfsB was immobilized on the bilayer surface via an N-terminal 6x-his tag, which was anchored to a nickel containing nitrilotriacetic acid ligand interdispersed within the bilayer. A) SM-FRET analysis of the variation in the fraction of folded NfsB as a function of the ratio of DOPG-to-DOPC in the bilayer showed an optimum in folded fraction between 15-50% DOPG. B) The increase in folded fraction in this optimum range coincided with an increase in the ensemble activity of immobilized NfsB on unilamellar vesicles with equivalent ratios of DOPG-to-DOPC. Relative activity for NfsB for each lipid composition refers to the fraction of the maximum specific activity of tethered NfsB, which was observed for the 25% DOPG case. C) Analysis of the kinetics of unfolding and re-folding of tethered NfsB as a function of DOPG fraction from SM-FRET measurements. The rate constants for unfolding (blue circles) and re-folding (red circles) represent the frequency of transitions between conformations of the tethered NfsB on the lipid bilayer surface. In the optimum range for the folded fraction, the rate constant for re-folding was greatest while the rate constant for unfolding was smallest, suggesting the mixed bilayers actively mediated re-folding of denatured enzyme molecules.

In related studies, Fang and co-workers investigated the micelle-assisted re-folding of insulin on the surface of poly(ethylene glycol) (PEG)-phosphatidylethanolamine micelles[12]. The extent of re-folding of insulin in the presence of the micelles as well as the recovery of insulin activity as a result of re-folding was measured *in vitro* and *in vivo* in mice. In the presence of the micelles, the secondary structure of reduced insulin was similar to that of native insulin, indicating interactions with the micelle surface facilitated re-folding. The authors hypothesized that re-folding was enabled via the interaction of hydrophobic domains in insulin with the phosphatidylethanolamine core of the micelles as well as the encapsulation of individual insulin molecules by the PEG head group. By capturing and encapsulating denatured insulin molecules, it was concluded that the interaction of insulin with the micelles prevented aggregation and allowed the protein to re-fold in isolation. *In vivo* studies further showed that, upon incubation with the micelles, the re-folded protein reduced glucose levels in mice. Furthermore, Moree and co-workers recently reported a novel method for monitoring changes in protein conformation on

supported lipid bilayers based on second-harmonic generation[13]. In this approach, the protein is modified with a second-harmonic-active dye, which is used to provide information on changes in the orientation of the protein relative to the surface. Such changes may occur as a result of perturbations to the structure of the protein due to interactions between the protein and the surface. The utility of this approach to monitor structural changes on lipid bilayers, as well as other surfaces, was demonstrated by characterizing changes in structure upon ligand binding to calmodulin, maltose-binding protein, and dihydrofolate reductase.

#### 1.1.3.2 Polymer Brushes

As a means to improve the biocompatibility of protein-contacting interfaces, polymer brushes have, like lipid surfaces, been extensively studied. Of specific interest has been developing polymer brush surfaces and coatings from polyelectrolytes and zwitterionic polymers, which are widely believed to be protein resistant. Koenig and co-workers recently compared changes in the structure of glucose oxidase in the presence of brushes composed of poly(acrylic acid) and poly(2-vinylpyridine) at different pH values[14]. Analysis of changes in secondary structure by attenuated total reflection-Fourier transform infrared spectroscopy (ATR-FTIR) showed that while at pH 4 the structure of the enzyme was more strongly perturbed upon interaction with the poly(acrylic acid) brush relative to in solution, the opposite was observed at pH 5.6, where the structure was more strongly perturbed upon adsorption to the poly(2-vinylpyridine) brush surface. While differences in electrostatic interactions presumably play a role in these observations, such observations were also attributed to differences in the amount of enzyme adsorbed on the brushes. In particular, at low pH, it was suggested that increased unfolding on the poly(acrylic acid) brush may be due to an increase in enzyme adsorption, which can increase interfacial aggregation.

Takasu et al. also characterized changes in the structure of the model serum protein BSA immobilized non-covalently and covalently to cationic, anionic, and zwitterionic polymer brushes as well as to mixed cationic/zwitterionic brush surfaces[15]. The authors found that the structure of the enzyme was preserved most on poly(2-methacryloyloxyethyl phosphorylcholine)-block-poly(aminoethyl methacrylate) brush, which also supported higher enzyme activity relative to the other brush types.

While electrostatic interactions can play an important role in stabilizing proteins on brush surfaces, the grafting density of the brush was also recently shown to be critical to protein stability. Faulón Marruecos and colleagues specifically investigated the effect of the grafting density of PEG brushes on the structure and dynamics of fibronectin (FN) at the brush-solution interface[16]. Using high-throughput SM tracking methods, it was shown that, as the grafting density of PEG increased, unfolded FN was stabilized on the brush surface. The stabilization of unfolded protein was further shown to correlate with an increase in the rate of unfolding of surface-adsorbed protein molecules, as well as an increase in surface residence time and thus decrease in desorption rate constant of unfolded protein molecules from the brush. Importantly, these observations would have been impossible using traditional ensemble structural methods that fail to enable the direct correlation of protein adsorption, desorption, and structure. Notably, in a follow-up paper, the authors found that the increased unfolding and stabilization of surface-adsorbed FN may be explained by an increase in changes in local hydrophobicity in PEG brushes with increasing grafting density[17]. To observe the relationship between local hydrophobicity in the brush and grafting density, the authors developed and applied a novel method based on super-resolution fluorescence mapping, which entailed using an environmentally sensitive fluorescent probe. These findings have

important implications in designing PEG brushes where minimizing the accumulation of unfolded proteins is as important as mediating protein adsorption.

#### 1.1.3.3 Dense Polymer Films and Surfaces

Protein unfolding on polymeric surfaces is of broad interest due to the ubiquitous use of polymer materials in physiological and biologically-active milieus. In a recent study, Fromell and co-workers investigated the impact of the backbone and side-group flexibility of polymer films on the structure of surface-adsorbed complement factor 3 and coagulation factor XII[18]. Conformational changes of both proteins on poly(alkyl methacrlate) films as a function of polymer backbone and side-group flexibility was measured by assaying binding of conformation-specific antibodies. In this case, backbone and side-group flexibility was controlled by using monomers with different lengths and side-group branching. The results of antibody binding assays showed that the conformation of complement factor 3 and coagulation factor XII was perturbed to a larger extent as the rigidity of the polymer increased. Specifically, on hard films consisting of poly(butyl methacrylate), poly(isobutyl methacrylate), and poly(lauryl methacrylate), unfolding of complement factor 3 and coagulation factor XII was greater than on poly(styrene), which is relatively soft and flexible in comparison to the other surfaces. Based on this, it was suggested that the increase in protein stability may be related to the dynamics of the interface between the polymer and the protein. Thyparambyl et al. also investigated the impact of polymer chemistry on the stability of surface-adsorbed proteins to denaturants and surfactants[19]. In this study, the stability of proteins adsorbed to surfaces with three different chemistries (poly(methyl methacrylate), high-density polyethylene, and glass) and exposed to denaturant or surfactant was characterized by circular dichroism. Unexpectedly, their results showed that, the structure of the surface-adsorbed

proteins was the same with and without denaturant (guanidium hydrochloride and urea) added. In fact, in some cases, the surface-adsorbed proteins appeared to adopt a more native-like conformation in the presence of the denaturant, rather than a more unfolded structure. This observation was evident by an increase in helicity of the proteins on the surface in the presence compared to without the denaturant.

Additionally, while demonstrating the utility of hydrogen-deuterium exchange to measure protein unfolding on surfaces, Kim characterized the denaturation of BSA on tissue culture poly(styrene) and poly(propylene)[20]. In this approach, the extent of hydrogen-deuterium exchange was determined after pre-adsorbing BSA to the polymer surfaces and subsequently eluting BSA after exchange from the surface. The degree of exchange of the eluted protein, which correlates with the relative change in solvent exposure of residues in the protein upon unfolding, was measured by mass spectrometry (i.e., MALDI-TOF). Notably, the relative fraction of exchangeable protons in BSA was significantly altered on tissue culture poly(styrene) and poly(propylene) relative to in solution, indicating the conformation of BSA was significantly altered on both surfaces.

Novel computational methods for studying protein structure at interfaces have also been applied to polymer interfaces in recent years. Specifically, Abramyan and co-workers developed an improved method (TIGER2A) to sample conformational states of proteins at interfaces in molecular dynamic simulations[21]. Using this enhanced sampling approach, structural changes in hen egg white lysozyme (HEWL) were studied on the (110) crystal face of high-density poly(ethylene). Notably, in prior work, the authors validated the parameters for force fields to accurately describe the molecular interactions of proteins with the poly(ethylene) surface as well as silica glass and poly(methyl methacrylate) surfaces. The results of simulations using TIGER2A

showed a significant decrease in α-helix and increase in β-sheet content in lysozyme upon interaction with the crystalline surface. Importantly, the extent of such changes, which matched experimental results, were greater than those obtained in simulations using the conventional CHARMM force field. This finding highlights the significance of optimizing the parameters of the force field, which may differ considerably for interfacial systems versus for proteins in solution.

#### 1.1.3.4 High Surface Area Porous Materials

Although widely used in many areas within biotechnology, little is known about how three dimensional porous materials stabilize proteins and enzymes. Kisley and colleagues recently reported the use of fast relaxation imaging with FRET to elucidate the impact of polymer-protein interactions on the stability of proteins within three-dimensional hydrogels[22]. In this approach, spatial differences in the folding stability of proteins within the hydrogel were resolved from ultrafast measurements of thermal protein unfolding. Interestingly, it was shown that the stability of some proteins (e.g., phosphoglycerate kinase) was influenced more strongly by protein-polymer interactions than by the effects of confinement within the hydrogel network. Specifically, interactions between phosphoglycerate kinase and the polyacrylamide backbone enhanced the stability of phosphoglycerate kinase independent of the degree of confinement. However, at elevated temperatures, a decrease in protein stability within the hydrogel relative to in solution was observed, which was apparent by an increase in irreversible aggregation of the enzyme. Liao and co-workers also studied the effects of confinement on the structural stability of enzymes in metal organic frameworks[23]. In this work, the structural stability of catalase, which was immobilized in zeolitic imidazolate frameworks, was determined under denaturing conditions. Using tryptophan fluorescence, the authors showed that steric confinement within the zeolitic imidazolate

frameworks dramatically enhanced the stability of catalase relative to in solution. In this case, even if interactions with the metal organic framework were destabilizing, immobilization in the pores restricted the mobility of the enzyme, which can prevent unfolding.

#### 1.1.3.5 Self-Assembled Monolayers

As model surfaces to study the impact of surface chemistry on protein structure, self-assembled monolayers (SAMs) are favored due to their ease of preparation and range of accessible chemistries. Using optical microcavity sensing, Wilson et al. compared the structure of glucose oxidase on (3-trimethoxysilyl propyl) diethyltriamine, (3-trimethoxysilyl propyl) diethyltriamine, and 2-(methoxypoly( ethyleneoxy)propyl) trimethoxysilane SAMs as well as on unmodified glass[24]. The SAMs were prepared on a custom-built whispering gallery mode resonator, which enabled the sensitive measurement of protein adsorption kinetics and layer formation. From the kinetics of protein adsorption and layer formation, changes in the structure of glucose oxidase were inferred, and these structural changes were greatest on the fluorinated SAM and bare glass. The denaturation of glucose oxidase on these surfaces was thought to result from the formation of multiple protein layers, which may promote interfacial protein aggregation. Faulón Marruecos et al. studied the dynamics and conformational changes of FN via high-throughput SM fluorescence studies on two distinct SAMs: oligo(ethylene glycol) (OEG) and trimethylsilyl (TMS), which are hydrophilic and hydrophobic, respectively[25]. The results showed that FN was more conformationally labile and dynamic on TMS than OEG. Remarkably, unfolded FN molecules resided for shorter times on TMS than OEG, indicating that unfolded molecules interacted weaker with the hydrophobic surface with respect to the hydrophilic surface. Similarly, the strength of

protein interactions with the surface can be related to how easily they desorb (i.e., can be eluted) from a surface after rinsing steps.

### 1.1.4 Hard Material Interfaces

#### 1.1.4.1 Metal Nanostructures

In recent years, there has been increasing interest in metal nanoparticles (NPs) and nanorods (NRs) because of their unique physicochemical properties, nanometer size, plasmonic behavior, and biocompatibility. However, the rapid formation of protein coronas around metallic surfaces in physiological environments plays a critical role in the fate of the nanomaterial, which depends on the orientation, conformation, and composition of adsorbed proteins. Furthermore, the interactions between proteins and NPs are highly dependent on the morphology of the material. In a recent study, Chatterjee and co-workers used far-UV circular dichroism and tryptophan fluorescence to elucidate the conformational changes of accessory cholera enterotoxin (Ace) in contact with AuNPs of various sizes and shapes[26]. The authors used gold NRs of 10 nm cross-section and 38 nm length (AuNR10), and nanospheres of 10 and 100 nm diameter (AuNS10 and AuNS100, respectively). The authors found that the AuNR10 and AuNS100 induced a similar high degree of Ace unfolding (via chemical and thermal denaturation), while AuNS10 preserved the native conformation of the protein. The authors suggested that the large radius of curvature of AuNS100 and the high aspect ratio of AuNR10 increased the surface area of the nanomaterial and thus facilitated both stronger interactions and greater conformational perturbations of the protein. Additionally, in vivo experiments with mice revealed the efficacy of AuNR10 and AuNS100 for reduced fluid accumulation in the ileal loop, indicative of the loss of activity of Ace. Similarly,

Raoufi et al. studied the changes in conformation of FRET-labelled FN that adsorbed to bare and corona-coated AuNPs as a function of NP size, NP concentration, and solution pH[27]. The conformation of FN was indicated by the average FRET ratio of donor-to-acceptor fluorophores of nonspecifically labelled FN molecules. It was found that labelled FN proteins that directly accessed the bare AuNPs underwent a larger degree of unfolding, while FN molecules that associated with the protein corona via protein-protein interactions better preserved their native conformation. Additionally, the results showed that lower solution pH and smaller NPs had a greater stabilizing effect on FN, in agreement with the findings of Chatterjee and co-workers described above. Notably, higher concentrations of NPs led to higher FN stability for protein-coated NP, but not for bare AuNPs, which was attributed to the stabilizing effect of protein-protein interactions over protein-gold interactions.

Another example of the role of protein concentration on protein-NP interactions are the results reported by Dominguez-Medina et al.[28] The authors combined super-localization microscopy imaging and ensemble-level characterization tools to elucidate the mechanisms involved in AuNR and BSA association as a function of protein concentration. Interestingly, they found that incubation of NPs with low concentrations of BSA led to single-protein irreversible adsorption and unfolding on the particles, which triggered particle aggregation and increased cellular uptake by cancer cells, as compared to incubation with high concentrations of BSA. Conversely, higher concentrations of BSA led to the formation of a monolayer that prevented unfolding and consequent aggregation of the NPs. Remarkably, these observations held true for cationic-coated AuNPs, but not anionic-coated NPs. Furthermore, when fibrinogen and globulin were used instead of BSA, aggregation was observed at any concentration, highlighting the unique behavior and role of BSA. However, in a recent study by Capomaccio et al., it was shown that the

mere presence of citrate-stabilized AuNPs in solution protected human serum albumin (HSA) from losing its secondary structure under stressing conditions, such as UV irradiation, elevated temperatures, and storage under suboptimal conditions, as measured by synchrotron radiation circular dichroism[29]. The authors suggested that AuNPs could protect proteins from UV-induced damage by adsorbing part of the UV radiation, scavenging free radicals, or simply due to their negative surface charge, which could stabilize the negatively charged HSA molecules at physiological pH. Furthermore, thermal denaturation studies indicated that AuNPs likely stabilized HSA both by increasing its thermal stability and by reducing its propensity to aggregate.

While gold is the most commonly used metal in the field, other metals like silver and iron have also been explored for their unique properties. For example, Raghavendra et al. studied the interactions between apolipoprotein A-I (ApoA-I) and 100 nm silver NPs (AgNPs) with surfaces modified by four different surface functional groups (lipoic acid, PVP, citrate, and bPEI)[30]. Dynamic and electrophoretic light scattering studies showed that ApoA-I displaced surface coatings such as citrate, PVP, and bPEI. Circular dichroism studies showed that ApoA-I exhibited a loss in secondary structure >40% on all AgNPs, leading to complete loss of alpha-helix content for AgNP-bPEI and AgNP-lipoic acid. Furthermore, the authors used cyclic voltammetry (CV) to provide evidence for charge transfer interactions between proteins and the NP surface, which was believed to play an important role in ApoA-I unfolding. Specifically, stabilizing charges were transferred between proteins and the surface, as indicated by the appearance of peaks in current during CV scans. The changes in secondary structure correlated with the observed charge transfer between ApoA-I and AgNPs. While the unfolding of ApoA-I on AgNPs did not significantly affect their uptake and cytotoxicity, they strongly altered the generation of reactive oxygen species. Aghili et al. studied the interaction of HEWL with iron NPs (FeNPs)[31]. The authors showed that

the addition of HEWL to FeNPs caused an increase in charge distribution of the system, which mitigated aggregation and increased colloidal stability, as revealed by zeta potential and dynamic light scattering studies. The authors also showed via fluorescence quenching and protein-ligand docking studies that the protein-NP interactions involved hydrogen bonding and van der Waals interactions. However, synchronous fluorescence spectroscopy of HEWL-FeNP showed that the emission maximum wavelength of tryptophan was red-shifted, which indicated solvent exposure of hydrophobic residues. While circular dichroism experiments did not show any change in secondary structure with increasing concentrations of FeNP, there was a considerable decrease in melting temperature of HEWL in the presence of FeNP, which suggested the presence of unfavorable interactions.

#### 1.1.4.2 Metal Oxides

Metal oxide nanomaterials and surfaces are ubiquitous in the biomedical arena. Their relatively low toxicity to human cells, low cost, effective inhibition against a wide range of bacteria, numerous options for surface modification, and large-scale synthetic availability make them an attractive material for drug delivery, biomaterial design, and therapeutics, among others. Nevertheless, the understanding of protein adsorption and subsequent conformation changes upon contact with these materials, which can dictate the effectiveness and fate of the material, remains elusive. In the recent work done by Satzer et al., in which the authors studied the interactions of nine different proteins with silica NPs, it was found that only BSA and myoglobin underwent conformational changes upon adsorption, and that the changes were dependent on NP size (ranging from 30 to 1000 nm)[32]. In particular, conformational changes were observed only for particles

bigger than 150 nm. The authors used circular dichroism to track conformational changes as a function of NP size and time, which allowed for the measurement of myoglobin and BSA unfolding kinetics. Another recent study involving silica NPs was performed by Vitali et al., in which the authors compared the conformational properties of three intrinsically disordered proteins (IDPs) with lysozyme inside the hard corona (HC) of silica NPs using circular dichroism and FTIR spectroscopy[33]. IDPs inside HC preserved a large degree of structural disorder but exhibited minor increases in secondary structure and stabilization against further conformational transitions upon dehydration. Conversely, lysozyme lost helical segments in HC, as expected for globular proteins that adsorb on NP surfaces. Interestingly, it was observed that NPs enhanced α-synuclein aggregation kinetics in a dose-dependent fashion, despite the HC-induced increase of helical content in the protein rather than β-sheet. This observation suggested that the soft corona and local protein concentration likely modulate amyloid formation.

The use of silica in biomedical and biotechnological applications is not restricted to NPs; macroscopically flat surfaces are also widely used. For example, Perevozchikova et al. studied the aggregation of α-chymotrypsinogen (CT) and a monoclonal antibody (IgG1) mediated by their adsorption to water-silicon oxide (SiOx) interfaces, as a function of pH and ionic strength[34]. The authors performed neutron reflectivity on protein layers adsorbed to SiOx surfaces before and after rinsing steps. IgG1 molecules were found to lie flat on the SiOx surface upon adsorption and two layers were formed: a primary layer that was resistant to desorption and a diffuse overlayer that was easily removed by rinsing. In contrast, CT molecules, which are spherical, were easily removed if folded, but rarely left the surface if they appeared to be unfolded at the interface. The proteins that desorbed comprised mainly a mixture of monomer and small amounts of high molecular weight aggregates (for CT) or sub-visible particles (for IgG1). Additionally, the authors

observed changes in adsorption and unfolding with pH, which underscored the important role of electrostatic interactions in all cases.

SM studies have also been recently used to correlate the dynamics and unfolding of proteins on silica surfaces, which has led to newfound insight into the mechanisms of surface-induced denaturation. For example, Weltz and co-workers directly measured intermittent hopping diffusion and changes in the structure of T4 lysozyme on fused silica at the SM level by combining TIRF microscopy and FRET[35]. The results suggested that the unfolding of lysozyme on fused silica was mediated by surface diffusion and took place on rare nanoscale niches (i.e., denaturing sites) that exhibited distinct properties relative to the rest of the surface (**Figure 1.3 A** and **1.3 B**). These findings suggested that surface-mediated protein unfolding is a search process in which protein molecules explore the surface until they find a denaturing site. Gruian et al. used electron paramagnetic resonance spectroscopy in combination with site-directed spin labeling to investigate single protein and competitive adsorption kinetics of horse hemoglobin and BSA on a silica–calcium–phosphate bioceramic substrate[36]. Specifically, the authors tracked local mobility/flexibility changes within the proteins and tertiary structure dynamics upon adsorption. The results showed that the amount of adsorbed hemoglobin was significantly higher than that of BSA independent of buffer pH, and that hemoglobin had more anchoring points to the bioceramic substrate and could dissociate into smaller subunits to facilitate adsorption. Interestingly, when the substrate was covered by a layer of BSA, the native oligomeric structure of hemoglobin was preserved and dissociation was reduced by 71%. Additionally, solution pH, which changed the overall surface charge of the proteins, influenced both electrostatic and hydrogen bonds formed between the proteins and the substrate. Kubiak et al. also studied the adsorption of BSA, which is negatively charged at physiological conditions, to a model silica surface that was also negatively

charged using fully atomistic molecular dynamics in order to elucidate the effects of charge on protein-silica interactions[37]. The results provided detailed understanding of the electrostatic interactions that bind BSA molecules to silica, which were highly dependent on the orientation of the protein. For example, in the correct orientation, lysine residues extended toward the surface and created strong anchors that led to a stable adsorbed state, whereas in a partially correct orientation the protein desorbed easily. Overall, the negatively charged domains were kept away from the surface and the presence of counterions screened its repulsive influence.

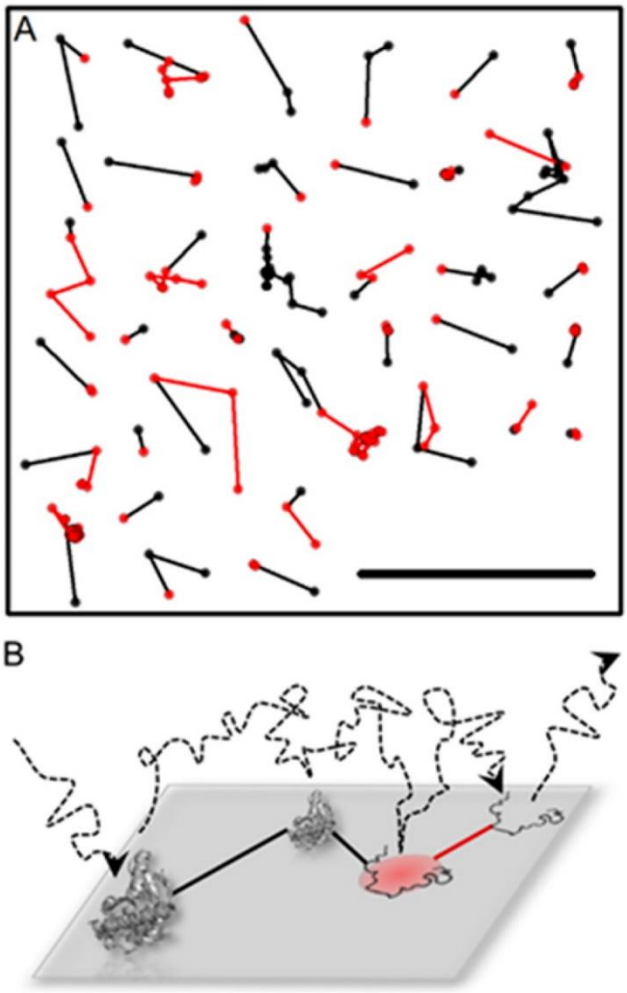


**Figure 1. 3.** SM observation of interfacial diffusion and conformation of T4 lysozyme at the fused silica-water interface, adapted from[35]. Molecular surface trajectories were tracked via high-throughput TIRF microscopy while simultaneously observing protein conformation with SM-FRET. A) Representative two-dimensional projections of the intermittent hopping trajectories of individual molecules of lysozyme on the fused silica surface from SM analysis. The apparent intermittent hopping diffusion entails a three-dimensional random walk in the bulk solution (adjacent to the surface) by the enzyme molecule before re-adsorbing at a new site. The trajectories were segmented based on conformation, with the black segments representing the portion of the trajectory where the molecule was folded and the red segments representing the portion of the trajectory where the molecule was unfolded. B) Based on SM analysis of the trajectories, a new model for surface-induced unfolding was proposed, which involved unfolding on anomalous surface sites that may arise from spatial heterogeneities in chemistry and/or topology.

Other metal oxides like alumina can be appealing in applications that require high stability of the particles and zeta potential in wide pH ranges. Interestingly, it has been shown that alumina-assisted renaturation of enzymes can give rise to the so-called "Phoenix" effect, which consists of an increased activity (180%) of renatured enzymes compared to the free enzyme in solution[38]. More recently, Volodina et al developed a high-yield method for the renaturation of negatively charged enzymes[39]. Briefly, the complexation of sol-gel alumina NPs with chemically denatured enzymes led to the refolding and prevention of aggregation of the enzymes on the alumina surface, as measured by activity assays and synchronous fluorescence. The refolded enzymes could then be easily removed from the surface by increasing the solution pH and the NPs could be recycled. Magnetic NPs, such as iron oxide NP (IONPs), are widely used in medical diagnosis and therapy, and treatment for tumor cells. Ghosh et al investigated the relationship between structure and function of HEWL and calf intestine alkaline phosphatase (CIAP) after their interaction with charged ligand-counterions coated IONPs in water, which provided a positive or negative charge to the surface of the particles[40]. The secondary structure of proteins was characterized using far UV circular dichroism spectroscopy, which showed that both proteins were irreversibly unfolded after incubation with IONPs due to counterion diffusion into the hydrophobic core of the bound proteins. Furthermore, unfolded proteins lost their bioactivity, as measured by activity assays, which proved the structure-function correlation of both HEWL and CIAP.

#### 1.1.4.3 Graphitic Materials

Graphitic materials such as carbon nanotubes (CNT) are promising nanomaterials for many biomedical and biotechnological applications (e.g., biomaterials or substrates for biosensors), due to their unique physicochemical properties, such as nanoscale diameter, wide size and length

distribution, and high aspect ratio, among others. Nevertheless, their toxicity to microorganisms has been reported, and associated important issues such as biocompatibility require a better understanding of protein adsorption and conformational state of the adsorbed protein molecules on graphitic materials. Zeinabad et al. studied the interaction of the single wall carbon nanotubes (SWCNT) and multiwall carbon nanotubes (MWCNT) with tau protein using far and near circular dichroism and fluorescence spectroscopy, among other techniques[41]. The results showed that SWCNT induced a higher degree of unfolding of tau proteins relative to MWCNT. Furthermore, while both types of CNT impaired the viability and complexity of PC12 cells, SWCNT induced apoptotic models of cell death and MWCNT induced necrotic modes. Chen et al. investigated the conformational changes of two microbial enzymes (lignin peroxidase and maleylpyruvate isomerase) in the presence and absence of SWCNTs by MD simulations[42]. The results showed that SWCNTs caused significant conformational changes in both enzymes, such as backbone fluctuations and changes in both protein compactness and cavities. Additionally, SWCNT interfered with microbial protein–protein interaction patterns. Such changes in enzyme conformation may inactivate the enzymes and disrupt the microbial metabolism. In a recent simulation study, Xu et al. used fully atomistic simulations to study the unfolding mechanisms of ubiquitin upon passage through a CNT-based nanopore[43]. One end of the protein was subjected to an external force, while the secondary structural components were sequentially peeled from the protein as it was pulled through the pore, exhibiting non-canonical unfolding behavior. Interestingly, the remaining part isolated above the nanopore maintained native-like characteristics, leading to the formation of stable intermediate states called “unfoldon”. Thus, pore-mediated unfolding proceeded via a many-state mechanism in which unfoldon intermediates progressively emerged and diminished.

Akhterov et al. immobilized T4 lysozyme on a CNT transistor to electronically monitor the conformational transitions of the enzyme as it reacted with the support[44]. The high temporal resolution of the method (2 μs) allowed for the direct observation of the transitions between lysozyme's open and closed conformations. The authors found that the motion from one conformation to the other lasted 37 μs on average, independently of the direction and whether the motion occurred during catalysis or nonproductive motions. Furthermore, the observation of smooth, continuous transitions indicated a concerted mechanism for glycoside hydrolysis with lysozyme's two domains closing upon the polysaccharide substrate in its active site. In another SM study, Barinov et al. used high-resolution AFM to demonstrate that highly oriented pyrolytic graphite (HOPG) induced denaturation of four blood plasma proteins: ferritin, fibrinogen, HSA and IgG[45]. The authors measured a decrease in the height of protein globules and a spreading of the unfolded molecules on the surface. Interestingly, when the surface was coated with a monolayer of oligoglycine-hydrocarbon, which is amphiphilic, the proteins preserved their native-like conformation. Finally, the unique properties of graphitic materials have remarkable applications, such as the ability to obtain holographic images of adsorbed proteins. Longchamp et al. developed a method to reveal the structural details of proteins (cytochrome C, BSA, and hemoglobin) at a SM level with sub-nanometer resolution[46]. The authors used low-energy electron holography to image individual protein molecules that were deposited via electrospray on freestanding graphene, which enabled chemical and conformational selection of the protein deposition.

### 1.1.5 Conclusions and Outlook

Building on a long history of studying the impact of near-surface environments on protein structure, recent studies have provided an improved understanding of the factors that contribute to surface-mediated protein unfolding. For example, the use of novel SM microscopy methods has provided unprecedented insight into the role of interfacial protein dynamics (e.g., adsorption, desorption, folding/re-folding, and intermittent hopping diffusion) on unfolding in near-surface environments. Furthermore, these methods have shown that various types of heterogeneities (e.g., dynamic, spatial, and population) can play a prominent role in modulating protein conformation. However, while qualitative correlations between surface properties (including charge and hydrophobicity) and protein unfolding exist, the ability to quantitatively predict the impact of materials on protein conformation remains elusive. For instance, while trends with respect to the impact of nanoparticle size on protein stability have been observed, these trends are highly dependent on the protein, environmental conditions, and surface properties of the nanoparticle. Ultimately, despite advances achieved through decades of research, it is critical to consider the details of the system being studied, and how differences between systems may impact the mechanisms of protein unfolding (or stabilization). Although a predictive understanding of surface-mediated protein unfolding remains elusive, advances in biophysical and computational methods present considerable opportunities. Of particular interest is exploring how molecular dynamic simulations may be combined with state-of-the-art microscopy and spectroscopy methods, which can access different timescales, to address this problem.

### 1.1.6 References


* Of special interest

** Of outstanding interest

(1) Secundo, F. *Chem. Soc. Rev.* **2013**, *42*, 6250–6261.
(2) Sheldon, R. A.; van Pelt, S. *Chem. Soc. Rev.* **2013**, *42*, 6223–6235.
(3) Mohamad, N. R.; Marzuki, N. H. C.; Buang, N. A.; Huyop, F.; Wahab, R. A. *Biotechnol. Equip.* **2015**, *29*, 205–220.
(4) Vénéreau, E.; Ceriotti, C.; Bianchi, M. E. *Front. Immunol.* **2015**, *6*, 1–11.
(5) Chung, L.; Maestas, D. R.; Housseau, F.; Elisseeff, J. H. *Adv. Drug Deliv. Rev.* **2017**, *114*, 184–192.
(6) Andorko, J. I.; Jewell, C. M. *Bioeng. Transl. Med.* **2017**, *2*, 139–155.
(7) Moussa, E. M.; Panchal, J. P.; Moorthy, B. S.; Blum, J. S.; Joubert, M. K.; Narhi, L. O.; Topp, E. M. *J. Pharm. Sci.* **2016**, *105*, 417–430.
(8) Jiskoot, W.; Kijanka, G.; Randolph, T. W.; Carpenter, J. F.; Koulov, A. V.; Mahler, H. C.; Joubert, M. K.; Jawa, V.; Narhi, L. O. *J. Pharm. Sci.* **2016**, *105*, 1567–1575.
(9) Randolph, T. W.; Carpenter, J. F. *AIChE J.* **2007**, *53*, 1902–1907.
(10) Findlay, H. E.; Booth, P. J. *Sci. Rep.* **2017**, *7*, 1–12.
(11**) Chaparro Sosa, A. F.; Kienle, D. F.; Falatach, R. M.; Flanagan, J.; Kaar, J. L.; Schwartz, D. K. *ACS Appl. Mater. Interfaces* **2018**, *10*, 19504–19513.

This paper provides direct evident of the mechanism of stabilization of proteins in contanct with lipid bilayers, which involves a chaperone-like mechanism whereby the bilayer actively mediates re-folding of the protein.

(12) Fang, X.; Yang, T.; Wang, L.; Yu, J.; Wei, X.; Zhou, Y.; Wang, C.; Liang, W. *Biomaterials*. **2016**, *77*, 139–148.
(13) Moree, B.; Connell, K.; Mortensen, R. B.; Liu, C. T.; Benkovic, S. J.; Salafsky, J. *Biophys. J.* **2015**, *109*, 806–815.
(14) Koenig, M.; Bittrich, E.; König, U.; Rajeev, B. L.; Müller, M.; Eichhorn, K. J.; Thomas, S.; Stamm, M.; Uhlmann, P. *Colloids Surfaces B Biointerfaces* **2016**, *146*, 737–745.
(15) Takasu, K.; Kushiro, K.; Hayashi, K.; Iwasaki, Y.; Inoue, S.; Tamechika, E.; Takai, M. *Sensors Actuators, B Chem.* **2015**, 216, 428–433.
(16*) Faulón Marruecos, D.; Kastantin, M.; Schwartz, D. K.; Kaar, J. L. *Biomacromolecules* **2016**, *17*, 1017–1025.

This paper shows that the protein adsorption and unfolding are inversely affected variations in grafting density of PEG brush surfaces, which has important implications for the rational design of PEG brushes as coatings for protein and blood-contacting materials.

(17) Faulón Marruecos, D.; Kienle, D. F.; Kaar, J. L.; Schwartz, D. K. *ACS Macro Lett.* **2018**, *7*, 498–503.

(18) Fromell, K.; Yang, Y.; Ekdahl, K. N.; Nilsson, B.; Berglin, M.; Elwing, H.; Fromell, K. *Biointerphases* **2017**, 12, 02D417.
(19) Thyparambil, A. A.; Wei, Y.; Latour, R.A. *Langmuir* **2015**, 31, 11814–11824.
(20) Kim, J. *Colloids Surfaces B Biointerfaces* **2016**, *141*, 513–518.
(21*) Abramyan, T. M.; Hyde-Volpe, D. L.; Stuart, S. J.; Latour, R. A. *Biointerphases* **2017**, *12*, 02D409.

This paper reports the optimization of the parameters for force fields for analyzing the impact of interfaces on protein structure via molecular dynamics simulations.

(22**)Kisley, L.; Serrano, K. A.; Guin, D.; Kong, X.; Gruebele, M.; Leckband, D. E. *ACS Appl. Mater. Interfaces* **2017**, *9*, 21606–21617.

This paper reports the development of an approach to characterize the folding stability of proteins in three-dimensional materials with spatial resolution that is based on single-molecule fast relaxation imaging, which was combined with FRET.

(23*) Liao, F. S.; Lo, W. S.; Hsu, Y. S.; Wu, C. C.; Wang, S. C.; Shieh, F. K.; Morabito, J. V.; Chou, L. Y.; Wu, K. C. W.; Tsung, C. K. *J. Am. Chem. Soc.* **2017**, *139*, 6530–6533.

This paper reports the dramatic stabilization of catalase upon immobilization in metal organic frameworks under extremely denaturing conditions, which was attributed to confinement effects.

(24) Wilson, K. A.; Finch, C. A.; Anderson, P.; Vollmer, F.; Hickman, J.J. *Biomaterials* **2015**, *38*, 86–96.
(25) Kastantin, M.; Faulón Marruecos, D.; Grover, N.; Yu McLoughlin, S.; Schwartz, D. K.; Kaar, J. L *J. Am. Chem. Soc.* **2017**, *139*, 9937-9948.
(26) Chatterjee, T.; Chatterjee, B. K.; Saha, T.; Hoque, K. M.; Chakrabarti, P. *Biochim. Biophys. Acta.* **2017**, *1861*, 977–986.
(27) Raoufi, M.; Hajipour, M.J.; Kamali Shahri, S.M.; Schoen, I.; Linn, U.; Mahmoudi, M. *Nanoscale* **2018**, *10*, 1228–1233.
(28*) Dominguez-Medina, S.; Kisley, L.; Tauzin, L. J.; Hoggard, A.; Shuang, B.; Indrasekara, A. S. D. S.; Chen, S.; Wang, L. Y.; Derry, P. J.; Liopo, A.; Zubarev, E. R.; Landes, C. F.; Link, S. *ACS Nano* **2016**, *10*, 2103–2112.

This paper provides novel insight into the consequences of nanoparticle-mediated protein unfolding, which were shown to be impacted by protein concentration using super-localization microscopy.

(29) Capomaccio, R.; Osório, I.; Ojea-Jiménez, I.; Ceccone, G.; Colpo, P.; Gilliland, D.; Hussain, R.; Siligardi, G.; Rossi, F.; Ricard-Blum, S.; Calzolai, L. *Biointerphases* **2016**, *11*, 04B310.
(30) Raghavendra, A. J.; Alsaleh, N.; Brown, J. M.; Podila, R. *Biointerphases* **2017**, *12*, 02D402.
(31) Aghili, Z.; Taheri, S.; Zeinabad, H. A.; Pishkar, L.; Saboury, A. A.; Rahimi, A.; Falahati, M. *PLoS One* **2016**, *11*, 1–21.

(32) Satzer, P.; Svec, F.; Sekot, G.; Jungbauer, A. *Eng. Life Sci.* **2016**, *16*, 238–246.
(33) Vitali, M.; Rigamonti, V.; Natalello, A.; Colzani, B.; Avvakumova, S.; Brocca, S.; Santambrogio, C.; Narkiewicz, J.; Legname, G.; Colombo, M.; Prosperi, D.; Grandori, R. *Biochim. Biophys. Acta-Gen Subj.* **2018**, *1862*, 1556–1564.
(34) Perevozchikova, T.; Nanda, H.; Nesta, D. P.; Roberts, C. J. *J. Pharm. Sci.* **2015**, *104*, 1946–1959.
(35*) Weltz, J. S.; Schwartz, D. K.; Kaar, J. L. *ACS Nano* **2016**, *10*, 730–738.

This paper highlights the utility of SM methods to simultaneously observe and connect diffusive behavior and perturbations in protein structure, which could not be resolved with traditional biophysical methods. By connecting diffusive behavior and perturbations in protein structure, a new paradigm for the mechanism of protein unfolding on surfaces was presented.

(36) Gruian, C. M.; Rickert, C.; Nicklisch, S. C. T.; Vanea, E.; Steinhoff, H. J.; Simon, S. *ChemPhysChem.* **2017**, *18*, 634–642.
(37) Kubiak-Ossowska, K.; Jachimska, B.; Mulheran, P. A. *J. Phys. Chem. B.* **2016**, *120*, 10463–10468.
(38) Vinogradov, V. V.; Avnir, D. *Sci. Rep.* **2015**, *5*, 1–7.
(39) Volodina, K. V.; Avnir, D.; Vinogradov, V. V. *Sci. Rep.* **2017**, *7*, 1–7.
(40) Ghosh, G.; Gaikwad, P. S.; Panicker, L.; Nath, B. B.; Mukhopadhyaya, R. *Colloids Surfaces B Biointerfaces* **2016**, *145*, 194–200.
(41) Zeinabad, H. A.; Zarrabian, A.; Saboury, A. A.; Alizadeh, A. M. O.; Falahati, M. *Sci. Rep.* **2016**, *6*, 26508.
(42) Chen, M.; Zeng, G.; Xu, P.; Yan, M.; Xiong, W.; Zhou, S. *Environ. Sci. Nano.* **2017**, *4*, 1954–1960.
(43) Xu, Z.; Zhang, S.; Weber, J. K.; Luan, B.; Zhou, R.; Li, J. *Nanoscale* **2016**, *8*, 12143–12151.
(44) Akhterov, M. V.; Choi, Y.; Olsen, T. J.; Sims, P. C.; Iftikhar, M.; Gul, O. T.; Corso, B. L.; Weiss, G. A.; Collins, P. G. *ACS Chem. Biol.* **2015**, *10*, 1495–1501.
(45) Barinov, N. A.; Prokhorov, V. V.; Dubrovin, E. V.; Klinov, D. V. *Colloids Surfaces B Biointerfaces* **2016**, *146*, 777–784.
(46) Longchamp, J. N.; Rauschenbach, S.; Abb, S.; Escher, C.; Latychevskaia, T.; Kern, K.; Fink, H. W. *Proc. Natl. Acad. Sci.* **2017**, *114*, 1474–1479.

## 1.2 Objectives

The objective of this thesis is to elucidate the molecular mechanisms that drive protein adsorption, conformational changes, and dynamics of ligand-receptor binding on surfaces as a function of the chemical composition and architecture of the surface in order to modulate cell response. To accomplish so, single-molecule methods were utilized via fluorescence microscopy studies. Three broad approaches were used. First, the effects of polymer brush grafting density on protein adsorption and stability were characterized. Second, the dependence between ligand-receptor binding and protein conformation were tested as a function of surface chemistry. Third, the correlation between surface functionalization and cell response through protein stability were studied via the synthesis of random co-polymers and macrophage activation measurements. The work was broken down into three main aims:

1. Characterize protein *adsorption* and *stabilization* on PEG brushes as a function of grafting density (Chapters III and IV)
2. Connect ligand-receptor *binding* and protein *conformation* as a function of surface chemistry (Chapter V)
3. Improve protein *stabilization* by creating chemically heterogeneous polymer brushes (Chapter VI)

# Chapter II: Background

## 2.1 The Foreign Body Response to Biomaterials

Blood/tissue interactions with biomaterials take place immediately after bio-implantation[1]. First, plasma proteins rapidly adsorb on and around the surface of the material, which leads to the formation of a transient provisional matrix (i.e., initial thrombus) (**Figure 2.1**). This provisional matrix is rich in proteins like fibronectin, fibrinogen, and complement, as well as cytokines and growth factors. Altogether, the components of the matrix recruit cells of the innate immune system to the wound/implantation site, which initiates an acute inflammation. After this point, the fate of the biomaterial implantation will depend on the extent of injury and the physicochemical properties of the material, which could develop into either chronic inflammation (i.e., associated to tissue fibrosis and scarring) or wound healing. The outcome of biomaterial implantation is highly regulated by the proteins that adsorb on the surface of the material and, more importantly, the conformational changes that they undergo at the biomaterial-blood/tissue interface[2].

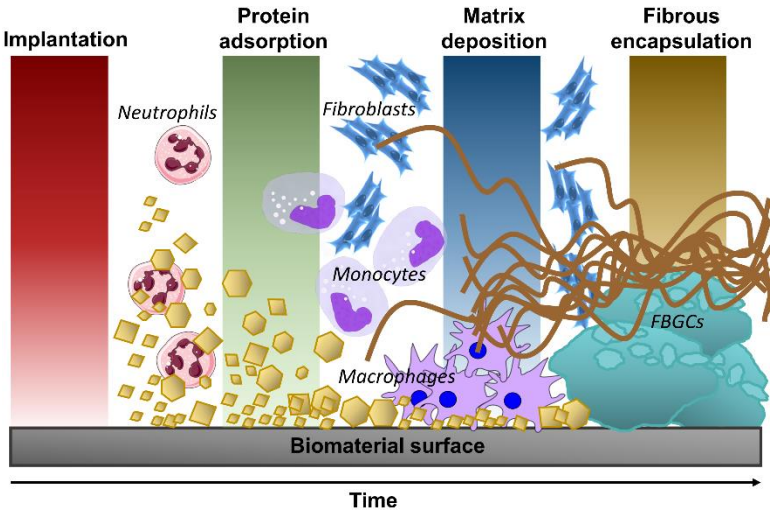


**Figure 2. 1.** Immune system reaction to the implantation of biomaterials, leading encapsulation.

Macrophages, derived from monocytes, respond very rapidly to the adsorbed proteins and are the main infiltrating cells. Particularly, the protein layer can influence monocyte/macrophage

adhesion and cell surface receptor-initiated mechanisms such as cytoskeletal organization, spreading, fusion to form multinucleated giant cells (FMGC), and apoptosis[3]. Depending on local stimuli, macrophages can be polarized into pro-inflammatory (M1) (classically activated) or anti-inflammatory (M2) (alternatively activated) macrophages (**Figure 2.2**). Specifically, alternatively activated macrophages can be divided into wound-healing and regulatory macrophages. However, there are many shades of activation between the three above-mentioned types, resulting in a spectrum of macrophage populations based on their function profiles (e.g., phagocytosis, adhesion, and cytokine release). The polarization of macrophages defines the type and outcome of immune defense and tissue regeneration[4–6].

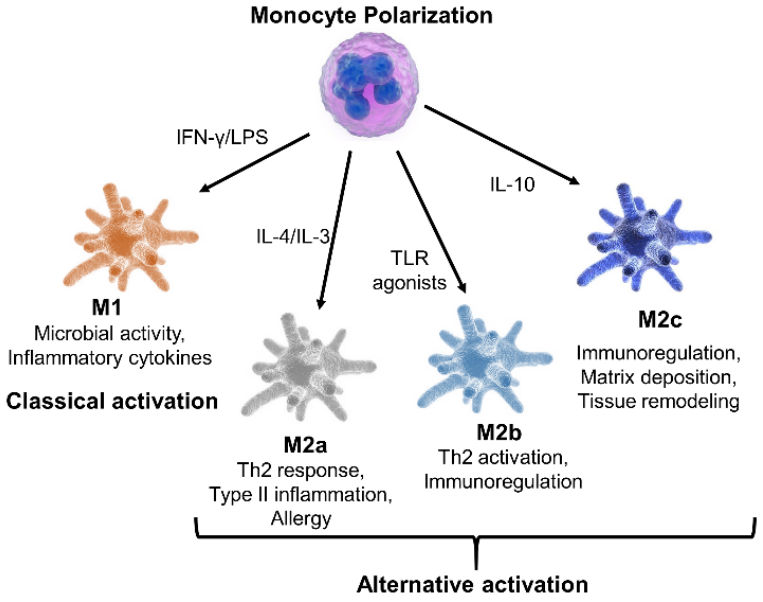


**Figure 2. 2.** Plasticity in the macrophage activation states.

Clinically, the FBR reaches relevance when triggered by medical devices and/or implants, including sensors, pacemakers, prostheses, devices for release of bioactive compounds and, more recently, scaffolds used in tissue engineering and regenerative medicine[1,7]. Inflammation and fibrosis are detrimental processes that compromise implant integration and long-term

functionality. Specifically, these processes may impair the bioactivity of the implant via the blockage of signaling between the biomaterial and the surrounding tissue due to the fibrous barrier or by accelerating biomaterial degradation[8]. Therefore, new strategies to control the inflammatory phase of the FBR and to limit fibrosis are critical to improve implant integration and long-term function. In order to successfully engineer biocompatible materials, it is critical to understand the molecular mechanisms underlying protein adsorption and unfolding on biomaterial surfaces, and how the physicochemical properties of the material affect the presentation of ligands that bind macrophage surface receptors[9]. The ligands that are more relevant to macrophage binding are found in ECM proteins, such as fibronectin, which have high affinity for interfaces and a great ability to undergo conformational changes. In the next sections, more detail about the ECM, fibronectin, and cell binding will be discussed.

### 2.1.1 The Extracellular Matrix

The ECM comprises the noncellular component of tissues, including water, proteins, and polysaccharides. Although the basic components remain the same, the ECM of each tissue has a unique composition and organization. In addition, the ECM of a tissue is highly dynamic and undergoes remodeling by cells, as well as changes in its structure by post-translational modifications to several ECM proteins. Fibrous ECM proteins such as collagen and FN, as well as glycosaminoglycans such as hyaluronic acid (HA), form complex three-dimensional scaffolds that mechanically support cells[10]. This support can exert signaling cues through a process known as mechanotransduction. For example, it has been shown that varying the rigidity of ECM substrate can affect the behavior of cells (e.g., adhesion, migration, and differentiation)[11–13]. In addition, the ECM also provides a large number of biochemical cues to cells through the presentation of specific

amino acid-binding sequences. Cells bind to ECM proteins through ECM receptors such as syndecans, discoidin domain receptors, and most importantly for this work, integrins[14–16]. Integrin binding to ECM proteins initiates signaling responses in cells that control cell behavior and, in turn, orchestrate many physiological processes (**Figure 2.3**). FN is the main ECM protein involved in cell behavior thanks to its ability to bind integrins, other ECM proteins, growth factors, and itself[17,18]. As a result, FN plays a key role in many cell and tissue behaviors, such as morphogenesis and wound healing. FN is capable of binding different integrins, and the selectivity of integrin association can lead to distinct cell responses.

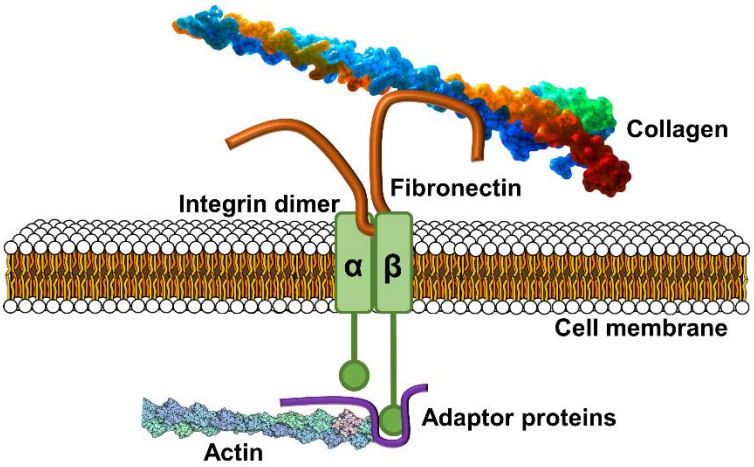


**Figure 2. 3.** Integrin connects the ECM with the actin cytoskeleton inside the cell.

### 2.1.2 FN Structure

FN is a dimeric glycoprotein containing two identical ~250 kDa subunits that are covalently linked through a pair of disulfide bonds near their C-termini. Each subunit is composed of three types of repeating modules: Type I (12 modules), Type II (2 modules), and Type III (15–17 modules) (**Figure 2.4**). Type III repeats, the ones of interest for this work, are ~90 amino acids long, composed of antiparallel β-sheets linked together with flexible loops and stabilized mainly

by hydrogen bonds[19–22]. As a result, Type III repeats are highly sensitive to force-mediated unfolding, which make FN a key mechanotransducer[23]. Fibronectin is present as soluble form in body fluids (plasma FN) and insoluble fibrils in ECM matrices (cellular FN). While the role of plasma FN in physiology and pathology remains elusive, plasma FN conditional knockout mice studies have shown that plasma FN modulates the FBR to biomaterial discs implanted subcutaneously[24,25].

As discussed previously, a major role of FN is the regulation of integrin binding. Although there are many different integrins that bind to FN, the classic receptors are the α5β1 integrin receptor and the $\alpha_V\beta_3$. An isolated peptide sequence arginine–glycine–aspartic acid–serine (RGDS) has been identified as a key cell-binding site within FN, and a second, distant synergistic site (PHSRN) within the cell-binding domain provides recognition effectively mediating adhesion and cytoskeletal organization[26–28]. The next section is dedicated to the selectivity of integrin binding as a function of FN conformation.

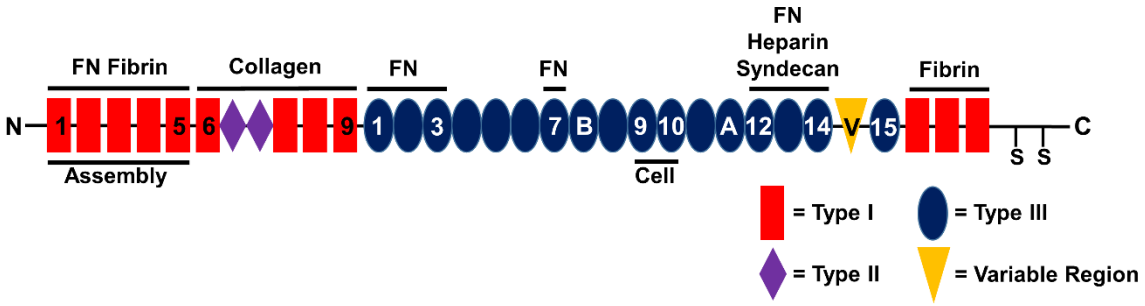


**Figure 2. 4.** The modular structure of FN and its binding domains.

### 2.1.3 Integrin-FN Binding

Integrins are heterodimeric proteins containing one α-subunit and one β-subunit that physically connect the intracellular protein complexes and the extracellular environment[16]. Some

integrins can bind multiple ECM proteins, and some ECM proteins can bind to different integrin heterodimers. The presentation of specific ligands located in ECM proteins dictate which integrins bind. The active site pocket in integrins that binds peptides and provides ligand specificity is located between the α- and β-subunits (i.e., integrin crevice). The major cell-binding site for many integrins is the three amino acid sequence RGD on the 10th type III repeat of FN[28,29]. Integrins that engage FN through RGD include $\alpha_{IIb}\beta_3$, $\alpha_V\beta_3$, $\alpha_V\beta_6$, $\alpha_V\beta_1$, $\alpha_5\beta_1$, and $\alpha_8\beta_1$. Recognition of RGD by integrins is highly sensitive to changes in FN conformation and the presentation of neighboring amino acid sequences. For example, integrin binding can be hindered by conformational restrictions of nearby amino acid residues that inhibit the activity of RGD[30]. Integrin binding can also be regulated by the activity of synergistic peptide sequences on neighboring domains[31,32]. For instance, integrin $\alpha_5\beta_1$ can only bind FN with the help of the PHSRN sequence, which is located on the ninth type III domain of FN, adjacent to the RGD loop. The synergy site is separated from the RGD loop on the $10^{th}$ type III repeat by about 32 A˚. Given the elasticity of the type III repeats, the ninth and tenth domains can be presented to integrins in many different conformations, which will in turn affect integrin binding selectivity. Integrins that do not bind the synergy site, such as $\alpha_V\beta_3$, are not affected by this separation, but it is still dependent on the local conformation of the RGD loop[33]. Thus, the spatial conformation of RGD and PHSRN has dramatic implications for integrin binding and, in turn, cell behavior.

### 2.1.4 Molecular Mechanisms of FN Unfolding and Effects on Integrin Binding

FN is a structurally dynamic protein. Not only hydrogen bonding plays a critical role in the stability of its structure, as discussed in the previous section, but also electrostatic interactions. It was shown that at low ionic strength FN had a compact, irregularly coiled structure, while at high

ionic strength it took on a more extended conformation with fewer intrachain bends[34]. Furthermore, it was found that salt bridges play a critical role in the conformational stability of type III domains in FN molecules. Carr et al. found that FNIII10 had extraordinary flexibility using 15N nuclear spin relaxation, which enables exceptional mechanical sensitivity[35]. Both AFM and SMD simulations showed that the β-strand attached to the RGD loop (FNIII10) was the first to break away from the module under tension, and therefore pull the loop into a deformed conformation[36–39]. Thus, deformations in FNIII10 result in changes in RGD loop accessibility to integrin binding. Other studies showed that an increase in the distance between the RGD and PHSRN sites led to a decrease in $\alpha_5\beta_1$ binding in favor of $\alpha_V\beta_3$[23,40]. Additionally, studies using FRET labeling of FNIII7 and FNIII15 showed that FN unfolded into an extended conformation as a function of increasing denaturant concentrations[41,42]. Tying back to the role of FN-integrin binding in the FBR, it has been directly observed that integrin specificity between the RGD and PHSRN sites can direct cells down a migratory/repair phenotype necessary for wound healing processes[33]. It has been shown that the relationship between the synergy site and the cryptic site has enhanced effects on cell response when FNIII7-10 is used versus an RGD-PHSRN oligopeptide, highlighting the importance of neighboring amino acids and full domain conformation[43]. Finally, the conformation of the RGD peptide also had an effect on integrin specificity: linear RGD was bound primarily by $\alpha_5\beta_1$, whereas cyclic RGD preferred $\alpha_V\beta_3$ integrins[44].

### 2.1.5 Effects of Surface Chemistry on FN Conformation, Integrin Binding, and Cell Adhesion

The type, quantity, and conformation (activity) of adsorbed proteins are influenced by the underlying substrate. Specifically, different surface chemistries can influence protein adsorption, conformation and subsequent cell adhesion. García et al. used a modified ELISA to compare the conformational changes of FN adsorbed to uncharged and charged tissue culture polystyrenes, using four antibodies specific for distinct epitopes in FN[45]. The results showed that FN underwent a higher degree of unfolding on the uncharged surface and that such surface-induced conformational changes directly impacted integrin binding of human fibroblasts. The results also showed that the charged polystyrene surface increased binding to integrin $\alpha_5\beta_1$ relative to $\alpha_V\beta_3$. Keselowsky et al. studied the effects of surface chemistry on the conformation of FN by quantifying integrin binding to FN adsorbed onto different types of SAMs by ELISA and immunofluorescence staining[46]. The results indicated decreasing accessibility of binding domains in FN, integrin binding, and cell adhesion as a function of SAM chemistry following the trend: $OH>COOH=NH_2>CH_3$. Thus, increasing surface hydrophobicity led to unfolding of FN, and therefore decreased integrin binding affinity, which in turn decreased cell adhesion. In another study, it was found that $\alpha_5\beta_1$ integrins preferentially bound to surfaces rich in hydroxyl groups, while $\alpha_V\beta_3$ integrins preferred surfaces with carboxyl groups[47]. Interestingly, this variation in surface chemistry modulated the composition of the resulting focal adhesion complex.

### 2.1.6 Effects of Surface Chemistry on Macrophage Adhesion and Polarization

Macrophages are extremely plastic cells, adopting a wide spectrum of phenotypes in response to different stimuli. The physicochemical and topographical features of biomaterials can affect

macrophage polarization, resulting in macrophages that are either predominantly pro-inflammatory (M1) or anti-inflammatory (M2)[48]. Appropriate regulation of macrophage activation post-implantation is extremely important, since these cells can tip the balance between chronic inflammation and resolution/wound healing after biomaterial implantation[4,5]. Biomaterial surface chemistry is the main factor that impacts cellular responses, since it controls the amount, identity, and conformation of adsorbed proteins on the surface (first step of the FBR)[49]. The goal is to be able to change functional properties and phenotypes of macrophages by rationally tuning the chemistry of biomaterials, which would enable the development of materials will cell-instructive properties. Rostam et al showed that monocytes cultured on hydrophilic $O_2$ plasma-activated PS surface were polarized towards an M1-like, while monocytes cultured on the hydrophobic PS surface exhibited an M2-like phenotype[49]. The authors attributed such differences to the presentation of adsorbed protein molecules on the surfaces. It was found via XPS and ToF-SIMS that the greatest total amount of protein was adsorbed on hydrophilic $O_2$ and that ions assigned to hydrophilic amino acids were more prevalent on $O_2$, while ions assigned to hydrophobic amino acids were more prevalent on PS. However, others have reported that FN binds to hydrophobic PS surfaces more than to hydrophilic surfaces[50]. McBane et al showed that a degradable hydrophobic, ionic polyurethane scaffold was more successful than a tissue culture plastic surface in eliciting an anti-inflammatory phenotype from monocyte-derived macrophages. In a follow-up work, the authors showed that variations in protein adsorption led to different profiles of cytokine release that modulated the FBR[51,52].

A well-known interaction is macrophage engagement with FN on implanted biomaterial surfaces through leukocyte β2 integrin receptors (Mac-1 mediator), which triggers macrophage activation and secretion of inflammatory cytokines such as IL-6, IL-1α, TNF-β[53–55]. Zaveri et al

demonstrated that varying integrin binding had different effects on macrophage responses to implanted polyethylene terephthalate (PET) biomaterials[56]. Specifically, the authors disrupted the function of integrin Mac1 and RGD binding integrins via a mouse knock out model and integrin blocking, respectively. Mac1 knockout mice displayed reduced cytokine secretion compared to the wild type controls as well as reduced fibrous capsule thickness by 27%. Similarly, blocking RGD ligands decreased the fibrous capsule thickness by 45%. It is clear that, while protein adsorption and ligand presentation can considerably moderate the inflammatory response, these all can be modulated by changing inherent material properties such as surface chemistry. A better molecular understanding that correlates surface properties, protein presentation, and ligand-receptor binding with macrophage activation/polarization is required to design new, improved biomaterials.

## 2.2 Polymer brushes: Antifouling Behavior

Polymer brushes are thin films of polymer chains covalently anchored to surfaces. Recent advances in theories to describe polymer brushes as well as new synthetic and characterization tools have led to a better understanding of their unique features, which has triggered the growth of their applications[57]. In a typical polymer brush, the number of attachment (e.g., tethering points) is sufficiently high that the crowded polymer chains are forced to stretch normal to a planar surface[58,59]. Covalently attached brushes may be prepared via a "grafting to" or a "grafting from" approach. In the first, polymer chains present in solution contain a reactive group in one of their ends that reacts with the surface. The polymers become chemically linked to the surface and form the brush, enabling brush formation from polymers of extraordinarily high molecular weight. However, this method cannot readily form a dense brush, given the steric hindrance that the long polymer chains exert to each other. In the 'grafting from' approach, the surface is coated first with initiator molecules that will start the polymerization from the surface in the presence of monomers in solution, as well as a catalyst. The monomers are added sequentially to the growing polymer chain until the reaction is stopped. This method permits the formation of very dense polymer brushes, while the polydispersity of the resulting brush is typically lower than that achieved via a 'grafting to' approach. Typical 'grafting from' procedures are Atom Transfer Radical (ATR) and Reversible Addition-Fragmentation chain Transfer (RAFT) polymerizations.

If the area per end-group is large enough, the chains do not overlap. In this, so called 'mushroom' regime, the chains assume essentially the equilibrium configurations of the free polymers in solution. In good solvent conditions the polymers are swollen and their Flory radius is $R_F \approx aN^{3/5}$ where a is the monomer size[60]. The brush regime occurs when the area per chain is small compared to the cross section of the free coil, $\sigma < R_F^2 \approx a^2 N^{6/5}$ [61]. In this range, the

neighboring chains crowd each other. As a result, the chains stretch out perpendicular to the surface, and thereby increase the layer thickness L. Stretched conformations produce both extension of the chains and restricted mobility. The behavior of polymer brushes can therefore be quite different from the typical behavior of flexible polymer chains in solution or the melt where chains adopt a random walk. Polymer brushes are well-known for transforming the nature of a surface with a layer just a few nanometers thick. Control of wetting properties, prevention of nonspecific binding of biomolecules, colloidal stabilization, and resistance to fouling are all examples of successful application of polymer brushes. For the purpose of this work, we are only going to focus on the protein repellant properties of polymer brushes.

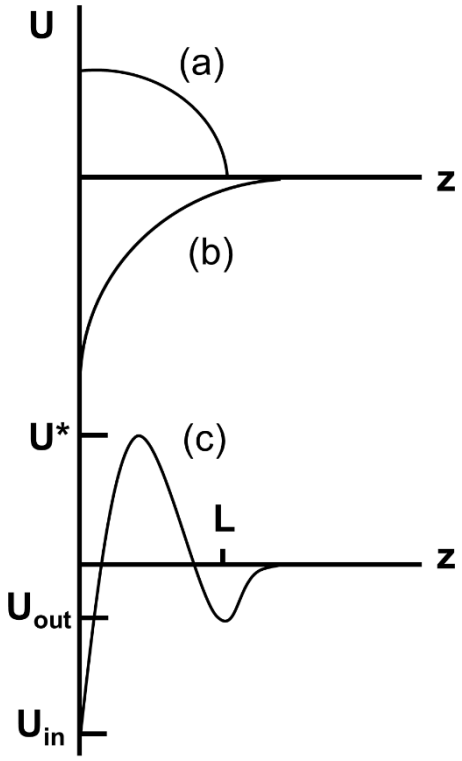


**Figure 2. 5.** Interaction potential experienced by a soluble protein approaching a brush-covered surface. The (a) brush potential $U_{brush}$ (z) and (b) attractive van der Waals potential $U_{vdW}$ (z) superimpose to give (c) the net interaction potential between the protein and brush-coated surface.

The interaction potential between the protein and the surface determines the adsorption behavior, both in terms of thermodynamics and kinetics. When a protein approaches a bare adsorbing surface, it encounters an attractive potential $U_{bare}$ (z), where z represents the distance from the surface in the normal plane (**Figure 2.5**). The interaction potential is dramatically altered when the surface is coated with a polymer brush. The overlap of the protein with the brush gives rise to a free energy penalty, which is a purely repulsive interaction ($U_{brush}$(z)). This interaction reflects the work consumed in overcoming the osmotic pressure within the brush as the protein approaches the surface. The sum of both contributions lead to the effective interaction potential between the protein and the brush-coated surface (**Figure 2.5**):

$$U_{eff}(z) = U_{bare}(z) + U_{brush}(Z) \quad \text{(eq. 2.1)}$$

In general, $U_{eff}$ may exhibit two minima: a primary minimum, close to the surface with depth $U_{in}$, and a secondary minimum with depth $U_{out}$, at the outer edge of the brush. Consequently, these two minima can give rise to two adsorption modes: a primary adsorption of the protein at the surface, which is strong and long-lived, and a secondary adsorption at the edge of the brush, which is weaker and short-lived. These minima are separated by a maximum energy barrier of height $U^*$. Primary adsorption is then an activated process, in which the protein must cross the potential barrier. In the absence of the brush (i.e., bare surface), adsorption is simply diffusion-controlled. While these two types of adsorption are extreme cases, protein adsorption can also take place within the brush, which is described as the tertiary adsorption mode. The presence of this mode arises from the different protein-brush interactions and brush chain fluctuations that take place as the protein diffuses within the brush. For the purpose of this work, we are only going to focus on the extreme cases rather than the continuum of possible scenarios.

To supress protein adsorption altogether it is obviously necessary to eliminate both modes. Secondary protein adsorption can only be repressed thermodynamically, which implies that the brush must be engineered so that $U_{out} = 0$, ensuring that $U_{out} = 0 > -kT$. Primary protein adsorption can be suppressed thermodynamically by constructing a brush where $U_{in} > 0$ (or at least $> -kT$), or kinetically by making $U^* >> kT$ (greatly increasing the timescale of adsorption). The three parameters that control the adsorption behavior ($U_{in}$, $U_{out}$, and $U^*$) depend on parameters such as protein shape, protein size, protein surface exposed residues, polymer composition, polymer molecular weight, and polymer grafting density.

The Alexander model, which describes the essential features of polymer brushes, states that the monomer volume fraction within the brush, $\phi$, is constant, and all the chains are stretched uniformly with their ends at an altitude L from the surface. While this model contains scaling corrections, the Flory version of the model will be explained for simplicity in the next lines. The brush thickness, L, is the result of the balance of two forces: the repulsive monomer-monomer interactions give rise to an osmotic force that favors a larger L. The osmotic pressure is:

$$\phi^2 \approx \frac{\pi a^3}{kT} \quad \text{(eq. 2.2)}$$

where $\phi = \frac{Na^3}{\sigma L}$. The corresponding force per chain is then $\pi\sigma$. This force is balanced by the elastic force that resists the chain extension. The free energy penalty due to the chain stretching, assuming that the polymer behaves as an ideal random coil, is $F_{el}/kT \approx L^2/a^2N$. The resulting elastic force is:

$$\frac{f_{el}}{kT} = \frac{L}{N\,a^2} \quad \text{(eq. 2.3)}$$

The force balance yields the equilibrium brush thickness:

$$\frac{L}{a} \approx N\left(\frac{a^2}{\sigma}\right)^{1/3} \quad \text{(eq. 2.4)}$$

Therefore, the monomer volume fraction in the unperturbed brush is:

$$\phi \approx \frac{Na^3}{L\sigma} \approx \left(\frac{a^2}{\sigma}\right)^{2/3} \quad \text{(eq. 2.5)}$$

Finally, the osmotic pressure can be calculated as:

$$\frac{\pi a^3}{kT} \approx \left(\frac{a^3}{\sigma}\right)^{4/3} \quad \text{(eq. 2.6)}$$

The force balance discussed above is equivalent to minimizing the free energy per chain, F, which comprises two terms: the interaction free energy that allows for monomer-monomer repulsion ($F_{int} \approx \pi\sigma L$) and the Gaussian elastic free energy ($F_{el}$). At equilibrium, both terms are comparable and result in equation 2.6.

Going back to the prevention of both primary and secondary adsorption, we can now formulate it in a mathematical form:

(a) Secondary adsorption, purely thermodynamically controlled.

$U_{out}$ is the only parameter to be tuned. If assumed that it is purely due to van der Waals attraction, protein adsorption will be suppressed if $U_{vdW}(L) > -kT$. For a cylindrical protein like fibronectin with radius R and length H, the brush thickness must exceed[62]:

$$L \approx \left(\frac{A}{12\sqrt{2}}\right)^{2/3} R^{1/3} H^{2/3} \quad \text{(eq. 2.7)}$$

where A is the Hamaker constant. As a reminder, L can be tuned by changing N or σ.

(b) Primary adsorption, kinetically and thermodynamically controlled.

The approach of the protein to the surface varies with the size of the protein. The following analysis considers only spherical proteins of radius R. Large proteins (R>>L) can only approach the surface by compressing the brush, which alters the local brush structure and the free energy penalty is much larger than for small proteins. As a result, large proteins will preferentially undergo secondary adsorption. In contrast, small proteins (R<L) will penetrate the layer via an invasive mechanism that causes little perturbation to the brush.

The invasive mechanism involves diffusion across a free energy barrier ($U^*$). Applying the Kramers rate theory (which accounts for the effect of random forces generated by the surrounding fluid on the rate of the reaction ) at the high viscosity limit, the rate constant for adsorption can be calculated as[62]:

$$k_{ads} \approx \frac{D}{\alpha L} exp\left(\frac{U^*}{kT}\right) \approx \frac{D}{\alpha L} exp\left(\frac{\pi R^3}{kT}\right) \approx \frac{D}{\alpha L} exp\left(\frac{R}{\sqrt{\sigma}}\right)^3 \quad \text{(eq. 2.8)}$$

where α is the width of the barrier and D is the diffusion coefficient. From the above expression, it is clear that the adsorption rate decreases with increasing brush thickness L and, especially, with increasing U*. Thus, in order to reduce the adsorption rate, the brush must be designed such that $R/\sigma^{1/2} >> 1$. Therefore, primary adsorption is repressed by increasing grafting density (σ). Meanwhile, the molecular weight (N) plays a secondary role in the problem, since it only alters L and has negligible effect on U*. In addition, the choice of σ depends on R.

Finally, from a thermodynamics perspective, the depth of the primary adsorption minimum is decreased by the same osmotic penalty, $\pi R^3$, which leads to:

$$U_{in} \approx U_{ads} + kT\left(\frac{R}{\sqrt{\sigma}}\right)^3 \quad \text{(eq. 2.9)}$$

where $U_{ads}$ is the interaction potential of the adsorbed protein at the bare surface. Thus, the same design rules decrease the thermodynamic driving force for adsorption and the rate of adsorption. As shown here, grafting density is one of the most important parameters in the design of antifouling polymer brushes. In Chapter III, the effects of polymer brush grafting density are explored in detail with respect to the model protein fibronectin.

*The mathematical model described in this section has been adapted from D. Leckband, S. Sheth, and A. Halperin, Journal of Biomaterials Science, Polymer Edition (1999).*

## 2.3 The Use of Single-Molecule Tracking to Resolve Microscopic Protein Dynamics

As explained above, the first event in the FBR is the adsorption of proteins on the biomaterial surface, followed by changes in orientation, conformation, and dynamics, which depends on the protein and physicochemical properties of the surface, as well as environmental factors. Despite the extensive research done in the field, many questions remain regarding protein adhesion, layer formation, and unfolding at solid-liquid interfaces. Ultimately, a fundamental understanding that links the biofunctional properties of the adsorbed proteins to environmental conditions (e.g., protein composition in solution, concentration, surface chemistry, surface architecture, etc.) is required. Interfacial protein behavior is often measured by exposing a surface to proteins in solution and measuring the net accumulation over time, until saturation coverage is reached. The medium can then be replaced with one that does not contain protein, allowing net migration away from the surface to be measured over time. In addition to protein coverage, the average protein conformation can be measured using different spectroscopic techniques, as covered in Section 1.1. These data can be interpreted using models of protein–surface interactions, leading to parameters that describe microscopic interfacial protein behaviors and how they vary with environmental factors. Such parameters may include: rate constants for adsorption, desorption, and unfolding, average surface area per protein, and irreversibly adsorbed fraction. This top-down approach to understanding protein–surface interactions is widely used but leads to conclusions that depend strongly on the assumptions of the models (**Figure 2.6**). Furthermore, models that are easy to apply often overlook key phenomena and complexities that have been observed in detailed molecular-level studies of interfacial protein behavior. For example, it is common to use a Langmuir model to extract adsorption rate constants from variation in the average macroscopic protein surface

coverage with time or concentration of protein in solution. These basic models, as discussed below, neglect the effects of interfacial diffusion on protein–protein interactions as well as orientational and conformational changes; these are kinetic processes with characteristic energy barriers independent of those for adsorption. The extracted apparent adsorption energy barrier will reflect contributions from many different individual processes, complicating the interpretation of the data about the fundamental protein-surface interactions.

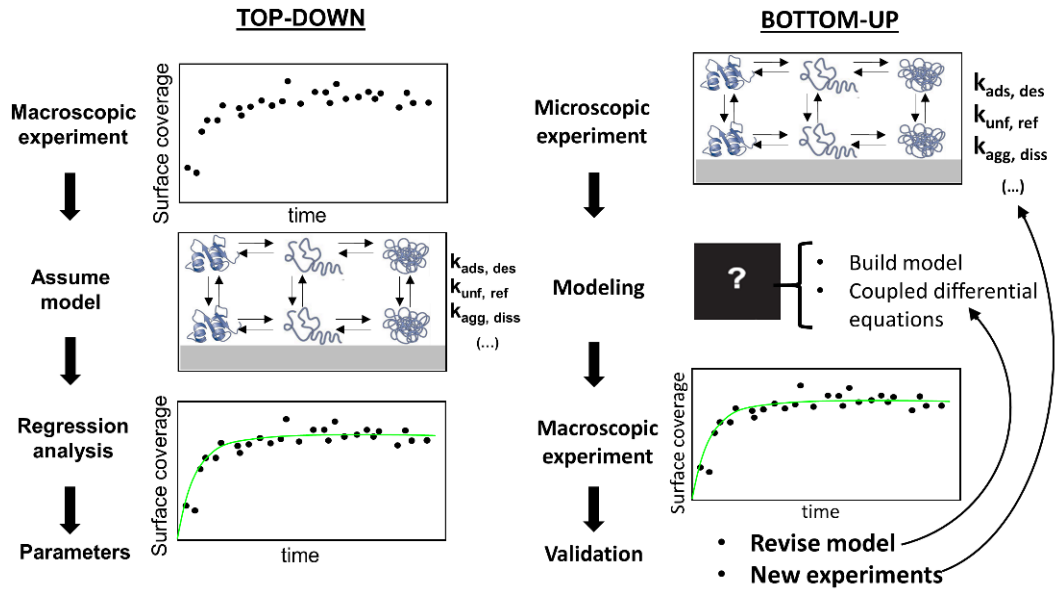


**Figure 2. 6.** Illustration of the bottom-up and top-down approaches to understanding interfacial protein dynamics.

New experimental techniques permit direct observations of interfacial protein behaviors at the single-molecule level. However, it is important to keep in mind that any single-molecule experiment measures only a subset of the parameters in a more complex, macroscopic system or ensemble. Thus, it is not always simple to compare microscopic and macroscopic observations. The suggested approach is to adopt a bottom-up approach in which microscopic observations from single-molecule experiments are fed into sophisticated models of protein layer formation, which are then used to predict macroscopic behaviors.

### 2.3.1 Protein Adsorption and Desorption

While both adsorption and desorption of protein molecules at interfaces have been widely studied using ensemble-average techniques such as ellipsometry[63–65], surface plasmon resonance[66,67], or quartz crystal microbalance[68,69], new insights into these processes have been more recently provided by single-molecule tracking (SMT) experiments[70–73]. Specifically, as discussed further in Section 2.3.3, total internal reflection fluorescence (TIRF) spectroscopy holds promise as a method to independently identify adsorption and desorption processes. SMT takes advantage of the fluorescence emission of labeled proteins to observe them on a molecule-by-molecule basis, therefore enabling the identification of adsorption events, diffusion at the interface, and desorption from the surface into the bulk solution. Thus, the time that a molecule spends on the surface (i.e., time elapsed between adsorption and desorption) is a direct measure of a protein's surface residence time. By accumulating the surface residence time of a large number of trajectories, a probability distribution of surface residence times can be constructed. The resulting integrated surface residence time distribution can be fit to a desorption process that follows first-order kinetics, and the characteristic desorption rate constant can be obtained. However, it is common to observe the presence of at least two distinct populations: one that is in rapid dynamic equilibrium with the bulk solution and one with much slower dynamic behavior. Multiple populations can be fit from the same integrated surface residence time distribution by the addition of other first-order kinetics processes to the model. Thus, the apparent macroscopic desorption rate represents contributions from multiple desorption pathways that are characterized by different rate constants. In fact, multiple populations are often observed in SMT experiments on proteins,

peptides, and DNA, and the shorter-lived populations are generally found to represent a much greater fraction of the full ensemble[74–77].

However, when modelling protein adsorption on surfaces as a function of time from macroscopic observations (e.g., tracking the growth of a protein layer on the surface), the following Langmuir model is used[78]:

$$\theta(t) = \frac{c}{c+\frac{k_d}{k_a}}\left(1 - e^{-(k_a c + k_d)t}\right) \quad \text{(eq. 2.10)}$$

where θ is the surface coverage, $c$ is the concentration of protein in solution and $k_a$ and $k_d$ are the first-order adsorption and desorption rate constants, respectively. This model operated under the assumptions that adsorption and desorption are not rate-limited by diffusion and that there are no interactions between protein adsorption sites in the lattice model. The equation captures the fact that increasing protein concentration in bulk solution increases interfacial surface coverage and that the rate of net accumulation decreases as surface coverage increases. After fitting this model to experimental data, the individual rate constants for adsorption and desorption can be extracted.

There are some limitations associated to this:

(a) The kinetic behavior at short times and thus low surface coverages is very sensitive to $k_a$, which makes it highly error-prone.

(b) Corresponding desorption experiments at steady-state coverage are required to obtain an independent measure of $k_d$ using the following expression:

$$\theta(t) = \frac{c}{c+\frac{k_d}{k_a}} e^{-k_d t} \quad \text{(eq. 2.11)}$$

This method loses accuracy if re-adsorption of protein to the interface is not negligible. Particularly, a significant concentration boundary layer will likely be present and allow for protein re-adsorption.

(c) The presence of a remaining irreversibly adsorbed fraction of proteins requires ad hoc correction of equation 2.11.

(d) While the steady-state form of eq. 2.10 (Langmuir isotherm) predicts full surface coverage for $c >> k_d/k_a$, it is often experimentally observed that there is a maximum surface coverage reached (max) that is much smaller than 1 at high $c$. This phenomenon is called the 'jamming' limit, and depends on protein geometry and protein-protein interactions. Ad hoc corrections in equation 2.10 are needed to account for it[79,80].

The subsequent addition of ad hoc corrections systematically increase the uncertainty in the calculation of $k_d$ and $k_a$. Furthermore, these models overlook the dynamic interfacial behavior of proteins, such as their ability to undergo excursions into the bulk solution as well as their ability to diffuse, which leads to rapid rearrangements on the surface. Moreover, the surfaces themselves are not homogeneous; they likely display a continuum of different site-protein binding energies, which cannot be captured by the above-mentioned models[81]. In summary, top-down approaches rely on models that operate under many assumptions to calculate adsorption and desorption rate constants. These models seek to extract unknown parameters that represent unobservable microscopic protein behavior from macroscopically observable surface coverage. There is a risk of over-fitting the data as well as a risk of claiming that a single model provides a unique description of the results over many other alternative models.

### 2.3.2 Protein Conformational Changes

It is often found in the literature that macroscopic studies of protein adsorption on surfaces leads to the irreversible adsorption of a fraction of proteins, typically indicated by extensive rinsing steps that fail at removing the entire proteinaceous layer from the surface[82,83]. However, there is still discrepancy in the interpretation of these observations: is adsorption truly irreversible (i.e., non-equilibrium process) or a certain population of proteins simply exhibits a very long characteristic timescale for desorption? Furthermore, it is possible that proteins undergo conformational changes followed by clustering/aggregation events that slow down the kinetics of desorption, leading to the observed long-lived populations. Irreversible adsorption is often referred to as 'relaxation', which includes both protein unfolding and orientational changes with respect to the surface. As discussed in the introduction, there is a vast amount of experimental evidence that the *average* structure of an adsorbed protein population often becomes increasingly denatured over time[84,85]. However, the overall, macroscopic observation of protein denaturation encompasses many different individual folding and unfolding events, as well as potential protein-protein interactions that trigger interfacial aggregation. Each one of these processes require their own observation and characterization in order to obtain a mechanistic understanding of protein unfolding. Studies in our group demonstrated, that while unfolded proteins remain on the surface longer, they are not necessarily irreversibly adsorbed[72,86,87]. This implies that the surface could also affect the balance of the populations of folded and unfolded proteins in solution.

A complete description of protein conformational dynamics requires a multidimensional energy landscape that defines the relative probabilities of the conformational states (thermodynamics) and the energy barriers between them (kinetics)[88]. Sophisticated biophysical methods are needed to measure the physical properties from which the dynamics can be inferred.

SMT holds great promise in the field, since it allows for the direct measurement of folding and unfolding processes in a molecule-by-molecule basis, as it will be described later. Protein dynamics are characterized not only by the timescale of the fluctuations (a kinetic component) but also by the amplitude and the directionality of the fluctuations (a structural component), as depicted in **Figure 2.7**. The dynamics of protein conformational changes can be divided into 'slow' and 'fast' timescales. Fast timescale dynamics (tier-1 and tier-2 dynamics) define fluctuations within the well of a tier-0 state. A large ensemble of structurally similar states that are separated by energy barriers of less than 1 *kT* result in more-local, small-amplitude picosecond-to-nanosecond fluctuations at physiological temperature (loop motions and sidechain rotations). Dynamics on a 'slow' timescale (tier-0 dynamics) define fluctuations between kinetically distinct states that are separated by energy barriers of several *kT*, corresponding to timescales of microseconds and milliseconds. Typically, these are larger-amplitude collective motions between relatively small numbers of states. The protein is not static within one of these tier-0 states, since it fluctuates around the average structure on faster timescales, exploring a large ensemble of closely related structures. Transitions between tier-0 states are rare, however, owing to the low probability of the conformation that allows transition. Nevertheless, these transitions become important in the context of interfacial phenomena, since surface-induced protein unfolding occurs on this timescale. Owing to the relatively long lifetimes of each state, these individual states can either be observed directly and the kinetics of interconversion of these states can also be detected.

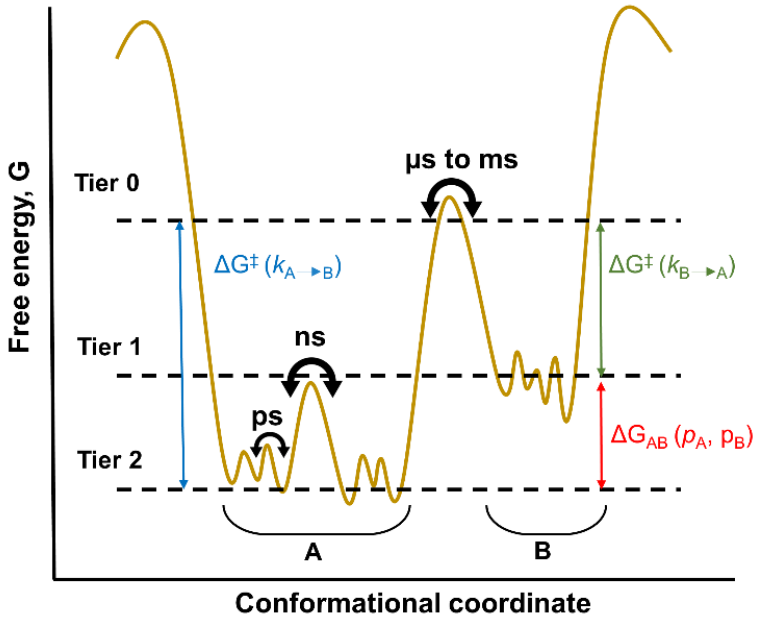


**Figure 2. 7.** One-dimensional cross-section through the highdimensional energy landscape of a protein showing the hierarchy of protein dynamics and the energy barriers. A state is defined as a minimum in the energy surface, whereas a transition state is the maximum between the wells. Populations A and B ($p_A$, $p_B$) are defined as Boltzmann distributions as a function of the free energy, $\Delta G_{AB}$. The barrier between these states ($\Delta G^{\ddagger}$) determines the rate of interconversion ($k$). A change in the system such as ligand binding or the environment (e.g., external conditions) will alter the energy landscape (e.g., shift the equilibrium between states). Adapted from[88].

SMT, when combined with other spectroscopic techniques that allow for the determination of protein conformational states (see Section 2.3.4), can be used to calculate the dwell times of individual protein molecules in a given conformation on the surface. In an analogous fashion as described for the calculation of desorption rate constants, the accumulation of a large dataset of conformation-specific dwell times allows for the calculation of apparent folding and unfolding rate constants ($k_{fold}$, $k_{unf}$), assuming again that each process follows first-order kinetics. Furthermore, the steady-state relative fraction of folded and unfolded populations can be readily obtained from SM experiments.

### 2.3.3 Total Internal Reflection Fluorescence Microscopy

When using fluorescence microscopy to study biological systems, it is sometimes necessary to restrict the excitation and detection of fluorophores to a thin section of the sample. For instance, for the study of protein interactions and conformation at interfaces, only the near-surface environment is of interest, and therefore the removal of fluorescence from the bulk protein solution presents a challenge. Elimination of background fluorescence from outside the focal plane can drastically improve the signal-to-noise ratio, and thus, the spatial resolution of the objects and events of interest. As shown in **Figure 2.8**, total internal reflection microscopy (TIRFM) uses an induced evanescent wave to excite fluorophores in a limited volume near the interface between two media with different refractive indices[89,90]. Specifically, the technique takes advantage of Snell's law and the optical phenomenon of total internal reflection: when light waves (in this case from a laser) propagating through a medium (e.g. glass) are incident at an interface with another medium that has a lower refractive index (e.g. water) above some critical angle, such that the light is total internally reflected. At this interface, an evanescent wave is created in the second medium, exciting fluorophores that are within approximately 100 nm from the surface. The intensity of the evanescent wave decays exponentially with distance from the interface, as a function of the angle of incidence and light wavelength. Therefore, fluorophores in the bulk solution at further distance from the interface are not excited, greatly reducing the background that is present in other fluorescent microscopy techniques such as wide-field epi-fluorescence. TIRFM's reduction in background and surface sensitivity makes it an ideal technique for observing single molecules with fluorescent labels at the solid-liquid interface.

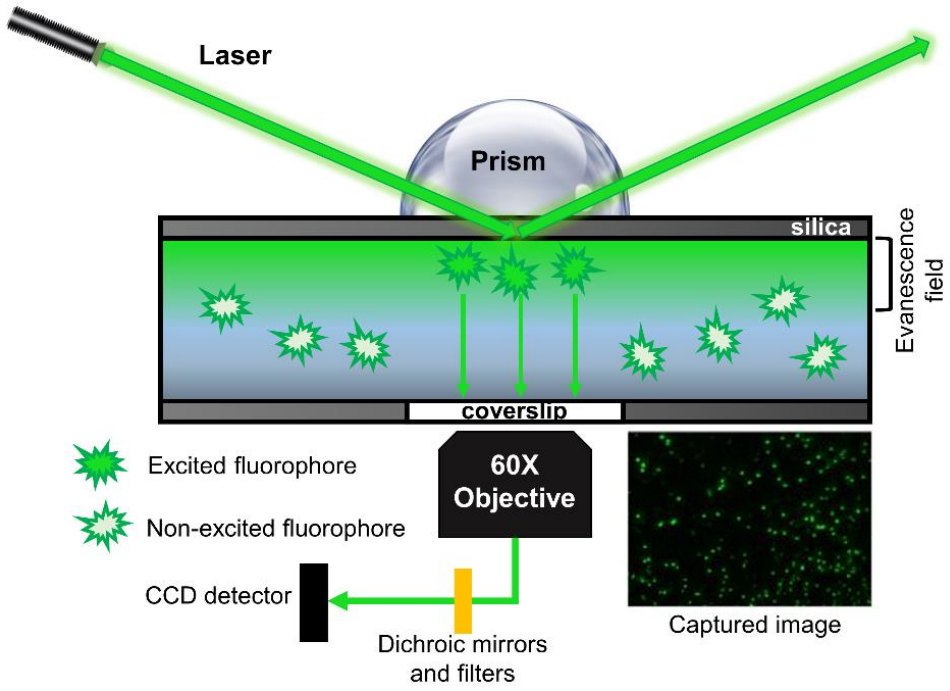


**Figure 2. 8.** Prism-based TIRFM setup.

### 2.3.4 Förster Resonance Energy Transfer

Conformational changes in proteins are generally accompanied by changes in the morphology of the molecule's 3D structure. Specifically, when a protein unfolds, the loss in secondary and tertiary structure translates into an increase in the relative distance between the residues that are being pulled apart. Thus, spatial information in fluorescence imaging is necessary in order to discern the conformational state of protein molecules. Such information can be acquired *via* resonance energy transfer (RET)[86,91]. This technique involves the non-radiative energy transfer from a donor fluorophore to an acceptor fluorophore that occurs when the two fluorophores are within 1-10nm, where the specific distance-dependence is characteristic of the specific RET-pair[92]. For RET to occur, the emission spectrum of the donor fluorophore must have significant overlap with the excitation spectrum of the acceptor fluorophore. The spectral overlap integral ($J$) with respect to wavelength ($\lambda$) can be calculated as:

$$J=\int f_D(\lambda)\epsilon_A(\lambda)\lambda^4 d\lambda \quad \text{(eq. 2.12)}$$

where subscripts *A* and *D* represent acceptor and donor, respectively, $f_D$ is the normalized emission spectrum and $\epsilon_A$ the molar extinction coefficient. Combining the spectral overlap integral, the refractive index ($n$) of the medium, the donor fluorophore quantum yield ($Q_D$), the dipole orientation factor ($\kappa^2$) and Avagadro's number ($N_A$), the Förster radius ($R_o$) can be calculated as:

$$R_o^6 = \frac{9Q_D(\ln 10)\kappa^2 J}{128\pi^5 n^4 N_A} \quad \text{(eq. 2.13)}$$

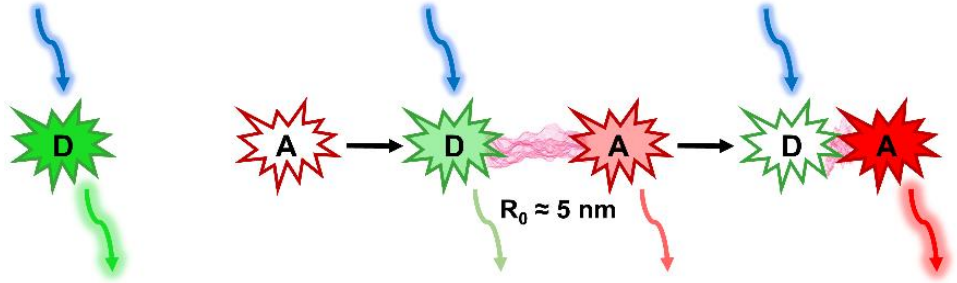


**Figure 2. 9.** Schematic of resonance energy transfer between a donor fluorophore *D* and acceptor fluorophore *A* as a function of distance. 50% RET efficiency is achieved around 5 nm for most *D*-*A* pairs.

The Förster radius represents the distance where the non-radiative energy transfer between donor and acceptor fluorophores is 50% (**Figure 2.9**). The Förster radius coupled with the experimentally observed fluorescence intensity of the donor ($F_D$) and acceptor ($F_A$) can be used to calculate the separation of the RET pair:

$$r = R_0 \left(\frac{F_{A,r\to 0}}{F_{D,r\to\infty}}\right)^{1/6} \left(\frac{F_D}{F_A}\right)^{1/6} \quad \text{(eq. 2.14)}$$

The ratio of acceptor fluorescence at zero separation and donor fluorescence at infinite separation is expected to be on the order of unity. Due to the uncertainty in this assumption, as well as in the calculation of $R_o$, it is challenging to calculate an exact value for $r$ during RET

experiments. Therefore, in this work the relative end-to-end distance (*d*) is used to characterize protein conformation, which is calculated as:

$$d = \left(\frac{\mathrm{F_D}}{\mathrm{F_A}}\right)^{1/6} \quad \text{(eq. 2.15)}$$

Therefore, high *d* values (i.e., low FRET states) can be attributed to unfolded protein molecules. Conversely, low *d* values (i.e., high FRET states) indicate that protein molecules are folded or in their native conformation. Alternatively, this work also utilizes the calculation of FRET efficiencies (E), defined as:

$$E = \frac{F_A}{F_A + F_D} = \frac{1}{1 + d^6} \quad \text{(eq. 2.16)}$$

where *E* can only display values between 0 and 1. With this definition, low *E* values correspond to unfolded protein molecules while high *E* values can be attributed to folded or compact conformations of the protein molecules.

## 2.4 References


(1) Anderson, J. M.; Rodriguez, A.; Chang, D. T. *Seminars in Immunology* **2008**, *20*, 86–100.
(2) Tang, L.; Thevenot, P.; Hu, W. *Curr. Top. Med. Chem.* **2008**, *8*, 270–280.
(3) Babensee, J. E.; Anderson, J. M.; McIntire, L. V.; Mikos, A. G. *Ad. Drug Deliv. Rev.* **1998**, *33*, 111–139.
(4) Chung, L.; Maestas, D. R.; Housseau, F.; Elisseeff, J. H. *Adv. Drug Deliv. Rev.* **2017**, *114*, 184–192.
(5) Lynn, A. D.; Bryant, S. J. *Acta Biomater.* **2011**, *7*, 123–132.
(6) Sussman, E. M.; Halpin, M. C.; Muster, J.; Moon, R. T.; Ratner, B. D. *Ann. Biomed. Eng.* **2014**, *7*, 1508–1516.
(7) Morais, J. M.; Papadimitrakopoulos, F.; Burgess, D. J. *AAPS J.* **2010**, *12*, 188–196.
(8) Ward, W. K. A. *Journal of Diabetes Science and Technology* **2008**.
(9) Major, M. R.; Wong, V. W.; Nelson, E. R.; Longaker, M. T.; Gurtner, G. C. *Plast. Reconstr. Surg.* **2015**, *135*, 1489–1498.
(10) Frantz, C.; Stewart, K. M.; Weaver, V. M. *J. Cell. Sci.* **2010**, *123*, 4195–4200.
(11) Mochitate, K.; Pawelek, P.; Grinnell, F. *Exp. Cell. Res.* **1991**, *193*, 198–207.
(12) Lo, C. M.; Wang, H. B.; Dembo, M.; Wang, Y. L. *Biophys. J.* **2000**, *79*, 144–152.
(13) Engler, A. J.; Sen, S.; Sweeney, H. L.; Discher, D. E. *Cell* **2006**, *126*, 677–689.
(14) Xian, X.; Gopal, S.; Couchman, J. R. *Cell and Tissue Research* **2010**, *339*, 31–46.
(15) Leitinger, B.; Hohenester, E. *Matrix Biology* **2007**, *26*, 146–155.
(16) Humphries, J. D.; Byron, A.; Humphries, M. J. *J. Cell Sci.* **2006**, *119*, 3901–3903.
(17) Zollinger, A. J.; Smith, M. L. *Matrix Biology* **2017**, *60*, 27–37.
(18) Johansson, S.; Svineng, G.; Wennerberg, K.; Armulik, A.; Lohikangas, L. *Front. Biosci.* **1997**, *2*, 126–146.
(19) Baron, M.; Norman, D.; Willis, A.; Campbell, I. D. *Nature* **1990**, *345*, 642–646.
(20) Pickford, A. R.; Potts, J. R.; Bright, J. R.; Phan, I.; Campbell, I. D. *Structure* **1997**, *5*, 359–370.
(21) Main, A. L.; Harvey, T. S.; Baron, M.; Boyd, J.; Campbell, I. D. *Cell* **1992**, *71*, 671–678.
(22) Gao, M.; Craig, D.; Lequin, O.; Campbell, I. D.; Vogel, V.; Schulten, K. *Proc. Natl. Acad. Sci.* **2003**, *100*, 14784–14789.
(23) Krammer, A.; Craig, D.; Thomas, W. E.; Schulten, K.; Vogel, V. *Matrix. Biol.* **2002**, *21*, 139–147.
(24) Sakai, T.; Johnson, K. J.; Murozono, M.; Sakai, K.; Magnuson, M. A.; Wieloch, T.; Cronberg, T.; Isshiki, A.; Erickson, H. P.; Fässler, R. *Nat. Med.* **2001**, *7*, 324–330.
(25) Ni, H.; Yuen, P. S. T.; Papalia, J. M.; Trevithick, J. E.; Sakai, T.; Fassler, R.; Hynes, R. O.; Wagner, D. D. *Proc. Natl. Acad. Sci.* **2003**, *100*, 2415–2419.
(26) Yamada, K. M.; Akiyama, S. K.; Hasegawa, T.; Hasegawa, E.; Humphries, M. J.; Kennedy, D. W.; Nagata, K.; Urushihara, H.; Olden, K.; Chen, W. T. *Journal of Cellular Biochemistry* **1985**, *103*, 1649–166.
(27) Akiyama, S. K.; Nagata, K.; Yamada, K. M. *Reviews on Biomembranes* **1990**, *1031*, 91–110.
(28) Dufour, S.; Duband, J. L.; Humphries, M. J.; Obara, M.; Yamada, K. M.; Thiery, J. P. Attachment, *EMBO J.* **1988**, *7*, 2661–2671.
(29) Pierschbacher, M. D.; Ruoslahti, E. *Nature* **1984**, *309*, 30–33.
(30) Pierschbacher, M. D.; Ruoslahti, E. *J. Biol. Chem.* **1987**, *262*, 17294–17298.

(31) Mardon, H. J.; Grant, K. E. *FEBS Lett.* **1994**, *340*, 197–201.
(32) Mould, A. P.; Askari, J. A.; Aota, S. I.; Yamada, K. M.; Irie, A.; Takada, Y.; Mardon, H. J.; Humphries, M. J. *J. Biol. Chem.* **1997**, *272*, 17283–17292.
(33) Brown, A. C.; Rowe, J. A.; Barker, T. H. *Tissue Eng. Part A* **2011**, *17*, 139–150.
(34) Erickson, H. P.; Carrell, N. A. *J. Biol. Chem.* **1983**, *258*, 14539–14544.
(35) Carr, P. A.; Erickson, H. P.; Palmer, A. G. *Structure* **1997**, *5*, 949–959.
(36) Oberhauser, A. F.; Marszalek, P. E.; Erickson, H. P.; Fernandez, J. M. *Nature* **1998**, *393*, 181–185.
(37) Krammer, A.; Lu, H.; Isralewitz, B.; Schulten, K.; Vogel, V. *Proc. Natl. Acad. Sci.* **1999**, *96*, 1351–1356.
(38) Craig, D.; Krammer, A; Schulten, K.; Vogel, V. *Proc. Natl. Acad. Sci.* **2001**, *98*, 5590–5595.
(39) Oberhauser, A. F.; Badilla-Fernandez, C.; Carrion-Vazquez, M.; Fernandez, J. M. *J. Mol. Biol.* **2002**, *319*, 433–447.
(40) Grant, R. P.; Spitzfaden, C.; Altroff, H.; Campbell, I. D.; Mardon, H. J. *J. Biol. Chem.* **1997**, *272*, 6159–6166.
(41) Baneyx, G.; Baugh, L.; Vogel, V. *Proc. Natl. Acad. Sci.* **2001**, *98*, 14464–14468.
(42) Baneyx, G.; Baugh, L.; Vogel, V. *Proc. Natl. Acad. Sci.* **2002**, *99*, 5139–5143.
(43) Petrie, T. A.; Capadona, J. R.; Reyes, C. D.; García, A. J. *Biomaterials* **2006**, *27*, 5459–5470.
(44) Ochsenhirt, S. E.; Kokkoli, E.; McCarthy, J. B.; Tirrell, M. *Biomaterials* **2006**, *27*, 3863–3874.
(45) Garcia, A. J.; Vega, M. D.; Boettiger, D. *Mol. Biol. Cell* **1999**, *10*, 785–798.
(46) Keselowsky, B. G.; Collard, D. M.; García, A. J. *J. Biomed. Mater. Res. Part A* **2003**, *66*, 247–259.
(47) Bachman, H.; Nicosia, J.; Dysart, M.; Barker, T. H. *Adv. Wound Care* **2015**, *4*, 501–511.
(48) Ogle, M. E.; Segar, C. E.; Sridhar, S.; Botchwey, E. A. *Experimental Biology and Medicine* **2016**, *241*, 1084–1097.
(49) Rostam, H. M.; Singh, S.; Salazar, F.; Magennis, P.; Hook, A.; Singh, T.; Vrana, N. E.; Alexander, M. R.; Ghaemmaghami, A. M. *Immunobiology* **2016**, *221*, 1237–1246.
(50) Grinnell, F.; Feld, M. K. *J. Biol. Chem.* **1982**, *257*, 4888–4893.
(51) McBane, J. E.; Matheson, L. A.; Sharifpoor, S.; Santerre, J. P.; Labow, R. S. *Biomaterials* **2009**, *30*, 5497–5504.
(52) Battiston, K. G.; Labow, R. S.; Santerre, J. P. *Biomaterials* **2012**, *33*, 8316–8328.
(53) Tang, L.; Ugarova, T. P.; Plow, E. F.; Eaton, J. W. *J. Clin. Invest.* **1996**, *97*, 1329–1334.
(54) Rostam, H. M.; Singh, S.; Vrana, N. E.; Alexander, M. R.; Ghaemmaghami, A. M. *Biomaterials Science* **2015**, *3*, 424–441.
(55) Flick, M. J.; Du, X.; Degen, J. L. *Experimental Biology and Medicine*; **2004**, *11*, 1105–1110.
(56) Zaveri, T. D.; Lewis, J. S.; Dolgova, N. V.; Clare-Salzler, M. J.; Keselowsky, B. G. Integrin-*Biomaterials* **2014**, *35*, 3504–3515.
(57) Chen, W. L.; Cordero, R.; Tran, H.; Ober, C. K. *Macromolecules* **2017**, *50*, 4089–4113.
(58) Leckband, D.; Sheth, S.; Halperin, A. *J. Biomater. Sci. Polym. Ed.* **1999**, *10*, 1125–1147.
(59) Utrata-Wesoek, A. *Polimery/Polymers* **2013**, *58*, 685–696.
(60) de Gennes, P. G. *Advances in Colloid and Interface Science* **1987**, *27*, 189–209.
(61) Alexander, S. *J. Phys.* **1977**, *38*, 983–987.

(62) Halperin, A. *Langmuir* **1999**, *15*, 2525–2533.
(63) Emilsson, G.; Schoch, R. L.; Feuz, L.; Höök, F.; Lim, R. Y. H.; Dahlin, A. B. *ACS Appl. Mater. Interfaces* **2015**, *7*, 7505–7515.
(64) Hook, F.F.; Vörös, J.; Rodahl, M.; Kurrat, R.; Böni, P.; Ramsden, J. J.; Textor, M.; Spencer, N. D.; Tengvall, P.; Gold, J.; et al. *Colloids Surfaces B Biointerfaces* **2002**, *24*, 155-170.
(65) Jönsson, U.; Malmqvist, M.; Ronnberg, I. *J. Colloid Interface Sci.* **1985**, *70*, 96–100.
(66) Snopok, B. A.; Kostyukevich, E. V. *Anal. Biochem.* **2006**, *348*, 222–231.
(67) Green, R. J.; Davies, J.; Davies, M. C.; Roberts, C. J.; Tendler, S. J. B. *Biomaterials* **1997**, *18*, 405–43.
(68) Berglin, M.; Pinori, E.; Sellborn, A.; Andersson, M.; Hulander, M.; Elwing, H. Fibrinogen *Langmuir* **2009**, *25*, 5602–5608.
(69) Jin, J.; Jiang, W.; Yin, J.; Ji, X.; Stagnaro, P. *Langmuir* **2013**, *29*, 6624–6633.
(70) Myers, G. A.; Gacek, D. A.; Peterson, E. M.; Fox, C. B.; Harris, J. M. *J. Am. Chem. Soc.* **2012**, *134*, 19652–19660.
(71) Langdon, B. B.; Kastantin, M.; Schwartz, D. K. *Biophys. J.* **2012**, *102*, 2625–2633.
(72) Faulón Marruecos, D.; Kastantin, M.; Schwartz, D. K.; Kaar, J. L. *Biomacromolecules* **2016**, *17*, 1017–1025.
(73) Weltz, J. S.; Schwartz, D. K.; Kaar, J. L. *ACS Nano* **2016**, *10*, 730–738.
(74) Traeger, J. C.; Schwartz, D. K. *Langmuir* **2017**, *33*, 12651–12659.
(75) Monserud, J. H.; Schwartz, D. K. *Biomacromolecules* **2012**, *13*, 4002–4011.
(76) Monserud, J. H.; Macri, K. M.; Schwartz, D. K. *Angew. Chemie. - Int. Ed.* **2016**, *55*, 13710–13713.
(77) Nelson, N.; Walder, R.; Schwartz, D. K. *Langmuir* **2012**, *28*, 12108–12113.
(78) Karpovich, D. S.; Blanchard, G. J. *Langmuir* **1994**, *99*, 3951–3958.
(79) Norde, W.; Anusiem, A. C. I. *Colloids and Surfaces* **1992**, *21*, 73–80.
(80) Zhou, H. X.; Rivas, G.; Minton, A. P. *Annu. Rev. Biophys.* **2008**, *37*, 375–397.
(81) Rabe, M.; Verdes, D.; Seeger, S. *Adv. Colloid Interface Sci.* **2011**, *162*, 87–106.
(82) Mrksich, M.; Sigal, G. B.; Whitesides, G. M. *Langmuir* **1995**, *11*, 4383–4385.
(83) Kim, D. T.; Blanch, H. W.; Radke, C. J. *Langmuir* **2002**, *18*, 5841–5850.
(84) Hook, F.; Brzezinski, P.; Rodahl, M.; Kasemo, B. *Faraday Discuss* **1997**, *107*, 229–246.
(85) Tunc, S.; Maitz, M. F.; Steiner, G.; Vázquez, L.; Pham, M. T.; Salzer, R. *Colloids Surfaces B Biointerfaces* **2005**, *42*, 219–225.
(86) McLoughlin, S. Y.; Kastantin, M.; Schwartz, D. K.; Kaar, J. L. *Proc. Natl. Acad. Sci.* **2013**, *110*, 19396–19401.
(87) Kastantin, M.; Faulón Marruecos, D.; Grover, N.; Yu McLoughlin, S.; Schwartz, D. K.; Kaar, J. L. *J. Am. Chem. Soc.* **2017**, *139*, 9937–9948.
(88) Henzler-Wildman, K.; Kern, D. *Nature* **2007**, *450*, 964–972.
(89) Wazawa, T.; Ueda, M. *Advances in Biochemical Engineering/Biotechnology* **2005**, *95*, 77–106.
(90) Lok, B. K.; Cheng, Y. L.; Robertson, C. R. *J. Colloid Interface Sci.* **1983**, *91*, 104–116.
(91) Zarrabi, N.; Ernst, S.; Verhalen, B.; Wilkens, S.; Börsch, M. *Methods* **2014**, *66*, 168–179.
(92) Lakowicz, J. R.; Masters, B. R. *J. Biomed. Opt.* **2008**, *13*, 041303.

# Chapter III: Dense Poly(ethylene glycol) Brushes Reduce Adsorption and Stabilize the Unfolded Conformation of Fibronectin

David Faulón Marruecos, Mark Kastantin, Daniel K. Schwartz, and Joel L. Kaar

(Published February, 2016: Biomacromolecules, 17(3), 1017-1025)

## 3.1 Abstract

Polymer brushes, in which polymers are end-tethered densely to a grafting surface, are commonly proposed as stealth coatings for various biomaterials. However, while their use has received considerable attention, a mechanistic understanding of the impact of brush properties on protein adsorption and unfolding remains elusive. We investigated the effect of grafting density of poly(ethylene glycol) (PEG) brushes on the interactions of the brush with fibronectin (FN) using high-throughput single-molecule tracking methods, which directly measure protein adsorption, diffusion, and unfolding within the brush. We observed that as grafting density increased, the rate of FN adsorption decreased; however, surface-adsorbed FN unfolded more readily and unfolded molecules were retained on the surface for longer residence times relative to folded molecules. These results, which are critical for the rational design of PEG brushes, suggest there is a critical balance between protein adsorption and conformation that underlies the utility of such brushes in physiological environments.

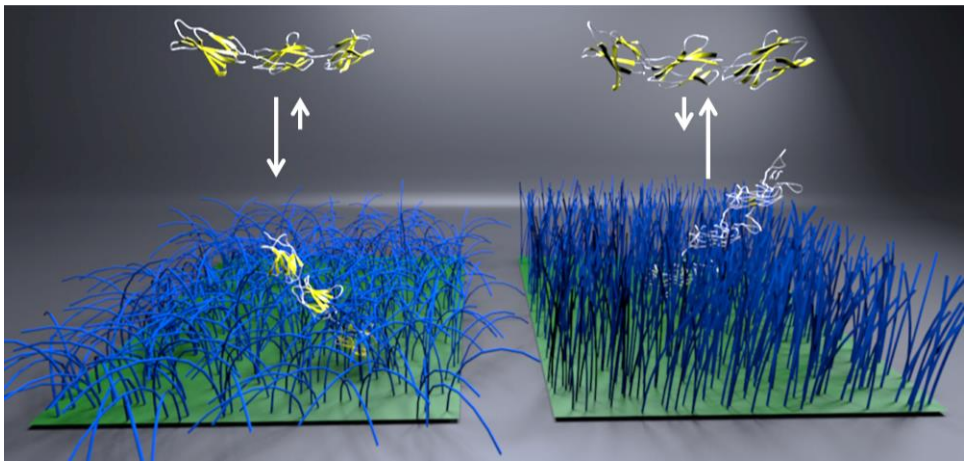

**Figure 3. 1.** Schematic representation of the impact of grafting density of PEG brushes on protein adsorption and conformation at the solution-brush interface.

## 3.2 Introduction

The use of polymer brushes as coatings to improve the biocompatibility of materials in physiological environments or in contact with proteins (*e.g.*, biomaterials for tissue engineering and drug delivery, medical devices, biosensors, contact lenses, food packaging materials) has received considerable attention[1-7]. Such coatings consist of a densely packed layer of polymer chains that are terminally anchored to a surface and may be prepared by a "grafting to" or "grafting from" approach[8-11]. The grafted polymer layer provides a steric barrier, shielding the surface from protein adsorption while simultaneously minimizing protein denaturation at the solution-solid interface. Due to its apparent protein resistance, poly(ethylene glycol) (PEG), is the most extensively studied material for the development of polymer brush coatings[6].

Despite a widespread interest in applications of PEG brushes, a mechanistic understanding of the connection between brush properties (e.g. grafting density and brush thickness) and non-specific protein adsorption and denaturation remains elusive. Previous studies, using macroscopic ensemble-averaging methods, have shown a non-monotonic trend of protein accumulation with grafting density, where accumulation decreases at low grafting densities and then increases again at very high grafting densities. This behavior is hypothesized to be due to an increase in PEG hydration with grafting density up to an optimal point, after which hydration of the brush decreases[12-17]. While this hypothesis is plausible, it neglects alternative hypotheses, including a potential indirect effect where protein accumulation is influenced by the impact of grafting density on protein conformation. For example, it is plausible that, at high grafting density, the rate of protein adsorption is actually decreased, but an increase in unfolding of adsorbed proteins leads to increased surface residence time. Accordingly, increased protein accumulation may result from differences in the surface residence time of folded and unfolded protein molecules, rather than an

increase in the rate of protein adsorption. Moreover, increased unfolding at high PEG grafting density may also lead to surface aggregation, further increasing the surface residence time of molecules on the brush. Ultimately, this gap in understanding prohibits the rational design of PEG brushes for improved biocompatibility and thus limits the utility of PEG brushes as protein resistant coatings.

To fully elucidate the link between protein accumulation and grafting density for PEG brushes, new methods to directly correlate protein adsorption and conformation on brush surfaces are required[18]. Typical ensemble-averaging methods relate protein adsorption and conformation indirectly, by correlating changes in average protein conformation with the total amount of adsorbed protein[19,20]. Such indirect measurements of protein conformation are necessary due to challenges in measuring protein structure at solid-liquid interfaces. Because changes in protein conformation are generally inferred from indirect ensemble-average measurements, interpretations may be overly simplified or even incorrect, yielding a misleading view of the impact of brush properties on protein adsorption. Importantly, such interpretations often ignore heterogeneity associated with the protein, the brush, or the protein-brush interactions.

Single-molecule (SM) methods have significant advantages with respect to characterizing protein-brush interactions that involve population and dynamic heterogeneity. In particular, we have previously employed high-throughput SM fluorescence tracking (using total internal reflection fluorescence microscopy, TIRFM) combined with intramolecular Förster resonance energy transfer (FRET), to obtain mechanistic insight into the interaction of proteins with surfaces[21]. By employing site-specific protein engineering approaches for tethering donor and acceptor fluorophores to a protein, structural information can be extracted from changes in intramolecular FRET. Importantly, this approach permits the direct observation and subsequent

correlation of protein adsorption with changes in protein conformation on a molecule-by-molecule basis, and provides opportunities to study the impact of brush properties and protein resistance with unprecedented resolution.

In this work, we investigated the interaction of site-specifically labeled fibronectin (FN) with PEG ($M_w$ 5,000) brushes that ranged in grafting density. We used a recombinant FN construct that comprised the type III 8-10 domains, which contained the RGD and PHSRN sites involved in cell adhesion[32,33]. High-throughput analysis of $10^4$-$10^6$ trajectories enabled the direct correlation between FN adsorption and structure on different brush surfaces while capturing the influence of dynamic and population heterogeneity. Our results illuminate the complexity of the underlying mechanism of protein adsorption on PEG brushes and, specifically, highlight how protein resistance and conformation on the brush surface are inter-related, which is critical for rationally designing PEG brushes to prevent non-specific protein adsorption as well as control cellular responses to non-specifically adsorbed protein in the physiological milieu.

## 3.3 Material and Methods

### 3.3.1 Preparation of Recombinant FN

Recombinant FN type III 8-10 domains were initially amplified via polymerase chain reaction from plasmid DNA that contained the gene for FN type III 8-10 domains (from Thomas Barker, Georgia Institute of Technology) and subsequently cloned into pET-21b (Novagen) with a C-terminal 6xhis tag. Following cloning, the TAG stop codon was introduced in place of residue 1381 while residue 1500 was mutated to cysteine via site-directed mutagenesis to permit fluorophore attachment. Note, the residue numbers correspond to the amino acid positions in full-

length FN. The resulting construct to be used for FRET ($FN_{FRET}$), as well as wild-type FN type III 8-10, was co-expressed with pDule2 pCNF RS (from Ryan Mehl, Oregon State) in BL21 (DE3) *Escherichia coli* via auto-induction in minimal media containing 4-azido-L-phenylalanine (Chem-Impex)[22,23]. $FN_{FRET}$ and wild-type FN type III 8-10 were purified from cell lysate via affinity chromatography using a copper-charged Bio-Scale Mini column (Bio-Rad). During purification, care was taken to minimize exposure of $FN_{FRET}$ to UV light to avoid reduction of the azide group prior to labeling.

### 3.3.2 Site-specific Labeling of FN

Dual labeled $FN_{FRET}$ was prepared by initially dialyzing the protein against 10 mM sodium phosphate buffer (pH 7.4) at 4 ºC for 18 h. The protein was then reacted with dibenzocyclooctyne-activated Alexa Fluor 555 (Life Technologies) using a 3:1 molar ratio of fluorophore-to-protein in a total reaction volume of 100 μL for 18 h in the dark. Upon donor labeling, acceptor was attached via a second reaction with maleimide-activated Alexa Fluor 647 (Life technologies), also in the dark, for 18 h using a 3:1 fluorophore-to-protein molar ratio and a reaction volume of 100 μL. To facilitate acceptor labeling, Cys1500 was reduced via addition of a 5-molar excess of tris-(2-carboxyethyl)phosphine hydrochloride for 30 min at room temperature prior to the reaction. After the completion of both labeling reactions, the residual free dye in solution was separated from the dual-labeled protein using a Bio-Rad SEC 70 10x300 mm column. Labeling efficiency was determined using the molar extinction coefficient for each fluorophore (155,000 $M^{-1}cm^{-1}$ for Alexa Fluor 555 at 565 nm and 270,000 $M^{-1}cm^{-1}$ for Alexa Fluor 647 at 668 nm) as well as that for $FN_{FRET}$ (32,890 $M^{-1}cm^{-1}$ at 280 nm). Correcting for absorbance of the dyes at 280 nm, the labeling

efficiency was found to be 60% and 30% for Alexa Fluor 555 and 647, respectively, for dual-labeled $FN_{FRET}$.

### 3.3.3 Preparation of PEG Brush Surfaces

Surfaces containing PEG brushes were prepared by grafting α–methoxy-ω-triethoxy PEG ($M_w$ 5,000 Da; Laysan Bio Inc.) to fused silica wafers. To systematically vary the PEG grafting density, the solvent quality was adjusted during functionalization as described previously[24]. Briefly, prior to functionalization, the wafers were extensively washed sequentially with Micro-90 (International Product Corp.), ultrapure water, and piranha and subsequently treated with UV/ozone for 30 min. After washing, the wafers were functionalized with α–methoxy-ω-triethoxy PEG (1 mM) in 100% acetone, 75% acetone/25% diethyl ether, 50% acetone/50% diethyl ether for 15 h at 30 °C with gentle shaking (25 rpm) in a constant temperature incubator. The surface functionalization reaction was catalyzed by the addition of N-butylamine at a 1:20 volumetric ratio of the catalyst-to-reaction mixture. Wafers were modified in triplicate in separate reactions.

The thickness of the dry brush was measured by ellipsometry using a J.A. Woollam variable angle spectroscopic ellipsometer (model VASE-VB-250). For ellipsometry measurements, oxidized silicon wafers, which were functionalized using the same method as the fused silica wafers, were used. A spectral scan of the surface was collected between 500-900 nm with an incident angle between 60-80°, in increments of 5°. The dry brush thickness ($h_{dry}$) was determined using a three-layer planar model of the solid surface from the collected spectra, considering the refractive index of air (n=1.003), PEG (n=1.45), fused silica upper layer (n=1.457), and silicon (n=3.881) and subsequently related to grafting density ($\sigma$) using the relationship $\sigma = \rho_{dry} h_{dry} N_A / M_w$ where $\rho_{dry}$ is the dry density of the PEG monomer repeat unit (1 g/cm$^3$), $N_A$ is Avogadro's number, and $M_w$ is the average molecular weight of the PEG polymer (5 kDa).[25]

Additionally, the distance ($D$) between grafting points (*i.e.*, tether distance) was calculated using the relationship $D = (1/\sigma)^{1/2}$ [25].

### 3.3.4 Single-molecule FRET Imaging and Image Processing

SM-FRET experiments using $FN_{FRET}$ were performed as described in detail previously[26] using a custom built TIRF microscope. For image collection, a 50 mW 532 nm diode-pumped solid-state laser (Samba, Cobolt) was used to illuminate the solution-solid interface via a cylindrical prism. The fluorescence emission from molecules at the interface was split in distinct spectral channels using a dichroic mirror and filtered using separate band-pass filters for the donor and acceptor emission. A Cascade-II 512 EMCCD camera (Photometrics) was used to collect the intensity in both channels with an acquisition time (*i.e.,* temporal resolution) of 100 ms. For all single-molecule experiments, $FN_{FRET}$ was introduced to the relevant surface in phosphate buffered saline with an ionic strength of 137 mM and pH of 7.4.

Objects were localized and connected into trajectories as previously described[27]. Briefly, diffraction-limited objects in each spectral channel were distinguished by convolution with a disk matrix and intensity thresholding after background subtraction. The position of each object was assigned using the center-of-intensity method. FRET was identified by the presence of objects that appeared at the same (x,y) coordinate in both channels in a given frame. Trajectories were constructed by connecting objects that appeared within a tracking radius 2.2 μm in consecutive frames. To avoid false connections, the number of objects in the field of view (2,450 $\mu m^2$) was limited to less than 100 via using a concentration of $FN_{FRET}$ of $10^{-9}$-$10^{-10}$ M. Previously reported results with the same dyes, filters, and experimental setup confirmed that the crosstalk between channels and photo-blinking was negligible[21].

### 3.3.5 Adsorption Rate Constants, Surface Residence Times, and Kinetics of Conformational Changes

Adsorption rate constants were determined from single-molecule experiments and expressed as the total number of adsorption events relative to the elapsed time of a movie (100 s), the area of the field of view (2,450 $\mu m^2$), and the $FN_{FRET}$ concentration ($5.5x10^{-9}$ M for experiments on PEG brushes or $1x10^{-10}$ M for experiments on unmodified fused silica). The trajectory of an individual molecule was counted as an adsorption event if the molecule appeared in both the donor and acceptor channel at some point in the trajectory and, moreover, resided on the surface for 4 frames or longer. Furthermore, neither initial conformational state (folded or unfolded) nor subsequent conformational changes were considered to select the trajectories.

To quantitatively characterize desorption kinetics, the complementary cumulative surface residence time distribution for the molecules was accumulated. These distributions comprised the surface residence times for each trajectory from the time interval between adsorption and desorption. Objects with residence times of a single frame were ignored due to the sensitivity of the methodology used for object identification (*i.e.,* random noise could dominate these single-frame trajectories). The surface residence times for all molecules in an experiment were subsequently used to create a complementary cumulative residence time distribution ($F(t)$), representing the number of molecules residing on the surface for time $t$ or longer. These distributions were fit to an exponential mixture model $F(t) = A^{-1}\sum_{k=1}^{N} x_k e^{-t/\tau_k}$ , where $F(t)$ is the probability that an object has a residence time $\geq t$, $x_k$ is the relative fraction of all the objects that follows the desorption pathway $k$, and $\tau_k$ represents the characteristic surface residence time of that pathway (*i.e.*, population)[28]. In this model, which included three populations for the always

folded molecules and four populations for the always unfolded molecules, each pathway was assumed to be a first-order process.

To characterize the unfolding and apparent folding kinetics, the initial state residence time for each molecule was measured. The initial state residence time represents the time that the molecule remains in the conformational state observed in the initial frame immediately after adsorption. Complementary cumulative distributions of the initial state residence time were constructed as described for the analysis of desorption kinetics. The probability distribution of initial state residence times ($p(t_i)$) was adjusted to account for the finite residence times of proteins at the interface before converting it to a complementary cumulative form[29]. The distribution was fitted to a two exponential mixture model to account for folding and unfolding processes as previously described[28].

## 3.4 Results and Discussion

### 3.4.1 Site-specific Labeling of Fibronectin

FN is a large, multi-domain extracellular matrix protein that is highly abundant in serum and plays a central role in the biological response to foreign materials. Specifically, FN, which contains known integrin-binding motifs, can recruit cells to the material upon adsorption and activate various cellular processes, including inflammation, thrombosis, differentiation, and motility[30]. The role of FN in the response of cells to foreign materials underscores the importance of investigating the interaction of FN with polymer brushes and other biomaterials.

Given the large size of native FN (~440kDa), which makes it difficult to produce in most host expression systems and thus engineer for site-specific labeling, a truncated FN construct was

used. This construct (FNIII 8-10) comprised the type III 8-10 domains, which was cloned from the full-length protein and possesses similar cell-binding activity as native FN (**Figure 3.2**)[31-33]. Notably, FNIII 8-10 contains the well-characterized RGD and PHSRN integrin-binding motifs that mediate cell adhesion, spreading, and activation on biomaterial surfaces[34,35]. FNIII 8-10 was site-specifically labeled using orthogonal labeling reactions with dibenzocyclooctyne-Alexa Fluor 555 (donor) and maleimide-Alexa Fluor 647 (acceptor) adjacent to the RGD and PHSRN sites. The RGD and PHSRN sites are in adjoining domains, which unfold independently from each other as well as the other domains in FN[30,36,37]. Given that the individual domains of FN unfold independently, the FNIII 8-10 construct may be used to obtain relevant structural information about the cell-binding region of full-length FN. Such relevant structural information includes the relative distance between the RGD and PHSRN sites in native FN, which is critical to integrin and thus cell binding[33].

Labeling was enabled via introducing *p*-azido-phenylalanine (AzF) and a cysteine at amino acid positions 1500 and 1381, respectively, which correspond to residue numbers in full-length FN. Importantly, FNIII 8-10 lacks any native cysteine residues, which eliminates the potential for mislabeling or the attachment of multiple acceptor fluorophores. By labeling these positions, the distance between the RGD and PHSRN sites (which has previously been shown to influence cell binding activity and is expected to increase upon unfolding of FN) can be directly measured by FRET. Incorporation of AzF in *E. coli* was permitted via suppression of the amber stop codon (TAG), which was inserted via mutagenesis of the native codon at the position corresponding to amino acid 1381[21,38]. In addition to being adjacent to the RGD and PHSRN sites, the mutated residues, which are separated by 2.8 nm in the crystal structure of wild-type FNIII 8-10, are entirely solvent exposed and thus well suited for FRET labeling. Since the Förster radius of the donor-

acceptor pair used in this work was 5.1 nm, changes in FRET efficiency were suitable for monitoring changes between the labeled sites in FNIII 8-10. The structural impact of the mutations in FNIII 8-10 was shown to be negligible by circular dichroism (**Figure A.1**), and the attachment of both fluorophores was confirmed by in-gel fluorescence imaging (**Figure A.2**). Additionally, measurement of the average FRET signal from labeled FNIII 8-10 (referred to as $FN_{FRET}$) upon chemical denaturation in solution confirmed that folded and unfolded $FN_{FRET}$ had unique FRET signatures (**Figure A.3**). The results of solution FRET measurements, in turn, established the utility of the construct for distinguishing between folded and unfolded $FN_{FRET}$ as a function of FRET signal.

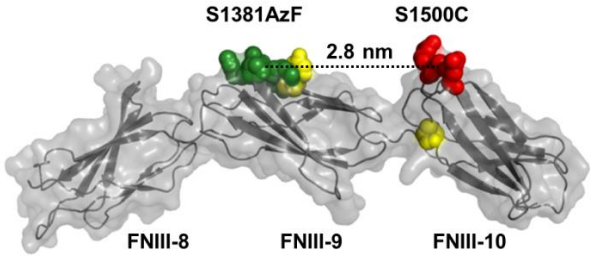


**Figure 3. 2.** Structure of $FN_{FRET}$. The mutated sites S1500C and S1381AzF are shown as red and green spheres, respectively. Residue numbers correspond to those of full-length fibronectin. The yellow spheres indicate the location of the RGD (in the $10^{th}$ type III domain) and the PHSRN synergy (in the $9^{th}$ type III domain) sites relative to the mutated positions. The distance between the labeling sites in the crystal structure of the FN type III repeat domains (PDB code 1FNF) is 2.8 nm (dashed line).

### 3.4.2 Single-Molecule Analysis of FN Adsorption

Adsorption of $FN_{FRET}$ on PEG brushes as a function of grafting density was directly measured via molecular tracking of individual protein molecules in single-molecule experiments. To investigate the effect of grafting density on adsorption, fused silica surfaces were modified with

a silane reactive PEG ($M_w$ 5,000 Da) in the presence of varying ratios of acetone and diethyl ether. The resulting grafting density (σ) of the brush surfaces, which was determined by ellipsometry, varied between 0.16–0.34 chains/nm$^2$, corresponding to a range of 1.7–2.5 nm between grafting points (*i.e.*, tether distance). This range represents the range in grafting density accessible using "grafting to" approaches and also corresponds to the range over which significant differences in protein adsorption have been observed[12,13,25,39-41]. **Table 3.1** shows the grafting density and tether distance of the resulting brush surfaces as well as the measured dry brush thickness. Based on the tether distance and radius of gyration of the PEG used, it was assumed that the polymer chains adopted a relatively extended conformation, consistent with the brush regime[25,42]. The preparation of brush surfaces with greater than 50% diethyl ether was not possible due to poor solubility of the reactive PEG in the binary mixtures above this concentration.

**Table 3. 1.** Structural parameters of PEG brush-functionalized surfaces prepared using mixtures of acetone and diethyl ether. The numbers in parentheses correspond to the uncertainty in the least significant digit, and represent the standard deviation of three independent replicates.

| **Solvent Mixture (Acetone/Ether)** | **Dry Brush Thickness (nm)** | **Grafting density (chains/nm$^2$)** | **Tether distance (nm)** |
|---|---|---|---|
| 100/0 | 1.4(1) | 0.16(1) | 2.48(8) |
| 75/25 | 1.9(1) | 0.22(1) | 2.13(5) |
| 50/50 | 2.9(1) | 0.34(1) | 1.73(3) |

For single-molecule experiments, dilute $FN_{FRET}$ ($5.5x10^{-9}$ M for functionalized or $1x10^{-10}$ M for bare surfaces) that was labeled with donor and acceptor was introduced into a flow cell

containing either PEG-functionalized or bare (*i.e.*, unfunctionalized) fused silica in phosphate buffered saline (pH 7.4 and ionic strength 137 mM). The adsorption of individual molecules was tracked via excitation of the donor fluorophore of molecules at the solution-solid interface under conditions for total internal reflection. Fluorescence emission from the donor and acceptor fluorophore of excited molecules was imaged and collected in spatially aligned, but spectrally distinct channels and used to determine the steady-state adsorption rate constant ($k_{ads}$). The adsorption rate constant measured this way is representative of the *absolute* steady state adsorption rate, which is uniquely accessible via single-molecule analysis, as opposed to the *net* rate of protein accumulation. Molecules that failed to exhibit measurable emission of the donor and acceptor labels, as well as those that were observed on the surface for less than 0.4 s (*i.e.*, < 4 frames), were excluded from analysis to eliminate random noise, artifacts due to impurities, or improperly labeled molecules. Furthermore, super-resolution mapping of the adsorption sites via motion blur point accumulation for imaging in nanoscale topography (mbPAINT)[38] showed that the brush surfaces were essentially uniform (**Figure A.4**). In particular, the mapping showed that, while all surfaces contained rare sites with anomalously high number of adsorption events of single protein molecules (sites with ≥ 2 adsorption events), the fraction of adsorption events at these sites represented only a very small fraction (0.2%-0.4%) of the total number of adsorption events (**Table A.1**).

At the low concentrations and surface coverages used in these experiments, the absolute adsorption rate is assumed to be proportional to the solution concentration of protein, and the proportionality factor is equivalent to the adsorption rate constant. The measured adsorption rate constants, which are summarized in **Figure 3.3** (and **Table A.2**), therefore denote the number of molecules that adsorb in a given area on the surface per unit time, normalized to the concentration

of protein in the bulk solution, and have units that can be reduced by appropriate unitary conversions to distance per time (*i.e.*, μm/s). Intuitively, the numerical value of the adsorption rate constant represents the thickness of a "slab" of solution containing the number of adsorbate molecules that adsorb each second, which is independent of concentration in the low concentration regime[43-47]. Remarkably, even at the lowest grafting density, the adsorption rate constant (0.023 μm/s) was reduced by more than an order of magnitude compared to that on the unfunctionalized silica surface (0.41 μm/s). Additionally, as the grafting density was increased, the adsorption rate constant of $FN_{FRET}$ decreased further, with the rate at the highest grafting density (0.005 μm/s) approximately five times less than at the lowest density. For comparison, the measured adsorption rate constants are similar in magnitude to those measured previously in analogous single-molecule experiments. For example, we previously reported values of $k_{ads}$ in a similar range (0.003 – 1 μm/s) for BSA adsorption on bare fused silica in experiments that systematically varied pH and ionic strength to modulate the strength of electrostatic interactions[45]. Likewise, the rate constant for the adsorption of a fluorescently-labeled $C_{12}$ fatty acid on hydrophobic trimethylsilyl-functionalized silica varied from ~0.1–2 μm/s as a function of composition of the methanol/water solvent[46].

The observed trend of adsorption rate constants with grafting density is consistent with certain theoretical predictions. Specifically, for long-chain, stretched PEG brushes, it has been suggested that steric repulsion is a dominant mechanism of protein resistance. This mechanism involves a repulsive osmotic force due to the unfavorable entropy associated with chain compression[48-50], which competes with attractive short range interactions between the PEG and protein[51,52]. Thus, the balance between long-range repulsive and short range attractive interactions has been predicted to mediate the adsorption of protein molecules, which can be controlled by tuning the grafting density[6,18,49,50]. In particular, as grafting density is increased, the polymer chains

adopt a more extended conformation, which, in turn, increases the barrier for adsorption, presumably decreasing the absolute adsorption rate as observed here. Notably, our results confirm this relationship under dilute steady-state conditions in the absence of interfacial protein-protein interactions, which could potentially lead to deviations in the expected macroscopic behavior of protein molecules in the near-brush environment.

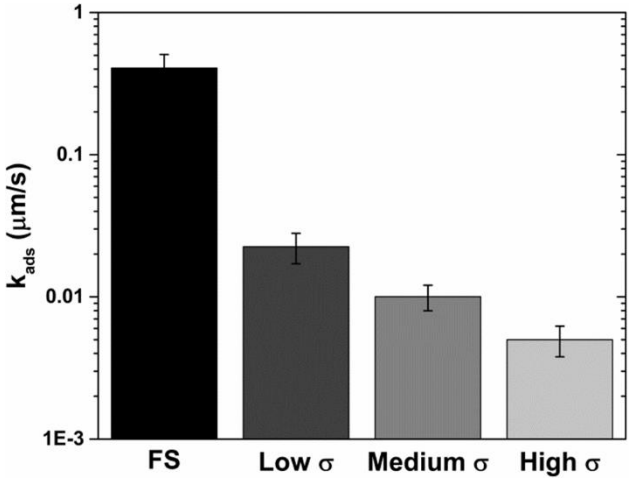


**Figure 3. 3.** Adsorption rate constants of FN at room temperature as a function of PEG grafting density. Error bars represent the standard deviation across 20 data sets for each experiment. Adsorption rate constant were measured in phosphate buffered saline (pH 7.4 and ionic strength 137 mM).

### 3.4.3 Single-Molecule FRET Analysis of FN Conformation

To determine whether grafting density influenced FN conformation, the relative fluorophore-to-fluorophore distance, $d = (F_D/F_A)^{1/6}$, between labeled sites in $FN_{FRET}$ was determined from the accumulated molecular trajectories, where $F_D$ and $F_A$ represent the donor and acceptor emission intensities, respectively. **Figure 3.4** shows the time-average distribution of *d*-values for initially folded molecules (with high acceptor intensity upon adsorption) that resided on the surface for 0.4 s or longer (the same criterion as used in the analysis of adsorption). From the

histogram, distinct FRET populations of folded and unfolded $FN_{FRET}$ were identified, which corresponded to the peaks at $d$=0.9 and $d$=1.45, respectively. Notably, the $d$-values of the peaks closely matched the characteristic ensemble $d$-values for the native and unfolded states of $FN_{FRET}$ in guanidine denaturation experiments (**Figure A.3**). Using the value for which the probability was minimized between the two peaks, a threshold of $d$=1.15 for folding/unfolding was determined, and used as a criterion to determine the folding state in the subsequent analysis. Using the same criterion as for adsorption analysis, any molecule that appeared only in the donor or acceptor channel over its entire surface lifetime was eliminated from subsequent analysis, thereby ensuring that only molecules with a functional donor and acceptor were included in the FRET analysis. In particular, this selection criterion prevented the inclusion of mislabeled molecules that could be misconstrued as always unfolded. Samples of raw images from the FRET analysis that show the identification of molecules in the donor and acceptor channel are provided in **Figure A.5**.

Interestingly, on the surfaces with PEG brushes, the steady-state ratio of folded-to-unfolded $FN_{FRET}$ decreased markedly (from 0.81 to 0.36) with increasing grafting density (**Figure 3.4**). While it is plausible that this decrease was due to increased unfolding of $FN_{FRET}$ at high grafting densities, we found that the fraction of molecules that were explicitly observed to undergo unfolding was small in absolute terms (~7% of all molecules), and the fraction of initially-folded molecules that apparently unfolded was virtually the same on all surfaces (**Table A.3**). It is important to note that we could not resolve unfolding events for molecules that adsorbed in a folded state and unfold immediately upon adsorption (*i.e.*, in a time much shorter than the 100 ms time resolution of the experiment).

An alternative hypothesis was that the apparent shift in average folding state was due to differences in the relative surface residence times of unfolded versus folded molecules at different

grafting densities. Specifically, if interactions between the surface and unfolded molecules were more favorable at high grafting densities compared to low grafting densities, unfolded molecules would be retained longer, resulting in an increase in the time-average *d*-value. While it is plausible that ionic strength and pH influenced the adsorption and unfolding of $FN_{FRET}$ upon interaction with the brush, the buffer conditions used were the same for all grafting densities. Thus, this influence would not explain differences with respect to relative adsorption rate constants and extent of unfolding on the surfaces studied.

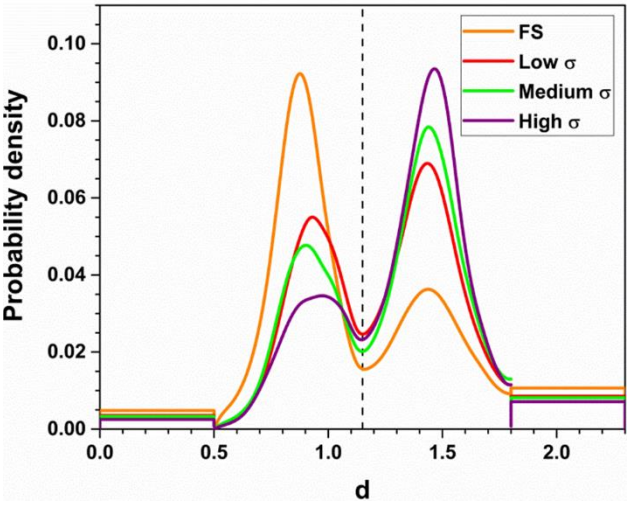


**Figure 3. 4.** Distribution of the relative fluorophore-to-fluorophore distance (*d*) of $FN_{FRET}$ on bare FS (orange line) and functionalized FS with PEG brushes with low (red line), medium (green line), and high (purple line) grafting densities. The peaks at $d$=0.9 and $d$=1.45 represent folded and unfolded states of $FN_{FRET}$, respectively. The regions of the distribution corresponding to $d<0.5$ and $d>1.8$ denote the fraction of molecules lacking measurable intensity in either the donor or acceptor. The vertical dashed line at $d$=1.15 indicates the cutoff criterion used to distinguish folded from unfolded molecules. The ratios of folded-to-unfolded molecules based on the apparent distributions for bare FS, low σ, medium σ, and high σ were 2.60, 0.81, 0.60, and 0.36, respectively.

### 3.4.4 Impact of FN Conformation on Surface Residence Time

To confirm that the shift in ratio of folded-to-unfolded molecules at high grafting density was due to an increase in surface residence time of unfolded molecules, we analyzed the surface residence times of always-folded and always-unfolded molecules as a function of grafting density. For this analysis, molecules with an apparent surface residence time of 0.1 s were ignored to account for the temporal resolution of the experimental data. Given the resolution of the movies captured, molecules with surface residence times of 0.1 s or less could not be distinguished from random noise, which was minimized by excluding these molecules. Moreover, the exclusion of real trajectories with such short surface residence times would not have significantly impacted our analysis.

Complementary cumulative surface residence time distributions for always-folded (A) and always-unfolded (B) molecules, representing the fraction of molecules with a given residence time or longer, are shown in **Figure 3.5**. Notably, the apparent surface residence time of unfolded molecules increased with grafting density, confirming that the apparent increase of unfolded molecules at high grafting densities was due to an increase in surface residence time. Additionally, the surface residence time distributions indicated that folded molecules had much shorter residence times than unfolded molecules at all grafting densities. The characteristic surface residence time constants for always-folded and always-unfolded molecules were determined by fitting the distributions to an exponential mixture model with three populations for always-folded molecules and four populations for always-unfolded molecules (**Table A.4**). The resulting time constants and population fractions were used to calculate weighted average desorption rate constants ($k_{des}$). For folded molecules, the values of $k_{des}$ at low, medium, and high grafting density were 19.2, 20.79, and 23.8 $s^{-1}$, respectively. For unfolded molecules, the values for $k_{des}$ at low, medium, and high

grafting density were 3.3, 3.12, and 2.63 $s^{-1}$, respectively. Based on these values, the desorption of folded and unfolded molecules exhibited opposite trends with grafting density, and folded molecules desorbed an order of magnitude faster than unfolded molecules. These results ultimately corroborated the notion that interactions between the brush and the unfolded state were favored over interactions with the folded state, and that the unfolded state interacted with the brush at high grafting densities more strongly than at low grafting densities. More generally, it was noteworthy that both folded and unfolded molecules ultimately desorbed from the surface, indicating that the adsorption of protein molecules to the brush was highly dynamic, as opposed to irreversible, as has been widely assumed. This finding is in agreement with our earlier results in which we found that the adsorption of the enzyme organophosphorus hydrolase to fused silica was also reversible and thus highly dynamic using dynamic single-molecule tracking[21].

Reversible protein adsorption has been frequently observed under the dilute (*i.e.,* non-fouling) conditions employed in these experiments[21,38,53,54]. Specifically, under the conditions used, the fractional surface coverage of $FN_{FRET}$ was ultra-low (~$10^{-6}$), so the protein-protein interactions that may lead to stable protein layer formation were negligible. The fractional surface coverage was estimated from the number of adsorbed molecules on the surface and the approximate rectangular footprint of the folded form of $FN_{FRET}$ based on the crystal structure of FNIII 8-10. Photophysical artifacts, such as photobleaching, which could potentially influence the apparent residence times of adsorbed molecules, were carefully studied in previous work and shown to be insignificant[21,55,56]. For example, the time constant for donor (*i.e.,* Alexa Fluor 555) photobleaching was measured to be 170 s,[21] which was nearly two orders of magnitude longer than the characteristic time scales associated with desorption and unfolding in this work.

The impact of grafting density on the interaction of unfolded $FN_{FRET}$ with PEG brushes has several potential origins. For example, one might expect an increase of protein entanglement within the brush layer with increasing grafting density. While this explanation is plausible, entanglement would likely lead to an increase in surface residence time of both unfolded and folded molecules, presumably with a larger effect for the unfolded $FN_{FRET}$. However, the opposite trend was in fact observed for folded molecules (*i.e.,* the surface residence time of folded molecules decreased with increasing grafting density). In light of this, although entanglement may play a role on the interaction of unfolded $FN_{FRET}$ with PEG brushes, other phenomena may simultaneously impact such interactions.

A potentially complementary or alternative mechanism is related to changes in the hydration of the brush as a function of grafting density. As grafting density increases, an increase in inter- and intra-chain interactions can reduce the accessibility of the chains to form hydrogen bonds with water, leading to reduced hydration[12,57-59]. Such reduced hydration in regions of the brush may, in turn, favor interactions with the unfolded state of $FN_{FRET}$ at these sites. Because the prevalence of these sites would presumably increase with increasing grafting density, the surface residence time of unfolded $FN_{FRET}$ would likely also increase with grafting density, consistent with the observed trends. Conversely, folded $FN_{FRET}$ would preferentially interact with hydrated regions of the brush and thus have shorter surface residence times, also consistent with our observations.

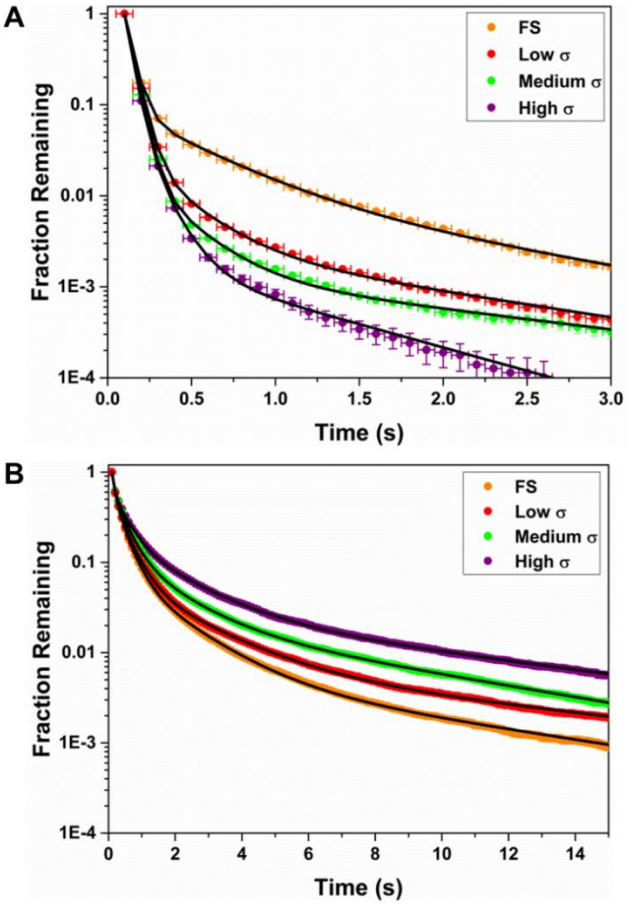


**Figure 3. 5.** Complementary cumulative surface residence time distributions for molecules that were (A) always folded and (B) always unfolded on bare fused silica and various PEG brushes as annotated. Each distribution was fit to an exponential mixture model (black lines), yielding the characteristic surface residence time constant for sub-populations that were present on each surface. The error shown for each data point is based on a 68% confidence interval for the mean of the data, which is described by a Poisson distribution.

### 3.4.5 Kinetics of FN Unfolding and Apparent Re-folding

Analysis of the surface residence times of folded and unfolded $FN_{FRET}$ on PEG brushes suggests that grafting density has a marked impact on protein dynamics at the solution-brush interface. To develop a comprehensive view of this impact, the kinetics of the apparent unfolding and re-folding of $FN_{FRET}$ on the different brush surfaces was determined using initial-state-time distributions. While only a small fraction of molecules were observed to change folding state

during their residence time on the surface (~10% of all molecules), an analysis of these rare events may still provide useful information about the interactions between the brush and the folded and unfolded states. The apparent unfolding kinetics for $FN_{FRET}$ was determined by analyzing the time between adsorption in the folded state (*i.e.*, $d<1.15$) and the first frame in which the molecule was unfolded (*i.e.*, $d\geq1.15$). Similarly, the apparent re-folding kinetics for $FN_{FRET}$ was determined by analyzing the time between adsorption in the unfolded state (*i.e.*, $d\geq1.15$) and the first frame in which the molecule appeared folded (*i.e.*, $d<1.15$).

Because the physical process of protein unfolding presumably occurred too rapidly (*i.e.*, μs) to be resolved in our experiments, the measured apparent rate constants were likely associated with a process leading to unfolding events as opposed to the rapid unfolding itself. In previous work, we demonstrated that proteins generally unfolded at localized "denaturing sites", so that surface-mediated protein unfolding could be equated to a search process for such sites[38]. Notably, the expected time scale of such a search process (via intermittent surface diffusion) is on the order of 0.1 s, which is similar to the time scales of the measured apparent rate constants. Thus, the apparent rate constants for unfolding may reflect the search time required for a folded molecule to encounter a denaturing site on the brush surface, or the converse for a re-folding event. Importantly, although "re-folding" molecules underwent a low-to-high FRET transition, it was not possible to conclude with certainty that the re-entrant high FRET state was structurally identical to the native state, or if the new state represented a compact misfolded state.

The integrated initial state residence time distribution for molecules that underwent a conformational transition from an initial folded or unfolded state are shown in **Figures 3.6 A** and **3.6 B**, respectively. Given the sparse coverage of $FN_{FRET}$ on the surface, the impact of the interaction of molecules on the surface on unfolding and re-folding was negligible. We therefore

assumed that the unfolding kinetics could be described by a superposition of two first-order processes with an exponential mixture model, yielding characteristic rate constants and population fractions for unfolding or re-folding (**Table A.5**). The mean unfolding rate constant ($k_{unf}$) increased from 0.89–1.4 $s^{-1}$, whereas the mean folding rate constant ($k_{fold}$) decreased from 0.23–0.13 $s^{-1}$ for the PEG brush surfaces with increasing grafting density. Interestingly, the apparent kinetics of unfolding increased with increasing grafting density, indicating that molecules more rapidly encountered denaturing sites as grafting density increased (**Figure 3.6 A**). Such a decrease in search times was presumably the result of the brush having a higher density of denaturing regions, which was likely related to a correlation between high local brush density and low local hydration. Conversely, the relationship between the apparent re-folding of $FN_{FRET}$ and grafting density was the opposite (*i.e.,* molecules re-folded more rapidly with decreasing grafting density). The relationship between re-folding and grafting density was also consistent with the presence of fewer regions on the surfaces that interacted more strongly with the denatured state. Interestingly, the apparent observation of re-folding of $FN_{FRET}$ while in contact with the brush may be related to the previously reported chaperone-like activity of PEG[60].

Using single-molecule methods, our results provide unprecedented insight into the connection between changes in protein structure upon adsorption on PEG brushes and grafting density. These findings may help explain previous observations of the impact of grafting density on protein accumulation on PEG brushes. For example, in a series of seminal papers, Unsworth and co-workers[12,13,16] previously found that the relationship between protein accumulation and grafting density was non-monotonic for PEG chains of different lengths. Specifically, for PEG with the same molecular weight and similar range of grafting density used here, an optimal grafting density for protein resistance (~0.27 chains/$nm^2$) was reported. This finding was obtained by

measuring the accumulation of irreversibly-adsorbed lysozyme via radiolabeling under high protein concentration conditions. Under these conditions, unlike in our experiments, stable protein layers may form due to fouling, which is a complex process that is presumably the combined result of multiple individual elementary process. Based on our results, we hypothesize that the presence of this optimum grafting density may be due to a compromise between adsorption rate and conformational state. Specifically, while higher grafting density above the optimum would further decrease the adsorption rate, increased unfolding of the protein may enhance protein-protein associations, stabilizing the adsorbed protein layer. Higher order processes, such as interfacial protein aggregation, are not directly probed using ensemble-averaging methods; however, using single-molecule intermolecular FRET we have previously shown that the macroscopic protein resistance of biomaterial surfaces was correlated to the concentration-dependence of protein-protein associations (both number and duration)[54].

However, for other proteins, studies using traditional ensemble-averaging methods (e.g. surface plasmon resonance, ellipsometry, and quartz crystal microbalance) have reported a monotonic decrease of non-specific protein accumulation over a similar range of grafting density. For example, Schneck and co-workers[40] observed a monotonic decrease in myoglobin accumulation with grafting density on PEG brushes using neutron reflectometry. They also found that proteins penetrated the brush layer and interacted with the polymer within the brush itself.[41] Similar trends had been previously described by Malmsten et al.[39] and Sofia et al.[25] using *in situ* and *ex situ* ellipsometry, respectively, for several proteins, including full-length human fibronectin. Emilsson and co-workers[8] also recently reported that the irreversible accumulation of BSA on PEG brushes decreased monotonically as the near-surface concentration of monomer was increased (which is qualitatively similar to increasing grafting density). Since these trends are consistent with

those observed here for adsorption rate constants alone, it is possible that conformational change was not a major factor for these specific combinations of proteins and surfaces. The variability of the trends observed with different proteins and under different conditions highlights the importance of decoupling the abovementioned elementary processes to understand the effect of brush properties on protein adsorption, unfolding, aggregation, etc. in particular cases.

Our results, taken together, have important implications for the rational design of PEG brushes for use as a biomaterial in physiological environments. Notably, our results suggest that altering the grafting density inversely affects protein adsorption and the retention of natively folded protein on the surface. In light of these effects, there is inherently a balance between resisting protein adsorption and the stabilization of unfolded protein on the surface that arises from increasing grafting density. An understanding of this balance is critical given that, in physiological environments, the cellular response to PEG brushes may, in fact, be mediated by rare populations of unfolded protein molecules at the solution-brush interface, rather than the total amount of adsorbed protein[7,61]. For example, a critical step in the foreign body reaction to implantable biomaterials is widely thought to be the recognition of macrophages to unfolded serum proteins on the biomaterial surface.[62] In relation to this, Sivaraman and co-workers[19] reported that platelets bind to adsorbed albumin via recognition of binding sites in albumin that are exposed and/or formed by adsorption-induced unfolding. In this work, beyond a critical degree of unfolding, the level of platelet adhesion correlated strongly with the amount of unfolded albumin on the surface. Accordingly, when designing PEG brushes for biomaterial applications, consideration of the impact of grafting density on both protein adsorption and the presentation of unfolded proteins is ultimately critical, and likely to directly impact the function of the biomaterial. Importantly, this impact may be further influenced by interfacial protein-protein interactions at protein

concentrations that are higher than those used in our experiments. Additionally, there are many other examples, including the storage stability of therapeutic protein formulations, where it is more critical to prevent protein unfolding (*e.g.*, due to the immunogenic potential of denatured protein molecules upon release from the wall of a glass syringe) rather than to simply reduce the amount of adsorbed protein.

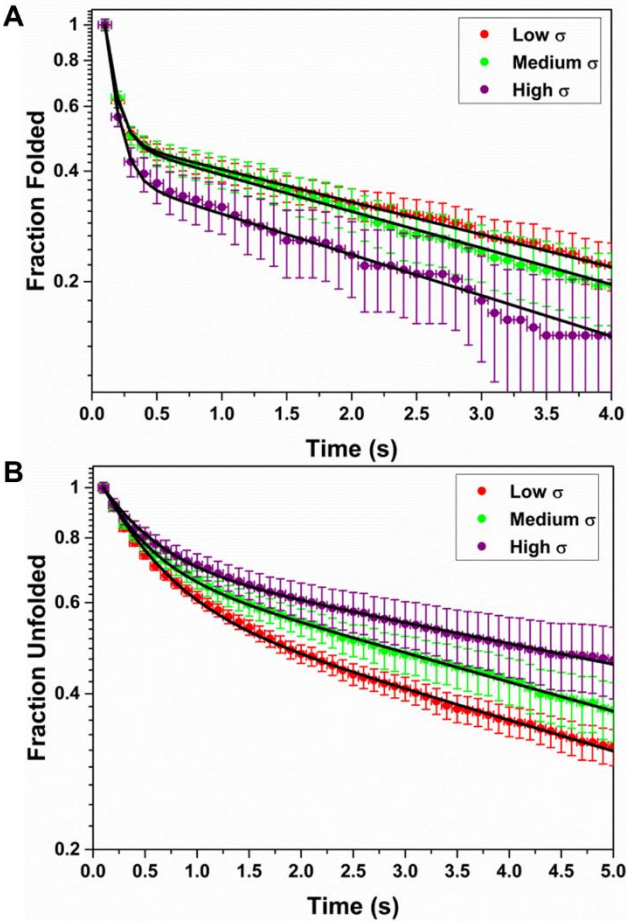


**Figure 3. 6.** Complementary cumulative initial state residence time distribution for molecules that underwent a conformational change from an initial (A) folded or (B) unfolded state, showing the kinetics of unfolding and re-folding, respectively, on fused silica or PEG brushes, as annotated. Each distribution was fit to an exponential mixture model (black lines) to determine the characteristic time constants and population fractions for unfolding or re-folding. The error shown for each data point is based on a 68% confidence interval for the mean of the data, which is described by a Poisson distribution. Because a conformation-specific residence time cannot be

determined for a time of 0 s, the initial time for each distribution is 0.1 s, which corresponds to the time at which the first image was collected.

## 3.5 Conclusions

We have shown using single-molecule methods that the interactions of proteins with PEG brushes are highly complex and vary as a function of grafting density. In particular, increasing the PEG grafting density led to lower adsorption rate constants of $FN_{FRET}$ while resulting in an increase in unfolding kinetics and the retention of unfolded protein molecules. These findings provide insight into the connection between interfacial protein dynamics and protein conformation with unprecedented resolution. Such insight could only be obtained using single-molecule methods that permit the direct correlation of protein adsorption, desorption, and structure on a molecule-by-molecule basis. This insight ultimately has important implications for the rational design of PEG brushes to resist protein adsorption as well as the adsorption of unfolded protein molecules, which may trigger adverse biological responses. Given our findings, depending on the environment, there is likely an optimal grafting ratio that minimizes both total adsorption and the presentation of unfolded molecules.

**SUPPORTING INFORMATION**

Solution characterization of $FN_{FRET}$ structure and ensemble denaturation, analysis of $FN_{FRET}$ labeling, results of super-resolution mapping, representative fluorescent images from SM-FRET experiments, detailed parameterization of kinetic processes, and tables with adsorption rate constants and fraction of unfolding events can be found in **Appendix A**.

## 3.6 References


(1) Utrata-Wesolek, A. *Polimery-W* **2013**, *58*, 685-695.
(2) Morra, M. *J Biomat Sci-Polym E* **2000**, *11*, 547-569.
(3) Azzaroni, O. *J Polym Sci Pol Chem* **2012**, *50*, 3225-3258.
(4) Banerjee, I.; Pangule, R. C.; Kane, R. S. *Adv Mater* **2011**, *23*, 690-718.
(5) Chen, S. F.; Li, L. Y.; Zhao, C.; Zheng, J. *Polymer* **2010**, *51*, 5283-5293.
(6) Leckband, D.; Sheth, S.; Halperin, A. *J Biomat Sci-Polym E* **1999**, *10*, 1125-1147.
(7) Tanaka, M.; Hayashi, T.; Morita, S. *Polym J* **2013**, *45*, 701-710.
(8) Emilsson, G.; Schoch, R. L.; Feuz, L.; Hook, F.; Lim, R. Y. H.; Dahlin, A. B. *Acs Appl Mater Inter* **2015**, *7*, 7505-7515.
(9) Jo, S.; Park, K. *Biomaterials* **2000**, *21*, 605-616.
(10) Taylor, W.; Jones, R. A. L. *Langmuir* **2010**, *26*, 13954-13958.
(11) Rodriguez-Emmenegger, C.; Brynda, E.; Riedel, T.; Houska, M.; Subr, V.; Alles, A. B.; Hasan, E.; Gautrot, J. E.; Huck, W. T. *Macromol Rapid Commun* **2011**, *32*, 952-957.
(12) Unsworth, L. D.; Sheardown, H.; Brash, J. L. *Langmuir* **2008**, *24*, 1924-1929.
(13) Unsworth, L. D.; Sheardown, H.; Brash, J. L. *Langmuir* **2005**, *21*, 1036-1041.
(14) Vanderah, D. J.; La, H. L.; Naff, J.; Silin, V.; Rubinson, K. A. *J Am Chem Soc* **2004**, *126*, 13639-13641.
(15) Li, L. Y.; Chen, S. F.; Zheng, J.; Ratner, B. D.; Jiang, S. Y. *J Phys Chem B* **2005**, *109*, 2934-2941.
(16) Unsworth, L. D.; Tun, Z.; Sheardown, H.; Brash, J. L. *J Colloid Interf Sci* **2006**, *296*, 520-526.
(17) Zheng, J.; Li, L. Y.; Chen, S. F.; Jiang, S. Y. *Langmuir* **2004**, *20*, 8931-8938.
(18) Fang, F.; Satulovsky, J.; Szleifer, I. *Biophys J* **2005**, *89*, 1516-1533.
(19) Sivaraman, B.; Latour, R. A. *Biomaterials* **2010**, *31*, 1036-1044.
(20) Xia, N.; Castner, D. G. *J Biomed Mater Res A* **2003**, *67A*, 179-190.
(21) McLoughlin, S. Y.; Kastantin, M.; Schwartz, D. K.; Kaar, J. L. *P Natl Acad Sci USA* **2013**, *110*, 19396-19401.
(22) Hammill, J. T.; Miyake-Stoner, S.; Hazen, J. L.; Jackson, J. C.; Mehl, R. A. *Nat Protoc* **2007**, *2*, 2601-2607.
(23) Peeler, J. C.; Mehl, R. A. *Methods Mol Biol* **2012**, *794*, 125-134.
(24) Arcot, L.; Ogaki, R.; Zhang, S.; Meyer, R. L.; Kingshott, P. *Appl Surf Sci* **2015**, *341*, 134-141.
(25) Sofia, S. J.; Premnath, V. V.; Merrill, E. W. *Macromolecules* **1998**, *31*, 5059-5070.
(26) Kastantin, M.; Keller, T. F.; Jandt, K. D.; Schwartz, D. K. *Adv Funct Mater* **2012**, *22*, 2617-2623.
(27) Walder, R.; Kastantin, M.; Schwartz, D. K. *Analyst* **2012**, *137*, 2987-2996.
(28) Kastantin, M.; Schwartz, D. K. *Chemphyschem* **2013**, *14*, 374-380.
(29) Kastantin, M.; Schwartz, D. K. *Small* **2013**, *9*, 933-941.
(30) Pickford, A. R.; Smith, S. P.; Staunton, D.; Boyd, J.; Campbell, I. D. *Embo J* **2001**, *20*, 1519-1529.
(31) van der Walle, C. F.; Altroff, H.; Mardon, H. J. *Protein Eng* **2002**, *15*, 1021-1024.
(32) Altroff, H.; Choulier, L.; Mardon, H. J. *J Biol Chem* **2003**, *278*, 491-497.
(33) Altroff, H.; van der Walle, C. F.; Asselin, J.; Fairless, R.; Campbell, I. D.; Mardon, H. J. *J Biol Chem* **2001**, *276*, 38885-38892.

(34) Redick, S. D.; Settles, D. L.; Briscoe, G.; Erickson, H. P. *J Cell Biol* **2000**, *149*, 521-527.
(35) Aota, S.; Nomizu, M.; Yamada, K. M. *J Biol Chem* **1994**, *269*, 24756-24761.
(36) Bork, P.; Blomberg, N.; Nilges, M. *Nat Genet* **1996**, *13*, 22-23.
(37) Campbell, I. D.; Downing, A. K. *Nat Struct Biol* **1998**, *5 Suppl*, 496-499.
(38) Weltz, J. S.; Schwartz, D. K.; Kaar, J. L. *ACS Nano* **2015** (*in press*).
(39) Malmsten, M.; Emoto, K.; Van Alstine, J. M. *J Colloid Interf Sci* **1998**, *202*, 507-517.
(40) Schneck, E.; Schollier, A.; Halperin, A.; Moulin, M.; Haertlein, M.; Sferrazza, M.; Fragneto, G. *Langmuir* **2013**, *29*, 14178-14187.
(41) Schneck, E.; Berts, I.; Halperin, A.; Daillant, J.; Fragneto, G. *Biomaterials* **2015**, *46*, 95-104.
(42) Devanand, K.; Selser, J. C. *Macromolecules* **1991**, *24*, 5943-5947.
(43) Walder, R.; Nelson, N.; Schwartz, D. K. *Nat Commun* **2011**, *2*,515.
(44) Walder, R.; Schwartz, D. K. *Soft Matter* **2011**, *7*, 7616-7622.
(45) McUmber, A. C.; Randolph, T. W.; Schwartz, D. K. *J Phys Chem Lett* **2015**, *6*, 2583-2587.
(46) Mabry, J. N.; Skaug, M. J.; Schwartz, D. K. *Anal Chem* **2014**, *86*, 9451-9458.
(47) Nelson, N.; Schwartz, D. K. *J Phys Chem Lett* **2013**, *4*, 4064-4068.
(48) Israelachvili, J. N. *Intermolecular and Surface Forces, 3rd Edition* **2011**, 1-674.
(49) Szleifer, I. *Biophys J* **1997**, *72*, 595-612.
(50) Jeon, S. I.; Lee, J. H.; Andrade, J. D.; Degennes, P. G. *J Colloid Interf Sci* **1991**, *142*, 149-158.
(51) Abbott, N. L.; Blankschtein, D.; Hatton, T. A. *Macromolecules* **1992**, *25*, 3932-3941.
(52) Sheth, S. R.; Leckband, D. *P Natl Acad Sci USA* **1997**, *94*, 8399-8404.
(53) Kastantin, M.; Langdon, B. B.; Chang, E. L.; Schwartz, D. K. *J Am Chem Soc* **2011**, *133*, 4975-4983.
(54) Langdon, B. B.; Kastantin, M.; Schwartz, D. K. *Biomacromolecules* **2015**, *16*, 3201-3208.
(55) Mabry, J. N.; Kastantin, M.; Schwartz, D. K. *ACS Nano* **2015**, *9*, 7237-7247.
(56) Monserud, J. H.; Schwartz, D. K. *Biomacromolecules* **2012**, *13*, 4002-4011.
(57) Jeon, S. I.; Andrade, J. D. *J Colloid Interf Sci* **1991**, *142*, 159-166.
(58) Yandi, W.; Mieszkin, S.; Martin-Tanchereau, P.; Callow, M. E.; Callow, J. A.; Tyson, L.; Liedberg, B.; Ederth, T. *Acs Appl Mater Inter* **2014**, *6*, 11448-11458.
(59) Jin, J.; Jiang, W.; Yin, J. H.; Ji, X. L.; Stagnaro, P. *Langmuir* **2013**, *29*, 6624-6633.
(60) Cleland, J. L.; Builder, S. E.; Swartz, J. R.; Winkler, M.; Chang, J. Y.; Wang, D. I. C. *Bio-Technol* **1992**, *10*, 1013-1019.
(61) Tziampazis, E.; Kohn, J.; Moghe, P. V. *Biomaterials* **2000**, *21*, 511-520.
(62) Franz, S.; Rammelt, S.; Scharnweber, D.; Simon, J. C. *Biomaterials* **2011**, *32*, 6692-6709.

# Chapter IV: Grafting Density Impacts Local Nanoscale Hydrophobicity in Poly(ethylene glycol) Brushes

David Faulón Marruecos, Daniel F. Kienle, Joel L. Kaar, and Daniel K. Schwartz

(Published April, 2018: ACS Macro Letters, 7(4), 498-503)

## 4.1 Abstract

Accumulated single-molecule observations of a fluorescent solvatochromic probe molecule were found to provide detailed local information about nanoscale hydrophobicity in polymer brushes. Using this approach, we showed that local hydrophobicity in poly(ethylene glycol) (PEG) brushes was spatially heterogeneous and increased with the surface grafting density of the polymer chains. These findings may provide an explanation for prior observations of the denaturation of surface-adsorbed proteins on PEG brushes with high grafting densities, which is believed to influence protein-mediated cell-surface interactions. Moreover, by employing the broad range of existing environmentally sensitive fluorophores, this approach can potentially be used to characterize nanoscale changes in a variety of physico-chemical properties within polymeric materials.

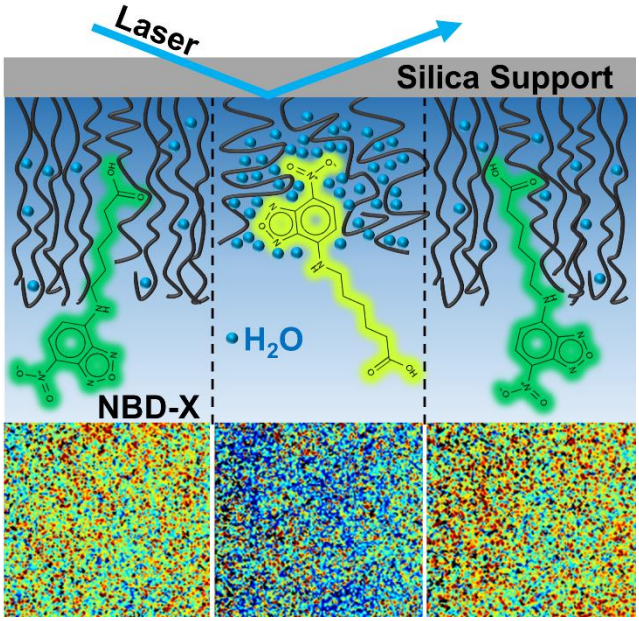


**Figure 4. 1.** The fluorescent probe NBD-X, which emits at different wavelengths depending on the hydrophobicity of its environment, was used to map PEG brushes with different grafting densities. Super-resolution maps generated from accumulated NBD-X trajectories are shown in the bottom, where warmer colors indicate higher local hydrophobicity. The chemical structure of NBD-X, which is considerably smaller than the swollen height of the PEG brushes, is not drawn to scale for visualization purposes.

## 4.1 Introduction

Polymer brushes composed of poly(ethylene glycol) (PEG) are widely used as a steric barrier to inhibit the adsorption of proteins to materials in biological milieu[1-8]. However, while PEG brushes often reduce protein adsorption, they do not eliminate it entirely, and the adsorption of proteins to PEG brushes depends upon the grafting density ($\sigma$) of PEG as well as the molecular weight (MW) of the PEG chains[9-18]. In particular, for a given PEG MW, there is often an apparent optimum "protein-resistant" range of grafting density outside of which protein accumulation increases[9,10,16-19]. While the molecular basis for this optimum is unclear, it has been hypothesized to arise from the emergence of nanoscale hydrophobic regions in the brush at higher grafting density. Unfolded protein molecules may have strong affinity to such regions, which would enhance surface-mediated protein aggregation and increased adsorption.

We recently investigated the relationship between grafting density and protein adsorption and unfolding on PEG brushes using single-molecule (SM) Förster resonance energy transfer methods that are uniquely sensitive to interfacial dynamics and conformational changes[20]. Interestingly, while brushes with higher grafting density decreased the overall rate of protein adsorption, they also stabilized unfolded protein molecules and increased the rate of protein unfolding, leading to a greater fraction of accumulated unfolded proteins. Since unfolded protein molecules are presumably stabilized on hydrophobic sites, these findings support the hypothetical connection between grafting density and a decrease in the local hydration within the brush layer.

While some findings have suggested that dense PEG brushes may exhibit an increased hydrophobic character[10,15,17], this counters the more conventional belief that increasing the amount of PEG on a given surface also increases the overall hydrophilicity of that surface. The explicit

resolution of this issue has remained elusive due to the lack of available experimental methods to detect nanoscale changes in hydrophobicity within the brush layer. Using conventional methods for measuring surface hydrophobicity, such subtle and local changes are typically masked by the ensemble-averaging nature of such measurements on surfaces that are intrinsically heterogeneous. For example, the effect of PEG brush density on the static contact angle of water is empirically undetectable. Additionally, traditional methods are insensitive to temporal fluctuations in the existence of nanoscale hydrophobic niches due to dynamic changes in the conformation of the polymer chains. Although sum frequency generation spectroscopy may also be used to characterize the *in situ* hydration of polymer brushes, as well as provide information about the interaction of water molecules with the polymer chains, the information provided by this technique is also ensemble-averaged[8,21].

Here, we developed and employed a new method to investigate the impact of grafting density on the local hydration of PEG brushes via super-resolution fluorescence mapping. This approach, which was based on mapping using accumulated probe trajectories (MAPT)[22-24], exploited the solvatochomic properties of the environmentally sensitive fluorophore nitrobenzoxadiazole (NBD). Notably, the fluorescent emission of the NBD derivative 6-(*N*-(7-nitrobenz-2-oxa-1,3-diazol-4-yl)amino)hexanoic acid (NBD-X) undergoes a dramatic red-shift and has reduced intensity in a hydrophilic (polar) environment compared with the emission in a hydrophobic (nonpolar) environment[25,26]. Changes in the emission wavelength of NBD-X were mapped molecule-by-molecule with nanoscale resolution on PEG brushes with low (0.16 chains/nm$^2$) and high (0.34 chains/nm$^2$) grafting density.

## 4.2 Results and Discussion

Super-resolution maps of these changes at the brush-liquid interface were generated using SM total internal reflection fluorescence (TIRF) microscopy of the brush surfaces during exposure to solutions containing NBD-X probe molecules (**Figure 4.2 a**). The resulting maps provided new insights into the increase in nanoscale hydrophobic sites with grafting density, which is critical for tuning the interaction between protein and PEG brushes and, in turn, modulating cell responses to denatured protein on the brush surface[27-31].

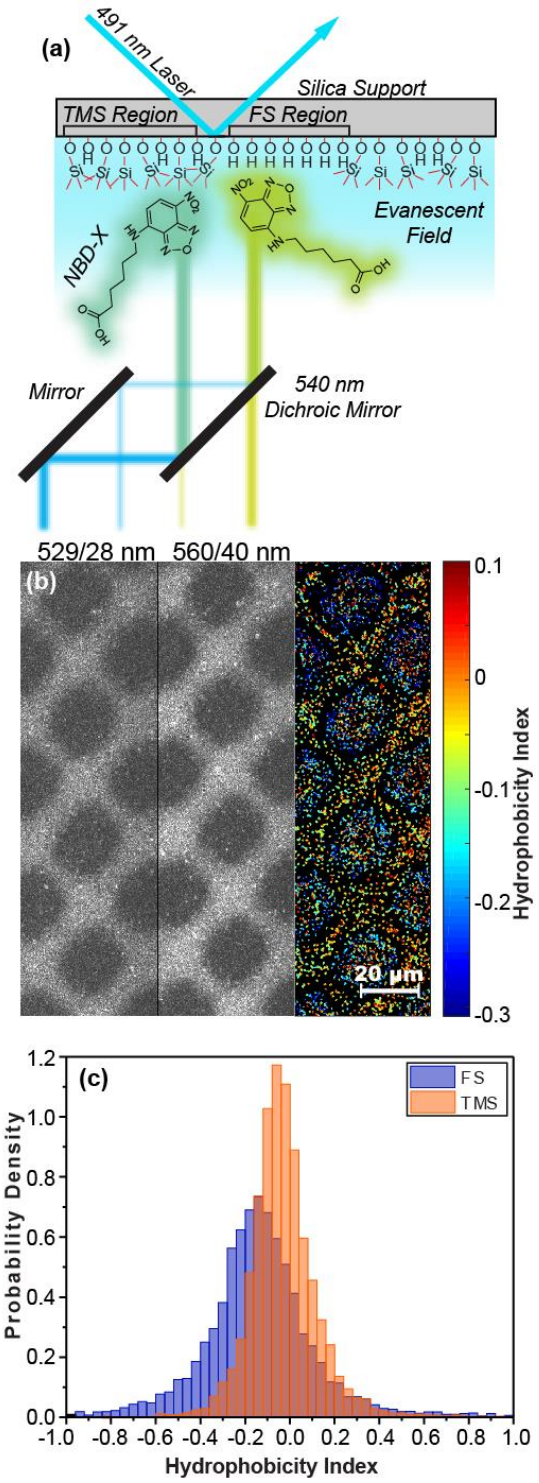


**Figure 4. 2.** (a) Experimental schematic. The excitation laser is totally internally reflected at the silica-water interface, creating an evanescent field that excites dissolved NBD-X molecules. Upon adsorption on hydrophilic (FS) patches, the dye emits at a longer wavelength than on hydrophobic (TMS) patches. Emitted photons are spectrally separated and steered to different regions of a camera sensor. (b) Super-resolution map of a patterned surface, with FS squares surrounded by

TMS regions, generated from $2x10^6$ NBD-X trajectories. The color scale represents changes in local hydrophobicity based on the parameter HI as described in the text. (c) Probability density distributions of HI values. A time-averaged image was used to define regions corresponding to FS and TMS. The HI values from these regions were used to generate the corresponding probability density distributions. The p-value of the Student t-test on the mean of the distributions was $< 1x10^{-15}$, indicating that the distributions were statistically different.

The nanoscale mapping of surface hydrophobicity via spectral shift of NBD-X was validated by characterizing nanopatterned surfaces comprising hydrophilic fused silica (FS) and hydrophobic trimethylsiloxane (TMS) domains. Dual-channel images were acquired by splitting the fluorescent emission of the NBD-X molecules into spectral channels with peak transmission wavelengths at 529 nm and 560 nm, respectively (**Figure 4.2 b**, left and middle panels). The positions and dual channel intensities of individual NBD-X molecules from each sequential image were identified and tracked using custom software. Detailed descriptions of the surface preparation, experimental apparatus, and software algorithms are provided in the Supporting Information.

The intensities from each channel corresponding to individual objects were used to define a "Hydrophobicity Index" (HI) as

$$Hydrophobicity\ Index = log_{10}\left(\frac{I_{529}}{I_{560}}\right) \quad \text{(eq. 4.1)}$$

where $I_{529}$ was the object intensity measured in the 529 nm channel and $I_{560}$ was the object intensity measured in the 560 nm channel. Larger values of HI corresponded to a more hydrophobic environment while an HI value of zero represented a site with similar hydrophobic and hydrophilic character. As such, sites that had an HI value of zero were amphiphilic in nature, where the hydrophobicity and hydrophilicity of the site was equally balanced. This allowed us to characterize the local chemical environment surrounding each probe molecule with resolution limited only by

the localization precision of 70 ± 30 nm. Super-resolution surface maps of HI were created by binning all objects by spatial position. For this, we divided the field of view into an array of 217x217 $nm^2$ bins. The HI bin values were calculated by averaging the HI values of all objects that occupied a bin throughout the video.

A spatial map of HI, along with a probability density of the data corresponding to the FS and TMS regions, is shown in **Figure 4.2 b** (right panel) and **Figure 4.2 c**, respectively. As expected, the objects in TMS regions were systematically shifted to larger HI values than the FS regions, as indicated by the blue shift of the NBD-X emission. Interestingly, a small hydrophobic region was observed at the center of each FS square, suggesting that the TMS layer was not fully degraded during photo-patterning. The same measurement and analytical methods were applied to PEG polymer brushes with low and high grafting densities, which were made by using a grafting to- approach with a good and a poor solvent, respectively[32] (see the Supporting Information for details of brush preparation). The brushes were characterized by ellipsometry in the dry state, and the thickness was converted to a grafting density as described previously[20].

For the PEG brush surfaces, the HI maps (**Figure 4.3 a**) indicated that the high grafting density brush exhibited more regions of greater hydrophobicity. This difference was further shown via comparison of the corresponding probability density distributions of HI for the low and high grafting densities (**Figure 4.3 b**). These observations represented direct nano-scale experimental confirmation of steric repulsion theory[33-37], which predicts a decrease in internal brush hydration and a corresponding increase in brush hydrophobicity with increasing grafting density due to a greater number of favorable PEG chain-chain interactions vs. PEG-water interactions[10,38-40]. Furthermore, they provided a fundamental explanation of previous single-molecule observations in which unfolding of fibronectin (FN) was favored in PEG brushes with higher grafting density[20].

Specifically, these combined observations demonstrate that an increase in grafting density leads to an increase in both surface hydrophobicity and FN unfolding, supporting the hypothesis that stronger stabilization of unfolded protein molecules and faster unfolding occurred in an environment predominately composed of low-hydration denaturing regions. This direct link between grafting density, local brush hydrophobicity and protein unfolding has critical implications for polymer brush design. Notably, when measured by static contact angle, the wettability of the surfaces was identical within experimental error (~30°), indicating the inability to measure such differences with standard methods (**Figure B.1**). Additionally, the approximate swollen brush height was calculated to be roughly 10 nm for both the low (9 nm) and high (11 nm) grafting densities using Alexander-DeGennes scaling theory[35]. This distance is considerably larger than the size of NBD-X (~0.7 nm) and was considerably smaller than the penetration depth of the evanescence TIRF field (~100 nm). Furthermore, the approximate separation between grafting points were 2.5 nm and 1.7 nm for the low and high grafting density surfaces, respectively. Given this, the hydrophobic niches that were imaged may be within the brush layer in addition to on the surface of the brush.

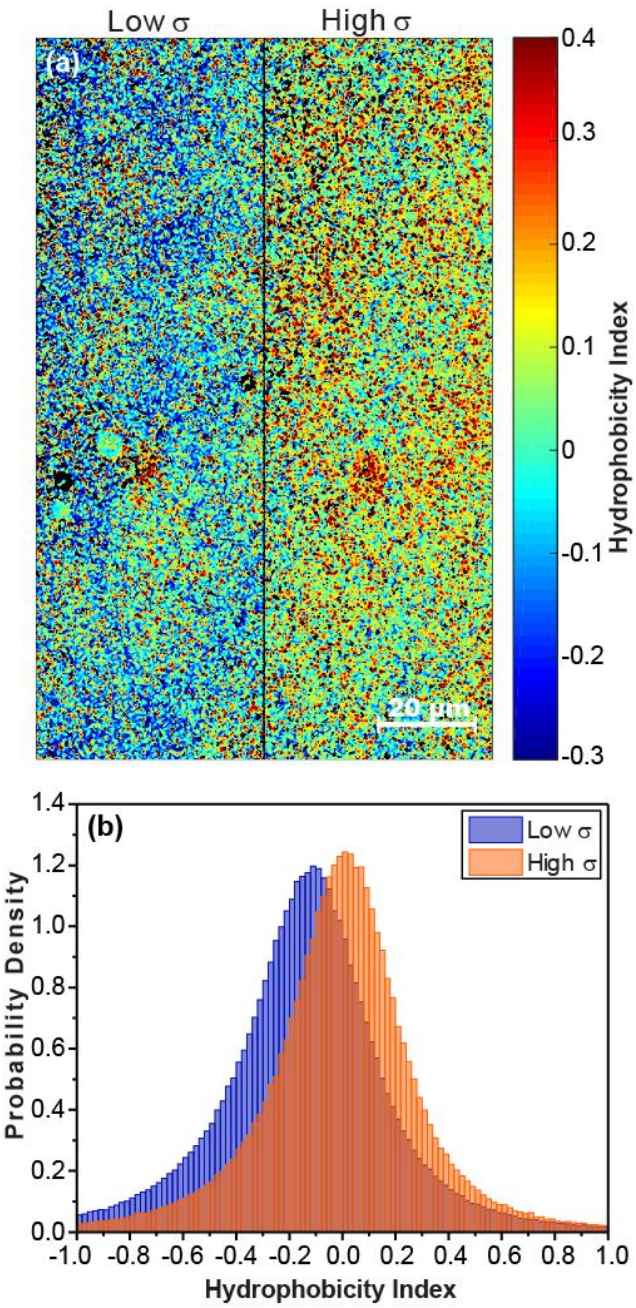


**Figure 4. 3.** (a) Super-resolution maps generated from accumulated NBD-X trajectories for both high and low grafting density PEG brush surfaces ($6x10^5$ and $1x10^6$ trajectories, respectively). The color scale indicates the differences in local hydrophobicity based on the parameter HI. (b) Probability density distributions of HI values for both surfaces. The p-value of the Student t-test on the mean of the distributions was < $1x10^{-15}$, indicating that the distributions were statistically different.

Molecules experiencing different chemical environments are likely to exhibit different dynamic behavior, governed by the distinct molecule-surface interactions. Thus, we sought to test whether the regions representing different HI values also resulted in distinctive physical consequences and to directly connect local HI with molecular dynamics. To do so, it was necessary to identify dynamic behavior dominated by local interactions within the brush layer, and we found that desorption (i.e., surface residence time) met this criterion. In contrast, for example, the adsorption rate of molecules to the brush layer was dominated by the overall steric repulsion of the brush (as described in the Supporting Information).

Unlike adsorption, the desorption of molecules from the surface is dominated by non-electrostatic short-range van der Waals or hydrophobic interactions[41], which we hypothesized would be sensitive to local changes in surface hydrophobicity. Thus, we used the residence time of molecules to probe correlations between HI and dynamic NBD-X behavior. **Figure 4.4** shows the normalized mean residence time of NBD-X molecules as a function of the average HI experienced during a trajectory. The fact that these data exhibit clear and systematic trends indicates that the dynamic behavior of probe molecules was directly sensitive to HI, further demonstrating that HI was a valid measure of the local physical environment.

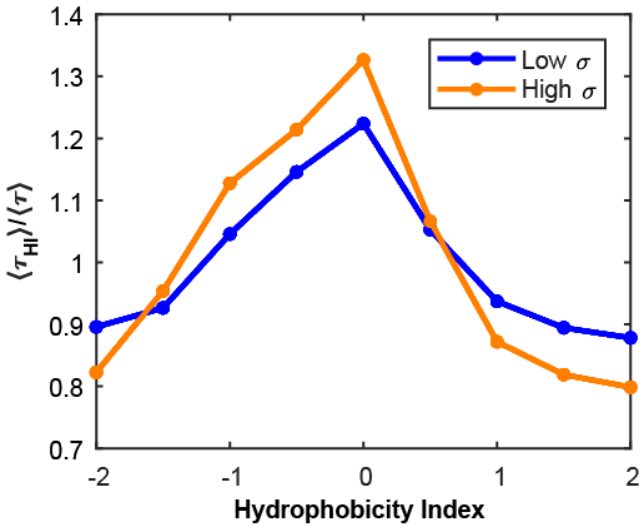


**Figure 4. 4.** Mean surface residence time for trajectories whose average HI was within a given 0.5 HI unit bin centered at each data point, $\langle\tau_{HI}\rangle$, for both high (orange) and low (blue) grafting density PEG brushes. Data points were normalized by the mean residence time corresponding to all trajectories within the range -2 < mean HI < 2, $\langle\tau\rangle$, which were 0.64 s and 0.55 s for the high and low grafting density surfaces, respectively.

Interestingly, the relationship between residence time and local HI exhibited a non-monotonic trend for both surfaces with a maximum residence time for trajectories that experienced a value of HI close to 0. As noted above, a hydrophobic index of 0, due to the way in which HI is defined, represented a site that had comparable hydrophobic and hydrophilic character. This observation may be due to the amphiphilic nature of the probe, which comprises a carboxylic acid group (expected to have higher affinity for hydrophilic regions) and aromatic rings (with greater affinity to hydrophobic areas). Thus, the longer residence times at HI values close to 0 suggested that the probe had a strong overall affinity for local amphiphilic binding sites. With respect to more extreme HI values, the NBD-X showed slightly greater affinity (longer residence times) for strongly hydrophilic regions than for strongly hydrophobic regions, suggesting a weaker interaction between the hydrophobic group and the surface, which may be related to the anomalous (depleted and fast-moving) behavior of water molecules near hydrophobic surfaces[42,43]. We have

previously observed that molecules diffuse and desorb rapidly on hydrophobic surfaces[44,45]. The normalized mean residence times of each HI range, $\langle \tau_{HI} \rangle$ showed virtually identical trends on both surfaces. Overall, as demonstrated by the data shown in **Figure 4.4**, the NBD-X trajectories provide a nuanced view of the ways in which the local chemical environment influences molecular dynamics. The fact that the absolute residence times were longer at high grafting densities was presumably due to a complex function of physical structure (e.g., entanglement), mass transport, and local interactions, and could not be understood solely in terms of hydrophobicity.

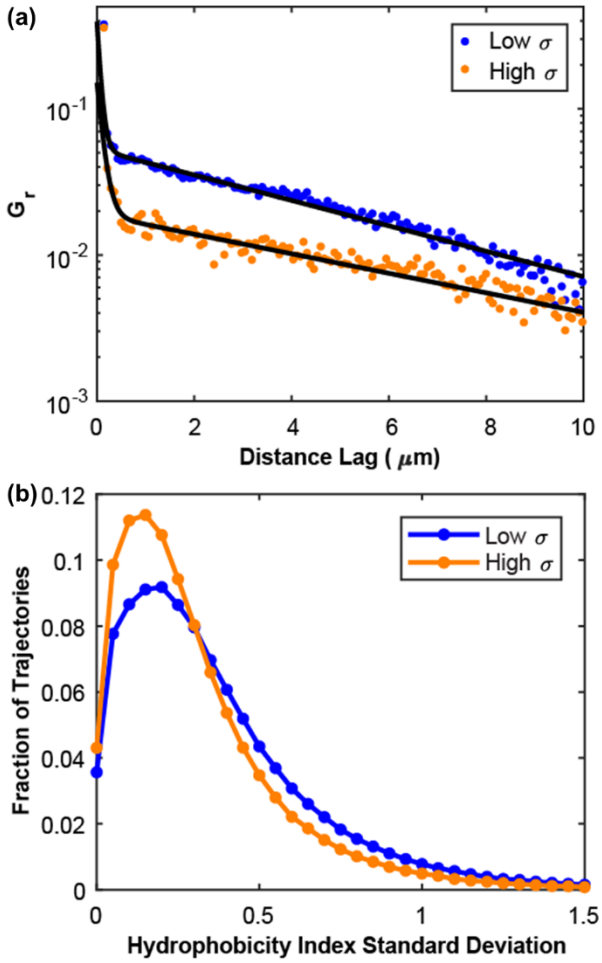


**Figure 4. 5.** (a) Normalized radial autocorrelation functions ($G_r$) of HI values for the low σ surface (blue dots) and the high σ surface (orange dots), calculated with the software *Gwyddion*. Data points were fit to a mixture of two exponential functions, from which the characteristic decay

lengths were calculated. (b) Distribution of HI standard deviation for individual trajectories on both the low σ surface (blue dots) and the high σ surface (orange dots).

In order to quantify the length scales of the observed spatial heterogeneity, a radial autocorrelation function of HI values was calculated (**Figure 4.5 a**). The function was fit to a mixture of two exponential functions, reflecting the presence of heterogeneity at two different length scales. The short distance decay length (sub-micron/sub-pixel scale) was 0.07 μm and 0.12 μm for the low and high grafted surfaces, respectively. The long distance decay length (mesoscopic scale) was 6.5 μm and 5 μm for the low and high grafted surfaces, respectively, which are consistent with the size of the domains that can be seen in **Figure 4.3 a**. Interestingly, the magnitude of the heterogeneity was stronger by a factor of ~3 on the low density brush. This observation could be explained by the greater mobility and conformational freedom of the polymer chains in the low grafting density surface, which allowed for a higher number of possible brush arrangements and conformations. In order to further support this hypothesis, the temporal fluctuations of individual molecular trajectories were characterized by analyzing the distribution of the standard deviation of HI values in each trajectory. **Figure 4.5 b** shows that individual trajectories indeed exhibited larger fluctuations in the low density brush, although significant fluctuations were observed on both surfaces. These results highlight that, while nanoscale hydrophobic domains exist, their presence is dynamic and the location of these sites may vary temporally.

Although variations in the value of HI have been interpreted above in terms of changes in local nanoscale hydrophobicity, it is clear that such changes are strongly coupled to local differences in the dielectric environment, to the extent that these two effects cannot be readily isolated, and a more nuanced discussion is in order. In particular, because changes in dielectric

environment and hydrophobicity are both directly related to the local density and structure of water, it is intrinsically difficult to disentangle these effects. The connection of these factors to the emission of NBD is particularly challenging since the molecular-level mechanism for environmental-sensitivity is not conclusively understood. For example, while the variation in HI between FS and TMS regions on the patterned control surfaces is not readily explained by changes in the effective dielectric constant, it is certainly plausible that the NBD emission could respond to local variations in the structure of water vicinal to the FS and TMS regions. Similarly, in the case of PEG brushes, while there is an overall systematic variation in the effective dielectric constant due to changes in average PEG concentration with grafting density, it is also likely that the structure of water in the hydration shells of PEG segments may be spatially heterogeneous at the nanoscale. While these effects cannot be conclusively separated, we note that we observed a direct and complex correlation between the residence times of NBD-X molecules and local HI, suggesting a connection between the emission spectrum and the local environment. This may be directly due to interactions between NBD-X and hydrophobic PEG moieties, or indirectly through the influence of PEG density on local water structure.

## 4.3 Conclusions

In summary, we presented a new way to characterize the nanoscale hydrophobicity of hydrated systems *in situ* with sub-diffraction resolution. This approach was applied to the characterization of PEG brushes, which showed that the polymer brushes were spatially and temporally heterogeneous. Specifically, we found that the dynamic behavior, including the surface residence time, of the dye upon contact with the brush was sensitive to average local hydrophobicity as well as the magnitude of local fluctuations in hydrophobicity in the brush layer.

Moreover, PEG brushes with high grafting density exhibited more nanoscale hydrophobic niches relative to PEG brushes with low grafting density. The presence of such niches at high grafting density correlates with the observation of increase protein folding on PEG brushes from prior studies. As such, our findings have important implications for controlling protein fouling as well as the biocompatibility of PEG brushes in contact with physiological fluids, cells or tissues. These results ultimately suggest that it is critical to consider the role of nanoscale heterogeneities as well as fluctuations in local properties on biomaterial surfaces on biomaterial function. Furthermore, due to the general nature of this approach, the use of super-resolution mapping to characterize heterogeneous niches has broad utility beyond the characterization of PEG surfaces. This approach may, in principle, be applied to the identification of hydrophobic regions on other types of biomaterial surfaces, as well as used in conjunction with other types of environmentally-sensitive dyes (e.g., pH, viscosity, voltage).

## SUPPORTING INFORMATION

Experimental details, image processing and data analysis, and supporting figures can be found in **Appendix B**.

## 4.4 References


(1) Utrata-Wesolek, A. *Polimery* **2013**, *58*, 685-695.
(2) Azzaroni, O. *J. Polym. Sci., Part A: Polym. Chem.* **2012**, *50*, 3225-3258.
(3) Banerjee, I.; Pangule, R. C.; Kane, R. S. *Adv. Mater.* **2011**, *23*, 690-718.
(4) Chen, S. F.; Li, L. Y.; Zhao, C.; Zheng, J. *Polymer* **2010**, *51*, 5283-5293.
(5) Leckband, D.; Sheth, S.; Halperin, A. *J. Biomater. Sci. Polym. Ed.* **1999**, *10*, 1125-1147.
(6) Schottler, S.; Becker, G.; Winzen, S.; Steinbach, T.; Mohr, K.; Landfester, K.; Mailander, V.; Wurm, F. R. *Nat. Nanotechnol.* **2016**, *11*, 372-377.
(7) Leng, C.; Sun, S. W.; Zhang, K. X.; Jiang, S. Y.; Chen, Z. *Acta Biomater.* **2016**, *40*, 6-15.
(8) Leng, C.; Hung, H. C.; Sieggreen, O. A.; Li, Y. T.; Jiang, S. Y.; Chen, Z. *J. Phys. Chem. C* **2015**, *119*, 8775-8780.
(9) Unsworth, L. D.; Sheardown, H.; Brash, J. L. *Langmuir* **2005**, *21*, 1036-1041.
(10) Unsworth, L. D.; Sheardown, H.; Brash, J. L. *Langmuir* **2008**, *24*, 1924-1929.
(11) Sofia, S. J.; Premnath, V. V.; Merrill, E. W. *Macromolecules* **1998**, *31*, 5059-5070.
(12) Malmsten, M.; Emoto, K.; Van Alstine, J. M. *J. Colloid Interface Sci.* **1998**, *202*, 507-517.
(13) Schneck, E.; Berts, I.; Halperin, A.; Daillant, J.; Fragneto, G. *Biomaterials* **2015**, *46*, 95-104.
(14) Schneck, E.; Schollier, A.; Halperin, A.; Moulin, M.; Haertlein, M.; Sferrazza, M.; Fragneto, G. *Langmuir* **2013**, *29*, 14178-14187.
(15) Ostaci, R. V.; Damiron, D.; Grohens, Y.; Leger, L.; Drockenmuller, E. *Langmuir* **2010**, *26*, 1304-1310.
(16) Vanderah, D. J.; La, H. L.; Naff, J.; Silin, V.; Rubinson, K. A. *J. Am. Chem. Soc.* **2004**, *126*, 13639-13641.
(17) Li, L. Y.; Chen, S. F.; Zheng, J.; Ratner, B. D.; Jiang, S. Y. *J. Phys. Chem. B* **2005**, *109*, 2934-2941.
(18) Unsworth, L. D.; Tun, Z.; Sheardown, H.; Brash, J. L. *J. Colloid Interface Sci.* **2006**, *296*, 520-526.
(19) Zheng, J.; Li, L. Y.; Chen, S. F.; Jiang, S. Y. *Langmuir* **2004**, *20*, 8931-8938.
(20) Faulon Marruecos, D.; Kastantin, M.; Schwartz, D. K.; Kaar, J. L. *Biomacromolecules* **2016**, *17*, 1017-1025.
(21) Leng, C.; Han, X. F.; Shao, Q.; Zhu, Y. H.; Li, Y. T.; Jiang, S. Y.; Chen, Z. *J. Phys. Chem. C* **2014**, *118*, 15840-15845.
(22) Walder, R.; Nelson, N.; Schwartz, D. K. *Nat. Commun.* **2011**, *2*.
(23) Walder, R.; Kastantin, M.; Schwartz, D. K. *Analyst* **2012**, *137*, 2987-2996.
(24) Bongiovanni, M. N.; Godet, J.; Horrocks, M. H.; Tosatto, L.; Carr, A. R.; Wirthensohn, D. C.; Ranasinghe, R. T.; Lee, J. E.; Ponjavic, A.; Fritz, J. V.; Dobson, C. M.; Klenerman, D.; Lee, S. F. *Nat. Commun.* **2016**, *7*.
(25) Feryforgues, S.; Fayet, J. P.; Lopez, A. *J. Photochem. Photobiol., A* **1993**, *70*, 229-243.
(26) Lin, S.; Struve, W. S. *Photochem. Photobiol.* **1991**, *54*, 361-365.
(27) Swartzlander, M. D.; Barnes, C. A.; Blakney, A. K.; Kaar, J. L.; Kyriakides, T. R.; Bryant, S. J. *Biomaterials* **2015**, *41*, 26-36.
(28) Anderson, J. M.; Rodriguez, A.; Chang, D. T. *Semin. Immunol.* **2008**, *20*, 86-100.
(29) Sivaraman, B.; Latour, R. A. *Biomaterials* **2010**, *31*, 832-839.
(30) Franz, S.; Rammelt, S.; Scharnweber, D.; Simon, J. C. *Biomaterials* **2011**, *32*, 6692-6709.
(31) Deng, J.; Ren, T.; Zhu, J.; Mao, Z.; Gao, C. *Regen. Biomater.* **2014**, *1*, 17-25.

(32) Arcot, L.; Ogaki, R.; Zhang, S.; Meyer, R. L.; Kingshott, P. *Appl. Surf. Sci.* **2015**, *341*, 134-141.
(33) Israelachvili, J. N. *Intermolecular and surface forces, 3rd Edition* **2011**, 381-413.
(34) Szleifer, I. *Biophys. J.* **1997**, *72*, 595-612.
(35) Jeon, S. I.; Lee, J. H.; Andrade, J. D.; Degennes, P. G. *J. Colloid Interface Sci.* **1991**, *142*, 149-158.
(36) Halperin, A. *Langmuir* **1999**, *15*, 2525-2533.
(37) Sheth, S. R.; Leckband, D. *Proc. Natl. Acad. Sci. U.S.A.* **1997**, *94*, 8399-8404.
(38) Jeon, S. I.; Andrade, J. D. *J. Colloid Interface Sci.* **1991**, *142*, 159-166.
(39) Yandi, W.; Mieszkin, S.; Martin-Tanchereau, P.; Callow, M. E.; Callow, J. A.; Tyson, L.; Liedberg, B.; Ederth, T. *ACS Appl. Mater. Interfaces* **2014**, *6*, 11448-11458.
(40) Jin, J.; Jiang, W.; Yin, J. H.; Ji, X. L.; Stagnaro, P. *Langmuir* **2013**, *29*, 6624-6633.
(41) McUmber, A. C.; Randolph, T. W.; Schwartz, D. K. *J. Phys. Chem. Lett.* **2015**, *6*, 2583-2587.
(42) Patel, A. J.; Varilly, P.; Chandler, D. *J. Phys. Chem. B* **2010**, *114*, 1632-1637.
(43) Godawat, R.; Jamadagni, S. N.; Garde, S. *Proc. Natl. Acad. Sci. U.S.A.* **2009**, *106*, 15119-15124.
(44) Kastantin, M.; Faulon Marruecos, D.; Grover, N.; Yu McLoughlin, S.; Schwartz, D. K.; Kaar, J. L. *J. Am. Chem. Soc.* **2017**, *139*, 9937-9948.
(45) Langdon, B. B.; Kastantin, M.; Schwartz, D. K. *Biomacromolecules* **2015**, *16*, 3201-3208.

# Chapter V: Connecting Protein Conformation and Dynamics with Ligand-Receptor Binding Using Three-Color FRET Tracking

David Faulón Marruecos, Mark Kastantin, Navdeep Grover, Sean Yu McLoughlin, Daniel K. Schwartz, and Joel L. Kaar

(Published June, 2017: JACS, 139(29), 9937-9948)

## 5.1 Abstract

Specific binding between biomolecules, *i.e.*, molecular recognition, controls virtually all biological processes including the interactions between cells and biointerfaces, both natural and synthetic. Such binding often relies on the conformation of biomacromolecules, which can be highly heterogeneous and sensitive to environmental perturbations, and therefore difficult to characterize and control. An approach is demonstrated here that directly connects the binding kinetics and stability of the protein receptor integrin $\alpha_v\beta_3$ to the conformation of the ligand fibronectin (FN), which are believed to control cellular mechanosensing. Specifically, we investigated the influence of surface-adsorbed FN structure and dynamics on $\alpha_v\beta_3$ binding using high-throughput single-molecule three-color FRET tracking methods. By controlling FN structure and dynamics through tuning surface chemistry, we found that as the conformational and translational dynamics of FN increased, the rate of binding, particularly to folded FN, and stability of the bound FN–$\alpha_v\beta_3$ complex decreased significantly. These findings highlight the importance of the conformational plasticity and accessibility of the arginine-glycine-aspartic acid (RGD) binding site in FN, which, in turn, mediate cell signaling in physiological and synthetic environments.

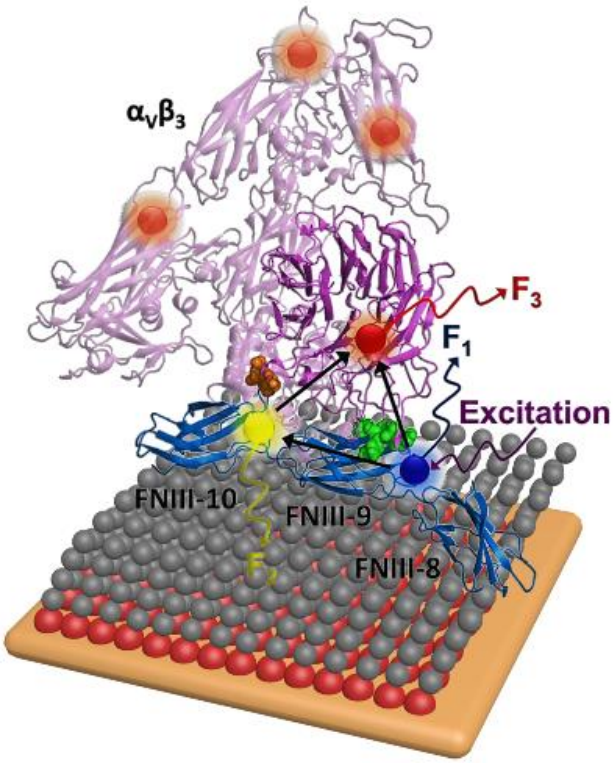


**Figure 5. 1.** Triple-FRET schematic. Fluorescently-labeled fibronectin and integrin $\alpha_v\beta_3$ are shown as a complex on a self-assembled monolayer surface.

## 5.2 Introduction

In physiological environments, the recognition of extracellular matrix proteins (ECM) by cell surface receptors known as integrins is crucial to the ability of cells to sense and respond to their surrounding environment. A particularly prominent example involves the ECM protein fibronectin (FN), which contains the important and widely-studied RGD integrin-binding motif. Through integrin binding, FN, which is pervasive in serum and connective tissue in vertebrates, mediates many critical cellular processes, including differentiation, survival, and proliferation[1-5]. Additionally, when adsorbed on foreign materials, FN can recruit cells to the material surface and, in turn, promote cell adhesion and spreading, which is critical in many areas of biotechnology, including tissue engineering, cell culture, and drug delivery[6-9]. In this way, the interaction of integrins with extracellular cues, which allows signals to be transmitted across the cell membrane, is critical for "outside-in" signaling. Likewise, "inside-out" signaling via the activation of integrins by intracellular cues is critical for regulating cell-environment interactions[10-13].

To date, our understanding of structural basis for the binding of integrins to FN has emanated primarily from static crystal structures and electron microscopy projections. Leahy and co-workers[14] solved the structure of the FN type III 7-10 domains by x-ray crystallography, elucidating the local structure of the RGD site (in the $10^{th}$ type III domain) as well as the relative location of the RGD site to the PHSRN synergy site (in the $9^{th}$ type III domain). Notably, the RGD site was shown to reside within an ordered loop region that has a type II' β secondary structure, suggesting that local conformation may be important for integrin binding. This finding is consistent with reports that the affinity of many integrins is greater to cyclic RGD peptides, which mimic the local structure of the RGD loop, than linear RGD peptides[15-17]. Additionally, structures of complexes between $\alpha_V\beta_3$ and $\alpha_5\beta_1$ and RGD-containing motifs as well as FN fragments have

revealed the integrin-FN binding interface, including the molecular details of the residues involved in binding[18-22]. However, while static structural information provides important insight into the nature of binding, the role of dynamics on the molecular recognition of FN by integrins remains elusive. Of relevance to this role, the RGD loop was previously shown by NMR to be intrinsically flexible and undergo conformational changes that may alter integrin binding[23]. Thus, in addition to the impact of integrin activation state (particularly relevant for "inside-out" signaling) on FN binding, which has been recently reported[20], it is critical to uncover how the conformation and dynamics of FN influence the molecular recognition of FN by integrins. Importantly, the conformation and dynamics of FN and thus extent of integrin "outside-in" signaling as a result of FN binding may be altered by the surrounding ECM environment.

As a tool for addressing this fundamental gap in understanding, dynamic single-molecule (SM) tracking, which is uniquely sensitive to structural and interfacial dynamics, holds considerable promise. Such methods, in particular, include the use of high-throughput SM tracking by means of total internal reflection fluorescence (TIRF) microscopy in combination with *intramolecular* Förster resonance energy transfer (FRET). Our group has recently applied SM-FRET with high-throughput tracking to elucidate the transient and dynamic behavior of proteins in near-surface environments[24-26]. To enable SM analysis of transient unfolding via FRET, bioorthogonal labeling approaches are used to site-specifically introduce donor and acceptor fluorophores.

In this approach, as many as $10^6$ protein molecules are tracked as they freely adsorb, desorb, diffuse, and simultaneously undergo conformational changes and/or intermolecular associations at the solution-solid interface, permitting the statistical identification of dynamic, spatial, and population heterogeneity. The subsequent correlation of these dynamic behaviors on a molecule-

by-molecule basis via large-scale multi-variate analyses, moreover, provides new insights into the connection between interfacial dynamics and protein structure on a molecule-by-molecule basis. Importantly, the detailed analysis of these observations yields direct information about elementary mechanistic processes, such as the rate of integrin binding (*i.e.*, the "on-rate") and the stability of the bound FN-integrin complex (*i.e.*, the "off-rate"), which are influenced by FN conformation and dynamics. This understanding is necessary to elucidate fundamental questions about the mechanisms through which cells sense and respond to environmental cues, including viscoelastic forces. For example, it is widely believed that differences in the adhesion of cells to ECM as a function of ECM rigidity arise from variations in the rates of binding and unbinding of integrins to FN[27-31]. Specifically, the ratio of binding and unbinding rates is hypothetically coupled to the flexibility of the ECM, altering the steady-state number of integrin-FN interactions between the cell and ECM.

While used infrequently, three-color SM-FRET[32,33] is a proven approach to monitor the spatial arrangement of components of a molecular complex. Here, high-throughput dynamic three-color SM-FRET tracking (of mobile, freely adsorbing molecules) was applied to determine the impact of FN conformation and interfacial dynamics on $\alpha_v\beta_3$ integrin binding, and thus the structural basis for FN signaling via "outside-in" integrin activation. Specifically, this approach allowed us to distinguish the conformational state (*i.e.*, folded or unfolded) of a given FN molecule, and to independently identify binding and unbinding events of $\alpha_v\beta_3$ integrin to that FN molecule. To control the conformation and, in particular, the dynamics of FN, FN was adsorbed on oligo(ethylene glycol) (OEG) and trimethylsilyl (TMS) self-assembled monolayers. This approach exploited our previous observations that FN conformation and dynamics may be dramatically altered by tuning the surface chemistry to which FN is adsorbed[26,34,35]. Ultimately, our results shed

light on the importance of FN conformation and dynamics on integrin binding and paint an intriguing picture of previously inaccessible mechanisms that regulate the function of FN. Furthermore, the development of three-color SM-FRET tracking opens the door to address other biophysical questions involving the relation between conformation and molecular associations.

## 5.3 Materials and Methods

### 5.3.1 Protein Expression, Purification, and Labeling

The $FN_{FRET}$ construct that was used for high-throughput SM-FRET tracking experiments was expressed, purified, and labeled as described previously[26]. Briefly, $FN_{FRET}$ was co-expressed with orthogonal tyrosyl-tRNA/tRNA synthetase from *Methanococcus jannaschii* in autoinduction media, which was supplemented with *p*-azidophenylalanine (Chem-Impex), at 37 °C for 4 h and then 28 °C for 20 h, and purified via affinity chromatography using a Bio-Scale Mini Profinity IMAC cartridge (Bio-Rad). The orthogonal tyrosyl-tRNA/tRNA synthetase used for incorporation of *p*-azidophenylalanine was encoded by the pDule2 pCNF RS plasmid, which was kindly provided by Ryan Mehl (Oregon State University).

For labeling, purified $FN_{FRET}$ was sequentially modified with dibenzocyclooctyne-Alexa Fluor 555 (Life Technologies) and maleimide-Alexa Fluor 594 (Life Technologies) using a 3:1 molar excess of dye-to-$FN_{FRET}$ for each fluorophore. Prior to modification with the maleimide-Alexa Fluor 594, tris-(2-carboxyethyl)phosphine hydrochloride was added to $FN_{FRET}$ to reduce the engineered cysteine. Dual-labeled $FN_{FRET}$ was further purified by size exclusion chromatography to remove excess unreacted dye. The extent of labeling of Alexa Fluor 555 and 594 was determined by the relative absorbance of dye-to-protein. For labeling of $\alpha_V\beta_3$, recombinant human $\alpha_V\beta_3$ (R&D

Systems) was dissolved in PBS (100 μg/mL) and reacted with Alexa Fluor-647 NHS ester (Life Technologies) at a dye-to-protein molar ratio 5:1 in PBS at room temperature for 6 h in the dark. After removing excess free dye via de-salting, the average number of fluorophores per molecule of $\alpha_V\beta_3$ was determined using a calibration curve of fluorescence intensity versus concentration of free dye and the concentration of protein.

### 5.3.2 Preparation of OEG and TMS Surfaces

Surfaces containing OEG and TMS monolayers were prepared using established methods for the vapor-phase deposition of methoxy(triethyleneoxy)-propoylmethoxysilane (Gelest, Inc.) and hexamethyldisilazane (>99%, Sigma-Aldrich), respectively, on fused silica wafers[34]. Initially, contaminants were removed from the wafers via treatment with Mico-90 detergent (International Product Corp.), ultrapure water, piranha, and UV-ozone. For functionalization with OEG, wafers were subsequently reacted with methoxy(triethyleneoxy)-propoylmethoxysilane in toluene with *n*-butylamine, which was added to catalyze monolayer formation, overnight at room temperature. The volumetric ratio of *n*-butylamine to methoxy(triethyleneoxy)-propoylmethoxysilane to toluene was 1:2:20. For functionalization with TMS, the wafers were exposed to the vapors of a solution of hexamethyldisilazane for 48 h at room temperature. Following functionalization, modification of the wafers was confirmed via measurement of static water contact angle as well as ellipsometry.

### 5.3.3 High-throughput SM-FRET Imaging

Dilute dual-labeled $FN_{FRET}$ ($5x10^{-14}$ M) was introduced into a flow cell (maintained at 25.0 ± 0.1 °C), containing either OEG- or TMS-functionalized fused silica in phosphate buffered saline (pH 7.4 and ionic strength 137 mM) with 0.1 μM of BSA. For three-color SM experiments, 1 mM of $MgCl_2$ was added with $5x10^{-12}$ M acceptor-labeled $\alpha_V\beta_3$. For imaging, a custom-built prism-based illumination system and Nikon TE-2000 microscope with 60x plan Apo water immersion objective were used. Additionally, the sample was excited using a 532 nm Cobolt Samba 50 mW diode-pumped solid-state laser that was coupled to a single mode fiber optic cable. The laser was coupled to the fiber optic cable using a free space laser-fiber launch (Oz Optics), resulting in the retention of 60% of the incident light. Emitted light from the fiber optic was focused on the sample with a beam diameter of 48 μm (defined as the distance between the points in a Gaussian intensity profile at which the beam intensity is $1/e^2$ of its maximum value).

To collect three-channel images, an Optosplit III (Cairn Research) image splitter employed two BrightLine® Dichroic Beamsplitters from Semrock. A FF605-Di02 mirror (nominal separation wavelength of 605 nm) was used to reflect light into the low-wavelength channel while a FF662-FDi01 mirror was used to separate light into the mid- and high-wavelength channels. Additional bandpass filters (Semrock) were used to further select for fluorescence emission in each channel. All bandpass filters had a 90% transmission width of 40 nm and were centered at 585 nm, 628 nm, and 685 nm, for the low-, mid-, and high-wavelength channels, respectively. After fluorescence emission was split and filtered, each channel was projected onto a separate region of an Andor DU-888 EMCCD camera cooled to −90 °C. Sequential images were obtained with an exposure time of 70 ms, which translated to a frame rate of 13.95 $s^{-1}$ after allowing 1.68 ms for sensor readout. For experiments that required only dual-channel imaging, the high-wavelength

channel was blocked but all other optical elements and camera acquisition settings remained unchanged.

The three channels were aligned to within 2 pixels by aligning common features of an alignment mask in brightfield illumination. Additionally, due to imperfections in the optical elements and slight differences in the path length for each channel, slight differences in magnification were observed for each channel. Therefore, both the offset and magnification differences between channels were accounted for in order to enable identification of a given molecule in multiple wavelength channels and to eliminate apparent movement of molecules as FRET changes caused intensity changes in each channel.

Prior to object identification and the linking of molecular trajectories, the images in each channel were re-scaled to equivalent magnifications and aligned to less than 1 pixel, as described previously[36]. This procedure involved identifying 3-5 anomalously bright marker objects that could be imaged in all 3 channels during a single frame. Such objects made up a very small number of the observable objects on the screen, and were likely protein aggregates. The in-plane positions of these molecules were calculated as described below and used to manually adjust the in-plane offsets and the magnifications so that the pattern of molecules in all three channels were aligned with sub-pixel precision. While the magnification corrections were less than 2%, this step was necessary to allow accurate extraction of object intensities in all three channels during the object identification and tracking steps.

### 5.3.4 High-throughput SM-FRET Tracking

For two- and three-channel tracking, a thresholding algorithm was used to identify all objects that appeared in any of the channels on a given frame, with thresholds that were set separately for each channel. Pixel values and in-plane positions of each pixel were recorded for the object in the channel in which it appeared. Additionally, the corresponding pixel values in the other two channels were also recorded for each identified object and the intensity values were summed for each channel after the local background was subtracted. Hereafter, $F_1$, $F_2$, and $F_3$ refer to the intensity values in the low-, mid-, and high-wavelength channels, respectively. Notably, each object was associated with an intensity value for each of the three channels even if the intensity was above the identification threshold in only one channel. Although this strategy sometimes created duplicate identifications, which were addressed in a subsequent step, it added robustness to the object identification strategy based on the ability to identify molecules that were bright in any single channel. This approach is useful for multi-channel tracking because inherent variations in FRET efficiency cause the intensity in a given channel to rise and fall above or below background levels with conformational changes and/or molecular binding events.

In addition to fluorescence intensity in each channel, the interfacial position of each molecule was determined by a centroid of intensity calculation using the pixels in the original channel of identification. This quantitative position determination then allowed a detailed comparison of objects between different channels. Duplicate (or triplicate) objects were removed in a two-step process that began by comparing all the objects identified in the low-wavelength channel to those in the mid-wavelength channel based on their interfacial position. Objects that were identified in the same interfacial position were merged by assigning the interfacial position calculated in the brightest channel. This channel alignment procedure ensured that channel

intensity and position were nearly independent of the original identification channel, and the protocol described above minimized the effects of channel-specific fluctuations in background fluorescence.

Subsequently, redundant objects were removed by comparing the unique objects that remained after merging the low- and mid-wavelength channels with those in the high-wavelength channel. This process was applied to all frames for each movie. Molecular trajectories were then created by connecting objects that appeared within a tracking radius of 2.2 μm in consecutive frames[37]. For each frame, the folding parameter ($\chi_{Fold}$), which was defined as $\chi_{Fold} = F_2 / (F_1 + F_2)$, and binding parameter ($\chi_{Bind}$), which was defined as $\chi_{Bind} = F_3 / (F_1 + F_2 + F_3)$, were calculated to provide an index of both FN conformation and FN-integrin binding state, respectively. Importantly, these values were used as order parameters to identify each state as folded or unfolded, and bound or unbound, and were not intended to indicate absolute molecular distances. While the ratios used to calculate $\chi_{Fold}$ and $\chi_{Bind}$ resemble equations for FRET efficiency, $\chi_{Fold}$ and $\chi_{Bind}$ themselves do not represent true values of FRET efficiencies because the intensity values were raw and not corrected for crosstalk between channels.

### 5.3.5 Intramolecular FRET Analysis of Surface Residence Time, Initial State Residence Time, and Diffusion Coefficient

Desorption kinetics of protein molecules were quantitatively calculated using cumulative surface residence time distributions constructed separately for folded and unfolded FN. These distributions contained the surface residence times for individual trajectories from the time that lapsed between adsorption and desorption of the molecule on the surface. The collection of surface

residence times for all molecules in each experiment was utilized to generate the experimental cumulative residence time distribution ($C(t)$), which represents the number of molecules with a surface residence time of *t* or longer (equation 5.1):

$$C(t) = \frac{\sum_{t'=t+t_{ac}}^{t_{max}} m_{t'}\rho(t')}{\sum_{t'=t_{min}}^{t_{max}} m_{t'}\rho(t')} \quad \text{(eq. 5.1)}$$

where $m_t$ is the number of objects found to have a given surface residence time, $t_{max}$ is the maximum experimentally observable residence time (4 images less than the length of the movie), $t_{min}$ is the minimum observable residence time and corresponds to 4 images in this work, and $t_{ac}$ is the acquisition time (70 ms). This expression contains a correction factor ($\rho(t)$) to account for the fact that movies have a finite length and thus fewer opportunities to observe both adsorption and desorption of long-lived molecules (equation 5.2)[38]:

$$\rho(t) = \left[H(L-t)\left(1-\frac{t}{L}\right)\right]^{-1} \quad \text{(eq. 5.2)}$$

where H is the Heaviside step function and L is the length of the movie.

The distributions were fit to an exponential mixture model (see Supporting Information).

As noted above, trajectories with residence times of less than four frames were ignored to reduce the likelihood of object misidentification due to random noise in these multi-channel single-fluorophore FRET experiments. Moreover, an intrinsic temporal resolution in these experiments was related to the image acquisition time (70 ms), which limited our ability to quantify fast dynamics. In particular, individual events (e.g. surface residence times or FRET fluctuations) lasting less than 70 ms could generally not be resolved. However, the quantitative analysis methods used here (e.g. exponential mixture models), coupled with large data sets that extended over many

decades, were capable of extracting fast characteristic time constants by extrapolating the modeled behavior to longer time intervals (i.e. using information encoded in the tails of the distributions). Thus, the choice to neglect trajectories shorter than 4 frames reflected a choice to reduce artifacts in the data at the expense of a decreased sensitivity to highly transient objects. Moreover, as will be seen later, at least three frames were required to quantify the duration of integrin binding events because it required the observation of unbound states both before and after a binding event.

The initial state residence time for each molecule was measured in order to characterize the unfolding and apparent folding kinetics. The initial state residence time represents the time interval that a single molecule spends in the conformational state that it exhibited in the first frame immediately after adsorption on the surface. The threshold folding parameter for determining folded versus unfolded FN was determined to be $\chi_{Fold}$ = 0.42 and 0.5 on OEG- and TMS-coated surfaces, respectively. Cumulative distributions of the initial state residence time were created in an analogous way to the desorption kinetics. The probability distribution of initial state residence times ($p(t_i)$) was corrected before converting it to an integrated form to account for the fact that molecules can desorb before undergoing a change in conformation (equation 4.3)[39]:

$$p(\mathrm{t_i}) = \frac{1}{\rho}\frac{\mathrm{n(t_i)}}{\mathrm{n(t_r > t_i)}} \quad \text{(eq. 4.3)}$$

where ($n(t_i)$ is the number of observations of a given change time, $n(t_r > t_i)$ is the number of trajectories that exhibited a surface residence time $t_r$ equal or greater than the change time, and $\rho = \sum_i \frac{n(t_i)}{n(t_r > t_i)}$ is a normalization factor that converts the relative probability into an absolute probability. The cumulative distribution can be constructed from the raw probability distribution as indicated in equation 4.4:

$$C(t_j) = \sum_{t_i > t_j} p(t_i) \quad \text{(eq. 4.4)}$$

The distributions were fit to a two exponential mixture model to account for folding and unfolding processes (see Supporting Information).

Cumulative squared displacement distributions (CSDD) were used to determine the characteristic diffusion coefficients of adsorbed protein molecules[40]. The cumulative distribution is a function of squared displacement and lag time, $C(r^2, t)$. The displacements were calculated by measuring the position of molecules in consecutive frames, and the lag time was the image acquisition time, $t_{ac}$ = 0.07 s. $C(r^2, t)$ represents the probability that a molecule moves a distance equal or greater than $r$ in a time interval $t$. As in the previous analyses, objects with residence times of less than 4 frames were ignored. The distribution was experimentally calculated by sorting the squared displacement data in ascending order and ranking each data point (equation 4.5):

$$C(r_k^2, t) = 1 - \frac{k}{N} \quad \text{(eq. 4.5)}$$

where $k$ is the rank in the sorted order and N is the total number of sorted data points. To account for the fact that measured CSDD data may represent multiple modes of diffusion, a Gaussian mixture model was used to fit the CSDD (see Supporting Information).

### 5.3.6 Intermolecular FRET Analysis of Bound-State Residence Time and Time-to-Binding

Intermolecular FRET was used to quantify the stability of the FN-integrin complex and its correlation to FN conformation. Integrin binding events were quantified using cumulative residence time distributions of the bound state, where separate distributions were determined for

binding events that immediately followed a folded FN conformation versus those that followed unfolded FN.

In this process, the discrete integrin binding state (*i.e.*, bound or unbound) was determined using the value of $\chi_{Bind}$, with a threshold value of $\chi_{Bind} > 0.3$ used to define the bound state. The duration of each binding event was recorded along with the values of $\chi_{Fold}$ immediately preceding binding and following the subsequent unbinding. Binding or unbinding events that coincided with the beginning or end of a trajectory were not included in the analysis due to uncertainty in the duration of the binding event (*i.e.*, the binding event could have preceded adsorption or continued after desorption). Importantly, $\chi_{Fold}$ was not analyzed during integrin binding events due to the very low absolute intensities in the low- and mid-wavelength channels during binding events. While methods have been developed for quantitative triple-FRET measurements, the signal-to-noise ratios typical of our widefield imaging and dynamic high-throughput tracking methods prevented accurate quantification of FN conformation during integrin binding, even with extensive FRET controls. Instead, we to linked FN conformation to integrin binding by correlating each binding event with the FN conformation immediately before and after binding. As shown below, in the vast majority of cases, FN conformation was unchanged before and after integrin binding. After binarization of each trajectory into binding events, with associated FN conformations, the cumulative residence time distribution of the bound state was determined such that $C(t)$ represented the number of binding events with a duration of $t$ or longer. Separate distributions were constructed for binding events preceded by folded FN and unfolded FN. The cumulative distributions were fit to an exponential mixture model (see SI).

Additionally, the time-to-binding distribution was generated by measuring the time interval between the adsorption of a given FN molecule to the first integrin binding event in that molecule's

trajectory. Again, this distribution was analyzed in cumulative form through an exponential mixture model whereby $C(t)$ represented the probability that FN remained unbound for a duration of $t$ or longer. This analysis was conceptually similar to the initial state residence time used to assess FN conformation, with the difference that the "initial state" was defined by integrin binding rather than a change in FN conformation. The effect of FN conformation on time-to-binding was assessed using the final FN conformation of the unbound interval. For this analysis, the integrin binding event was not required to end before desorption of the molecule. While it was also possible to have multiple integrin binding events in a single trajectory, only the initial unbound interval was used to create time-to-binding distributions. This choice was made because subsequent binding events could potentially result from unbinding followed by re-binding of the same integrin, making these unbound intervals representative of a different process than the initial "search".

## 5.4 Results

### 5.4.1 FN Conformation and Dynamics

As an initial step in developing high-throughput dynamic SM-FRET methods to study ligand-receptor interactions, the influence of surface chemistry on adsorbed FN was determined. Specifically, the conformation and dynamics of FN on OEG and TMS surfaces were measured by high-throughput SM-FRET tracking using an FN construct comprising the type III 8-10 domains. For SM-FRET experiments, the construct, which included the functionally important RGD and PHSRN motifs, was site-specifically labeled with donor (Alexa Fluor 555) and acceptor (Alexa Fluor 594) dyes at residues 1381 and 1500, respectively. To permit orthogonal labeling at these sites, the unnatural amino acid *p*-azidophenylalanine (at residue 1381) and a cysteine (at residue

1500) were incorporated in the construct, which was devoid of native cysteines. We have previously shown that this construct ($FN_{FRET}$) is structurally well-folded and has distinctive FRET signatures for the folded and unfolded state, allowing changes in conformation to be monitored[26].

The impact of surface interactions on $FN_{FRET}$ conformation was quantitatively determined by analyzing the distribution of $\chi_{Fold}$, which represented an order parameter related to the *intramolecular* FRET efficiency for surface-adsorbed molecules. Labeled $FN_{FRET}$ molecules in contact with the OEG or TMS surfaces (in the presence of 0.1 μM BSA) were excited via TIRF illumination and monitored by wide-field imaging in both donor and acceptor emission channels. **Figure 5.2** shows the distributions of $\chi_{Fold}$ that was measured for all $FN_{FRET}$ molecules in all movie frames (for ~$10^6$ molecular trajectories) on TMS and OEG surfaces. This is equivalent to the distribution associated with a representative snapshot of the folding state of $FN_{FRET}$ on each surface. As detailed in **Table C.1**, in a representative snapshot of the surface, both folded and unfolded states of $FN_{FRET}$ were found to be substantially present in the adsorbed population, and the folded state was modesty more prevalent on OEG than on TMS. To make these observations more quantitative, the value of $\chi_{Fold}$ at the local minimum probability between the folded and unfolded populations for each surface (0.42 for OEG and 0.5 for TMS) was used to segment the trajectories with respect to conformation. Using this criterion, slightly more than half (56%) of the adsorbed $FN_{FRET}$ was folded on OEG, while slightly less than half (44%) was folded on TMS. A sensitivity analysis showed that the relative fractions of folded and unfolded $FN_{FRET}$ were only slightly sensitive to the choice of threshold between 0.42 and 0.5, which did not affect the overall trends. Moreover, the impact of the threshold on the measured kinetics of binding and unbinding (described below) was negligible. Additionally, an alternative analysis involving the distributions of the median $\chi_{Fold}$ value of each $FN_{FRET}$ trajectory, which indicated the predominant conformation

per trajectory, showed a similar fraction of folded molecules on OEG (66%) and TMS (42%) (**Figure C.1**).

The variation in surface chemistry also altered the dynamics of $FN_{FRET}$, as demonstrated by analyzing the surface residence time distributions of always-folded and always-unfolded molecules, which comprised ~$10^5$ molecular trajectories (**Figure 5.3** and **Table C.2**). Specifically, the surface residence time of unfolded $FN_{FRET}$ on TMS was significantly shorter than on OEG, suggesting that $FN_{FRET}$ was more dynamic on TMS than on OEG, which is consistent with prior SM-FRET tracking experiments that found analogous behavior with other proteins[34,35,40]. Samples of raw trajectories of donor and acceptor fluorescence intensity and $\chi_{Fold}$ for two-color single-molecule experiments are shown in **Figure C.2**.

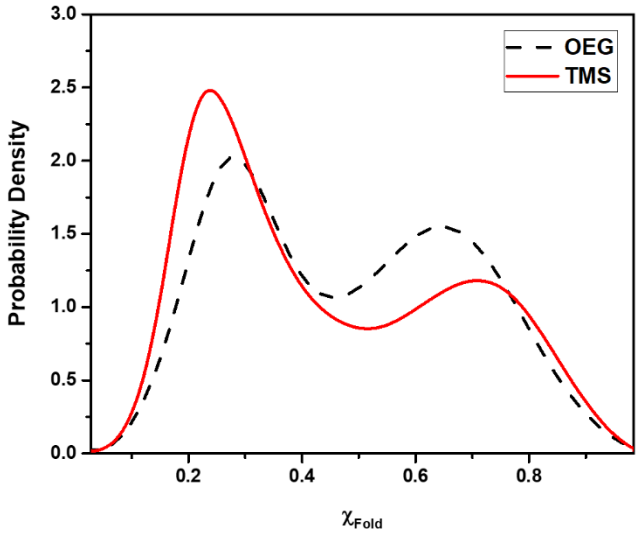


**Figure 5. 2.** Probability density of the distribution of $\chi_{Fold}$ values for $FN_{FRET}$ on FS functionalized with OEG (black dashed line) and TMS (red solid line). In the distribution, distinct populations representing the folded state and unfolded state of $FN_{FRET}$ were observed. The population representing the folded state was centered at $\chi_{Fold}$ values of 0.62 on OEG and 0.69 on TMS, respectively. For the unfolded state, the population was centered at $\chi_{Fold}$ values of 0.28 on OEG and 0.23 on TMS, respectively. A critical value of 0.42 on OEG and 0.5 on TMS, which corresponded to the minimum probability in $\chi_{Fold}$ between populations, was used to partition folded

from unfolded molecules. The distribution was generated from ~$10^6$ molecular trajectories on both surfaces.

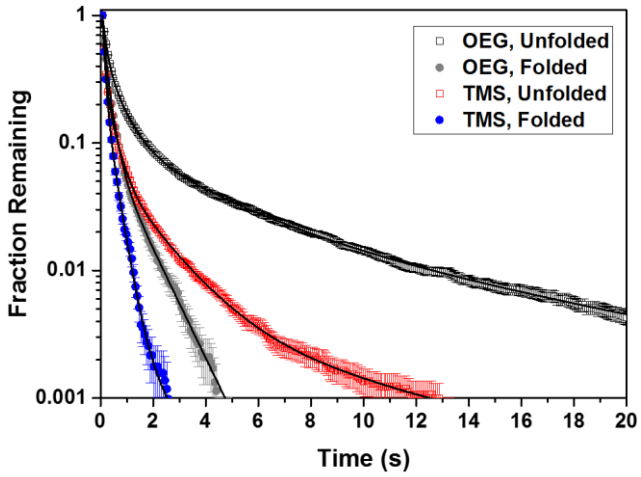


**Figure 5. 3.** Cumulative surface residence time distributions for $FN_{FRET}$ on FS functionalized with OEG and TMS as a function of folding state. The distributions for molecules that were always folded (filled circles) and always unfolded (open squares) were fit to an exponential mixture model (black line), which assumed a superposition of three first-order desorption processes. Based on the fitting parameters, the characteristic surface residence time for each sub-population of folded or unfolded molecules on each surface was determined. Error bars represent a 68% confidence interval based on a Poisson distribution for each data point. Each distribution was generated from ~$10^5$ molecular trajectories.

Complementing these observations, we also found that surface-adsorbed $FN_{FRET}$ was more conformationally labile and exhibited greater translational mobility on TMS than on OEG. As evidence of this, the cumulative initial state residence time distributions for initially folded (**Figure 5.4 A**) and unfolded (**Figure 5.4 B**) $FN_{FRET}$ (~$10^4$ molecular trajectories), which indicate the probability that a molecule resides on the surface in its initial conformational state for time *t* or longer prior to a change in conformation, were quantified (fitting parameters shown in **Table C.3**). The rate of conformational change was significantly greater on TMS than on OEG, regardless of the initial state adopted by adsorbed FN. Specifically, the mean folding rate constant for molecules

that underwent an apparent unfolded-to-folded transition ($k_{fold}$) was markedly greater on TMS (0.57 $s^{-1}$) than on OEG (0.086 $s^{-1}$), and for molecules that underwent an apparent folded-to-unfolded transition, the mean rate constant of unfolding ($k_{unf}$) was roughly three times as great on TMS (3.06 $s^{-1}$) than on OEG (1.06 $s^{-1}$). These findings suggest that, although the apparent re-folding of $FN_{FRET}$ was slower than the unfolding of $FN_{FRET}$ on both surfaces, overall $FN_{FRET}$ was significantly more conformationally labile on TMS than on OEG.

Finally, the mobility of adsorbed folded and unfolded $FN_{FRET}$ (~$10^5$ molecular trajectories) was quantified by calculating the cumulative squared displacement distributions (**Figure 5.5**), which indicated that the interfacial mobility of both folded and unfolded $FN_{FRET}$ on TMS was greater than that on OEG. Based on the mean diffusion coefficient ($\bar{D}$), the folded (0.266 $\mu m^2/s$), and unfolded (0.254 $\mu m^2/s$) states were equally mobile on TMS (**Table C.4**). On OEG, the mobility of both conformational states was greatly reduced, and folded $FN_{FRET}$ (0.086 $\mu m^2/s$) was significantly more mobile than unfolded (0.050 $\mu m^2/s$) $FN_{FRET}$. Collectively, these results, combined with the residence time results described above, indicate that adsorbed $FN_{FRET}$ was highly dynamic on TMS, suggesting relatively weak surface binding, and much more static and strongly bound on OEG. As shown below, these distinctive behaviors have a significant influence on the likelihood and duration of integrin binding.

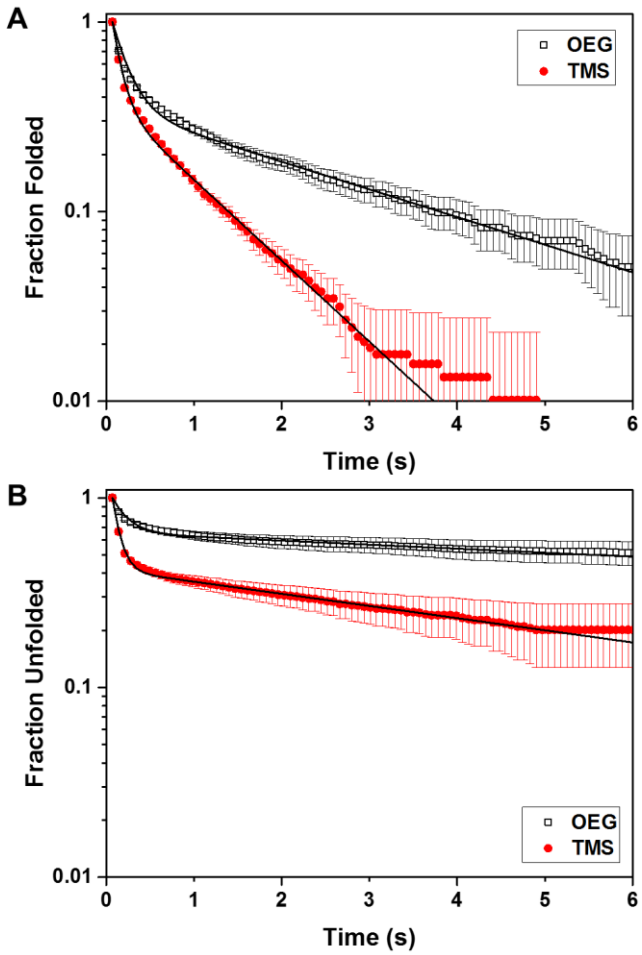


**Figure 5. 4.** Cumulative initial state residence time distributions for folded (A) and unfolded (B) $FN_{FRET}$ on OEG (open squares) and TMS (red circles). Each distribution was fit to an exponential mixture model (black line), which assumed a superposition of two first-order apparent high-to-low FRET or low-to-high FRET transitions. Analysis of the model fit yielded the relative fraction and characteristic time constants for each sub-population in each distribution. Error bars represent a 68% confidence interval based on a Poisson distribution for each data point. Each distribution was generated from ~$10^4$ molecular trajectories.

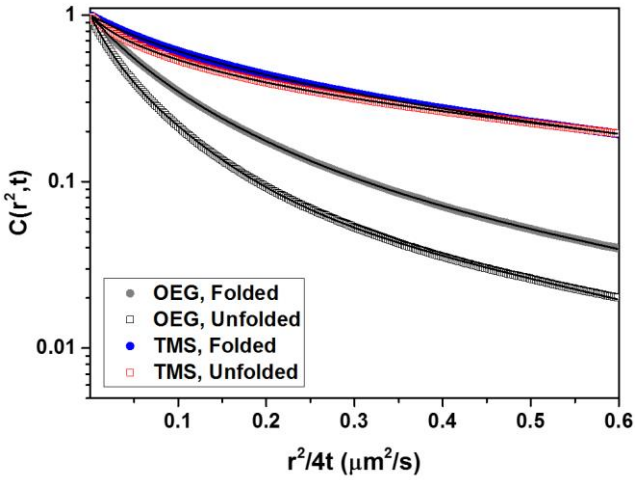


**Figure 5. 5.** Cumulative squared displacement distributions for always folded (filled circles) and always unfolded (open squares) $FN_{FRET}$ on FS functionalized with OEG and TMS. Solid lines represent fits to a Gaussian-mixture model as described in the text. Error bars represent a 68% confidence interval based on a Poisson distribution for each data point. Each distribution was generated from ~$10^5$ molecular trajectories.

### 5.4.2 Correlation of FN Conformation and Integrin Binding

The striking differences in conformation, surface binding, and interfacial mobility of $FN_{FRET}$ on OEG and TMS allowed us to study the impact of $FN_{FRET}$ conformation and surface chemistry on integrin binding. Binding of the extracellular domain of $\alpha_v\beta_3$ to surface-adsorbed $FN_{FRET}$ was specifically monitored in three-color SM-FRET tracking experiments (in the presence of 0.1 μM BSA as a non-specific competitive binder). In particular, the two-color *intramolecular* SM-FRET experiments described above were combined with *intermolecular* SM-FRET using labeled integrin, to identify correlations between binding and FN conformation. For these experiments, the extracellular domain of $\alpha_v\beta_3$ was labeled with a third dye (Alexa Fluor 647) by reacting the dye with random primary amines in the integrin. As such, in addition to energy transfer from the donor ($F_1$) to acceptor ($F_2$) attached to $FN_{FRET}$, energy transfer from both $F_1$ and $F_2$ to the

dye attached to $\alpha_v\beta_3$ ($F_3$), as depicted schematically in **Figure 5.6 A**, was possible. By monitoring the intensity of all three dyes, multiple populations of $FN_{FRET}$ and of the $FN_{FRET}$-integrin complex were observed. Notably, this enabled the identification of states where each of the conformational states of $FN_{FRET}$ was either bound or unbound to $\alpha_v\beta_3$ (**Figure 5.6 B**). While the peaks for the bound states were small relative to those corresponding to the unbound states, the absolute number of binding events was large, enabling quantitative analysis of the $FN_{FRET}$-$\alpha_v\beta_3$ binding. For this analysis, folding and binding parameters were calculated using the relationships $\chi_{Fold} = F_2/(F_1 + F_2)$ and $\chi_{Bind} = F_3/(F_1 + F_2 + F_3)$, respectively. As with $\chi_{Fold}$, $\chi_{Bind}$ is an order parameter related to (but not identical to) FRET efficiency, as explained in the method section.

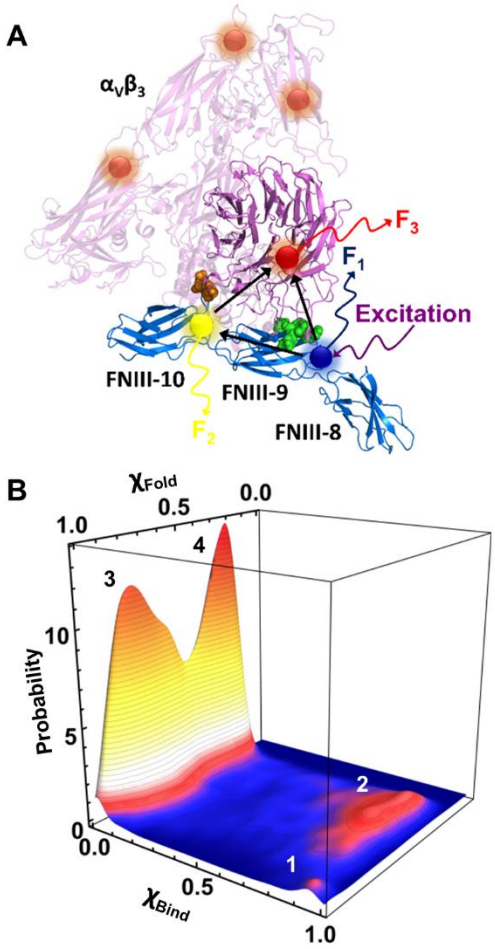


**Figure 5. 6.** Correlation of $FN_{FRET}$ conformation and $\alpha_v\beta_3$ binding by three-color SM-FRET tracking. (A) Schematic of three-color SM-FRET tracking experiments used to identify $FN_{FRET}$ conformation via *intramolecular* FRET and $\alpha_v\beta_3$ binding via *intermolecular* FRET. In the schematic, the structure of the bound $FN_{FRET}$–$\alpha_v\beta_3$ complex is shown, illustrating the location of the donor ($F_1$) and acceptor ($F_2$) fluorophores on $FN_{FRET}$ (blue cartoon) with respect to the integrin binding interface. For these experiments, $\alpha_v\beta_3$ (purple cartoon) was non-specifically labeled with a third fluorophore ($F_3$), which accepted energy transfer from both $F_1$ and $F_2$, thereby enabling binding to be observed. The orange and green spheres in $FN_{FRET}$ highlight the location of the RGD and PHSRN synergy sites, respectively, in the neighboring $10^{th}$ and $9^{th}$ type III domains. The structure of the bound $FN_{FRET}$–$\alpha_v\beta_3$ complex was generated from the crystal structures of the type III $10^{th}$ domain bound to $\alpha_v\beta_3$ (PDB code: 4MMX) and the type III $7^{th}$-$10^{th}$ domains (PDB code: 1FNF). (B) Identification of distinct populations, which correspond to: (1) folded, bound, (2) unfolded, bound, (3) folded, unbound, and (4) unfolded, unbound states of $FN_{FRET}$. The surface plot was generated from ~$10^4$ molecular trajectories.

Although minor bleed-through between channels for $F_1$, $F_2$, and $F_3$ was inevitable, such crosstalk affected only the absolute folding and binding parameters (*i.e.*, the positions) of the peaks corresponding to distinct states in Figure 5, and did not influence the ability to resolve or distinguish between states. As a result, the impact of spectral bleed-through on the identification of conformational states of $FN_{FRET}$ to which $\alpha_v\beta_3$ was bound or unbound was negligible. Our analysis used the parameters only for state identification (via the thresholding procedure described above), and did not interpret these parameters as FRET efficiencies, or use them to calculate donor-acceptor distances. Additionally, the non-specifically labeled $\alpha_v\beta_3$ contained on average ~12 fluorophores per protein molecule (out of a 101 possible modification sites in $\alpha_v\beta_3$). As with the case of spectral crosstalk, while the presence of multiple fluorophores on $\alpha_v\beta_3$ precluded the determination of quantitative donor-acceptor distance information upon binding of $\alpha_v\beta_3$ and $FN_{FRET}$, the measured $\chi_{Bind}$ was robustly used to distinguish between bound and unbound states. **Figure 5.7** shows representative raw trajectories from the three-color SM-FRET experiments, including the time-dependent traces of the relative change in intensities of $F_1$, $F_2$ and $F_3$ (**Figure 5.7 A**) as well as corresponding time-dependent changes in $\chi_{Fold}$ and $\chi_{Bind}$ (**Figure 5.7 B**). As would be expected in the case of FRET, fluctuations in the fluorescence intensity of $F_3$ and that of $F_1$ and $F_2$ upon binding and dissociation of $\alpha_v\beta_3$ were anti-correlated. Additional sample trajectories and movies showing raw data from the three-color SM-FRET experiments are shown in the Supporting Information (**Figure C.3**).

Importantly, a significantly higher concentration of $\alpha_v\beta_3$ relative to $FN_{FRET}$ was used in the binding experiments, resulting in a large excess of $\alpha_v\beta_3$ capable of binding $FN_{FRET}$ in the bulk solution. As a result, the rate of $\alpha_v\beta_3$ binding to $FN_{FRET}$, which was measured in the presence of $MgCl_2$ (1 mM) to facilitate binding[41], was independent of transport limitations associated with the

diffusion of $\alpha_v\beta_3$. Moreover, the impact of hypothetical unfolded $\alpha_v\beta_3$ molecules, which may not be capable of strong binding to $FN_{FRET}$, was minimized. Using surface plasmon resonance, we confirmed that the introduction of labeling sites as well as attachment of $F_1$ and $F_2$ did not significantly perturb the binding of $FN_{FRET}$ to $\alpha_v\beta_3$ (**Table C.5**).

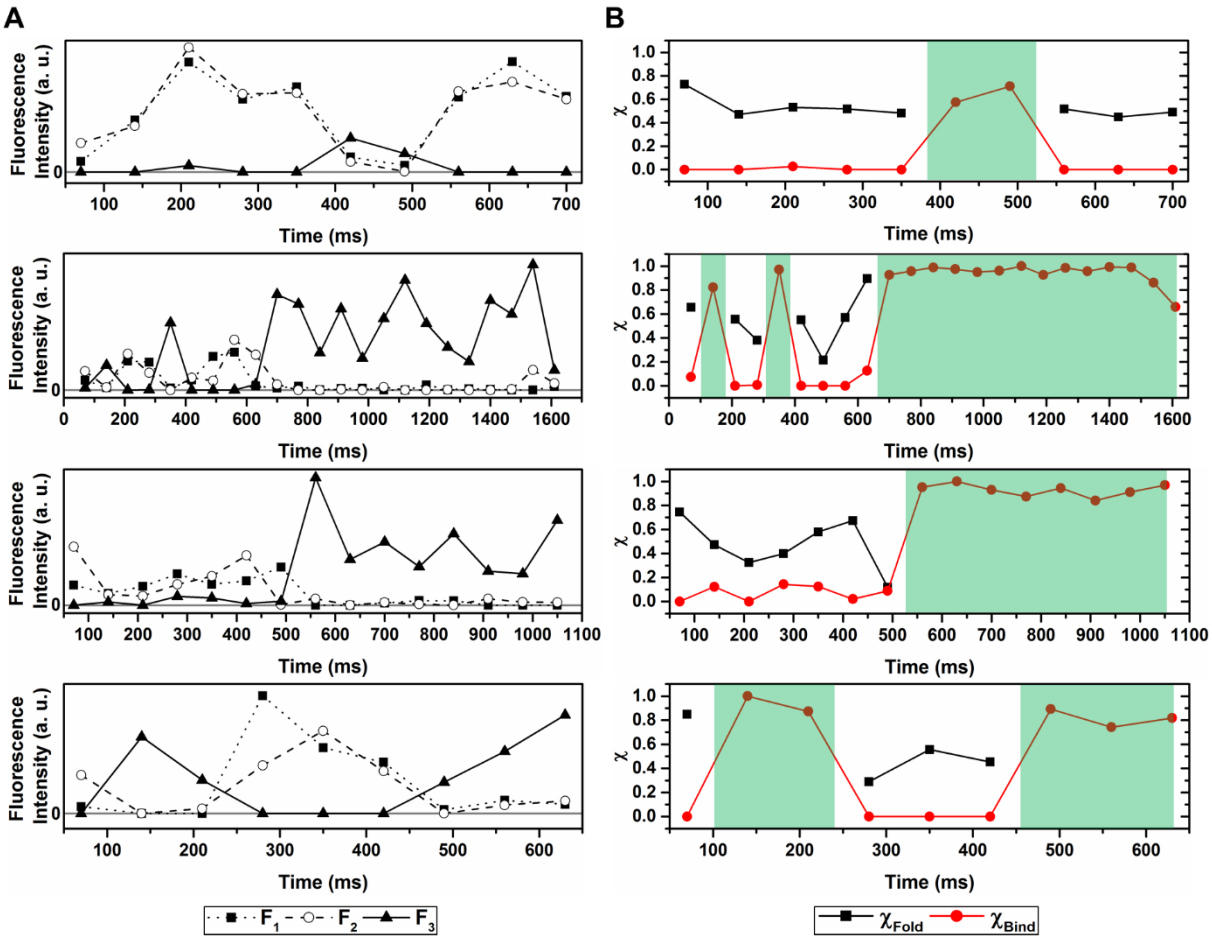


**Figure 5. 7.** Sample trajectories in three-color single-molecule experiments. (A) Fluorescence intensity of donor ($F_1$) and acceptor ($F_2$, and $F_3$) labels plotted on the same scale and axis. (B) The corresponding $\chi$ values associated with $FN_{FRET}$ conformation ($\chi_{Fold}$) and integrin binding ($\chi_{Bind}$). The green-shaded regions in panel B represent segments of trajectories in which binding of the integrin to FN was identified. Due to the low signal-to-noise of the intensities of $F_1$ and $F_2$ during the binding events, the data points corresponding to $\chi_{Fold}$ during the bound state time intervals were not included in the $\chi$ plots.

### 5.4.3 Integrin Binding Stability

The influence of $FN_{FRET}$ conformation and interfacial dynamics on the stability of $FN_{FRET}$–$\alpha_v\beta_3$ associations was characterized by analyzing the duration of binding events using the relevant FRET signal (*i.e.*, in the emission channel for $F_3$). To understand the impact of FN conformation on integrin binding, each binding event was associated with the conformational state of that particular FN molecule immediately prior to binding. This provided a more robust way to correlate binding stability with FN conformation compared to determining the conformation of each FN molecule during an integrin binding event itself (when both $F_1$ and $F_2$ emission intensities were small). For the analysis of binding times, only trajectories in which both binding and dissociation of the $FN_{FRET}$–$\alpha_v\beta_3$ complex was observed were included. Cumulative bound-state time distributions for $FN_{FRET}$ indicated that, on either surface, binding was significantly more stable for folded $FN_{FRET}$ than unfolded $FN_{FRET}$ (**Figure 5.8**), providing quantitative support for previous suggestions that the structure and conformational rigidity of the RGD site is important for integrin binding[15-17]. Moreover, on average, binding was modestly more stable on OEG than on TMS surfaces. The number of trajectories (~$10^3$) used to generate the cumulative bound-state time distributions for $FN_{FRET}$ on OEG and TMS are given in **Table C.6**.

Although $\chi_{Fold}$ during integrin binding events could not be quantified due to the low signal-to-noise of $F_1$ and $F_2$, fluctuations in the conformation of $FN_{FRET}$ were analyzed by comparing $\chi_{Fold}$ in the frames immediately before $\alpha_v\beta_3$ binding and after $\alpha_v\beta_3$ dissociation. Notably, analysis of the distribution in the difference in $\chi_{Fold}$ in the frames immediately before $\alpha_v\beta_3$ binding and after $\alpha_v\beta_3$ dissociation indicated the conformation of $FN_{FRET}$ after binding was almost always the same as before binding. As evidence of this finding, the distributions of the difference in $\chi_{Fold}$ values before

and after binding is shown in **Figure C.4.** In particular, these distributions were centered at zero, and very narrow compared to the measured differences between $\chi_{Fold}$ for folded and unfolded $FN_{FRET}$ on OEG (0.35) and TMS (0.45), which are indicated by dashed lines in **Figure C.4**. These data suggest that conformational changes of $FN_{FRET}$ during integrin binding were negligible, and that the measured conformation of $FN_{FRET}$ prior to binding is an appropriate representation. This was consistent with the fact that the characteristic binding times were significantly shorter than the characteristic timescales associated with conformational state changes for each surface.

The bound-state distributions were quantitatively described using an exponential mixture model that assumed the dissociation of the $FN_{FRET}$–$\alpha_v\beta_3$ complex could be described by a superposition of three first-order processes. Analysis of the model yielded fractions and characteristic binding-timescales for each binding mode to each conformational state on each surface (**Table C.7**). Quantitative analysis of the distributions revealed that in all cases, the bound-state time distributions exhibited the presence of short-lived, intermediate-lived, and long-lived bound populations. The short-lived associations had characteristic timescales of roughly ~0.1 s and comprised 72-87% of apparent binding events. The intermediate population (representing 12-21% of events) was also relatively short-lived, exhibiting timescales in the approximate range 0.2-0.6 s. The long-lived binding associations had characteristic timescales of approximately 1–6 s and represented only 1-8% of binding events. The presence and diversity of these apparent bound states suggested that, while a small fraction of binding events was strong and stable, many integrin-FN associations were much weaker, presumably due to perturbations in the conformation and/or reduced accessibility of the RGD site. Such effects may lead to the disruption of critical non-covalent interactions that stabilize binding and potentially inhibit complete binding of the integrin.

Interestingly, binding to folded $FN_{FRET}$ resulted in a more stable $FN_{FRET}$–$\alpha_v\beta_3$ complex than to unfolded $FN_{FRET}$ on both surfaces; this was apparent in both the average bound-state lifetimes and the characteristic lifetime of the long-lived state. Specifically, for folded $FN_{FRET}$ on OEG, the characteristic lifetime of the long-lived state was the longest (5.9 s), and the fraction of long-lived events (8%) was the largest, of any population on either TMS or OEG for either folded or unfolded $FN_{FRET}$ (also **Table C.7**). Moreover, the average bound-state lifetimes, which represented a weighted average of lifetimes of all of the states, were 0.68 s and 0.29 s for folded $FN_{FRET}$ on OEG and TMS, respectively. For comparison, the average bound-state lifetimes for unfolded $FN_{FRET}$ on OEG and TMS were 0.24 s and 0.08 s, respectively. In addition to integrin binding to folded $FN_{FRET}$ being more stable on both surfaces, these results indicated that, for a given folding state, integrin binding was more stable on OEG, where $FN_{FRET}$ was less dynamic.

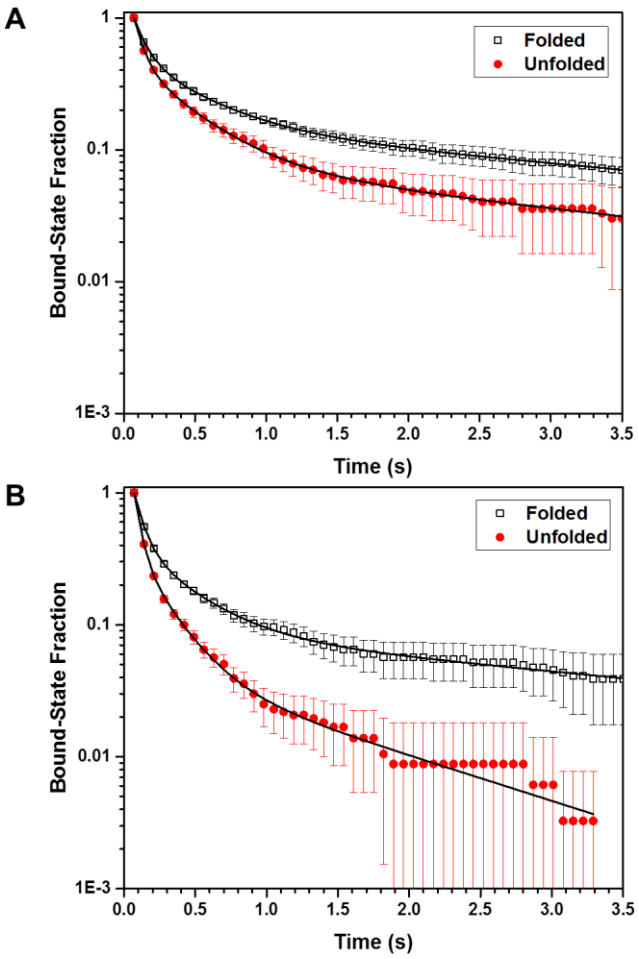


**Figure 5. 8.** Cumulative bound-state time distributions for the $FN_{FRET}$–$\alpha_v\beta_3$ complex on FS functionalized with OEG (A) and TMS (B) as a function of folding state of $FN_{FRET}$ that immediately preceded binding. The distributions for trajectories for folded (open squares) and unfolded (red circles) $FN_{FRET}$ were fit to an exponential mixture mode (black line), which assumed a superposition of three first-order dissociation processes. Based on the fitting parameters, the characteristic bound-state times for the short-lived, intermediate-lived, and long-lived complexes on each surface was determined. Error bars represent a 68% confidence interval based on a Poisson distribution for each data point. Each distribution was generated from ~$10^3$ molecular trajectories.

### 5.4.4 Likelihood of Integrin Binding

We also determined the impact of $FN_{FRET}$ conformation and interfacial dynamics on the likelihood of $\alpha_v\beta_3$ binding by measuring the time-to-binding for $\alpha_v\beta_3$ on OEG and TMS. The time-to-binding was defined as the time interval between the adsorption of a given $FN_{FRET}$ molecule

and the first FRET event indicating $\alpha_v\beta_3$ binding. As mentioned above, each binding event was associated with the conformation of FN immediately prior to the first frame in which binding was observed. In this analysis, the time-to-binding was representative of the rate of binding of the labeled $\alpha_v\beta_3$ to surface-adsorbed $FN_{FRET}$, which, in turn, was influenced by the energetic barrier to binding and/or the instantaneous accessibility of the binding site. **Figure 5.9** shows the cumulative time-to-binding distributions on OEG and TMS surfaces for folded and unfolded $FN_{FRET}$ with the number of trajectories ($\sim 10^3$) that make up the distributions given in **Table C.6**.

On OEG surfaces, the time-to-binding was considerably faster for folded than for unfolded $FN_{FRET}$, suggesting that, for the relatively static $FN_{FRET}$ on OEG, the energy barrier to binding and/or binding site accessibility was significantly influenced by FN conformation (**Figure 5.9 A**). However, on TMS, where $FN_{FRET}$ was highly dynamic, the time-to-binding distributions for folded and unfolded $FN_{FRET}$ were similar, suggesting that the accessibility of the binding site and the energy barrier to binding was relatively insensitive to the apparent conformation (**Figure 5.9 B**). Additionally, relative to $FN_{FRET}$ adsorbed to OEG, the time-to-binding even for folded $FN_{FRET}$ was slow on the TMS surface, and similar in magnitude to that for unfolded $FN_{FRET}$ on OEG. To quantify these observations, the time-to-binding distributions were fit to a two-population mixed exponential model, yielding the population fractions and characteristic rate constants for binding ($k_{bind}$) for each population and conformational state on OEG and TMS (**Table C.8**). Notably, on OEG, the mean value of $k_{bind}$, which represented $k_{on}$, for folded and unfolded $FN_{FRET}$ on OEG was 0.60 $s^{-1}$ and 0.060 $s^{-1}$, respectively, whereas the mean value of $k_{bind}$ for folded and unfolded $FN_{FRET}$ was 0.298 $s^{-1}$ and 0.141 $s^{-1}$, respectively, on TMS.

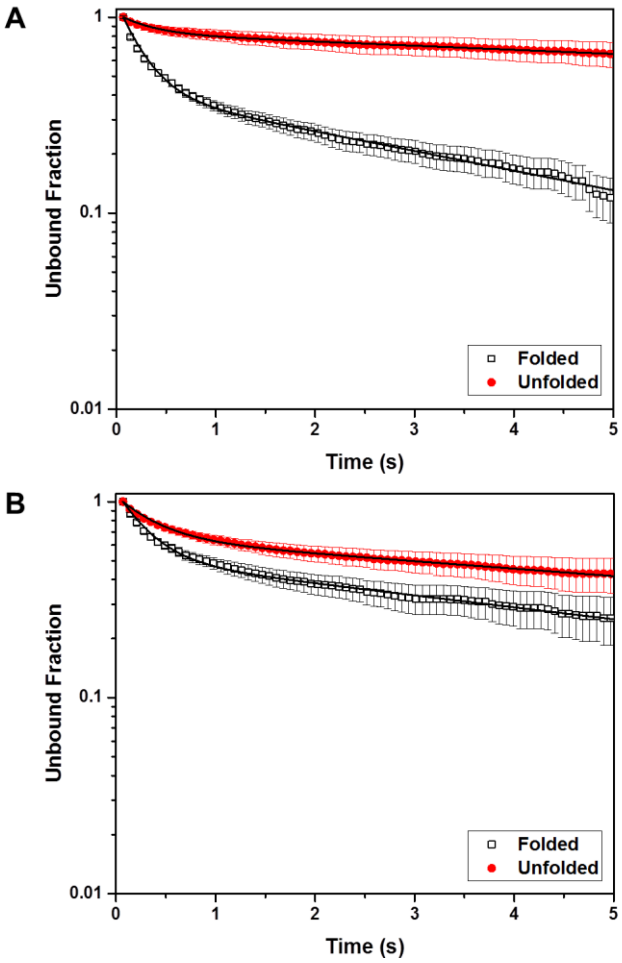


**Figure 5. 9.** Cumulative time-to-binding distributions for the association of the $FN_{FRET}$ and $\alpha_v\beta_3$ on FS functionalized with OEG (A) and TMS (B) as a function of folding state of $FN_{FRET}$ that immediately preceded binding. The distributions for trajectories for folded (open squares) and unfolded (red circles) $FN_{FRET}$ were fit to an exponential mixture mode (black line), which assumed a superposition of two first-order association processes. Error bars represent a 68% confidence interval based on a Poisson distribution for each data point. Each distribution was generated from ~$10^3$ molecular trajectories.

## 5.5 Discussion

The results reported here demonstrate the ability of high-throughput dynamic three-color SM-FRET tracking to unravel biophysical questions about the impact of conformation and dynamics on ligand-receptor binding in near-surface environments. This approach was applied to

investigate the structural basis for FN-integrin interactions at the solution-solid interface, which is directly relevant to "outside-in" integrin signaling. Our results show that the interfacial dynamics of FN directly influence both the stability of the bound FN–$\alpha_v\beta_3$ complex and time-to-binding for $\alpha_v\beta_3$ to FN. Specifically, the stability of the bound complex was greater for folded than unfolded $FN_{FRET}$ and, interestingly, for populations of FN that were less dynamic. Analysis of the bound-state time distributions indicated the presence of multiple binding modes, which were characterized by short, intermediate, and long binding times on both surfaces. The modes with short and intermediate binding times may be attributed to weak binding events due to non-native conformations of the RGD site, as well as to partial blockage of the RGD site either by the surface or structurally perturbed regions of $FN_{FRET}$. Additionally, it is plausible that some weak binding events may be associated with non-specific interactions (*e.g.*, between $\alpha_v\beta_3$ and regions of $FN_{FRET}$ that exclude the RGD site) as well as the transient adsorption of $\alpha_v\beta_3$ in close proximity to $FN_{FRET}$ on the surface. Conversely, the mode with long lifetimes was presumably due to specific binding interactions of $\alpha_v\beta_3$ with $FN_{FRET}$ molecules in which the RGD loop retained its native-like structure and was mostly accessible.

Given these observations, it was unsurprising that binding to folded $FN_{FRET}$ resulted in a more stable $FN_{FRET}$–$\alpha_v\beta_3$ complex, compared to unfolded $FN_{FRET}$, on both surfaces. However, it was interesting that the population fraction and characteristic lifetime associated with the long-lived bound state to folded $FN_{FRET}$ was significantly greater on OEG than on TMS. In contrast, one might have expected that integrin binding to folded $FN_{FRET}$ would be equally likely and stable, regardless of the underlying surface chemistry. We hypothesize that the reduced stability of binding on TMS stems from the greater conformational plasticity of $FN_{FRET}$ on TMS than on OEG. Specifically, in light of the increased dynamics on TMS, the RGD loop in the apparent folded state

$FN_{FRET}$ may presumably sample a larger conformational space than on OEG, resulting in subtle changes in the structure and accessibility of the integrin binding site, which, in turn, may weaken binding[42].

In addition to the influence of $FN_{FRET}$ dynamics on the stability of the integrin-FN complex, the rate of binding was also affected by conformational plasticity and mobility of $FN_{FRET}$. Under the conditions of these experiments, where integrin was present at high concentrations relative to $FN_{FRET}$, diffusional limitations of the integrin on binding were negligible. Accordingly, the time-to-binding reflected the accessibility of the RGD site as well as potential barriers to binding associated with non-native conformations of the binding site. On OEG, where the conformational state of $FN_{FRET}$ was well-defined and FN molecules were relatively static, integrin binding was rapid to folded $FN_{FRET}$, but significantly slower when $FN_{FRET}$ was unfolded. This is intuitive, since, for folded $FN_{FRET}$, the RGD site is well-structured and presumably accessible within the structure of $FN_{FRET}$. In contrast, while the RGD site may be accessible in some unfolded conformations of $FN_{FRET}$, there are likely to be many unfolded conformations of $FN_{FRET}$ in which the RGD site is less accessible, hindering integrin binding. Additionally, conformations of the RGD loop for which binding of integrin is highly strained may also impede binding. Thus, on average, it is reasonable that integrin binding would be slower to unfolded than folded $FN_{FRET}$.

Interestingly, however, this trend was not observed for $FN_{FRET}$ adsorbed to TMS, where $FN_{FRET}$ was conformationally flexible and highly dynamic, and, in fact, integrin binding was relatively slow regardless of the apparent conformation of $FN_{FRET}$. We speculate that the rapid dynamic motion of $FN_{FRET}$ in this environment contributed to increased heterogeneity in the orientation of the RGD site, which included orientations where the RGD site is blocked by the surface. Furthermore, such dynamics may lead to increased conformational heterogeneity, even

when $FN_{FRET}$ is in a nominally folded state, and as a result, the binding site is not as accessible, on average, as it is when $FN_{FRET}$ is adsorbed on OEG in a relatively static state. While orientational and conformational heterogeneity may reduce the kinetics of integrin binding, the increase in dynamics may also lead to orientations and conformations that favor binding, although, such orientations and conformations were presumably rare.

While elucidating the structural basis for FN signaling, our findings provide new insight into the missing link between viscoelastic material properties (*e.g.*, ECM stiffness) and cell-substrate interactions[43]. Based on our results, differences in these interactions as a function of viscoelasticity may be explained by the impact of properties like ECM stiffness on FN conformation and dynamics. Specifically, by altering the translational mobility and flexibility of FN, ECM stiffness may modulate the time-to-binding (and the time-to-rebinding after unbinding) for FN and integrins and thus the ratio of binding and unbinding rates. For example, if the ECM and thus FN is rapidly moving, the time between successive binding events for a given integrin would presumably increase. Such an increase in the time-to-binding may be attributed to a decrease in the likelihood of the integrin re-binding to the same FN molecule.

In direct connection with our results, prior studies have shown that the stability of cell adhesions with ECM increases with increasing stiffness of the surrounding ECM microenvironment[44-49]. The resulting increase in cell adhesion may be attributed to a "slowing-down" of the ECM microenvironment, which increases the likelihood of re-binding of an integrin upon dissociation. Accordingly, by increasing this likelihood, the number of steady-state integrin-FN interactions between the cell and ECM would presumably increase, resulting in an increase in cell adhesion. Interestingly, in these studies, the relevant timescales of ECM relaxation were measured to be of the same order of magnitude (*i.e.*, seconds to milliseconds) as that of the binding

and unbinding rates measured here[50]. Given this correlation, it is plausible that changes in the rate of ECM relaxation have a direct effect on the rates of binding and unbinding associated with FN-integrin interactions. Ultimately, our results combined with these studies highlight the likely connection between ECM stiffness, FN dynamics, and the rates of FN-integrin and unbinding, which underlies the mechanotransduction of viscoelastic forces to cells. This connection may, moreover, explain similar observations with synthetic hydrogels with ECM proteins or peptides that are widely used for tissue engineering, whereby cells reportedly adhere more strongly to synthetic hydrogels that have increasing stiffness[51,52].

## 5.6 Conclusions

In summary, as a novel biophysical approach to uncover the role of conformation and dynamics in ligand-receptor binding, dynamic three-color SM-FRET tracking presents considerable opportunities. Using this approach, we elucidated the impact of FN conformation and dynamics in FN-integrin binding, leading to an improved mechanistic understanding of FN-mediated cell signaling. Specifically, as FN dynamics increased, the likelihood of integrin binding, particularly to folded FN, as well as the stability of the bound FN–$\alpha_v\beta_3$ complex decreased markedly. This understanding provides previously inaccessible clues into the biophysical basis for the response of cells to changes in their local environment, including cellular mechanosensing. Specifically, by altering the ratio of the binding and unbinding rates of FN to integrins, these results illustrate how changes in local stiffness of ECM can mediate cell fate. The methods developed here may further be applied to quantify the impact of molecular conformation and dynamics on binding and unbinding rates of other biomolecular complexes. For example, three-color SM-FRET

tracking may be used to elucidate fundamental questions about the connection between conformational dynamics and ligand binding involving intrinsically disordered proteins, which have generally remained elusive due to limitations in existing methods. Such methods may also have far-reaching implications for the characterization of structure-function-dynamics relationships for other membrane proteins (*e.g.*, GPCRs) that are difficult to study in situ within cellular or unnatural membranes.

## SUPPORTING INFORMATION

Methods for the characterization of the dynamic behavior of $FN_{FRET}$ and surface plasmon resonance measurements, fitting parameters for SM results, results of measurement of dissociation constants, number of trajectories obtained during SM analysis, representative sample trajectories and movies of raw data for two-color and three-color SM-FRET experiments can be found in **Appendix C**.

## 5.7 References


(1) Rozario, T.; DeSimone, D. W. *Dev. Biol.* **2010**, *341*, 126.
(2) Midwood, K. S.; Williams, L. V.; Schwarzbauer, J. E. *Int. J. Biochem. Cell Biol.* **2004**, *36*, 1031.
(3) Schafer, M.; Werner, S. *Nat. Rev. Mol. Cell Biol.* **2008**, *9*, 628.
(4) Reinke, J. M.; Sorg, H. *Eur. Surg. Res.* **2012**, *49*, 35.
(5) Kadler, K. E.; Hill, A.; Canty-Laird, E. G. *Curr. Opin. Cell Biol.* **2008**, *20*, 495.
(6) Humphrey, J. D.; Dufresne, E. R.; Schwartz, M. A. *Nat. Rev. Mol. Cell Biol.* **2014**, *15*, 802.
(7) Mouw, J. K.; Ou, G. Q.; Weaver, V. M. *Nat. Rev. Mol. Cell Biol.* **2014**, *15*, 771.
(8) Parsons, J. T.; Horwitz, A. R.; Schwartz, M. A. *Nat. Rev. Mol. Cell Biol.* **2010**, *11*, 633.
(9) Kumra, H.; Reinhardt, D. P. *Adv. Drug Deliv. Rev.* **2016**, *97*, 101.
(10) Xiong, J. P.; Stehle, T.; Goodman, S. L.; Arnaout, M. A. *Blood* **2003**, *102*, 1155.
(11) Shattil, S. J.; Kim, C.; Ginsberg, M. H. *Nat. Rev. Mol. Cell Biol.* **2010**, *11*, 288.
(12) Calderwood, D. A. *J. Cell Sci.* **2004**, *117*, 657.
(13) Takagi, J.; Petre, B. M.; Walz, T.; Springer, T. A. *Cell* **2002**, *110*, 599.
(14) Leahy, D. J.; Aukhil, I.; Erickson, H. P. *Cell* **1996**, *84*, 155.
(15) Koivunen, E.; Wang, B.; Ruoslahti, E. *Biotechnology (NY)* **1995**, *13*, 265.
(16) Pasqualini, R.; Koivunen, E.; Ruoslahti, E. *Nat. Biotechnol.* **1997**, *15*, 542.
(17) Sobers, C. J.; Wood, S. E.; Mrksich, M. *Biomaterials* **2015**, *52*, 385.
(18) Xiong, J. P.; Stehle, T.; Zhang, R.; Joachimiak, A.; Frech, M.; Goodman, S. L.; Arnaout, M. A. *Science* **2002**, *296*, 151.
(19) Takagi, J.; Strokovich, K.; Springer, T. A.; Walz, T. *EMBO J.* **2003**, *22*, 4607.
(20) Van Agthoven, J. F.; Xiong, J. P.; Alonso, J. L.; Rui, X.; Adair, B. D.; Goodman, S. L.; Arnaout, M. A. *Nat. Struct. Mol. Biol.* **2014**, *21*, 383.
(21) Adair, B. D.; Xiong, J. P.; Maddock, C.; Goodman, S. L.; Arnaout, M. A.; Yeager, M. *J. Cell Biol.* **2005**, *168*, 1109.
(22) Nagae, M.; Re, S.; Mihara, E.; Nogi, T.; Sugita, Y.; Takagi, J. *J. Cell Biol.* **2012**, *197*, 131.
(23) Copie, V.; Tomita, Y.; Akiyama, S. K.; Aota, S.; Yamada, K. M.; Venable, R. M.; Pastor, R. W.; Krueger, S.; Torchia, D. A. *J. Mol. Biol.* **1998**, *277*, 663.
(24) McLoughlin, S. Y.; Kastantin, M.; Schwartz, D. K.; Kaar, J. L. *Proc. Natl. Acad. Sci. U.S.A.* **2013**, *110*, 19396.
(25) Weltz, J. S.; Schwartz, D. K.; Kaar, J. L. *ACS Nano* **2016**, *10*, 730.
(26) Faulon Marruecos, D.; Kastantin, M.; Schwartz, D. K.; Kaar, J. L. *Biomacromolecules* **2016**, *17*, 1017.
(27) Elosegui-Artola, A.; Bazellieres, E.; Allen, M. D.; Andreu, I.; Oria, R.; Sunyer, R.; Gomm, J. J.; Marshall, J. F.; Jones, J. L.; Trepat, X.; Roca-Cusachs, P. *Nat. Mater.* **2014**, *13*, 631.
(28) Chan, C. E.; Odde, D. J. *Science* **2008**, *322*, 1687.
(29) Bell, G. I. *Science* **1978**, *200*, 618.
(30) Huebsch, N.; Arany, P. R.; Mao, A. S.; Shvartsman, D.; Ali, O. A.; Bencherif, S. A.; Rivera-Feliciano, J.; Mooney, D. J. *Nat. Mater.* **2010**, *9*, 518.
(31) Humphries, J. D.; Byron, A.; Humphries, M. J. *J. Cell Sci.* **2006**, *119*, 3901.
(32) Hohng, S.; Joo, C.; Ha, T. *Biophys. J.* **2004**, *87*, 1328.
(33) Sun, Y.; Wallrabe, H.; Booker, C. F.; Day, R. N.; Periasamy, A. *Biophys. J.* **2010**, *99*, 1274.
(34) Langdon, B. B.; Kastantin, M.; Schwartz, D. K. *Biomacromolecules* **2015**, *16*, 3201.
(35) Langdon, B. B.; Kastantin, M.; Schwartz, D. K. *Biophys. J.* **2012**, *102*, 2625.

(36) Kastantin, M.; Keller, T. F.; Jandt, K. D.; Schwartz, D. K. *Adv. Funct. Mater.* **2012**, *22*, 2617.
(37) Walder, R.; Kastantin, M.; Schwartz, D. K. *Analyst* **2012**, *137*, 2987.
(38) Kastantin, M.; Schwartz, D. K. *ChemPhysChem* **2013**, *14*, 374.
(39) Kastantin, M.; Schwartz, D. K. *Small* **2013**, *9*, 933.
(40) Kastantin, M.; Langdon, B. B.; Chang, E. L.; Schwartz, D. K. *J. Am. Chem. Soc.* **2011**, *133*, 4975.
(41) Shimaoka, M.; Takagi, J.; Springer, T. A. *Annu. Rev. Biophys. Biomol. Struct.* **2002**, *31*, 485.
(42) Krammer, A.; Lu, H.; Isralewitz, B.; Schulten, K.; Vogel, V. *Proc. Natl. Acad. Sci. U.S.A.* **1999**, *96*, 1351.
(43) Carraher, C. L.; Schwarzbauer, J. E. *J. Biol. Chem.* **2013**, *288*, 14805.
(44) Discher, D. E.; Janmey, P.; Wang, Y. L. *Science* **2005**, *310*, 1139.
(45) Doyle, A. D.; Carvajal, N.; Jin, A.; Matsumoto, K.; Yamada, K. M. *Nat. Commun.* **2015**, *6*, 8720.
(46) Engler, A. J.; Sen, S.; Sweeney, H. L.; Discher, D. E. *Cell* **2006**, *126*, 677.
(47) Markowski, M. C.; Brown, A. C.; Barker, T. H. *J. Biomed. Mater. Res. Part A* **2012**, *100a*, 2119.
(48) Pelham, R. J.; Wang, Y. L. *Proc. Natl. Acad. Sci. U.S.A.* **1997**, *94*, 13661.
(49) Peyton, S. R.; Putnam, A. J. *J. Cell. Physio.* **2005**, *204*, 198.
(50) Mizuno, D.; Tardin, C.; Schmidt, C. F.; Mackintosh, F. C. *Science* **2007**, *315*, 370.
(51) Chaudhuri, O.; Gu, L.; Klumpers, D.; Darnell, M.; Bencherif, S. A.; Weaver, J. C.; Huebsch, N.; Lee, H. P.; Lippens, E.; Duda, G. N.; Mooney, D. J. *Nat. Mater.* **2016**, *15*, 326.
(52) Blakney, A. K.; Swartzlander, M. D.; Bryant, S. J. *J. Biomed. Mater. Res. Part A* **2012**, *100*, 1375.

# Chapter VI: Chemically Heterogeneous Polymer Brushes Stabilize Protein Conformation

Manuscript in preparation.

## 6.1 Abstract

Polymer brushes consisting of poly(ethylene glycol) (PEG) have been extensively studied as coatings to minimize protein adsorption and ultimately the foreign body response to biomaterials. However, while PEG brushes reduce protein adsorption, such surfaces may actually enhance protein unfolding as well as stabilize the presence of unfolded protein molecules on the surface. In this work, we investigated the extent to which protein conformation and dynamics may be controlled on polymer brushes that are chemically heterogeneous. To determine this extent, the conformation and dynamic behavior of fibronectin (FN) was characterized on random copolymer brushes consisting of PEG and poly(sulfobetaine) (PSB) using single-molecule (SM) methods. Through SM studies, we showed that the extent of fibronectin unfolding and the retention of fibronectin on PEG brushes was reduced by incorporating PSB. Perhaps most interestingly, the relationship between the fraction of PSB in the brush and fibronectin unfolding and accumulation in the denatured state was non-monotonic. This suggests there is an optimum PSB-to-PEG ratio that diminished interactions between unfolded fibronectin and the random block copolymer brush. Such an optimum may result from matching the heterogeneity of the brush to that of surface of the protein, which contains residues with a broad range of chemical identities. The stabilization of proteins on surfaces via protein-templated nano-scale self-assembly of heterogeneous surface represents a new paradigm for the design of biocompatabile materials.

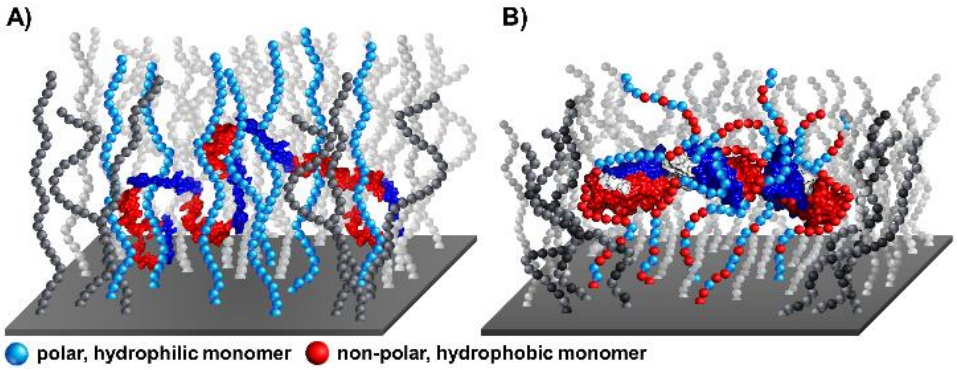


**Figure 6. 1.** Schematic of the stabilization of protein conformation by polymer brushes that are chemically heterogeneous. Unlike homogeneous brushes (A), brushes that are chemically heterogeneous (B), may self-assemble using the protein as a template. The blue and red copolymers and regions on the protein represent chemically different moieties. Through self-assembly of the brush, red copolymers may interact with regions on the protein with similar properties. Similarly, blue blocks will self-assemble with blue regions on the protein.

## 6.2 Introduction

A conventional biomaterials paradigm holds that surface hydrophobicity drives protein adsorption and subsequent protein unfolding, whereas hydrophilic/hydrated surfaces reduce protein adsorption and minimize interactions that lead to protein unfolding[1]. Therefore, approaches to improve the biocompatibility of biomaterials have often focused on altering the overall hydrophobicity of a surface (e.g., using hydrophilic biomaterials and/or coatings). Various materials have been used for this purpose, including poly(ethylene glycol) (PEG), poly(hydroxyethyl methacrylate), polymerized tetraglyme, and various zwitterionic materials such as poly(carboxybetaine methacrylate)[2–4]. However, this paradigm has proven to be overly simplistic, as numerous studies have shown that proteins also adsorb and unfold on hydrophilic materials, and that the unfolded state may actually be stabilized on hydrophilic relative to hydrophobic materials [5–8]. The unfolding and stabilization of denatured protein molecules, such as fibronectin (FN), may enhance protein-protein associations on the surface, which initiate fouling (i.e., the formation of robust proteinaceous layers). Additionally, protein unfolding on surfaces may expose epitopes that are recognized by inflammatory cells as damage-associated molecular pattern molecules (DAMPs) via toll-like receptors (TLRs), triggering adverse immunological reactions. Notably, hydrophilic materials that are considered nominally biocompatible have been shown to induce the foreign body response, which is presumed to be due to protein unfolding and, importantly, reduces the success of tissue engineering strategies[2,9,10].

An alternative paradigm for improving the biocompatibility of materials entails surfaces that are chemically heterogeneous and highly mobile[11–13]. First, by providing a chemically heterogeneous environment, like-interactions between the material and solvent-exposed residues on the protein can be matched, which preserve the native conformation of the protein. In turn,

unfavorable, destabilizing interactions that arise in homogeneous systems are minimized. Secondly, the system needs to be mobile (i.e. fluid) in order to freely rearrange and 'find' favorable interactions. In other words, the protein acts as a template for self-assembly with the surface. Such mobile systems can be polymer brushes or supported lipid bilayers. In the former, the conformational entropy of the polymer chains provide enough flexibility to accommodate the protein in an undisturbed conformation, while in the latter, the fast translational diffusion of the system and rearrangement of lipids is responsible for protein stabilization. Poly(sulfobetaine) (pSB) and poly(ethylene glycol) (PEG) are two widely used polymers that have shown promising applications in biomedicine and biomaterials arena. Despite their comparable antifouling performance reported in the literature, pSB and PEG have very different physicochemical properties. While pSB is a 'superhydrophilic' material that binds water molecules via electrostatic interactions, PEG is an amphiphilic material that can weakly bind proteins via both hydrophobic interactions and hydrogen bonding. Despite these postulated differences, the potential influence of mixed electrostatic and hydrophobic interactions between proteins and these polymers has not been investigated.

One of the primary difficulties in studying the interaction of proteins on polymer-coated surfaces is the lack of methods that allow to directly measure the conformation of adsorbed proteins. Particularly, typical ensemble-averaging methods relate protein adsorption and conformation indirectly from the average outcome of many populations. Thus, the interpretations and assumptions of models that agree with the observations may be overly simplified or even incorrect, especially because they typically ignore heterogeneities associated with the protein, the polymer, and the interactions between them[14]. Importantly, in the context of the FBR, the presentation of unfolded molecules (i.e., DAMPs) is directly influenced by the highly dynamic

and heterogeneous behavior of proteins in near-surface environments[15]. While processes like the transient unfolding and refolding or the rapid exchange of protein molecules between the surface and the bulk are likely involved in the FBR, their respective roles in the FBR have been all but ignored due to the lack of experimental techniques to directly observe these interfacial processes. However, in our group, we have showed that high-throughput single-molecule (SM) techniques allow us to decouple individual molecular mechanisms and dynamic heterogeneity[13,16,17]. Specifically, we combine Totally Internally Reflection Fluorescence Microscopy (TIRFM) with Forster Resonance Energy Transfer (FRET) to identify and track in real time the conformation of ~$10^6$ freely-diffusing protein molecules on different biomaterial surfaces.

Herein, we constructed random heteropolymer brushes via grafting-from (i.e. ATRP) with varying relative compositions of poly(sulfobetaine methacrylate) (pSBMA) and poly(oligoethylene glycol) methacrylate (pOEGMA), and studied the impact of brush chemical heterogeneity on FN stability and dynamics at the solid-liquid interface via high-throughput SM experiments. We found that the relationship between FN structural stabilization and PSB fraction was non-monotonic; specifically, an optimum pSBMA-to-pOEGMA ratio was identified that minimized interactions between unfolded FN and the random copolymer brush. We hypothesize that this optimum results from matching the chemical heterogeneity of the brush to that of the protein's surface, which would enhance the ability of the protein to act as a nanoscale template for the self-assembly of surrounding chemical blocks within the brush.

## 6.3 Methods

### 6.3.1 Preparation and Labeling of Recombinant FN

Recombinant FN type III 8-10 domains were initially amplified via polymerase chain reaction from plasmid DNA that contained the gene for FN type III 8-10 domains (from Thomas Barker, Georgia Institute of Technology) and subsequently cloned into pET-21b (Novagen) with a C-terminal 6xhis tag. Following cloning, the TAG stop codon was introduced in place of residue 1381 while residue 1500 was mutated to cysteine via site-directed mutagenesis to permit fluorophore attachment. Note, the residue numbers correspond to the amino acid positions in full-length FN. The resulting construct to be used for FRET ($FN_{FRET}$), as well as wild-type FN type III 8-10, was co-expressed with pDule2 pCNF RS (from Ryan Mehl, Oregon State) in BL21 (DE3) *Escherichia coli* via auto-induction in minimal media containing 4-azido-L-phenylalanine (Chem-Impex)[18,19]. $FN_{FRET}$ and wild-type FN type III 8-10 were purified from cell lysate via affinity chromatography using a copper-charged Bio-Scale Mini column (Bio-Rad). During purification, care was taken to minimize exposure of $FN_{FRET}$ to UV light to avoid reduction of the azide group prior to labeling.

Dual labeled $FN_{FRET}$ was prepared by initially dialyzing the protein against 10 mM sodium phosphate buffer (pH 7.4) at 4 ºC for 18 h. The protein was then reacted with dibenzocyclooctyne-activated Alexa Fluor 555 (Life Technologies) using a 3:1 molar ratio of fluorophore-to-protein in a total reaction volume of 100 μL for 18 h in the dark. Upon donor labeling, acceptor was attached via a second reaction with maleimide-activated Alexa Fluor 647 (Life technologies), also in the dark, for 18 h using a 3:1 fluorophore-to-protein molar ratio and a reaction volume of 100 μL. To facilitate acceptor labeling, Cys1500 was reduced via addition of a 5-molar excess of tris-(2-carboxyethyl)phosphine hydrochloride for 30 min at room temperature prior to the reaction. After

the completion of both labeling reactions, the residual free dye in solution was separated from the dual-labeled protein using a Bio-Rad SEC 70 10x300 mm column. Labeling efficiency was determined using the molar extinction coefficient for each fluorophore (155,000 $M^{-1}cm^{-1}$ for Alexa Fluor 555 at 565 nm and 270,000 $M^{-1}cm^{-1}$ for Alexa Fluor 647 at 668 nm) as well as that for $FN_{FRET}$ (32,890 $M^{-1}cm^{-1}$ at 280 nm). Correcting for absorbance of the dyes at 280 nm, the labeling efficiency was found to be 70% and 40% for Alexa Fluor 555 and 647, respectively, for dual-labeled $FN_{FRET}$.

### 6.3.2 Preparation of Polymer Brushes and Surface Characterization

#### 6.3.2.1 Initiator deposition

The self-assembled monolayers (SAMs) containing the polymerization initiator were formed as follows. First, fused silica wafers were immersed in a piranha solution for 2 h, followed by ozone-plasma activation of the hydroxyl groups on the surface for 30 min. Next, the surfaces were placed in a beaker containing a 0.5 mM toluene solution of ((chloromethyl)phenylethyl)trichlorosilane (CMPS, Gelest). The reaction took place at room temperature for 1 h. After the formation of SAMs, the fused silica wafers were thoroughly rinsed with toluene several times and dried under a stream of pure nitrogen. For surface characterization purposes (ellipsometry, contact angle, and FTIR), silicon wafers were used instead of fused silica, but the rest of the procedure was identical.

#### 6.3.2.2 Formation of Polymer Brushes

Polymer brushes were constructed from the initiator-coated surfaces via a typical ATRP procedure. Different molar feed ratios (0:1, 1:3, 1:1, 3:1, 1:0) of [2-(methacryloyloxy)ethyl]dimethyl-(3-sulfopropyl)ammonium hydroxide (SBMA, Sigma Aldrich) to poly(ethylene glycol) methacrylate Mn 360 (OEGMA, Sigma Aldrich) monomers were dissolved in 15 mL of a 4:1 water/methanol mixture (volumetric ratio), always maintaining a 500 mM total monomer concentration in solution. The resulting solution was purged with nitrogen for at least 30 min. CuBr (Sigma) (23 mg) and 2,2'-bipyridyl (bipy) (50 mg) were added into an oven-dried Schlenk flask and deoxygenated by three vacuum-nitrogen freeze-thaw-pump cycles. The degassed solution containing the monomer was transferred by cannula to the Schlenk flask. The resulting mixture was vortexed until homogenization and then was transferred into a customized reactor containing the CMPS-modified surfaces. The reactor was oxygen-free and under positive nitrogen pressure. The reaction was continued for 2 h at 60 °C. Then, the reactor was opened to allow the polymerization to stop upon contact with atmospheric oxygen. Finally, the surfaces were rinsed several times with warm water and methanol, and dried under a stream of pure nitrogen.

#### 6.3.2.3 Characterization of Polymer Brushes

Polymer brush-coated surfaces were characterized via three different techniques. First, the thickness of the dry brush was measured by ellipsometry using a J.A. Woollam variable angle spectroscopic ellipsometer (model VASE-VB-250). A spectral scan of the surface was collected between 500 and 900 nm with an incident angle between 60 and 80°, in increments of 5°. The dry brush thickness ($h_{dry}$) was determined using a three-layer planar model of the solid surface from the collected spectra, considering the refractive index of air (n = 1.003), OEGMA and SBMA (n

= 1.450), $SiO_2$ layer (n = 1.457), and silicon (n = 3.881). The spectroscopic scan was then fit to the model using Cauchy's equation in order to solve for $h_{dry}$. Secondly, the contact angle of each surface was calculated in order to determine the expected changes in surface hydrophobicity as a function of zwitterionic content in the brushes. Contact angle measurements were performed using a custom-built goniometer. A droplet of approximately 1 μL of Millipore water was placed on the polymer brush surface, and the contact angle was measured from the images taken. For each brush composition, contact angles were measured at three independent locations; the reported values and uncertainties were based on the mean and standard deviation of these measurements. Thirdly, FTIR-ATR was performed using a Thermo Scientific Nicolet 6700 FTIR. The IR spectra were taken with 1 $cm^{-1}$ resolution, using 1000 scans for background collection and 1000 scans for sample collection. Background spectra were obtained from CMPS-coated fused silica wafers, which is the underlying chemistry for all brush compositions.

### 6.3.3 Single-Molecule FRET Imaging and Image Processing

SM-FRET experiments of $FN_{FRET}$ in contact with polymer brush-coated glass were performed as explained in detail elsewhere[8] using a TIRFM microscope. Briefly, SM-FRET TIRFM measurements were performed using a custom-built prism-based illumination system, flow cell maintained at 25.0 ± 0.1 °C, and Nikon TE-2000 microscope with 60x plan Apo water immersion objective and 1.5x post-objective magnification lens. The solid-liquid interface was illuminated with a 50 mW 532 nm diode-pumped solid-state laser (Samba, Cobolt) using a cylindrical prism. The fluorescence emission from labeled protein molecules at the interface was split in two spectrally different channels using an Optosplit III beam splitter (Cairn Research) containing a 610 nm dichroic mirror (T610LPXR, Chroma). To reduce bleed-through of the donor

into the acceptor channel and remove residual excitation light, the spectrum from each channel was filtered with 90% transmission bandpass filters from Semrock: 585/40 for the donor and 685/40 for the acceptor. The intensity in both channels was collected by a an Andor iXon-888 EMCCD camera (model No. DU897; Andor Technology, Belfast, UK) cooled to −90 °C with a temporal resolution of 100 ms. For all experiments, $FN_{FRET}$ was added to the flow-cell containing the surface of interest at a concentration of $5x10^{-10}$ M in a phosphate buffer solution with ionic strength of 137 mM and pH of 7.4.

Objects in each channel were localized and connected into trajectories as previously described [2021]. Diffraction-limited objects were identified and differentiated by convolution with a disk matrix and thresholded based on their intensity after background subtraction. The location of each object was determined using the center-of-intensity method. FRET events were identified by the presence of objects that appeared at the same (x,y) coordinate in both channels in a given frame. Once identified, objects were connected into trajectories if they appeared within a 2.2 μm tracking radius in consecutive frames. Given the low concentration of $FN_{FRET}$ used in the experiments, the number of objects in the field of view (2,450 $\mu m^2$) always remained below 100, which avoided false connections during object tracking. Furthermore, previously reported results with the same dyes, filters, and experimental setup confirmed that the crosstalk between channels and photo-blinking was negligible[8].

### 6.3.4 Calculation of Adsorption Rate Constants, Surface Residence Times, and Kinetics of Conformational Changes

Adsorption rate constants were determined from single-molecule experiments and expressed as the total number of adsorption events relative to the elapsed time of a movie (100 s),

the area of the field of view (2,450 μm$^2$), and the $FN_{FRET}$ concentration (5x10$^{-10}$ M). The trajectory of an individual molecule was counted as an adsorption event if the molecule appeared in both the donor and acceptor channel at some point in the trajectory and, moreover, resided on the surface for 4 frames or longer. Furthermore, neither initial conformational state (folded or unfolded) nor subsequent conformational changes were considered to select the trajectories.

To quantitatively characterize desorption kinetics, the complementary cumulative surface residence time distribution for the molecules was accumulated. These distributions comprised the surface residence times for each trajectory from the time interval between adsorption and desorption. Objects with residence times of less than 4 frames were ignored due to the sensitivity of the methodology used for object identification (*i.e.*, random noise could dominate these single-frame trajectories). The surface residence times for all molecules in an experiment were subsequently used to create a complementary cumulative residence time distribution ($F(t)$), representing the number of molecules residing on the surface for time $t$ or longer. These distributions were fit to an exponential mixture model $F(t) = A^{-1}\sum_{k=1}^{N} x_k e^{-t/\tau_k}$, where $F(t)$ is the probability that an object has a residence time $\geq t$, $x_k$ is the relative fraction of all the objects that follows the desorption pathway $k$, and $\tau_k$ represents the characteristic surface residence time of that pathway (*i.e.*, population)[22]. In this model, which included four populations for both always folded and unfolded molecules, each pathway was assumed to be a first-order process.

To characterize the unfolding and apparent folding kinetics, the dwell times of protein molecules in either a folded or unfolded conformation within a trajectory were measured. Specifically, the dwell times represent the time that a molecule remains in an observed conformational state before undergoing a conformational change towards another state. If a molecule desorbed before undergoing a conformational change, the time elapsed was not

considered a dwell time. Complementary cumulative distributions of dwell times were constructed as described for the analysis of desorption kinetics. The probability distribution of dwell times ($p(t_i)$) was adjusted to account for the finite residence times of proteins at the interface before converting it to a complementary cumulative form[23]. The distribution was fitted to a three exponential mixture model to account for folding and unfolding processes as described elsewhere[22].

### 6.3.5 Super-resolution Mapping of Hydrophobic Regions within the Polymer Brushes

To characterize surface hydrophobicity, adsorption events of the environmentally sensitive probe NBD-X were spatially mapped on the surface. NBD-X undergoes both a blue shift and an increase in quantum yield in hydrophobic environments, while it is highly quenched in hydrophilic environments. By selecting a narrow bandwidth of fluorescence emission, we could image only the adsorption events that corresponded to NBD-X interacting with a hydrophobic environment. Briefly, these surface adsorption maps were generated by binning adsorption events onto a pseudoimage with 15 nm pixels. A Gaussian blur was applied to this pseudoimage with a radius of 100 nm to account for positional uncertainty.

## 6.4 Results

### 6.4.1 Mixed Polymer Brushes Constructed via SI-ATRP

To study how surface chemical heterogeneity affects protein adsorption, stability and dynamics, pSBMA and pOEGMA homopolymer brushes as well as p($SBMA_x$-co-$OEGMA_y$) copolymer brushes containing different ratios of SBMA and OEGMA units were synthesized via

Surface-Initiated Atom Transfer Radical Polymerization (SI-ATRP) (**Figure 6.2 A**). Specifically, by using different feed molar ratios of SBMA and OEGMA, five different polymer brush compositions were constructed from fused silica surfaces: pSBMA, p($SBMA_{25}$-co-$OEGMA_{75}$), p($SBMA_{50}$-co-$OEGMA_{50}$), p($SBMA_{75}$-co-$OEGMA_{50}$), and pOEGMA. **Figure 6.2 B** demonstrates that the brush dry thickness was constant across the five different compositions as measured by ellipsometry, and that the static water contact angle monotonically decreased as the SBMA content increased in the brush. Representative images of the contact angle measurements are found in **Figure D.1**. Similar dry thicknesses and contact angles of pure pSBMA and pOEGMA brushes have been reported in the literature for equivalent reaction conditions[24,25], which serve as comparable upper and lower limits for our mixed brushes.

The surface composition was determined by Attenuated Total Reflectance Fourier Transform Infrared (ATR-FTIR) to verify that both SBMA and OEGMA monomer units were incorporated into the copolymer brushes. The ATR-FTIR spectra of the polymer brush modified surfaces in the region from 900 $cm^{-1}$ to 2500 $cm^{-1}$ are shown in **Figure 6.2 C**. The presence of an identical peak for all surfaces at 1730 $cm^{-1}$, which corresponds to C=O stretching of the polymer backbone, indicates that the brushes reached a similar degree of polymerization. The peaks at 1193 $cm^{-1}$ ($SO_3^-$ asymmetric stretching), 1041 $cm^{-1}$ ($SO_3^-$ symmetric stretching), and 1485 $cm^{-1}$ (C−N stretching) are the signature of SBMA. Indeed, the intensities of the SBMA peaks increased with increasing SBMA composition in the copolymer. Finally, the broad peak located around 1063−1103 $cm^{-1}$ is indicative of different modes of C−O stretching, which became increasingly apparent as the content in OEGMA increased.

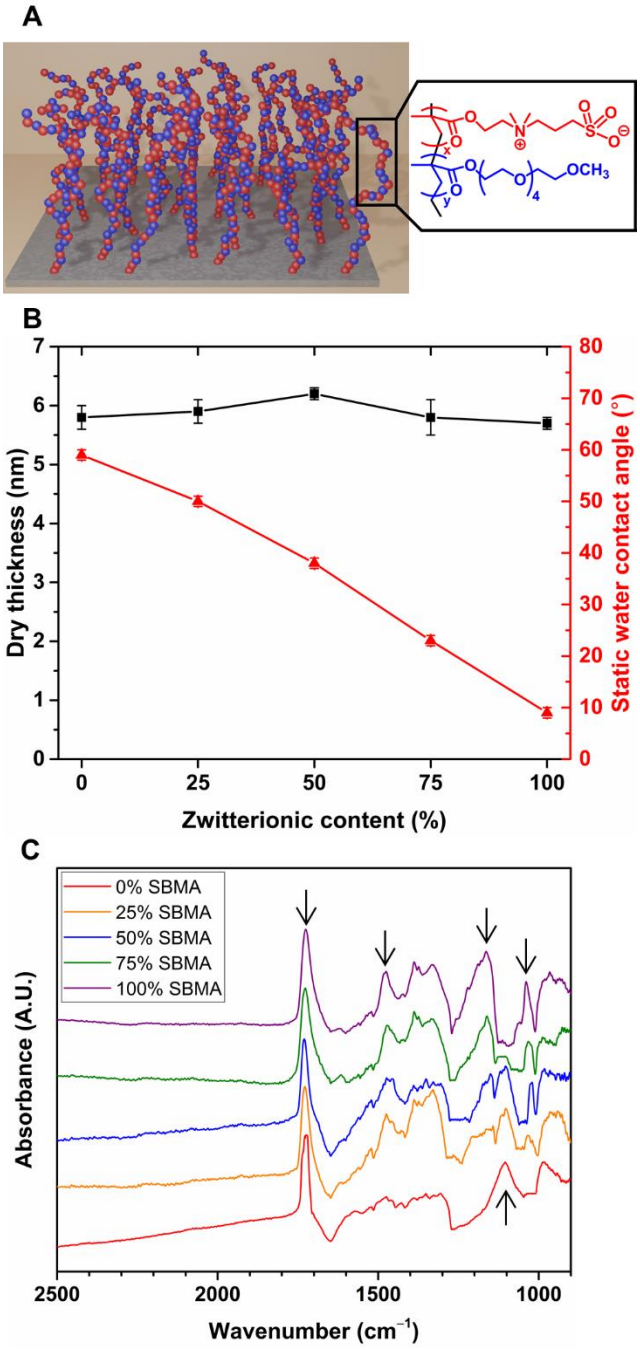


**Figure 6. 2.** A) Chemical composition and architecture of random p($SBMA_x$-co-$OEGMA_y$) polymer brushes grown from fused silica wafers. Briefly, fused silica surfaces were activated via $O_2$ plasma treatment, followed by the deposition of an ATRP initiator monolayer via a silane-coupling reaction. Finally, the polymerization took place in the presence of a ligand and a catalyst, for different feed ratios of the monomers SBMA and OEGMA. B) Dry thickness of synthesized polymer brushes (black squares), as measured with ellipsometry. Static water contact angle of synthesized polymer brushes (red triangles), as measured via sessile drop technique. C) Fingerprint region of ATR-FTIR spectra for p($SBMA_x$-co-$OEGMA_y$) brushes. Characteristic adsorption bands

are indicated with arrows: 1730 $cm^{-1}$ (C=O stretching), 1485 $cm^{-1}$ (C−N stretching), 1193 $cm^{-1}$ ($SO_3^-$ asymmetric stretching), 1041 $cm^{-1}$ ($SO_3^-$ symmetric stretching), and 1063−1103 $cm^{-1}$ (C−O stretching).

### 6.4.2 Single-Molecule FRET Analysis of FN Conformation

Investigation into the effect of surface chemical heterogeneity on interfacial protein conformation was carried out using FN type III domains 8-10 labeled with a donor and an acceptor FRET-pair in a site-specific manner ($FN_{FRET}$), as described in previous work[26]. FN was chosen because it plays a key role in the early stages of the foreign body response[27,28]. Specifically, the RGD loop located in domain 10 and the synergy (PHSRN) site located in domain 9 are responsible for cell recruitment and integrin binding[29–31]. The impact of polymer brush composition on $FN_{FRET}$ stability was determined by adding a very dilute solution of $FN_{FRET}$ in phosphate-buffered saline (PBS) into a flow-cell containing the brush-coated surfaces of interest. The polymer-liquid interface was illuminated via TIRF excitation with a 532 nm laser, which allowed for the excitation of protein molecules that freely interacted with the polymer brushes. Excited molecules were monitored via wide-field imaging using spectrally separated channels to capture donor and acceptor emission, which were spatially aligned on the brush surface. Heat maps of the intensities of the donor ($F_D$) and acceptor ($F_A$) fluorophores were created from the accumulated trajectories of $FN_{FRET}$ on each polymer brush surface (**Figure D.3**). The heat maps of all observations on each surface revealed the presence of two distinct populations: one with high $F_A$ and low $F_D$, representative of folded $FN_{FRET}$, and another with low $F_A$ and high $F_D$, representative of unfolded $FN_{FRET}$. In order to quantify the relative fraction of folded and unfolded populations, the fluorescence intensity pair values ($F_D$ and $F_A$) for each object at each trajectory were transformed into a relative distance parameter ($d$), calculated as: $d = \left(\frac{F_D}{F_A}\right)^{1/6}$. The probability density

distributions of *d* values for each surface is represented in **Figure 6.3**. The distributions exhibited again the presence of the two distinct populations: folded $FN_{FRET}$ (low *d* values) and unfolded $FN_{FRET}$ (high *d* values). From these distributions, the local minimum located between each population was used as a threshold to differentiate the folded and unfolded populations. The relative fraction of folded $FN_{FRET}$ was calculated for each surface as the area under the curve corresponding to the folded population divided by the total area (**Figure 6.4 A**). Interestingly, the steady-state conformation of interfacial FN followed a non-monotonic trend with respect to brush composition. Particularly, the surface containing p($SBMA_{75}$-co-$OEGMA_{25}$) exhibited the highest native-state retention (50%). Overall, copolymer brush surfaces led to higher protein stabilization compared to the homopolymer counterparts.

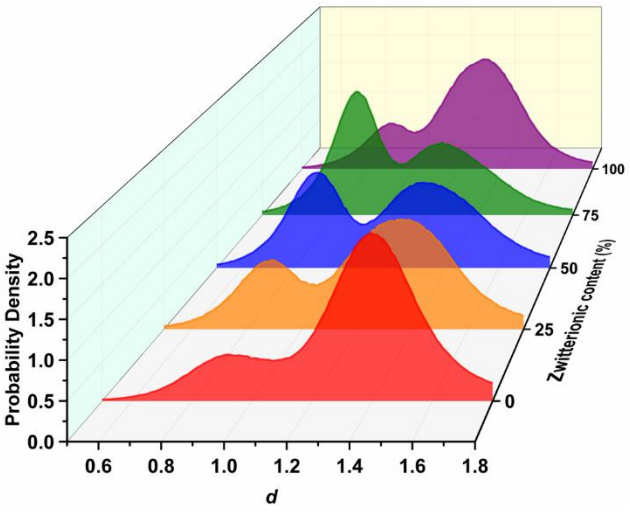


**Figure 6. 3.** Probability density distribution of *d* values for $FN_{FRET}$ on FS functionalized with p($SBMA_0$-co-$OEGMA_{100}$) (red), p($SBMA_{25}$-co-$OEGMA_{75}$) (orange), p($SBMA_{50}$-co-$OEGMA_{50}$) (blue), p($SBMA_{75}$-co-$OEGMA_{25}$) (green), and p($SBMA_0$-co-$OEGMA_{100}$) (purple). In the distribution, distinct populations representing the folded state and unfolded state of $FN_{FRET}$ were observed. The population representing the folded state was centered at $d$ = 0.9. For the unfolded state, the population was centered at $d$ = 1.4. A critical value of $d$ = 1.1, which corresponded to the minimum probability in *d* values between populations, was used to partition folded from unfolded molecules. The distribution was generated from ~$10^6$ molecular trajectories on each surface.

### 6.4.3 Impact of Chemical Heterogeneity on FN Dynamics

The steady-state analysis of $FN_{FRET}$ conformation from SM-FRET suggests that SBMA fraction had a marked impact on protein stability. To develop a more mechanistic view of the role of polymer brush composition on the stability of $FN_{FRET}$, the FRET trajectories were analyzed to determine the mean residence time constant of folded vs. unfolded molecules, as well as the mean dwell time constant of molecules than underwent conformational changes (e.g., apparent time constants of $FN_{FRET}$ unfolding and refolding). First, the mean residence time of folded and unfolded molecules was calculated for all molecules that resided on the surface for at least 4 frames (**Figure 6.4 B**). The mean residence time of folded molecules followed a non-monotonic trend with increasing content in SBMA, reaching a highest value at p($SBMA_{75}$-co-$OEGMA_{25}$) (0.50 ± 0.02 s). Conversely, the mean residence time of unfolded molecules followed the opposite non-monotonic trend, which reached the lowest value at p($SBMA_{75}$-co-$OEGMA_{25}$) (0.256 ± 0.009 s). Interestingly, the pure pOEGMA and pSBMA brushes had almost identical residence times, where unfolded molecules stayed on the brush the longest (~1 s) and folded molecules the shortest (~0.2 s) with respect to the mixed brushes. Similarly, the mean dwell time of protein molecules in a given conformation (i.e. folded or unfolded) before they underwent a conformational change were calculated to test whether brush chemical heterogeneity also affected the kinetics of folding and unfolding in a non-monotonic manner. **Figure 6.4 C** shows that the mean dwell times followed the same trend as the mean residence times: folded molecules lasted the longest on the p($SBMA_{75}$-co-$OEGMA_{25}$) brush before undergoing unfolding (2.1 ± 0.2 s), while unfolded molecules lasted the shortest before folding (6.1 ± 0.2s). Remarkably, p($SBMA_{75}$-co-$OEGMA_{25}$) increased the

retention time of $FN_{FRET}$ molecules in a folded state for an order of magnitude with respect to pure pSBMA or pOEGMA.

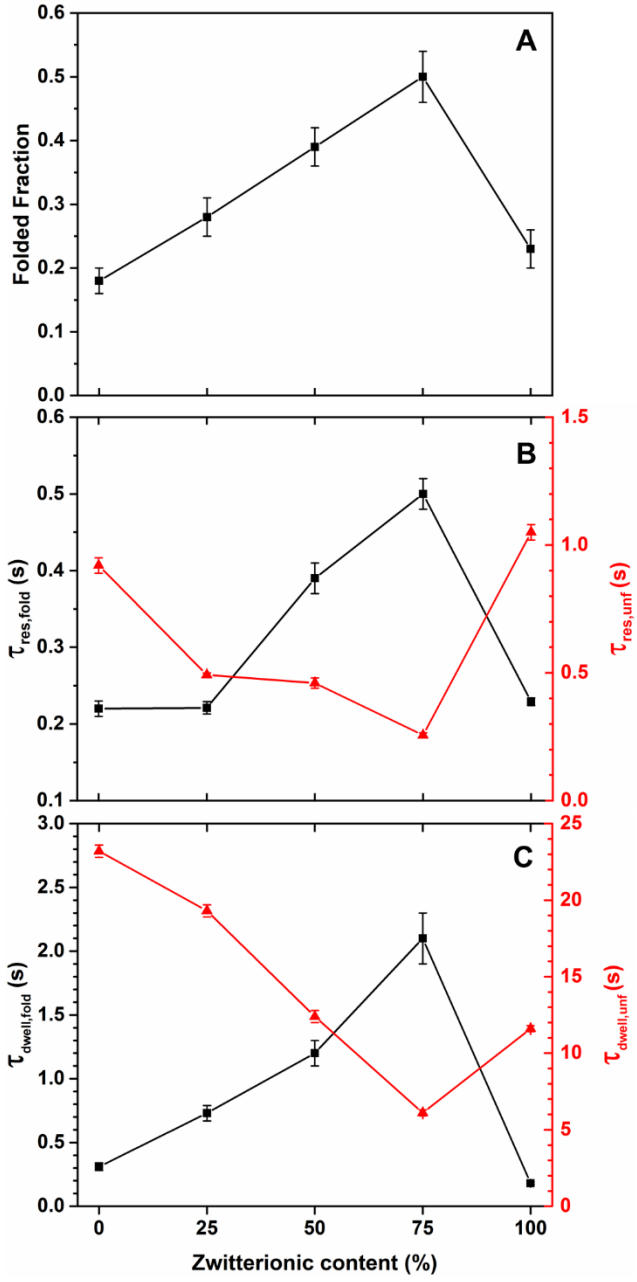


**Figure 6. 4.** A) Steady state fraction of observations in which $FN_{FRET}$ was folded for the 5 different polymer brush compositions. B) Mean residence time of $FN_{FRET}$ trajectories in which the protein was folded (black triangles) or unfolded (red squares) throughout the entire trajectory. C) Mean dwell time of $FN_{FRET}$ in a specific conformation (folded in black squares and unfolded in red triangles) before undergoing a conformational change within the same trajectory on the surface.

### 6.4.4 Identification and Characterization of Surface 'Hydrophobic Spots'

A possible hypothesis for the observation of a non-monotonic trend in the stability and dynamics of $FN_{FRET}$ as a function of polymer brush composition is the fact that varying ratios of OEGMA and SBMA within the brush alter the local hydrophobicity of the brushes and thus the potential to retain or unfold $FN_{FRET}$ molecules. In order to test this hypothesis, the environmentally sensitive probe NBD-X was used to map the surface local hydrophobicity. NBD-X is highly quenched in polar environments, but highly fluorescent in hydrophobic environments. Thus, observed fluorescence events on the surface are a direct marker of local regions with hydrophobic character. By accumulating a large number of NBD-X trajectories on the surface, a density map based on the number of adsorption events per site (i.e., area) can be created using the motion blur point accumulation for imaging in nanoscale topography (mbPAINT) method[32–34]. **Figure D.6** shows the super-resolution adsorption maps created from accumulated NBD-X trajectories on the different polymer brush surfaces. As seen in **Figure D.6**, the regions on the surface with anomalously high adsorption events decreased in frequency with increasing amounts of SBMA in the brushes for the same number of randomly selected trajectories (~80000). To quantify this observation, strong adsorption sites (i.e., hotspots) were defined as regions upon which more than seven NBD-X molecules adsorbed over the course of the experiments. Given the low surface coverage, the probability of observing more than one adsorption event in the same 100 nm region of the surface was extremely low if adsorption was random, indicating the strong hydrophobic character of the defined hotspot. Using this definition, we found that the fraction of trajectories that corresponded to adsorption events on hotspots over the total number of trajectories

monotonically decreased with increasing content of SBMA, going from 0.017 for pure pOEGMA to 0.005 for pure pSBMA (**Figure 6.5 A**).

The rate at which NBD-X molecules appeared (i.e., emitted fluorescence) on the surface is a direct measurement of the 'activation' or 'turn-on' rate of the fluorescent dye as a function of the local environment. Specifically, one would expect a faster 'turn-on' rate on a surface with predominantly hydrophobic character, since the probability of finding a low dielectric environment that 'activates' the dye is higher. **Figure 6.5 B** displays the mean 'turn-on' rate constants ($k_{on}$) for the different brush compositions, calculated as the number of total adsorption events observed per unit time, area (i.e., field of view), and normalized by the bulk concentration of NBD-X. It was found that $k_{on}$ monotonically decreased with increasing content in SBMA, in agreement with the decrease in the density of hydrophobic regions or hotspots on the brush surfaces. Similarly, the mean 'turn-off' or 'deactivation' rate constant ($k_{off}$) of NBX-X molecules was also calculated for the different polymer brush compositions. Specifically, $k_{off}$ was calculated as the inverse of the mean association lifetime of the dye with a hydrophobic region in the brush surface. Again, a monotonic trend was observed as a function of brush composition; $k_{off}$ increased with increasing content in SBMA within the brushes, which further indicates that adding SBMA to the brushes systematically reduced the hydrophobic character of the surfaces.

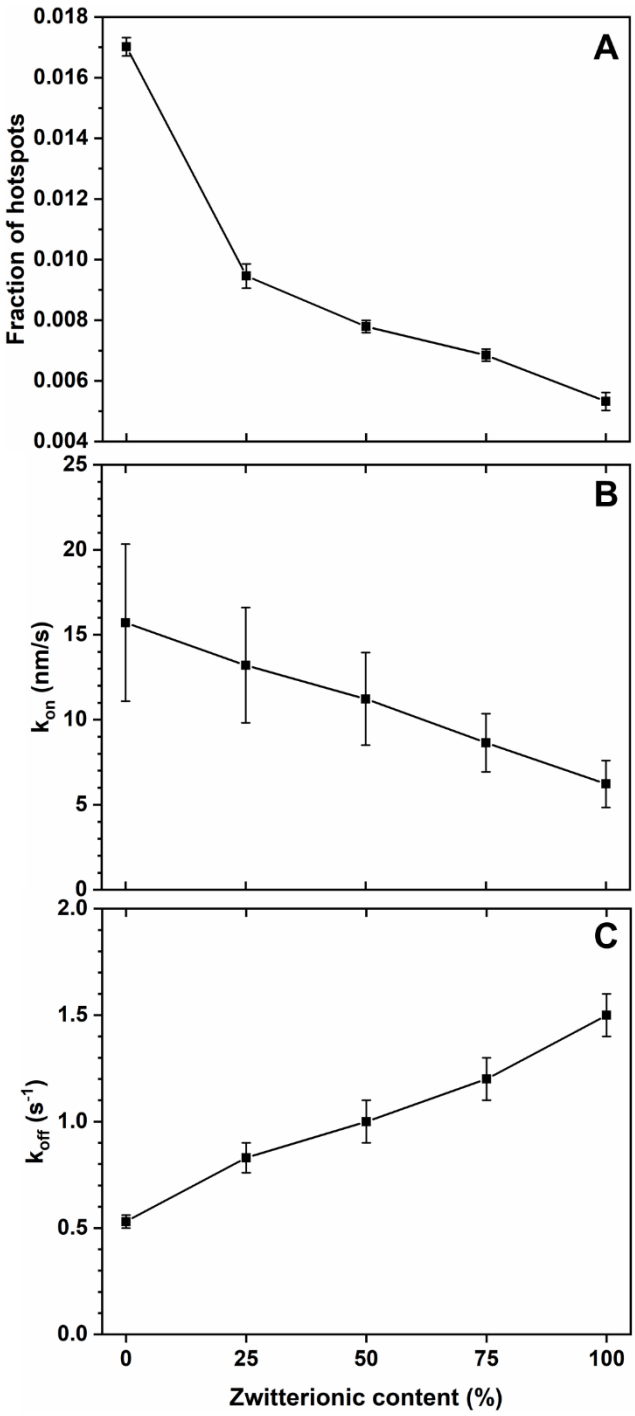


**Figure 6. 5.** Quantitative analyses from mbPAINT maps using NBD-X as a probe molecule. (A) Fraction of NBD-X trajectories that corresponded to hotspots (i.e., anomalously strong adsorption sites) with respect to the total number of trajectories for the different polymer brush compositions. (B) Mean 'turn-on' rate constant of NBD-X on the different brush surfaces. (C) Mean 'turn-off' rate constant of NBD-X on the different brush surfaces.

## 6.5 Discussion

Mixed OEGMA-SBMA brushes led to a higher fraction of steady state folded $FN_{FRET}$ adsorbed on the surface with respect to the homopolymer analogues. Such observation was a direct result of the dynamics of $FN_{FRET}$ on mixed brushes, where on average: unfolded molecules desorbed faster from the surface, folded molecules resided longer, unfolded molecules transitioned into a folded state faster, and folded molecules unfolded more slowly. Altogether, these results show that the dynamic, chemically heterogeneous nature of mixed brushes provided an environment that helped preserve the native conformation of $FN_{FRET}$ upon surface contact. In other words, such environment mitigated unfavorable interactions that would potentially lead to interfacial protein unfolding.

Interestingly, the surface with composition p($SBMA_{75}$-co-$OEGMA_{25}$) exhibited the highest stabilizing effect on $FN_{FRET}$. Given the surface heterogeneity of proteins, it is reasonable to assume that certain degree of chemical heterogeneity is necessary to allow for like-interactions between the protein and the polymer brush. Such interactions can presumably be matched without perturbing the protein structure via the dynamic motion and conformational flexibility of the brush system. Surfaces with, for example, sole hydrophilic or hydrophobic properties might be insufficient to preserve proteins' native conformation due to the intrinsic amphiphilic nature of protein molecules. This hypothesis inspired the development of "ambiguous" surfaces, in which the alternation of hydrophilic and hydrophobic groups within the polymer brush thermodynamically weakened protein-polymer interactions[12,35–37]. The end-goal would be to create a chaperone-like polymeric shell outside of a protein that can effectively improve protein stability by providing a barrier to resist protein conformational change upon surface contact. To form such a nanoscopic polymeric shell, protein-polymer interactions need to be strong enough to

favor association yet soft enough not to outcompete the forces governing protein folding. When a homopolymer is conjugated to a protein surface, monomer–amino acid interactions can affect protein folding, while amphiphilic heteropolymers can provide multiple weak binding sites that overall stabilize the diverse and complex 3D structure of proteins. Gudipati et al prepared hyperbranched fluoropolymer-PEG composite coatings and found that the amphiphilic surfaces showed an enhancing inhibition ability to protein adsorption and marine organism settling[38]. Similarly, Ishihara et al showed that amphiphilic copolymer systems containing both a hydrophilic unit (MPC) and a hydrophobic unit (BMA) that mimicked a phospholipid led to low protein adsorption and almost complete retention of protein conformation upon adsorption[39]. In a recent study, Panganiban et al designed a four-monomer random heteropolymer to mimic intrinsically disordered proteins for protein solubilization and stabilization in non-native environments[37]. This was achieved by controlling the statistical distribution of monomers with different properties (mainly hydrophobicity and electrostatics) in the heteropolymer.

We propose that the chemical groups within the brush may specifically interact with surface exposed patches (e.g., of hydrophobic or hydrophilic residues) on the protein to create favorable nano-environments that stabilize the protein in the folded state. Since such well-defined patches are more likely to be present on the surface of the three-dimensional structure of the folded protein compared to in the diverse ensemble of unfolded protein structures, it is plausible that such interactions would stabilize the folded state relative to the unfolded state. As one example, PEG, which is functionally amphiphilic, may segregate around patches of hydrophobic residues on FN while pSB, which is zwitterionic, may segregate around hydrophilic and/or charged patches. Through such structural rearrangement of the brush layer, which relies on the mobility of the

polymer chains, unfavorable interactions between chemical groups with dissimilar properties, which can lead to destabilization of the protein, can be avoided.

There is evidence in the literature of the interactions between protein surfaces and both PEG-based polymers as well as zwitterionic polymers. For instance, it has been reported that hydrophobic regions of PEG can bind hydrophobic regions of protein surfaces and even act like a chaperone to protect against protein aggregation[40–43.] However, because of the nature of such interactions, PEG has been shown to have a destabilizing effect on proteins and induce unfolding [444546]. Even though more recent, the effect of zwitterionic polymers on protein stability has also drawn significant attention. However, a mechanistic understanding and agreement on the outcome of zwitterion-protein interactions is still lacking. Given that poly(zwitterions) form inter- and intra-molecular interactions, it is plausible that they can also interact with charged patches of surface-exposed residues of proteins via electrostatic interactions. Furthermore, since proteins are ampholytes and zwitterionic at their isoelectric point, poly(zwitterionic) polymers might preferentially associate with protein surfaces over other polymer chains. Particularly, a diverse spacing between available unpaired or partially paired monomer charges on pSB likely exists that can interact with the proteins, as charge spacing on the proteins can be upward of 4 nm. Kisley et al showed that the interactions between soluble pSB and proteins led to a decrease in protein folding stability, highlighting the important role of polymer-protein associations[47]. Specifically, the authors found that pSB decreased protein thermal stability and increased protein folding cooperativity. Remarkably, among the three different protein studied in their work, the one that interacted least with pSB had the smallest and fewest oppositely charged surface patches. The authors also underscored that pSB flexibility enabled it to conformationally adapt and bind to charge distributions on the proteins, somewhat analogous to polymer adsorption driven by

statistical pattern matching. The authors explained the destabilizing effect of soluble pSB as favorable interactions between the polymer and proteins through enthalpic electrostatic attraction and the entropic release of water molecules and counterions. As the protein unfolded, the polymer can then interact with new residues, leading to the destabilization of the protein and increased cooperativity in protein folding.

We have shown in this work that the addition of pSBMA to pOEGMA brushes disrupted the presence of hydrophobic niches within the brush, increasing the overall hydrophilicity of the surface, as expected, and reducing the probability of $FN_{FRET}$ to encounter 'hotspots' where it can strongly bind and unfold. However, based on our findings, hydrophilicity cannot explain the entirety of $FN_{FRET}$-brush interactions. We hypothesize that, given the destabilizing effect that local charges (e.g., pSB side-chains) can have on charged patches present on the surface of $FN_{FRET}$, a stabilizing balance of forces and interactions is met at the composition p($SBMA_{75}$-co-$OEGMA_{25}$). Consequently, we hypothesize that the specific effect of pSB-to-pOEGMA ratio on protein folding stability is presumably protein-dependent due to differences in protein salt-sensitivity, surface charge, and structure.

## 6.6 Conclusions

In summary, we have shown that introducing chemical heterogeneity within polymer brushes can stabilize freely adsorbing FN molecules. Specifically, our findings suggest that mixed polymer brushes may stabilize adsorbed FN by increasing the rate of refolding relative to unfolding of enzyme molecules on the brush surface, as well as by retaining folded molecules on the surface longer relative to unfolded molecules. The extent of stabilization was strongly dependent on the fraction of SBMA in the polymer brush, which differentially mediated the interaction between the

brush and folded and unfolded FN. Importantly, these observations were enabled via exploiting SM methods that enable protein interfacial structure and dynamics as well as surface nanoscale heterogeneity to be directly measured and correlated. Ultimately, these findings have important practical implications in the design of novel biomaterial surfaces and coatings that enhance the stabilization (and presumably activity) of proteins that come into contact for use in biotechnological applications. Of further interest is exploring the extent to which this enhancement in stability and activity is general to other proteins that have varying surface properties and native environments within cells. Related to this, it is interesting to consider how the optimum mixture of lipids correlates with protein properties.

## 6.7 References


(1) Ratner, B. D.; Hoffman, A. S.; Schoen, F. J.; Lemons, J. E. *Biomaterials Science: An Introduction to Materials: Third Edition* **2013**.
(2) Shen, M.; Martinson, L.; Wagner, M. S.; Castner, D. G.; Ratner, B. D.; Horbett, T. A. *J. Biomater. Sci. Polym. Ed.* **2002**, *13*, 367–390.
(3) Iwasaki, Y.; Ishihara, K. *Analytical and Bioanalytical Chemistry* **2005**, 534–546.
(4) Morais, J. M.; Papadimitrakopoulos, F.; Burgess, D. J. *AAPS J.* **2010**, *12*, 188–196.
(5) Faulón Marruecos, D.; Kastantin, M.; Schwartz, D. K.; Kaar, J. L. *Biomacromolecules* **2016**, *17*, 1017–1025.
(6) Swartzlander, M. D.; Barnes, C. A.; Blakney, A. K.; Kaar, J. L.; Kyriakides, T. R.; Bryant, S. J. *Biomaterials* **2015**, *41*, 26–36.
(7) Wang, X.; Schmidt, D. R.; Joyce, E. J.; Kao, W. J. *J. Biomater. Sci. Polym. Ed.* **2011**, *22*, 1343–1362.
(8) McLoughlin, S. Y.; Kastantin, M.; Schwartz, D. K.; Kaar, J. L. *Proc. Natl. Acad. Sci.* **2013**, *110*, 19396–19401.
(9) Lynn, A. D.; Blakney, A. K.; Kyriakides, T. R.; Bryant, S. J. *J. Biomed. Mater. Res. - Part A* **2011**, *96*, 621–631.
(10) Lynn, A. D.; Kyriakides, T. R.; Bryant, S. J. *J. Biomed. Mater. Res. - Part A* **2010**, *93*, 941–953.
(11) Panganiban, B.; Qiao, B.; Jiang, T.; Delre, C.; Obadia, M. M.; Nguyen, T. D.; Smith, A. A. A.; Hall, A.; Sit, I.; Crosby, M. G.; et al. *Science* **2018**, *1243*, 1239–1243.
(12) Ye, Q.; Zhao, W.; Yang, W.; Pei, X.; Zhou, F. *Macromol. Chem. Phys.* **2017**, *218*.
(13) Chaparro Sosa, A. F.; Kienle, D. F.; Falatach, R. M.; Flanagan, J.; Kaar, J. L.; Schwartz, D. K. *ACS Appl. Mater. Interfaces* **2018**, *10*, 19504–19513.
(14) Kastantin, M.; Langdon, B. B.; Schwartz, D. K. *Adv. Colloid Interface Sci.* **2014**, *207*, 240–252.
(15) Anders, H.-J.; Schaefer, L. *J. Am. Soc. Nephrol.* **2014**, *25*, 1387–1400.
(16) Langdon, B. B.; Kastantin, M.; Schwartz, D. K. *Biomacromolecules* **2015**, *16*, 3201–3208.
(17) Kastantin, M.; Faulón Marruecos, D.; Grover, N.; Yu McLoughlin, S.; Schwartz, D. K.; Kaar, J. L. *J. Am. Chem. Soc.* **2017**, *139*, 9937–948.
(18) Hammill, J. T.; Miyake-Stoner, S.; Hazen, J. L.; Jackson, J. C.; Mehl, R. A. *Nat. Protoc.* **2007**, *2*, 2601–2607.
(19) Peeler, J. C.; Mehl, R. A. *Methods Mol. Biol.* **2012**, *794*, 125–134.
(20) Kastantin, M.; Keller, T. F.; Jandt, K. D.; Schwartz, D. K. *Adv. Funct. Mater.* **2012**, *22*, 2617–2623.
(21) Walder, R.; Kastantin, M.; Schwartz, D. K. *Analyst*. **2012**, *137*, 2987–2996.
(22) Kastantin, M.; Schwartz, D. K. *ChemPhysChem* **2013**, *14*, 374–380.
(23) Kastantin, M.; Schwartz, D. K. *Small* **2012**, 9, 933–94.
(24) Guo, S.; Jańczewski, D.; Zhu, X.; Quintana, R.; He, T.; Neoh, K. G. *J. Colloid Interface Sci.* **2015**, *452*, 43–53.
(25) Zhang, Z.; Chao, T.; Chen, S.; Jiang, S. *Langmuir* **2006**, *22*, 10072–10077.
(26) Faulón Marruecos, D.; Kastantin, M.; Schwartz, D. K.; Kaar, J. L. *Biomacromolecules* **2016**, *17*, 1017–1025.
(27) Anderson, J. M.; Rodriguez, A.; Chang, D. T. *Seminars in Immunology* **2008**, 86–100.
(28) Kadler, K. E.; Hill, A.; Canty-Laird, E. G. *Current Opinion in Cell Biology* **2008**, 495–501.

(29) Takagi, J.; Strokovich, K.; Springer, T. A.; Walz, T. *EMBO J.* **2003**, *22*, 4607–4615.
(30) Kolvunen, E.; Wang, B.; Ruoslahti, E. *Bio/Technology* **1995**, *13*, 265–270.
(31) Leahy, D. J.; Aukhil, I.; Erickson, H. P. *Cell* **1996**, *84*, 155–164.
(32) Chen, J.; Bremauntz, A.; Kisley, L.; Shuang, B.; Landes, C. F. *ACS Appl. Mater. Interfaces* **2013**, *5*, 9338–9343.
(33) Mabry, J. N.; Skaug, M. J.; Schwartz, D. K. *Anal. Chem.* **2014**, *86*, 9451–9458.
(34) Kisley, L.; Chen, J.; Mansur, A. P.; Dominguez-Medina, S.; Kulla, E.; Kang, M. K.; Shuang, B.; Kourentzi, K.; Poongavanam, M. V.; Dhamane, S.; et al. *J. Chromatogr. A* **2014**, *111*, 2075–2080.
(35) Bauer, S.; Arpa-Sancet, M. P.; Finlay, J. A.; Callow, M. E.; Callow, J. A.; Rosenhahn, A. *Langmuir* **2013**, *29*, 4039–4047.
(36) Baxamusa, S. H.; Gleason, K. K. *Adv. Funct. Mater.* **2009**, *19*, 3489–3496.
(37) Panganiban, B.; Qiao, B.; Jiang, T.; DelRe, C.; Obadia, M. M.; Nguyen, T. D.; Smith, A. A. A.; Hall, A.; Sit, I.; Crosby, M. G.; et al. *Science* **2018**, *359*, 1239–1243.
(38) Gudipati, C. S.; Finlay, J. A.; Callow, J. A.; Callow, M. E.; Wooley, K. L. *Langmuir* **2005**, *21*, 3044–3053.
(39) Iwasaki, Y.; Ishihara, K. *Analytical and Bioanalytical Chemistry* **2005**, *381*, 534–546.
(40) Sheth, S. R.; Leckband, D. *Proc. Natl. Acad. Sci. U. S. A.* **1997**, *94*, 8399–8404.
(41) Cleland, J. L.; Builder, S. E.; Swartz, J. R.; Winkler, M.; Chang, J. Y.; Wang, D. I. C. *Nature Biotechnology* **1992**, *10*, 1013–1019.
(42) Chao, S. H.; Schäfer, J.; Gruebele, M. *Biochemistry* **2017**, *56*, 5671–5678.
(43) Leckband, D.; Sheth, S.; Halperin, A. *J. Biomater. Sci. Polym. Ed.* **1999**, *10*, 1125–1147.
(44) Lee, L. L. Y.; Lee, J. C. *Biochemistry* **1987**, *26*, 7813–7819.
(45) Farruggia, B.; García, G.; D'Angelo, C.; Picó, G. *Int. J. Biol. Macromol.* **1997**, *20*, 43–51.
(46) Kumar, V.; Sharma, V. K.; Kalonia, D. S. *Int. J. Pharm.* **2009**, *366*, 38–43.
(47) Kisley, L.; Serrano, K. A.; Davis, C. M.; Guin, D.; Murphy, E. A.; Gruebele, M.; Leckband, D. E. *Biomacromolecules* **2018**, *19*, 3894–3901.

# BIBLIOGRAPHY


Abbott, N. L.; Blankschtein, D.; Hatton, T. A. *Macromolecules* **1992**.

Abramyan, T. M.; Hyde-Volpe, D. L.; Stuart, S. J.; Latour, R. A. *Biointerphases* **2017**.

Adair, B. D.; Xiong, J. P.; Maddock, C.; Goodman, S. L.; Arnaout, M. A.; Yeager, M. *J. Cell Biol.* **2005**.

Aghili, Z.; Taheri, S.; Zeinabad, H. A.; Pishkar, L.; Saboury, A. A.; Rahimi, A.; Falahati, M. *PLoS One* **2016**.

Akhterov, M. V.; Choi, Y.; Olsen, T. J.; Sims, P. C.; Iftikhar, M.; Gul, O. T.; Corso, B. L.; Weiss, G. A.; Collins, P. G. *ACS Chem. Biol.* **2015**.

Akiyama, S. K.; Nagata, K.; Yamada, K. M. *Reviews on Biomembranes* **1990**.

Alexander, S. *J. Phys.* **1977**.

Altroff, H.; Choulier, L.; Mardon, H. J. *J Biol Chem* **2003**.

Altroff, H.; van der Walle, C. F.; Asselin, J.; Fairless, R.; Campbell, I. D.; Mardon, H. J. *J Biol Chem* **2001**.

Anders, H.-J.; Schaefer, L. *J. Am. Soc. Nephrol.* **2014**.

Anderson, J. M.; Rodriguez, A.; Chang, D. T. *Semin. Immunol.* **2008**.

Anderson, J. M.; Rodriguez, A.; Chang, D. T. *Seminars in Immunology* **2008**.

Andorko, J. I.; Jewell, C. M. *Bioeng. Transl. Med.* **2017**.

Aota, S.; Nomizu, M.; Yamada, K. M. *J Biol Chem* **1994**.

Arcot, L.; Ogaki, R.; Zhang, S.; Meyer, R. L.; Kingshott, P. *Appl Surf Sci* **2015**.

Azzaroni, O. *J. Polym. Sci., Part A: Polym. Chem.* **2012**.

Babensee, J. E.; Anderson, J. M.; McIntire, L. V.; Mikos, A. G. *Ad. Drug Deliv. Rev.* **1998**.

Bachman, H.; Nicosia, J.; Dysart, M.; Barker, T. H. *Adv. Wound Care* **2015**.

Banerjee, I.; Pangule, R. C.; Kane, R. S. *Adv Mater* **2011**.

Baneyx, G.; Baugh, L.; Vogel, V. *Proc. Natl. Acad. Sci.* **2001**.

Baneyx, G.; Baugh, L.; Vogel, V. *Proc. Natl. Acad. Sci.* **2002**.

Barinov, N. A.; Prokhorov, V. V.; Dubrovin, E. V.; Klinov, D. V. *Colloids Surfaces B Biointerfaces* **2016**.

Baron, M.; Norman, D.; Willis, A.; Campbell, I. D. *Nature* **1990**.

Battiston, K. G.; Labow, R. S.; Santerre, J. P. *Biomaterials* **2012**.

Bauer, S.; Arpa-Sancet, M. P.; Finlay, J. A.; Callow, M. E.; Callow, J. A.; Rosenhahn, A. *Langmuir* **2013**.

Baxamusa, S. H.; Gleason, K. K. *Adv. Funct. Mater.* **2009**.

Bell, G. I. *Science* **1978**.

Berglin, M.; Pinori, E.; Sellborn, A.; Andersson, M.; Hulander, M.; Elwing, H. Fibrinogen *Langmuir* **2009**.

Blakney, A. K.; Swartzlander, M. D.; Bryant, S. J. *J. Biomed. Mater. Res. Part A* **2012**.

Bongiovanni, M. N.; Godet, J.; Horrocks, M. H.; Tosatto, L.; Carr, A. R.; Wirthensohn, D. C.; Ranasinghe, R. T.; Lee, J. E.; Ponjavic, A.; Fritz, J. V.; Dobson, C. M.; Klenerman, D.; Lee, S. F. *Nat. Commun.* **2016**.

Bork, P.; Blomberg, N.; Nilges, M. *Nat Genet* **1996**.

Brown, A. C.; Rowe, J. A.; Barker, T. H. *Tissue Eng. Part A* **2011**.

Calderwood, D. A. *J. Cell Sci.* **2004**.

Campbell, I. D.; Downing, A. K. *Nat Struct Biol* **1998**.

Capomaccio, R.; Osório, I.; Ojea-Jiménez, I.; Ceccone, G.; Colpo, P.; Gilliland, D.; Hussain, R.; Siligardi, G.; Rossi, F.; Ricard-Blum, S.; Calzolai, L. *Biointerphases* **2016**.

Carr, P. A.; Erickson, H. P.; Palmer, A. G. *Structure* **1997**.

Carraher, C. L.; Schwarzbauer, J. E. *J. Biol. Chem.* **2013**.

Chan, C. E.; Odde, D. J. *Science* **2008**.

Chao, S. H.; Schäfer, J.; Gruebele, M. *Biochemistry* **2017**.

Chaparro Sosa, A. F.; Kienle, D. F.; Falatach, R. M.; Flanagan, J.; Kaar, J. L.; Schwartz, D. K. *ACS Appl. Mater. Interfaces* **2018**.

Chatterjee, T.; Chatterjee, B. K.; Saha, T.; Hoque, K. M.; Chakrabarti, P. *Biochim. Biophys. Acta.* **2017**.

Chaudhuri, O.; Gu, L.; Klumpers, D.; Darnell, M.; Bencherif, S. A.; Weaver, J. C.; Huebsch, N.; Lee, H. P.; Lippens, E.; Duda, G. N.; Mooney, D. J. *Nat. Mater.* **2016**.

Chen, J.; Bremauntz, A.; Kisley, L.; Shuang, B.; Landes, C. F. *ACS Appl. Mater. Interfaces* **2013**.

Chen, M.; Zeng, G.; Xu, P.; Yan, M.; Xiong, W.; Zhou, S. *Environ. Sci. Nano.* **2017**.

Chen, S. F.; Li, L. Y.; Zhao, C.; Zheng, J. *Polymer* **2010**.

Chen, W. L.; Cordero, R.; Tran, H.; Ober, C. K. *Macromolecules* **2017**.

Chung, L.; Maestas, D. R.; Housseau, F.; Elisseeff, J. H. *Adv. Drug Deliv. Rev.* **2017**.

Cleland, J. L.; Builder, S. E.; Swartz, J. R.; Winkler, M.; Chang, J. Y.; Wang, D. I. C. *Bio-Technol* **1992**.

Copie, V.; Tomita, Y.; Akiyama, S. K.; Aota, S.; Yamada, K. M.; Venable, R. M.; Pastor, R. W.; Krueger, S.; Torchia, D. A. *J. Mol. Biol.* **1998**.

Craig, D.; Krammer, A; Schulten, K.; Vogel, V. *Proc. Natl. Acad. Sci.* **2001**.

de Gennes, P. G. *Advances in Colloid and Interface Science* **1987**.

Deng, J.; Ren, T.; Zhu, J.; Mao, Z.; Gao, C. *Regen. Biomater.* **2014**.

Devanand, K.; Selser, J. C. *Macromolecules* **1991**.

Discher, D. E.; Janmey, P.; Wang, Y. L. *Science* **2005**.

Dominguez-Medina, S.; Kisley, L.; Tauzin, L. J.; Hoggard, A.; Shuang, B.; Indrasekara, A. S. D. S.; Chen, S.; Wang, L. Y.; Derry, P. J.; Liopo, A.; Zubarev, E. R.; Landes, C. F.; Link, S. *ACS Nano* **2016**.

Doyle, A. D.; Carvajal, N.; Jin, A.; Matsumoto, K.; Yamada, K. M. *Nat. Commun.* **2015**.

Dufour, S.; Duband, J. L.; Humphries, M. J.; Obara, M.; Yamada, K. M.; Thiery, J. P. Attachment, *EMBO J.* **1988**.

Elosegui-Artola, A.; Bazellieres, E.; Allen, M. D.; Andreu, I.; Oria, R.; Sunyer, R.; Gomm, J. J.; Marshall, J. F.; Jones, J. L.; Trepat, X.; Roca-Cusachs, P. *Nat. Mater.* **2014**.

Emilsson, G.; Schoch, R. L.; Feuz, L.; Hook, F.; Lim, R. Y. H.; Dahlin, A. B. *Acs Appl Mater Inter* **2015**.

Engler, A. J.; Sen, S.; Sweeney, H. L.; Discher, D. E. *Cell* **2006**.

Erickson, H. P.; Carrell, N. A. *J. Biol. Chem.* **1983**.

Fang, F.; Satulovsky, J.; Szleifer, I. *Biophys J* **2005**.

Fang, X.; Yang, T.; Wang, L.; Yu, J.; Wei, X.; Zhou, Y.; Wang, C.; Liang, W. *Biomaterials*. **2016**.

Farruggia, B.; García, G.; D'Angelo, C.; Picó, G. *Int. J. Biol. Macromol.* **1997**.

Faulon Marruecos, D.; Kastantin, M.; Schwartz, D. K.; Kaar, J. L. *Biomacromolecules* **2016**.

Faulón Marruecos, D.; Kienle, D. F.; Kaar, J. L.; Schwartz, D. K.; *ACS Macro Lett.* **2018**.

Feryforgues, S.; Fayet, J. P.; Lopez, A. *J. Photochem. Photobiol., A* **1993**.

Findlay, H. E.; Booth, P. J. *Sci. Rep.* **2017**.

Flick, M. J.; Du, X.; Degen, J. L. *Experimental Biology and Medicine*; **2004**.

Frantz, C.; Stewart, K. M.; Weaver, V. M. *J. Cell. Sci.* **2010**.

Franz, S.; Rammelt, S.; Scharnweber, D.; Simon, J. C. *Biomaterials* **2011**.

Fromell, K.; Yang, Y.; Ekdahl, K. N.; Nilsson, B.; Berglin, M.; Elwing, H.; Fromell, K. *Biointerphases* **2017**.

Gao, M.; Craig, D.; Lequin, O.; Campbell, I. D.; Vogel, V.; Schulten, K. *Proc. Natl. Acad. Sci.* **2003**.

Garcia, A. J.; Vega, M. D.; Boettiger, D. *Mol. Biol. Cell* **1999**.

Ghosh, G.; Gaikwad, P. S.; Panicker, L.; Nath, B. B.; Mukhopadhyaya, R. *Colloids Surfaces B Biointerfaces* **2016**.

Godawat, R.; Jamadagni, S. N.; Garde, S. *Proc. Natl. Acad. Sci. U.S.A.* **2009**.

Grant, R. P.; Spitzfaden, C.; Altroff, H.; Campbell, I. D.; Mardon, H. J. *J. Biol. Chem.* **1997**.

Green, R. J.; Davies, J.; Davies, M. C.; Roberts, C. J.; Tendler, S. J. B. *Biomaterials* **1997**.

Grinnell, F.; Feld, M. K. *J. Biol. Chem.* **1982**.

Gruian, C. M.; Rickert, C.; Nicklisch, S. C. T.; Vanea, E.; Steinhoff, H. J.; Simon, S. *ChemPhysChem.* **2017**.

Gudipati, C. S.; Finlay, J. A.; Callow, J. A.; Callow, M. E.; Wooley, K. L. *Langmuir* **2005**.

Guo, S.; Jańczewski, D.; Zhu, X.; Quintana, R.; He, T.; Neoh, K. G. *J. Colloid Interface Sci.* **2015**.

Halperin, A. *Langmuir* **1999**.

Hammill, J. T.; Miyake-Stoner, S.; Hazen, J. L.; Jackson, J. C.; Mehl, R. A. *Nat Protoc* **2007**.

Henzler-Wildman, K.; Kern, D. *Nature* **2007**.

Hohng, S.; Joo, C.; Ha, T. *Biophys. J.* **2004**.

Hook, F.; Brzezinski, P.; Rodahl, M.; Kasemo, B. **1997**.

Hook, F.F.; Vörös, J.; Rodahl, M.; Kurrat, R.; Böni, P.; Ramsden, J. J.; Textor, M.; Spencer, N. D.; Tengvall, P.; Gold, J.; et al. *Colloids Surfaces B Biointerfaces* **2002**.

Huebsch, N.; Arany, P. R.; Mao, A. S.; Shvartsman, D.; Ali, O. A.; Bencherif, S. A.; Rivera-Feliciano, J.; Mooney, D. J. *Nat. Mater.* **2010**.

Humphrey, J. D.; Dufresne, E. R.; Schwartz, M. A. *Nat. Rev. Mol. Cell Biol.* **2014**.

Humphries, J. D.; Byron, A.; Humphries, M. J. *J. Cell Sci.* **2006**.

Israelachvili, J. N. *Intermolecular and Surface Forces, 3rd Edition* **2011**.

Israelachvili, J. N. *Intermolecular and surface forces, 3rd Edition* **2011**.

Iwasaki, Y.; Ishihara, K. *Analytical and Bioanalytical Chemistry* **2005**.

Jeon, S. I.; Andrade, J. D. *J Colloid Interf Sci* **1991**.

Jeon, S. I.; Lee, J. H.; Andrade, J. D.; Degennes, P. G. *J Colloid Interf Sci* **1991**.

Jin, J.; Jiang, W.; Yin, J. H.; Ji, X. L.; Stagnaro, P. *Langmuir* **2013**.

Jiskoot, W.; Kijanka, G.; Randolph, T. W.; Carpenter, J. F.; Koulov, A. V.; Mahler, H. C.; Joubert, M. K.; Jawa, V.; Narhi, L. O. *J. Pharm. Sci.* **2016**.

Jo, S.; Park, K. *Biomaterials* **2000**.

Johansson, S.; Svineng, G.; Wennerberg, K.; Armulik, A.; Lohikangas, L. *Front. Biosci.* **1997**.

Jönsson, U.; Malmqvist, M.; Ronnberg, I. *J. Colloid Interface Sci.* **1985**.

Kadler, K. E.; Hill, A.; Canty-Laird, E. G. *Curr. Opin. Cell Biol.* **2008**.

Karpovich, D. S.; Blanchard, G. J. *Langmuir* **1994**.

Kastantin, M.; Faulon Marruecos, D.; Grover, N.; Yu McLoughlin, S.; Schwartz, D. K.; Kaar, J. L. *J. Am. Chem. Soc.* **2017**.

Kastantin, M.; Keller, T. F.; Jandt, K. D.; Schwartz, D. K. *Adv Funct Mater.* **2012**.

Kastantin, M.; Keller, T. F.; Jandt, K. D.; Schwartz, D. K. *Adv. Funct. Mater.* **2012**.

Kastantin, M.; Langdon, B. B.; Chang, E. L.; Schwartz, D. K. *J Am Chem Soc* **2011**.

Kastantin, M.; Langdon, B. B.; Schwartz, D. K. *Adv. Colloid Interface Sci.* **2014**.

Kastantin, M.; Schwartz, D. K. *Chemphyschem* **2013**.

Kastantin, M.; Schwartz, D. K. *Small* **2013**.

Keselowsky, B. G.; Collard, D. M.; García, A. J. *J. Biomed. Mater. Res. Part A* **2003**.

Kim, D. T.; Blanch, H. W.; Radke, C. J. *Langmuir* **2002**.

Kim, J. *Colloids Surfaces B Biointerfaces* **2016**.

Kisley, L.; Chen, J.; Mansur, A. P.; Dominguez-Medina, S.; Kulla, E.; Kang, M. K.; Shuang, B.; Kourentzi, K.; Poongavanam, M. V.; Dhamane, S.; et al. *J. Chromatogr. A* **2014**.

Kisley, L.; Serrano, K. A.; Davis, C. M.; Guin, D.; Murphy, E. A.; Gruebele, M.; Leckband, D. E. *Biomacromolecules* **2018**.

Kisley, L.; Serrano, K. A.; Guin, D.; Kong, X.; Gruebele, M.; Leckband, D. E. *ACS Appl. Mater. Interfaces* **2017**.

Koenig, M.; Bittrich, E.; König, U.; Rajeev, B. L.; Müller, M.; Eichhorn, K. J.; Thomas, S.; Stamm, M.; Uhlmann, P. *Colloids Surfaces B Biointerfaces* **2016**.

Koivunen, E.; Wang, B.; Ruoslahti, E. *Biotechnology* **1995**.

Kolvunen, E.; Wang, B.; Ruoslahti, E. *Biotechnology* **1995**.

Krammer, A.; Craig, D.; Thomas, W. E.; Schulten, K.; Vogel, V. *Matrix. Biol.* **2002**.

Krammer, A.; Lu, H.; Isralewitz, B.; Schulten, K.; Vogel, V. *Proc. Natl. Acad. Sci. U.S.A.* **1999**.

Kubiak-Ossowska, K.; Jachimska, B.; Mulheran, P. A. *J. Phys. Chem. B.* **2016**.

Kumar, V.; Sharma, V. K.; Kalonia, D. S. *Int. J. Pharm.* **2009**.

Kumra, H.; Reinhardt, D. P. *Adv. Drug Deliv. Rev.* **2016**.

Lakowicz, J. R.; Masters, B. R. *J. Biomed. Opt.* **2008**.

Langdon, B. B.; Kastantin, M.; Schwartz, D. K. *Biomacromolecules* **2015**.

Langdon, B. B.; Kastantin, M.; Schwartz, D. K. *Biophys. J.* **2012**.

Leahy, D. J.; Aukhil, I.; Erickson, H. P. *Cell* **1996**.

Leahy, D. J.; Aukhil, I.; Erickson, H. P. *Cell* **1996**.

Leckband, D.; Sheth, S.; Halperin, A. *J Biomat Sci-Polym E* **1999**.

Lee, L. L. Y.; Lee, J. C. *Biochemistry* **1987**.

Leitinger, B.; Hohenester, E. *Matrix Biology* **2007**.

Leng, C.; Han, X. F.; Shao, Q.; Zhu, Y. H.; Li, Y. T.; Jiang, S. Y.; Chen, Z. *J. Phys. Chem. C* **2014**.

Leng, C.; Hung, H. C.; Sieggreen, O. A.; Li, Y. T.; Jiang, S. Y.; Chen, Z. *J. Phys. Chem. C* **2015**.

Leng, C.; Sun, S. W.; Zhang, K. X.; Jiang, S. Y.; Chen, Z. *Acta Biomater.* **2016**.

Li, L. Y.; Chen, S. F.; Zheng, J.; Ratner, B. D.; Jiang, S. Y. *J Phys Chem B* **2005**.

Liao, F. S.; Lo, W. S.; Hsu, Y. S.; Wu, C. C.; Wang, S. C.; Shieh, F. K.; Morabito, J. V.; Chou, L. Y.; Wu, K. C. W.; Tsung, C. K. *J. Am. Chem. Soc.* **2017**.

Lin, S.; Struve, W. S. *Photochem. Photobiol.* **1991**.

Lo, C. M.; Wang, H. B.; Dembo, M.; Wang, Y. L. *Biophys. J.* **2000**.

Lok, B. K.; Cheng, Y. L.; Robertson, C. R. *J. Colloid Interface Sci.* **1983**.

Longchamp, J. N.; Rauschenbach, S.; Abb, S.; Escher, C.; Latychevskaia, T.; Kern, K.; Fink, H. W. *Proc. Natl. Acad. Sci.* **2017**.

Lynn, A. D.; Blakney, A. K.; Kyriakides, T. R.; Bryant, S. J. *J. Biomed. Mater. Res. - Part A* **2011**.

Lynn, A. D.; Bryant, S. J. *Acta Biomater.* **2011**.

Lynn, A. D.; Kyriakides, T. R.; Bryant, S. J. *J. Biomed. Mater. Res. - Part A* **2010**.

Mabry, J. N.; Kastantin, M.; Schwartz, D. K. *ACS Nano* **2015**.

Mabry, J. N.; Skaug, M. J.; Schwartz, D. K. *Anal Chem* **2014**.

Main, A. L.; Harvey, T. S.; Baron, M.; Boyd, J.; Campbell, I. D. *Cell* **1992**.

Major, M. R.; Wong, V. W.; Nelson, E. R.; Longaker, M. T.; Gurtner, G. C. *Plast. Reconstr. Surg.* **2015**.

Malmsten, M.; Emoto, K.; Van Alstine, J. M. *J Colloid Interf Sci* **1998**.

Mardon, H. J.; Grant, K. E. *FEBS Lett.* **1994**.

Markowski, M. C.; Brown, A. C.; Barker, T. H. *J. Biomed. Mater. Res. Part A* **2012**.

McBane, J. E.; Matheson, L. A.; Sharifpoor, S.; Santerre, J. P.; Labow, R. S. *Biomaterials* **2009**.

McLoughlin, S. Y.; Kastantin, M.; Schwartz, D. K.; Kaar, J. L. *P Natl Acad Sci USA* **2013**.

McUmber, A. C.; Randolph, T. W.; Schwartz, D. K. *J Phys Chem Lett* **2015**.

Midwood, K. S.; Williams, L. V.; Schwarzbauer, J. E. *Int. J. Biochem. Cell Biol.* **2004**.

Mizuno, D.; Tardin, C.; Schmidt, C. F.; Mackintosh, F. C. *Science* **2007**.

Mochitate, K.; Pawelek, P.; Grinnell, F. *Exp. Cell. Res.* **1991**.

Mohamad, N. R.; Marzuki, N. H. C.; Buang, N. A.; Huyop, F.; Wahab, R. A. *Biotechnol. Equip.* **2015**.

Monserud, J. H.; Macri, K. M.; Schwartz, D. K. *Angew. Chemie. - Int. Ed.* **2016**.

Monserud, J. H.; Schwartz, D. K. *Biomacromolecules* **2012**.

Morais, J. M.; Papadimitrakopoulos, F.; Burgess, D. J. *AAPS J.* **2010**.

Moree, B.; Connell, K.; Mortensen, R. B.; Liu, C. T.; Benkovic, S. J.; Salafsky, J. *Biophys. J.* **2015**.

Morra, M. *J Biomat Sci-Polym E* **2000**.

Mould, A. P.; Askari, J. A.; Aota, S. I.; Yamada, K. M.; Irie, A.; Takada, Y.; Mardon, H. J.; Humphries, M. J. *J. Biol. Chem.* **1997**.

Moussa, E. M.; Panchal, J. P.; Moorthy, B. S.; Blum, J. S.; Joubert, M. K.; Narhi, L. O.; Topp, E. M. *J. Pharm. Sci.* **2016**.

Mouw, J. K.; Ou, G. Q.; Weaver, V. M. *Nat. Rev. Mol. Cell Biol.* **2014**.

Mrksich, M.; Sigal, G. B.; Whitesides, G. M. *Langmuir* **1995**.

Myers, G. A.; Gacek, D. A.; Peterson, E. M.; Fox, C. B.; Harris, J. M. *J. Am. Chem. Soc.* **2012**.

Nagae, M.; Re, S.; Mihara, E.; Nogi, T.; Sugita, Y.; Takagi, J. *J. Cell Biol.* **2012**.

Nelson, N.; Schwartz, D. K. *J Phys Chem Lett* **2013**.

Nelson, N.; Walder, R.; Schwartz, D. K. *Langmuir* **2012**.

Ni, H.; Yuen, P. S. T.; Papalia, J. M.; Trevithick, J. E.; Sakai, T.; Fassler, R.; Hynes, R. O.; Wagner, D. D. *Proc. Natl. Acad. Sci.* **2003**.

Norde, W.; Anusiem, A. C. I. *Colloids and Surfaces* **1992**.

Oberhauser, A. F.; Badilla-Fernandez, C.; Carrion-Vazquez, M.; Fernandez, J. M. *J. Mol. Biol.* **2002**.

Oberhauser, A. F.; Marszalek, P. E.; Erickson, H. P.; Fernandez, J. M. *Nature* **1998**.

Ochsenhirt, S. E.; Kokkoli, E.; McCarthy, J. B.; Tirrell, M. *Biomaterials* **2006**.

Ogle, M. E.; Segar, C. E.; Sridhar, S.; Botchwey, E. A. *Experimental Biology and Medicine* **2016**.

Ostaci, R. V.; Damiron, D.; Grohens, Y.; Leger, L.; Drockenmuller, E. *Langmuir* **2010**.

Panganiban, B.; Qiao, B.; Jiang, T.; Delre, C.; Obadia, M. M.; Nguyen, T. D.; Smith, A. A. A.; Hall, A.; Sit, I.; Crosby, M. G.; et al. **2018**.

Parsons, J. T.; Horwitz, A. R.; Schwartz, M. A. *Nat. Rev. Mol. Cell Biol.* **2010**.

Pasqualini, R.; Koivunen, E.; Ruoslahti, E. *Nat. Biotechnol.* **1997**.

Patel, A. J.; Varilly, P.; Chandler, D. *J. Phys. Chem. B* **2010**.

Peeler, J. C.; Mehl, R. A. *Methods Mol Biol* **2012**.

Pelham, R. J.; Wang, Y. L. *Proc. Natl. Acad. Sci. U.S.A.* **1997**.

Perevozchikova, T.; Nanda, H.; Nesta, D. P.; Roberts, C. J. *J. Pharm. Sci.* **2015**.

Petrie, T. A.; Capadona, J. R.; Reyes, C. D.; García, A. J. *Biomaterials* **2006**.

Peyton, S. R.; Putnam, A. J. *J. Cell. Physio.* **2005**.

Pickford, A. R.; Potts, J. R.; Bright, J. R.; Phan, I.; Campbell, I. D. *Structure* **1997**.

Pickford, A. R.; Smith, S. P.; Staunton, D.; Boyd, J.; Campbell, I. D. *Embo J* **2001**.

Pierschbacher, M. D.; Ruoslahti, E. *J. Biol. Chem.* **1987**.

Pierschbacher, M. D.; Ruoslahti, E. *Nature* **1984**.

Rabe, M.; Verdes, D.; Seeger, S. *Adv. Colloid Interface Sci.* **2011**.

Raghavendra, A. J.; Alsaleh, N.; Brown, J. M.; Podila, R. *Biointerphases* **2017**.

Randolph, T. W.; Carpenter, J. F. *AIChE J.* **2007**.

Raoufi, M.; Hajipour, M.J.; Kamali Shahri, S.M.; Schoen, I.; Linn, U.; Mahmoudi, M. *Nanoscale* **2018**.

Ratner, B. D.; Hoffman, A. S.; Schoen, F. J.; Lemons, J. E. *Biomaterials Science: An Introduction to Materials: Third Edition* **2013**.

Redick, S. D.; Settles, D. L.; Briscoe, G.; Erickson, H. P. *J Cell Biol* **2000**, *149*, 521-527.
Reinke, J. M.; Sorg, H. *Eur. Surg. Res.* **2012**.

Rodriguez-Emmenegger, C.; Brynda, E.; Riedel, T.; Houska, M.; Subr, V.; Alles, A. B.; Hasan, E.; Gautrot, J. E.; Huck, W. T. *Macromol Rapid Commun* **2011**.

Rostam, H. M.; Singh, S.; Salazar, F.; Magennis, P.; Hook, A.; Singh, T.; Vrana, N. E.; Alexander, M. R.; Ghaemmaghami, A. M. *Immunobiology* **2016**.

Rostam, H. M.; Singh, S.; Vrana, N. E.; Alexander, M. R.; Ghaemmaghami, A. M. *Biomaterials Science* **2015**.

Rozario, T.; DeSimone, D. W. *Dev. Biol.* **2010**.

Sakai, T.; Johnson, K. J.; Murozono, M.; Sakai, K.; Magnuson, M. A.; Wieloch, T.; Cronberg, T.; Isshiki, A.; Erickson, H. P.; Fässler, R. *Nat. Med.* **2001**.

Satzer, P.; Svec, F.; Sekot, G.; Jungbauer, A. *Eng. Life Sci.* **2016**.

Schafer, M.; Werner, S. *Nat. Rev. Mol. Cell Biol.* **2008**.

Schneck, E.; Berts, I.; Halperin, A.; Daillant, J.; Fragneto, G. *Biomaterials* **2015**.

Schneck, E.; Schollier, A.; Halperin, A.; Moulin, M.; Haertlein, M.; Sferrazza, M.; Fragneto, G. *Langmuir* **2013**.

Schottler, S.; Becker, G.; Winzen, S.; Steinbach, T.; Mohr, K.; Landfester, K.; Mailander, V.; Wurm, F. R. *Nat. Nanotechnol.* **2016**.

Secundo, F. *Chem. Soc. Rev.* **2013**.

Shattil, S. J.; Kim, C.; Ginsberg, M. H. *Nat. Rev. Mol. Cell Biol.* **2010**.

Sheldon, R. A.; van Pelt, S. *Chem. Soc. Rev.* **2013**.

Shen, M.; Martinson, L.; Wagner, M. S.; Castner, D. G.; Ratner, B. D.; Horbett, T. A. *J. Biomater. Sci. Polym. Ed.* **2002**.

Sheth, S. R.; Leckband, D. *P Natl Acad Sci USA* **1997**.

Sheth, S. R.; Leckband, D. *Proc. Natl. Acad. Sci. U.S.A.* **1997**.

Shimaoka, M.; Takagi, J.; Springer, T. A. *Annu. Rev. Biophys. Biomol. Struct.* **2002**.

Sivaraman, B.; Latour, R. A. *Biomaterials* **2010**.

Sivaraman, B.; Latour, R. A. *Biomaterials* **2010**.

Snopok, B. A.; Kostyukevich, E. V. *Anal. Biochem.* **2006**.

Sobers, C. J.; Wood, S. E.; Mrksich, M. *Biomaterials* **2015**.

Sofia, S. J.; Premnath, V. V.; Merrill, E. W. *Macromolecules* **1998**.

Sun, Y.; Wallrabe, H.; Booker, C. F.; Day, R. N.; Periasamy, A. *Biophys. J.* **2010**.

Sussman, E. M.; Halpin, M. C.; Muster, J.; Moon, R. T.; Ratner, B. D. *Ann. Biomed. Eng.* **2014**.

Swartzlander, M. D.; Barnes, C. A.; Blakney, A. K.; Kaar, J. L.; Kyriakides, T. R.; Bryant, S. J. *Biomaterials* **2015**.

Szleifer, I. *Biophys J* **1997**.

Takagi, J.; Petre, B. M.; Walz, T.; Springer, T. A. *Cell* **2002**.

Takagi, J.; Strokovich, K.; Springer, T. A.; Walz, T. *EMBO J.* **2003**.

Takasu, K.; Kushiro, K.; Hayashi, K.; Iwasaki, Y.; Inoue, S.; Tamechika, E.; Takai, M. *Sensors Actuators, B Chem.* **2015**.

Tanaka, M.; Hayashi, T.; Morita, S. *Polym J* **2013**.

Tang, L.; Thevenot, P.; Hu, W. *Curr. Top. Med. Chem.* **2008**.

Tang, L.; Ugarova, T. P.; Plow, E. F.; Eaton, J. W. *J. Clin. Invest.* **1996**.

Taylor, W.; Jones, R. A. L. *Langmuir* **2010**.

Thyparambil, A. A.; Wei, Y.; Latour, R.A. *Langmuir* **2015**.

Traeger, J. C.; Schwartz, D. K. *Langmuir* **2017**.

Tunc, S.; Maitz, M. F.; Steiner, G.; Vázquez, L.; Pham, M. T.; Salzer, R. *Colloids Surfaces B Biointerfaces* **2005**.

Tziampazis, E.; Kohn, J.; Moghe, P. V. *Biomaterials* **2000**.

Unsworth, L. D.; Sheardown, H.; Brash, J. L. *Langmuir* **2005**.

Unsworth, L. D.; Sheardown, H.; Brash, J. L. *Langmuir* **2008**.

Unsworth, L. D.; Tun, Z.; Sheardown, H.; Brash, J. L. *J Colloid Interf Sci* **2006**.

Utrata-Wesoek, A. *Polimery/Polymers* **2013**.

Utrata-Wesolek, A. *Polimery* **2013**.

Van Agthoven, J. F.; Xiong, J. P.; Alonso, J. L.; Rui, X.; Adair, B. D.; Goodman, S. L.; Arnaout, M. A. *Nat. Struct. Mol. Biol.* **2014**.

van der Walle, C. F.; Altroff, H.; Mardon, H. J. *Protein Eng* **2002**.

Vanderah, D. J.; La, H. L.; Naff, J.; Silin, V.; Rubinson, K. A. *J. Am. Chem. Soc.* **2004**.

Vénéreau, E.; Ceriotti, C.; Bianchi, M. E. *Front. Immunol.* **2015**.

Vinogradov, V. V.; Avnir, D. *Sci. Rep.* **2015**.

Vitali, M.; Rigamonti, V.; Natalello, A.; Colzani, B.; Avvakumova, S.; Brocca, S.; Santambrogio, C.; Narkiewicz, J.; Legname, G.; Colombo, M.; Prosperi, D.; Grandori, R. *Biochim. Biophys. Acta-Gen Subj.* **2018**.

Volodina, K. V.; Avnir, D.; Vinogradov, V. V. *Sci. Rep.* **2017**.

Walder, R.; Kastantin, M.; Schwartz, D. K. *Analyst* **2012**.

Walder, R.; Nelson, N.; Schwartz, D. K. *Nat Commun* **2011**.

Walder, R.; Schwartz, D. K. *Soft Matter* **2011**.

Wang, X.; Schmidt, D. R.; Joyce, E. J.; Kao, W. J. *J. Biomater. Sci. Polym. Ed.* **2011**.

Ward, W. K. A. *Journal of Diabetes Science and Technology* **2008**.

Wazawa, T.; Ueda, M. *Advances in Biochemical Engineering/Biotechnology* **2005**.

Weltz, J. S.; Schwartz, D. K.; Kaar, J. L. *ACS Nano* **2016**.

Wilson, K. A.; Finch, C. A.; Anderson, P.; Vollmer, F.; Hickman, J.J. *Biomaterials* **2015**.

Xia, N.; Castner, D. G. *J Biomed Mater Res A* **2003**.

Xian, X.; Gopal, S.; Couchman, J. R. *Cell and Tissue Research* **2010**.

Xiong, J. P.; Stehle, T.; Goodman, S. L.; Arnaout, M. A. *Blood* **2003**.

Xiong, J. P.; Stehle, T.; Zhang, R.; Joachimiak, A.; Frech, M.; Goodman, S. L.; Arnaout, M. A. *Science* **2002**.

Xu, Z.; Zhang, S.; Weber, J. K.; Luan, B.; Zhou, R.; Li, J. *Nanoscale* **2016**.

Yamada, K. M.; Akiyama, S. K.; Hasegawa, T.; Hasegawa, E.; Humphries, M. J.; Kennedy, D. W.; Nagata, K.; Urushihara, H.; Olden, K.; Chen, W. T. *Journal of Cellular Biochemistry* **1985**.

Yandi, W.; Mieszkin, S.; Martin-Tanchereau, P.; Callow, M. E.; Callow, J. A.; Tyson, L.; Liedberg, B.; Ederth, T. *ACS Appl. Mater. Interfaces* **2014**.

Ye, Q.; Zhao, W.; Yang, W.; Pei, X.; Zhou, F. *Macromol. Chem. Phys.* **2017**.

Zarrabi, N.; Ernst, S.; Verhalen, B.; Wilkens, S.; Börsch, M. *Methods* **2014**.

Zaveri, T. D.; Lewis, J. S.; Dolgova, N. V.; Clare-Salzler, M. J.; Keselowsky, B. G. Integrin- *Biomaterials* **2014**.

Zeinabad, H. A.; Zarrabian, A.; Saboury, A. A.; Alizadeh, A. M. O.; Falahati, M. *Sci. Rep.* **2016**.

Zhang, Z.; Chao, T.; Chen, S.; Jiang, S. *Langmuir* **2006**.

Zheng, J.; Li, L. Y.; Chen, S. F.; Jiang, S. Y. *Langmuir* **2004**.

Zhou, H. X.; Rivas, G.; Minton, A. P. *Annu. Rev. Biophys.* **2008**.

Zollinger, A. J.; Smith, M. L. *Matrix Biology* **2017**.

# Appendix A: Supporting Information for Chapter III

## A.1 Supporting Figures and Tables

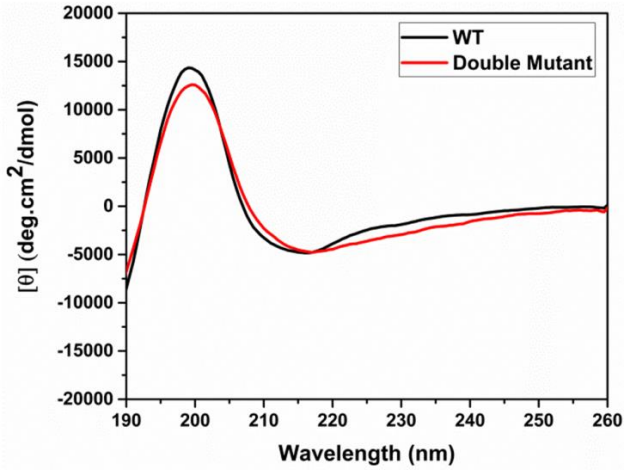


**Figure A. 1.** Circular dichroism spectrum for: wild-type FNIII 8-10 (black) and the double mutant S1381AzF/S1500C (red).

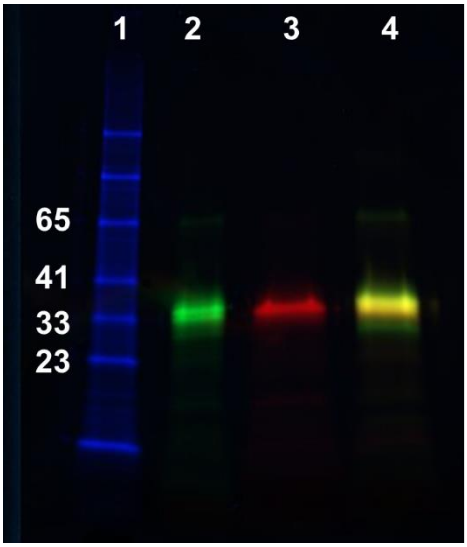


**Figure A. 2.** Labeling of S1381AzF/S1500C mutant with fluorophores Alexa Flour 555 and Alexa Flour 647, respectively. Column 2 corresponds to FN construct used with the single mutation S1381AzF (Alexa Flour 555 label), column 3 to single mutation S1500C (Alexa Flour 647 label)

and column 4 to the double mutant labeled with both dyes ($FN_{FRET}$). The gel was imaged with an Amersham (GE) Typhoon 9400 Variable Mode Imager.

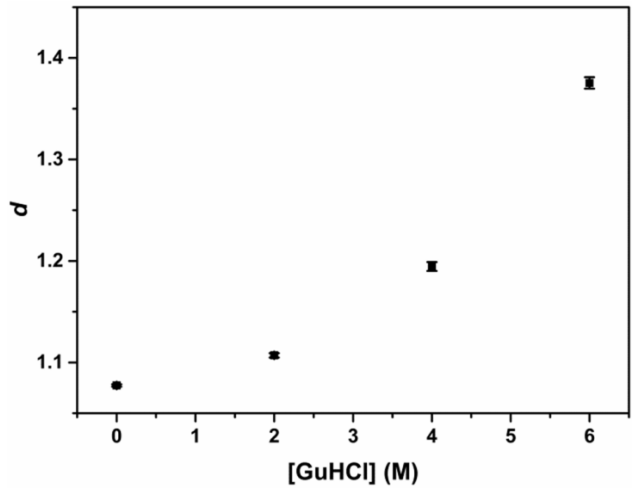


**Figure A. 3.** Changes in the relative distance between fluorophores as a function of the concentration of a denaturant agent (guanidine hydrochloride). Experiment done for $FN_{FRET}$ at a constant temperature of 20°C. Error bars represent the standard deviation of 3 replicates.

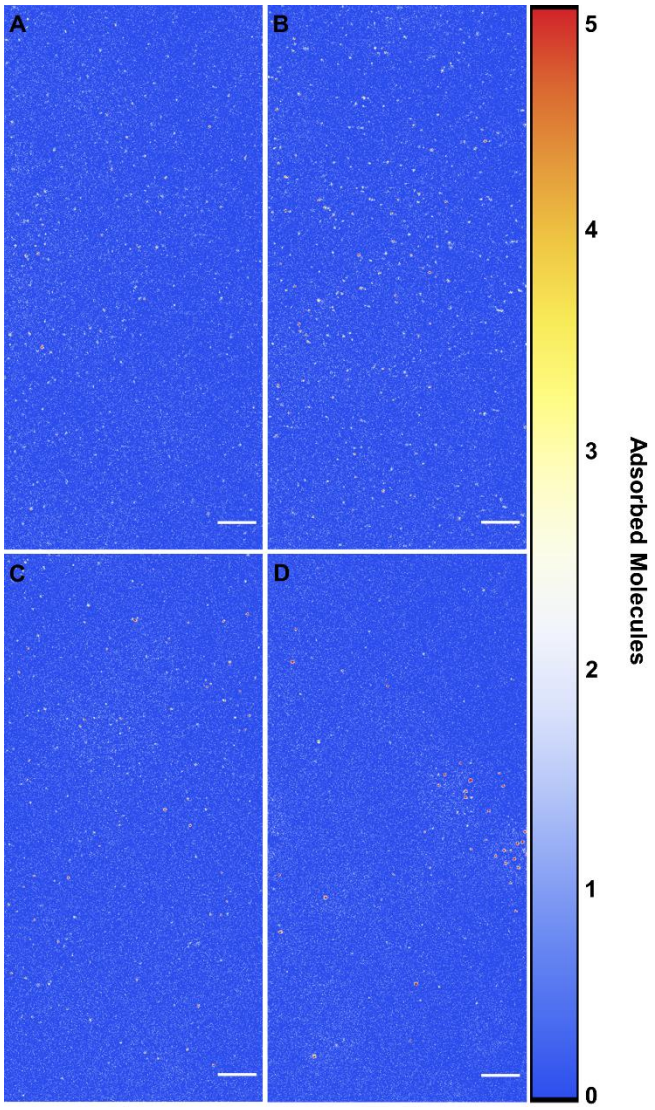


**Figure A. 4.** Super-resolution mapping of surface adsorption of labeled $FN_{FRET}$ using mbPAINT method for non-functionalized FS (A), low σ (B), medium σ (C), and high σ PEG brushes (D). Scale bars represent 5 μm.

**Table A. 1.** Fraction of adsorption events that took place at anomalously strong sites out of the total number of adsorption events for all the surfaces studied.

| Surface | Fraction of Adsorption Events at Anomalous Sites (%) |
|---|---|
| FS | 0.21 |
| Low σ | 0.40 |
| Medium σ | 0.20 |
| High σ | 0.29 |

**Table A. 2.** $FN_{FRET}$ adsorption rate constant ($k_{ads}$) values for unfunctionalized fused silica (FS) and PEG-functionalized surfaces of different grafting density (low σ, medium σ, and high σ). The numbers in parentheses correspond to the uncertainty in the least significant digit, and represent the standard deviation of 20 data sets. Only trajectories that lasted for at least 4 frames were considered.

| Surface | Adsorption Rate Constant, $k_{ads}$ (μm/s) |
|---|---|
| FS | 0.41(9) |
| Low σ | 0.023(5) |
| Medium σ | 0.010(2) |
| High σ | 0.005(1) |

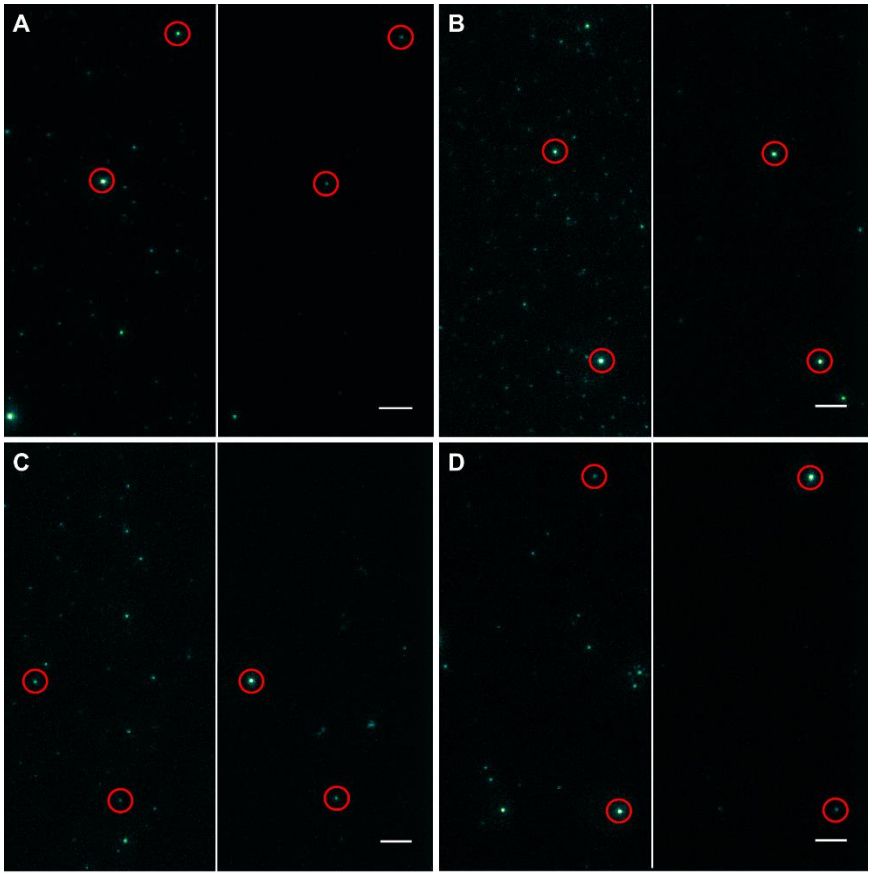


**Figure A. 5.** Representative fluorescence images captured from SM-FRET experiments. Each image is divided in two sections of exactly the same area, which represent the donor channel (left) and the acceptor channel (right). Images are shown for bare FS (A), low σ (B), medium σ (C), and high σ (D). Circled objects are representative of molecules that exhibited fluorescence at the same location (x,y) in both channels in the same frame. The scale bars represent 10 μm.

**Table A. 3.** Percentage of molecules that exhibited at least one unfolding event during their trajectory out of the total number of molecules that adsorbed on the surface in the folded state. Only trajectories that lasted for at least 4 frames were selected. Given values correspond to 20 data sets.

| Surface | Percentage of Unfolding Events (%) |
|---|---|
| FS | 59.5 |
| Low σ | 70.9 |
| Medium σ | 66.9 |
| High σ | 69.8 |

**Table A. 4.** The parameter values are the best fit values of equation: $F(t) = A^{-1}\sum_{k=1}^{N} x_k e^{-t/\tau_k}$, shown in Figure 3.5. These fit values were averaged by weighting each movie by the number of objects observed in that movie, and the numbers in parentheses correspond to the uncertainty in the least significant digit, which represents the standard error of the weighted fit values. Reported average time constants ($\langle\tau\rangle$) are given by $\sum_k x_k\tau_k$ and rate constants (k) are given by $\langle\tau\rangle^{-1}$.

| Surface (State) | $\langle\tau\rangle$ (s) | $k_{des}$ ($s^{-1}$) | $x_k$ | $\tau_k$ (s) |
|---|---|---|---|---|
| FS (Folded) | 0.0528(4) | 18.9(1) | 0.9866(2) | 0.0462(3) |
| | | | 0.0117(2) | 0.41(1) |
| | | | 0.00167(9) | 1.44(3) |
| Low σ (Folded) | 0.052(1) | 19.2(4) | 0.994(4) | 0.0500(2) |
| | | | 0.006(4) | 0.254(9) |
| | | | 0.00045(2) | 1.53(4) |
| Medium σ (Folded) | 0.0481(2) | 20.79(9) | 0.9961(3) | 0.0470(2) |
| | | | 0.0037(3) | 0.238(9) |
| | | | 0.000196(9) | 1.93(6) |
| High σ (Folded) | 0.0421(6) | 23.8(3) | 0.986(3) | 0.0408(5) |
| | | | 0.014(3) | 0.119(7) |
| | | | 0.00021(2) | 0.87(4) |
| FS (Unfolded) | 0.264(9) | 3.8(1) | 0.601(5) | 0.091(2) |
| | | | 0.354(4) | 0.344(4) |
| | | | 0.042(6) | 1.47(2) |
| | | | 0.0033(1) | 7.81(1) |
| Low σ (Unfolded) | 0.30(1) | 3.3(1) | 0.648(4) | 0.095(2) |
| | | | 0.313(4) | 0.406(5) |
| | | | 0.036(6) | 1.88(4) |
| | | | 0.0040(2) | 10.7(3) |
| Medium σ (Unfolded) | 0.321(9) | 3.12(9) | 0.611(4) | 0.071(2) |
| | | | 0.319(4) | 0.369(4) |
| | | | 0.060(6) | 1.38(2) |
| | | | 0.0110(2) | 6.99(5) |
| High σ (Unfolded) | 0.38(1) | 2.63(7) | 0.664(5) | 0.067(2) |
| | | | 0.248(4) | 0.404(6) |
| | | | 0.075(6) | 1.63(2) |
| | | | 0.0128(3) | 9.12(8) |

**Table A. 5.** The parameter values are the best fit values of equation: $F(t) = A^{-1}\sum_{k=1}^{N} x_k e^{-t/\tau_k}$, shown in Figure 3.6. These fit values were averaged by weighting each movie by the number of objects observed in that movie, and the numbers in parentheses correspond to the uncertainty in the least significant digit, which represents the standard error of the weighted fit values. Reported average time and rate constants ($\langle\tau\rangle$, $k_{fold/unf}$) were calculated as explained in Table A.4.

| **Surface, Initial State (Conformational change)** | **$\langle\tau\rangle$ (s)** | **$k_{fold/unf}$ ($s^{-1}$)** | **$x_k$** | **$\tau_k$ (s)** |
|---|---|---|---|---|
| FS, Unfolded (Folding) | 4.09(7) | 0.245(4) | 0.417(4) | 0.44(2) |
| | | | 0.583(4) | 6.7(1) |
| Low σ, Unfolded (Folding) | 4.34(6) | 0.230(3) | 0.436(5) | 0.52(2) |
| | | | 0.5634(5) | 7.3(1) |
| Medium σ, Unfolded (Folding) | 5.15(6) | 0.194(2) | 0.350(3) | 0.42(1) |
| | | | 0.650(3) | 7.69(9) |
| High σ, Unfolded (Folding) | 7.5(1) | 0.133(2) | 0.326(4) | 0.48(2) |
| | | | 0.674(4) | 10.9(2) |
| FS, Folded (Unfolding) | 1.10(7) | 0.91(6) | 0.68(2) | 0.13(2) |
| | | | 0.32(2) | 3.16(7) |
| Low σ, folded (Unfolding) | 1.12(5) | 0.89(4) | 0.784(9) | 0.080(4) |
| | | | 0.216(9) | 4.90(4) |
| Medium σ, Folded (Unfolding) | 1.03(5) | 0.97(5) | 0.78(1) | 0.085(6) |
| | | | 0.22(1) | 4.37(6) |
| High σ, Folded (Unfolding) | 0.74(8) | 1.4(2) | 0.83(2) | 0.088(9) |
| | | | 0.17(2) | 3.91(9) |

# Appendix B: Supporting Information for Chapter IV

## B.1 Methods

### B.1.1 Patterned Surface Preparation

Trimethylsiloxane (TMS) modified fused silica surfaces were prepared by chemical vapor deposition of hexamethydisilazane under ambient conditions for 24h. The TMS layers were photopatterned by UV-ozone degradation using a 1000 lines/inch nickel mesh (SPI supplies) as a photomask. The masked surfaces were illuminated for 5 minutes in air using a UV pen lamp resulting in a grid of hydrophobic TMS functionalized fused silica around islands of hydrophilic fused silica.

### B.1.2 PEG Brush Surface Preparation

Surfaces containing PEG brushes were prepared by grafting α–methoxy-ω-triethoxy PEG ($M_w$ 5,000 Da; Laysan Bio Inc.) to fused silica wafers in the presence of solvents with a different quality for PEG. By decreasing the quality of the solvent, PEG molecules shrank into smaller coils in solution, which led to a higher grafting density of the brush upon reaction with the surface[1]. Specifically, acetone is a good solvent for PEG, while diethyl ether is an extremely poor solvent.

Prior to functionalization, the silica wafers were extensively washed with Micro-90 (International Product Corp.), ultrapure water and piranha, and subsequently activated with UV/ozone for 30 min. After washing, the wafers were reacted with α–methoxy-ω-triethoxy PEG (1 mM) in 100% acetone or 50% acetone/50% diethyl ether (solubility limit of PEG in diethyl ether) for 15 h at 30 °C with gentle shaking (25 rpm) in a constant temperature incubator. The surface functionalization reaction was catalyzed by the addition of N-butylamine at a 1:20 volumetric ratio of the catalyst-to-reaction mixture.

In order to verify that the two surfaces exhibited different grafting densities, the thickness of the dry brushes was measured by elipsometry using a J.A. Woollam variable angle spectroscopy ellipsometer (model VASE-VB-250). The dry thickness was then converted into grafting density of the brushes as described previously[2]. The calculations showed that the grafting densities were 0.16(1) and 0.34(1) chains/nm$^2$ for the good and the poor solvent systems, respectively.

### B.1.3 High-throughput SM Imaging

Dilute NBD-X ($10^{-7}$ M) was introduced into a flow cell (maintained at 25.0 ± 0.1 °C), containing either TMS-nanopatterned fused silica or PEG brushes in DDI water. For imaging, a custom-built prism-based illumination system and Nikon Eclipse Ti microscope with 60x plan Apo water immersion objective were used. Additionally, the sample was excited using a 532 nm Cobolt Samba 50 mW diode-pumped solid-state laser that was coupled to a single mode fiber optic cable. The laser was coupled to the fiber optic cable using a free space laser-fiber launch (Oz Optics), resulting in the retention of 60% of the incident light.

To collect two-channel images, an Optosplit III (Cairn Research) image splitter employed a dichroic mirror with a nominal separation wavelength of 540 nm (model T540lpxr, Chroma), which separated light into the low- and high-wavelength channels. Additional bandpass filters (Semrock) were used to further select for fluorescence emission in each channel. A bandpass centered at 528 with a 90% transmission width of 28 nm and a bandpass centered at 560 with a 90% transmission width of 40 nm were used for the low- and high-wavelength channels, respectively. After fluorescence emission was split and filtered, each channel was projected onto a separate region of an Andor iXON3 EMCCD camera cooled to -90 °C. Sequential images were obtained with an exposure time of 200 ms.

### B.1.4 High-throughput SM Image Processing and Analysis

The two channels were aligned during post processing using a pixel displacement field. The displacement field was defined using images of a glass slide scratched with 2000 grit sand paper to form an irregular alignment image. The images were captured on the microscope just before starting the experiment using epi-illumination from a broad spectrum source (X-cite 120), and the dichroic and filter sets used in the experiment, typically using 500 ms to 1 s exposure time to reduce noise. The dual channel scratch image was split into two single channel images (henceforth referred to as ch1 and ch2) which were used to determine a non-uniform pixel displacement field to be applied to the ch2 images later in the analysis. To do this, The two single-channel images were each split into a corresponding grid of tiles, and each pair of tiles from ch1 and ch2 were aligned independently by a defining a uniform translation. The ch1 tiles and ch2 tiles were centered at identical locations relative to the top left corner of their respective images, but the ch1 tiles were 20 pixels larger in both dimensions to ensure that all features in the ch2 tile would be included in the ch1 tile (translations greater than 10 pixels are extremely rare). Prior to determining the translation required to align the tile pairs, the gradient of the tiles were taken to reduce the effect of extreme intensities. The required ch2 tile translation was determined as that corresponding to the maximum of a normalized cross-correlation matrix of the two tiles. This was done for each tile pair. The ch2 full image displacement field was defined an array with the same size as pixel dimensions of the ch2 image. The displacements corresponding to the center position of each tile pair were assigned the x and y displacement required to aligning the tiles, and all displacement in between were estimated using 2D linear interpolation. The pixels not bound by the tile center positions were assigned the nearest perimeter-pixel displacement value that was

defined by interpolation. This process was repeated using different tile grid sizes to optimize the registration of the two channels by maximizing the sum-product of the pixel intensity-gradients of the two channels after the pixel displacement was applied to ch2. The resulting alignment was consistently better (higher sum-product intensity gradients) than a simple uniform translation alignment, and resulted in more accurate co-localization of the objects in either channel.

Prior to defining the pixels that correspond to object fluorescence, the channels were split in the same manner as with the alignment image, and treated as separate images throughout the analysis. A global background was initially removed from each image to account for non-uniformity in the TIRF field when identifying objects. This was done by subtracting a Gaussian blur of each image from itself, where the Gaussian kernel standard deviation was at least five times larger than the radius of the detected objects. Following this, the non-uniform pixel displacement field determined as described above was applied to each ch2 frame. A Gaussian blur with a specified kernel diameter and standar deviation (for this work 5 and 2 pixels, respectively), was then applied to each frame, and the initial estimates of object locations ($\mu_{x0}$ and $\mu_{y0}$) was defined as any intensity peak in the blurred image that exceeds a user defined intensity threshold. The pixels corresponding to an object were defined as all pixels contained in a disk with a user specified object diameter (5 pixels in this case) centered at each position estimate. The intensity for the $i$th object pixel was taken as the raw pixel intensity (after alignment, but prior to blurring) with a local object background subtracted. The local background was defined as the median intensity of the ring of pixels surrounding the object-associated pixels.

The object positions were determined by fitting the background subtracted object pixel intensities (n-by-1 vector, $Z$) to a circular Gaussian point spread function, linearized with respect to the amplitude and peak position. The linear system was defined as follows:

$$Z/Z_{max} =$$

$$\begin{bmatrix} e^{\frac{-(x_1-\mu_{x0})^2-(y_i-\mu_{y0})^2}{2\sigma^2}} & \frac{A_0(x_1-\mu_{x0})^2}{2\sigma^2} e^{\frac{-(x_1-\mu_{x0})^2-(y_1-\mu_{y0})^2}{2\sigma^2}} & A_0 \frac{A_0(y_1-\mu_{y0})^2}{2\sigma^2} e^{\frac{-(x_1-\mu_{x0})^2-(y_1-\mu_{y0})^2}{2\sigma^2}} \\ \vdots & \vdots & \vdots \\ e^{\frac{-(x_n-\mu_{x0})^2-(y_n-\mu_{y0})^2}{2\sigma^2}} & \frac{A_0(x_n-\mu_{x0})^2}{2\sigma^2} e^{\frac{-(x_n-\mu_{x0})^2-(y_n-\mu_{y0})^2}{2\sigma^2}} & A_0 \frac{A_0(y_n-\mu_{y0})^2}{2\sigma^2} e^{\frac{-(x_n-\mu_{x0})^2-(y_n-\mu_{y0})^2}{2\sigma^2}} \end{bmatrix} \begin{bmatrix} A - A_0 \\ \mu_x - \mu_{x0} \\ \mu_y - \mu_{y0} \end{bmatrix},$$

(eq. B.1)

where $Z_{max}$ is the maximum pixel intensity of an object, $x_i$ and $y_i$ were the xy-positions of the pixel corresponding to $Z_i$, $A_0$ is the amplitude estimate which was set to 1, and $\sigma$ is the standard deviation which was also set to 1, corresponding to the typical observed point spread function for our optical system. The amplitude and xy-positions of each object ($A$, $\mu_x$, and $\mu_y$) were determined by linear least-squares fitting.

Uncertainty in the object intensity was defined as $\left[N_{disk}\left(1 + N_{perimeter}^{-1}\right)\right]^{1/2}$, where $\delta$ is the standard deviation of all pixels that were not associated with an object, $N_{disk}$ is the number of pixels in the disk (or the number of elements in Z) and $N_{perimeter}$ is the number of surrounding pixels used to determine the local background. The uncertainty of the object position (i.e. localization precision) was calculated as the uncertainty in the x and y position parameters of the linearized Gaussian fit added in quadrature. The parameter covariance was calculated using the equation $V = [X^T(\delta^2 I)^{-1}X]^{-1}$ where $X$ is the system matrix used to define the linearized Gaussian system in equation B.1. The localization precision was calculated as $\left(V_{2,2} + V_{3,3}\right)^{1/2}$ or the standard error of $\mu_x$, and $\mu_y$ added in quadrature.

Corresponding objects from each channel were identified as objects that were within two pixels of each other to compensate for any inaccuracy in the alignment of the two channels. When corresponding objects were found, the position was defined as the midpoint between the positions for each channel. If an object was detected in only one channel, the intensity corresponding to the other channel was estimated by applying the intensity calculation described above to the corresponding pixels in the channel where the object was not detected.

Molecular trajectories were identified by co-localizing objects in consecutive frames within a specified tracking radius. When multiple objects share multiple allowable destinations in the following frame, the permutation that maximizes the number of continuing trajectories while minimizing the total step displacement is used to assign a destination to each object. In the studied system, very little object motion was observed, so the tracking radius was set to one pixel or 0.227 μm. Trajectories that lasted less than two frames (0.4 seconds) were ignored. This along with the small tracking radius greatly reduce the probability of tracking noise. We estimate that on average 0.2% of the reported trajectories are due to noise tracking. Because the probability of tracking noise for more than two frames is virtually zero, this equates to ~0.5% of the two-frame trajectories being tracked noise with extremely rare noise contributions to longer trajectories. This estimate is based on applying the object identification and tracking algorithms to a simulated 100-frame movie where the pixel intensities are randomly sampled from a Gamma distribution that represents a fit to the background pixels of the experimentally acquired videos.

### B.1.5 Adsorption Rate Constant Analysis

The adsorption rate constant ($k_{ads}$) of NBD-X molecules on the brush surfaces was calculated as reported previously[2,3]. Briefly, the average total number of objects observed per movie was divided by the area of the field of view, the length of the movie and the bulk concentration of NBD-X. The outcome of such calculation leads to $k_{ads}$ expressed in units of nanometers per second, which represents the thickness of a "slab" of solution containing the number of adsorbate molecules that adsorb each second.

The results showed that the $k_{ads}$ of dye molecules decreased from 0.71 nm/s to 0.32 nm/s with increasing grafting density, as a result of the increasing steric repulsion induced by the action of more extended chains at higher grafting density[4-7]. In previous studies, we also observed a decrease in the $k_{ads}$ of fibronectin on PEG brushes within the same grafting density range: 23 nm/s and 5 nm/s on the low and high grafting density surface, respectively[2]. The order of magnitude difference in $k_{ads}$ for the dye (MW ≈ 294 g/mol) and the protein (MW ≈ 30,000 g/mol) was reasonable, given the larger size of the protein molecule and thus longer-range and stronger interactions with the surface.

## B.2 Supporting Figures

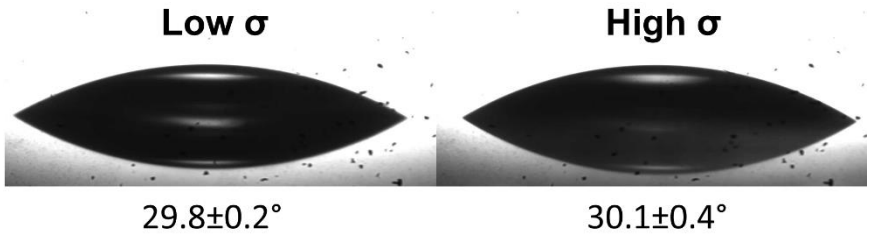


**Figure B. 1.** Representative static contact angle images of a low and a high grafting density PEG brush-coated glass surface. The reported uncertainties reflect both surface homogeneity (three different spots were tested on each surface) and variability between three different batches for each surface.

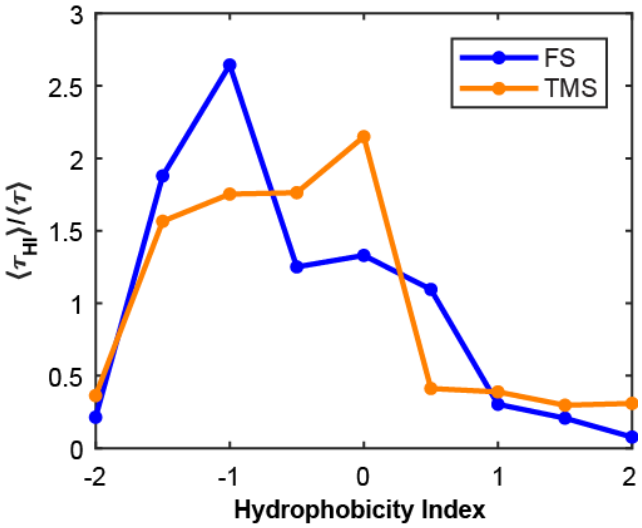


**Figure B. 2.** Mean surface residence time for trajectories whose average HI was within a given 0.5 HI unit bin centered at each data point, $\langle\tau_{HI}\rangle$, for both TMS (orange) and FS (blue) regions in the patterned surfaces. Data points were normalized by the mean residence time corresponding to all trajectories within the range -2 < mean HI < 2, $\langle\tau\rangle$, which were 0.54 s and 0.37 s for the FS and TMS regions, respectively.

**Figure B.3** shows a heat map of the complementary cumulative residence time distributions of objects with a mean HI within a range of x-values. This figure is an extension of **Figure 4.4** in the manuscript and **Figure B.2,** with greater resolution in the HI variable and the

full complementary cumulative distribution of HI-binned residence times. These maps also demonstrate that objects adsorbed to environments with more moderate HI tended to have longer residence times, and that the residence times tended to be longer in the hydrophilic environments compared with hydrophobic environments. Interestingly, the non-monotonic nature of the residence times is demonstrated in greater detail, with two apparent peaks at moderate HI and low, hydrophilic HI. This further emphasizes the complexity of the NBD-X-PEG interaction, and suggests that the observed interactions are most likely a combination of multiple probe binding orientations, each interacting with varying surface chemistries.

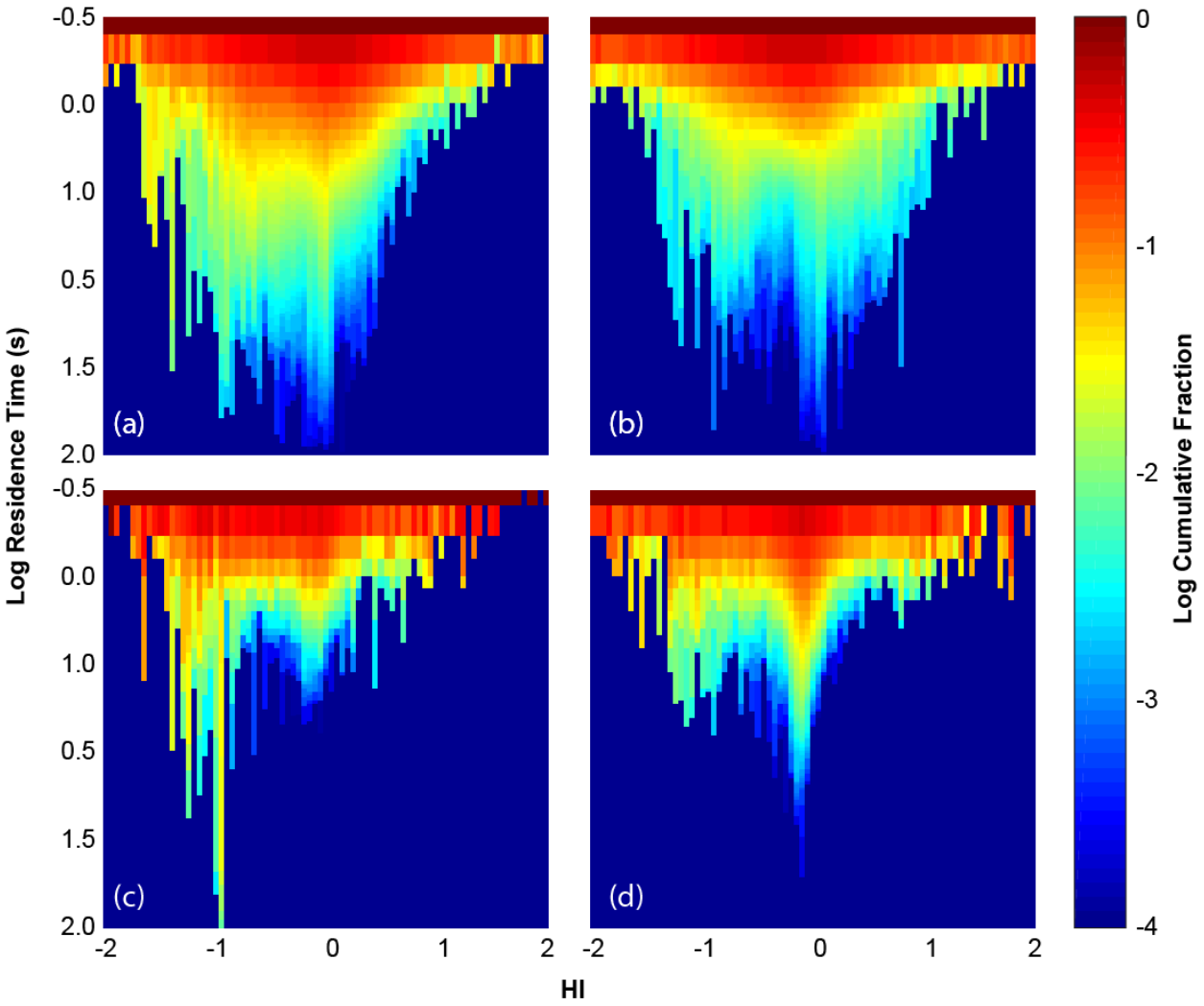


**Figure B. 3.** Heat maps showing the log-log complementary cumulative residence time distributions (CCDF) of trajectories binned by the mean HI of the trajectory for (a) low and (b) high grafting density PEG brushes, as well as FS (c) and TMS (d) regions of the patterned surfaces. The CCDF for each HI-bin is plotted on the color-y-plane while the x-axis indicates the HI-center of each bin.

## B.3 References


(1) Arcot, L.; Ogaki, R.; Zhang, S.; Meyer, R. L.; Kingshott, P. *Appl. Surf. Sci.* **2015**, *341*, 134-141.
(2) Marruecos, D. F.; Kastantin, M.; Schwartz, D. K.; Kaar, J. L. *Biomacromolecules* **2016**, *17*, 1017-1025.
(3) Walder, R.; Nelson, N.; Schwartz, D. K. *Nat. Commun.* **2011**, *2*.
(4) Israelachvili, J. N. Steric (polymer-mediated) and thermal fluctuation forces. *Intermolecular and Surface Forces, 3rd Edition* **2011**, 381-413.
(5) Halperin, A. *Langmuir* **1999**, *15*, 2525-2533.
(6) Sheth, S. R.; Leckband, D. *Proc. Natl. Acad. Sci. U.S.A.* **1997**, *94*, 8399-8404.
(7) Szleifer, I. *Biophys. J.* **1997**, *72*, 595-612.

# Appendix C: Supporting Information for Chapter V

## C.1 Supporting Methods

### C.1.1 Characterization of Dynamic Behavior of $FN_{FRET}$

Continuous probability density distributions (**Figure 5.2**) were obtained from discrete histograms that represented the frequency in the observation of any given small range of $\chi_{Fold}$ from all the single-molecule trajectories collected. Specifically, for each bin, the midpoint was calculated and the number of observations within that range (*i.e.*, bin width) divided by the total number of observations attributed to it. The obtained values were connected by solid lines and the distribution was normalized by the area under the curve in order to integrate to one. In the case of the distributions in **Figure 5.2**, each single molecule trajectory contained the $\chi_{Fold}$ values for all the frames, whereas in the case of the distributions in **Figure C.1**, each trajectory just contained the median $\chi_{Fold}$ value across all the frames. **Table C.1** contains the fractions of folded and unfolded populations for each probability density distribution, calculated from the area under the curve corresponding to each conformation. Values in parentheses correspond to the uncertainty in the least significant digit, which represents the sample standard deviation calculated from 5 different subsets of data.

Complementary cumulative probability distributions were fit to a weighted sum of first-order processes as in equation C.1:

$$F(t) = \sum_{k=1}^{N} x_k e^{-t/\tau_k} \quad \text{(eq. C.1)}$$

were *F(t)* is the probability of a molecule remaining in the initial state of interest for each process (e.g. adsorbed on the surface, in a folded or unfolded conformation, bound or unbound to an integrin…) for a time, *t*, or longer, and each first-order process, *k*, used to fit the complementary cumulative distributions could be described by a fraction of molecules, $x_k$, and a characteristic

time, $\tau_k$ , as described previously. The parameter values reported in **Tables C.2**, **C.3**, **C.7**, and **C.8** are the best fit values of equation C.1. The fit values were averaged by weighting each movie by the number of objects observed in that movie, and the numbers in parentheses correspond to the uncertainty in the least significant digit, which represents the standard error of the weighted fit values. Reported average time constants ($\langle\tau\rangle$) were given by $\sum_k x_k \tau_k$ and rate constants ($k$) were given by $\langle\tau\rangle^{-1}$.

Complementary cumulative squared displacement distributions were conveniently fit using a Gaussian mixture model for multiple modes of diffusion:

$$F(r^2, t) = \sum_{k=1}^{N} x_k e^{-r^2 / 4(D_k t + \sigma^2)} \quad \text{(eq. C.2)}$$

where $F(r^2, t)$ represents the probability that a molecule moves a distance equal or greater than a radius, $r$, over a time interval, $t$ (in this case, $t$ = 70 ms, the acquisition time), $x_k$ represents the fraction of observed displacements in mode $k$, characterized by the diffusion coefficient, $D_k$, and $\sigma$ is the positional uncertainty (assumed to be 35 nm in this work). Specifically, $\sigma$ is the standard deviation of an assumed Gaussian probability distribution for identifying an object at its true position, and it is used to take into account the effect of instrument noise on the quantification of diffusion coefficients. The parameter values reported in **Table S4** are the best fit values of equation C.2, and values in parentheses represent the fitting error and correspond to the error in the final digit. Reported average diffusion coefficients $\overline{D}$ were given by $\sum_k x_k D_k$ .

### C.1.2 Characterization of FN-Integrin Binding by Surface Plasmon Resonance

The binding affinity of $\alpha_v\beta_3$ for dual-labeled $FN_{FRET}$ and wild-type FN was assayed by surface plasmon resonance using a Biacore-3000 (GE Healthcare, United Kingdom). In these experiments, $\alpha_v\beta_3$ was unlabeled *(i.e.*, lacked Alexa Fluor 647) and either dual-labeled $FN_{FRET}$ or wild-type FN was immobilized to the sensor chip, which was coated with a linear polycarboxylate hydrogel. For immobilization, dual-labeled $FN_{FRET}$ or wild-type FN was covalently conjugated to the sensor chip using carbodiimide coupling chemistry with 200 mM 1-ethyl-3-(-3-dimethylaminopropyl) carbodiimide and 50 mM *N*-hydroxysuccinimide and a flow rate of 25 µL/min. To measure binding, $\alpha_v\beta_3$ (in phosphate buffered saline with 1 mM $MgCl_2$) was injected at 25 µL/min over the sensor chip containing 4000±1500 RU of the dual-labeled $FN_{FRET}$ or wild-type FN. The sensogram baseline for all measurements was corrected by subtracting the sensogram from control surfaces without immobilized dual-labeled $FN_{FRET}$ or wild-type FN. Kinetic parameters were determined by fitting the sensogram to a 1:1 Langmuir binding isotherm.

## C.2 Supporting Tables

**Table C. 1.** Relative fractions of folded and unfolded $FN_{FRET}$ on OEG and TMS functionalized FS surfaces. Fractions for the "all frames" and "median" distributions of $\chi_{Fold}$ were determined by integrating the area of the peaks for folded and unfolded $FN_{FRET}$ in Figures 1 and S1, respectively. Additionally, the thresholds used to distinguish the folded and unfolded populations were $\chi_{Fold}$ = 0.42 and 0.5 on OEG and TMS, respectively. The numbers in parentheses correspond to the uncertainty in the least significant digit, and represent the standard deviation of 5 data subsets.

| Distribution of $\chi_{Fold}$ | Surface | Folded fraction | Unfolded fraction |
|---|---|---|---|
| **All frames** | OEG | 0.555(1) | 0.445(1) |
| | TMS | 0.436(2) | 0.564(2) |
| **Median** | OEG | 0.659(2) | 0.341(2) |
| | TMS | 0.416(1) | 0.584(1) |

**Table C. 2.** Fitting parameters for integrated surface residence time distributions on OEG and TMS for folded and unfolded $FN_{FRET}$. The reported parameters were determined by fitting the cumulative residence time distributions for folded and unfolded $FN_{FRET}$ to an exponential mixture model with multiple populations. It was assumed that the desorption of each population could be described as a first-order process with $x_k$ and $\tau_k$ representing the relative fraction of each population and the characteristic surface residence time of each population, respectively. Additionally, $\langle\tau\rangle$ and $k_{des}$ represent the mean surface residence time and the mean characteristic desorption rate constant, respectively. The mean parameters $\langle\tau\rangle$ and $k_{des}$, which is equivalent to $\langle\tau\rangle^{-1}$, were determined from the weighted average of the individual population fractions times the population residence times. The numbers in parentheses correspond to the uncertainty in the least significant digit, and represent the standard error of the weighted fit values.

| Surface (State) | $\langle\tau\rangle$ (s) | $k_{des}$ ($s^{-1}$) | $x_k$ | $\tau_k$ (s) |
|---|---|---|---|---|
| **OEG (Folded)** | 0.205(4) | 4.9(1) | 0.49(1) | 0.074(4) |
| | | | 0.45(1) | 0.237(5) |
| | | | 0.061(1) | 1.017(9) |
| **OEG (Unfolded)** | 0.69(4) | 1.45(8) | 0.619(6) | 0.145(2) |
| | | | 0.298(5) | 0.63(1) |
| | | | 0.064(8) | 3.1(1) |
| | | | 0.019(2) | 11.2(5) |
| **TMS (Folded)** | 0.127(3) | 7.9(2) | 0.837(7) | 0.085(2) |
| | | | 0.160(7) | 0.325(9) |
| | | | 0.0026(6) | 1.4(1) |
| **TMS (Unfolded)** | 0.37(3) | 2.7(2) | 0.803(2) | 0.0683(8) |
| | | | 0.164(2) | 0.336(5) |
| | | | 0.00202(2) | 1.54(3) |
| | | | 0.031(3) | 8.3(5) |

**Table C. 3.** Fitting parameters for integrated initial state residence time distributions on OEG and TMS for initially folded and unfolded $FN_{FRET}$. The reported parameters were determined by fitting the cumulative residence time distributions for initially folded and unfolded $FN_{FRET}$ to an exponential mixture model with multiple populations. It was assumed that the initial state residence time of each population could be described as a first-order process with $x_k$ and $\tau_k$ representing the relative fraction of each population and the characteristic initial state residence time of each population, respectively. Additionally, $\langle\tau\rangle$ and $k_{fold/unf}$ represent the mean initial state residence time and the mean characteristic rate constant for folding or unfolding, respectively. The mean parameters $\langle\tau\rangle$ and $k_{fold/unf}$, which is equivalent to $\langle\tau\rangle^{-1}$, were determined from the weighted average of the individual population fractions times the population initial state residence times. The numbers in parentheses correspond to the uncertainty in the least significant digit, and represent the standard error of the weighted fit values.

| **Surface, Initial State (Conformational change)** | $\langle\tau\rangle$ **(s)** | $k_{fold/unf}$ **($s^{-1}$)** | $x_k$ | $\tau_k$ **(s)** |
|---|---|---|---|---|
| **OEG, Unfolded (Folding)** | 11.7(4) | 0.086(3) | 0.438(4) | 0.182(8) |
| | | | 0.562(4) | 20.6(7) |
| **TMS, Unfolded (Folding)** | 1.74(3) | 0.57(1) | 0.753(4) | 0.090(3) |
| | | | 0.247(4) | 6.78(7) |
| **OEG, Folded (Unfolding)** | 0.95(2) | 1.06(2) | 0.727(4) | 0.182(7) |
| | | | 0.273(4) | 2.98(4) |
| **TMS, Folded (Unfolding)** | 0.326(6) | 3.06(6) | 0.758(1) | 0.105(7) |
| | | | 0.242(1) | 1.02(1) |

**Table C. 4.** Fitting parameters for cumulative squared displacement distributions on OEG and TMS for folded and unfolded $FN_{FRET}$. The reported parameters were determined by fitting the cumulative squared displacement distributions for folded and unfolded $FN_{FRET}$ to a Gaussian mixture model for multiple modes of diffusion. It was assumed that surface diffusion of each population could be described as a random walk (Gaussian statistics) with $x_k$ and $D_k$ representing the relative fraction of each population and the characteristic diffusion coefficient of each population, respectively. Additionally, $\bar{D}$ represents the mean diffusion coefficient and was determined from the weighted average of the individual population fractions times the population diffusion coefficients. The numbers in parentheses correspond to the uncertainty in the least significant digit, and represent the standard error of the weighted fit values.

| Surface (State) | $\bar{D}$ by state (μm²/s) | $x_k$ | $D_k$ (μm²/s) |
|---|---|---|---|
| **OEG, Unfolded** | 0.050(1) | 0.102(2) | 0.258(5) |
| | | 0.54(1) | 0.0409(8) |
| | | 0.36(1) | 0.0029(4) |
| **OEG, Folded** | 0.086(2) | 0.162(5) | 0.297(6) |
| | | 0.56(1) | 0.061(1) |
| | | 0.28(1) | 0.0132(6) |
| **TMS, Unfolded** | 0.254(2) | 0.467(2) | 0.496(3) |
| | | 0.392(2) | 0.0567(9) |
| | | 0.141(3) | 0.0021(4) |
| **TMS, Folded** | 0.266(4) | 0.457(5) | 0.495(6) |
| | | 0.422(3) | 0.088(2) |
| | | 0.121(6) | 0.0191(9) |

**Table C. 5.** Characterization of the binding of $\alpha_v\beta_3$ to dual-labeled $FN_{FRET}$ and the wild-type FN construct without labeling sites via surface plasmon resonance.

| Construct | $k_{bind}$ (x $10^3$ $M^{-1}$ $s^{-1}$) | $k_{unbind}$ (x $10^{-4}$ $s^{-1}$) | $K_D$ (nM) |
|---|---|---|---|
| **Wild-type FN** | 12.8±3.1 | 7.0±0.3 | 56.0±12.0 |
| **Dual-labeled $FN_{FRET}$** | 8.0±2.1 | 1.9±0.0 | 25.0±6.5 |

**Table C. 6.** Number of trajectories used for the analysis of binding time stability and time-to-binding.

| Analysis | Surface | FN conformation | Number of trajectories |
|---|---|---|---|
| Binding time | OEG | Folded | 6158 |
| Binding time | OEG | Unfolded | 1325 |
| Binding time | TMS | Folded | 3947 |
| Binding time | TMS | Unfolded | 2237 |
| Time-to-binding | OEG | Folded | 3411 |
| Time-to-binding | OEG | Unfolded | 1290 |
| Time-to-binding | TMS | Folded | 2560 |
| Time-to-binding | TMS | Unfolded | 2875 |

**Table C. 7.** Fitting parameters for integrated bound-state distributions on OEG and TMS for folded and unfolded $FN_{FRET}$. The reported parameters were determined by fitting the cumulative bound-state residence time distributions for folded and unfolded $FN_{FRET}$ to an exponential mixture model with multiple populations. It was assumed that the unbinding of each population could be described as a first-order process with $x_k$ and $\tau_k$ representing the relative fraction of each population and the characteristic bound-state residence time of each population, respectively. Additionally, $\langle\tau\rangle$ and $k_{unbind}$ represent the mean bound-state residence time and the mean characteristic unbinding or 'off' rate constant of the FN-$\alpha_v\beta_3$ complex, respectively. The mean parameters $\langle\tau\rangle$ and $k_{unbind}$, which is equivalent to $\langle\tau\rangle^{-1}$, were determined from the weighted average of the individual population fractions times the population bound-state residence times. The numbers in parentheses correspond to the uncertainty in the least significant digit, and represent the standard error of the weighted fit values.

| **Surface (State before unbinding)** | $\langle\tau\rangle$ **(s)** | $k_{unbind}$ **($s^{-1}$)** | $x_k$ | $\tau_k$ **(s)** |
|---|---|---|---|---|
| **OEG (Folded)** | 0.68(6) | 1.5(1) | 0.72(2) | 0.11(2) |
| | | | 0.20 (2) | 0.64(6) |
| | | | 0.08(1) | 5.9(1) |
| **OEG (Unfolded)** | 0.24(4) | 4.2(7) | 0.76(1) | 0.063(6) |
| | | | 0.21(1) | 0.38(2) |
| | | | 0.03(1) | 3.6(2) |
| **TMS (Folded)** | 0.29(4) | 3.5(5) | 0.78(1) | 0.067(8) |
| | | | 0.18(1) | 0.36(3) |
| | | | 0.04(1) | 4.2(2) |
| **TMS (Unfolded)** | 0.08(1) | 13(2) | 0.87(1) | 0.045(6) |
| | | | 0.12(1) | 0.22(1) |
| | | | 0.01(1) | 1.26(9) |

**Table C. 8.** Fitting parameters for integrated time-to-binding distributions on OEG and TMS for folded and unfolded $FN_{FRET}$. The reported parameters were determined by fitting the time-to-binding distributions for folded and unfolded $FN_{FRET}$ to an exponential mixture model with multiple populations. It was assumed that the binding of each population could be described as a first-order process with $x_k$ and $\tau_k$ representing the relative fraction of each population and the characteristic time-to-binding of each population, respectively. Additionally, $\langle\tau\rangle$ and $k_{bind}$ represent the mean time-to-binding and the mean characteristic binding or 'on' rate constant of the FN-$\alpha_v\beta_3$ complex, respectively. The mean parameters $\langle\tau\rangle$ and $k_{bind}$, which is equivalent to $\langle\tau\rangle^{-1}$, were determined from the weighted average of the individual population fractions times the population times-to-binding. The numbers in parentheses correspond to the uncertainty in the least significant digit, and represent the standard error of the weighted fit values.

| Surface (State before binding) | $\langle\tau\rangle$ (s) | $k_{bind}$ ($s^{-1}$) | $x_k$ | $\tau_k$ (s) |
|---|---|---|---|---|
| **OEG (Folded)** | 1.6(3) | 0.60(1) | 0.654(4) | 0.25(1) |
| | | | 0.346(4) | 4.33(8) |
| **OEG (Unfolded)** | 16.6(3) | 0.060(1) | 0.207(2) | 0.34(2) |
| | | | 0.793(2) | 20.8(4) |
| **TMS (Folded)** | 3.36(5) | 0.298(4) | 0.551(4) | 0.32(1) |
| | | | 0.449(4) | 7.1(1) |
| **TMS (Unfolded)** | 7.1(1) | 0.141(2) | 0.398(3) | 0.41(1) |
| | | | 0.603(3) | 11.5(2) |

## C.3 Supporting Figures

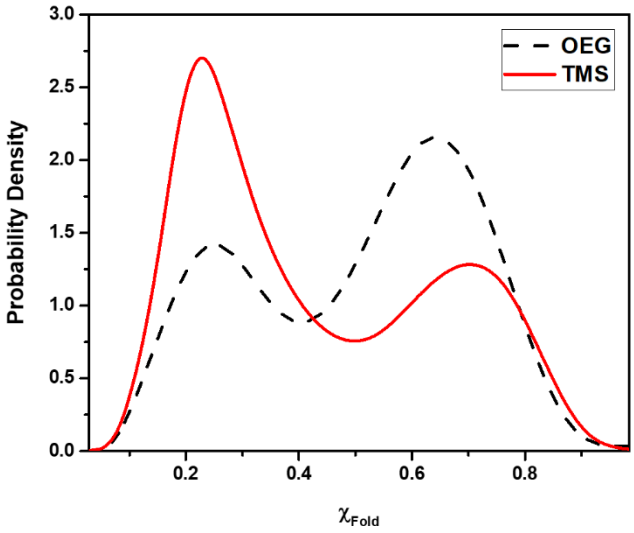


**Figure C. 1.** Probability density of the median distribution of $\chi_{Fold}$ on FS functionalized with OEG (black dashed line) and TMS (red solid line). In the distribution, distinct populations representing the folded state and unfolded state of $FN_{FRET}$ were observed. The population representing the folded state was centered at $\chi_{Fold}$ values of 0.62 on OEG and 0.69 on TMS, respectively. For the unfolded state, the population was centered at $\chi_{Fold}$ values of 0.28 on OEG and 0.23 on TMS, respectively. A critical value of 0.42 on OEG and 0.5 on TMS, which corresponded to the minimum probability in $\chi_{Fold}$ between populations, was used to partition folded from unfolded molecules. The median $\chi_{Fold}$ distribution was generated from ~$10^6$ molecular trajectories on both surfaces.

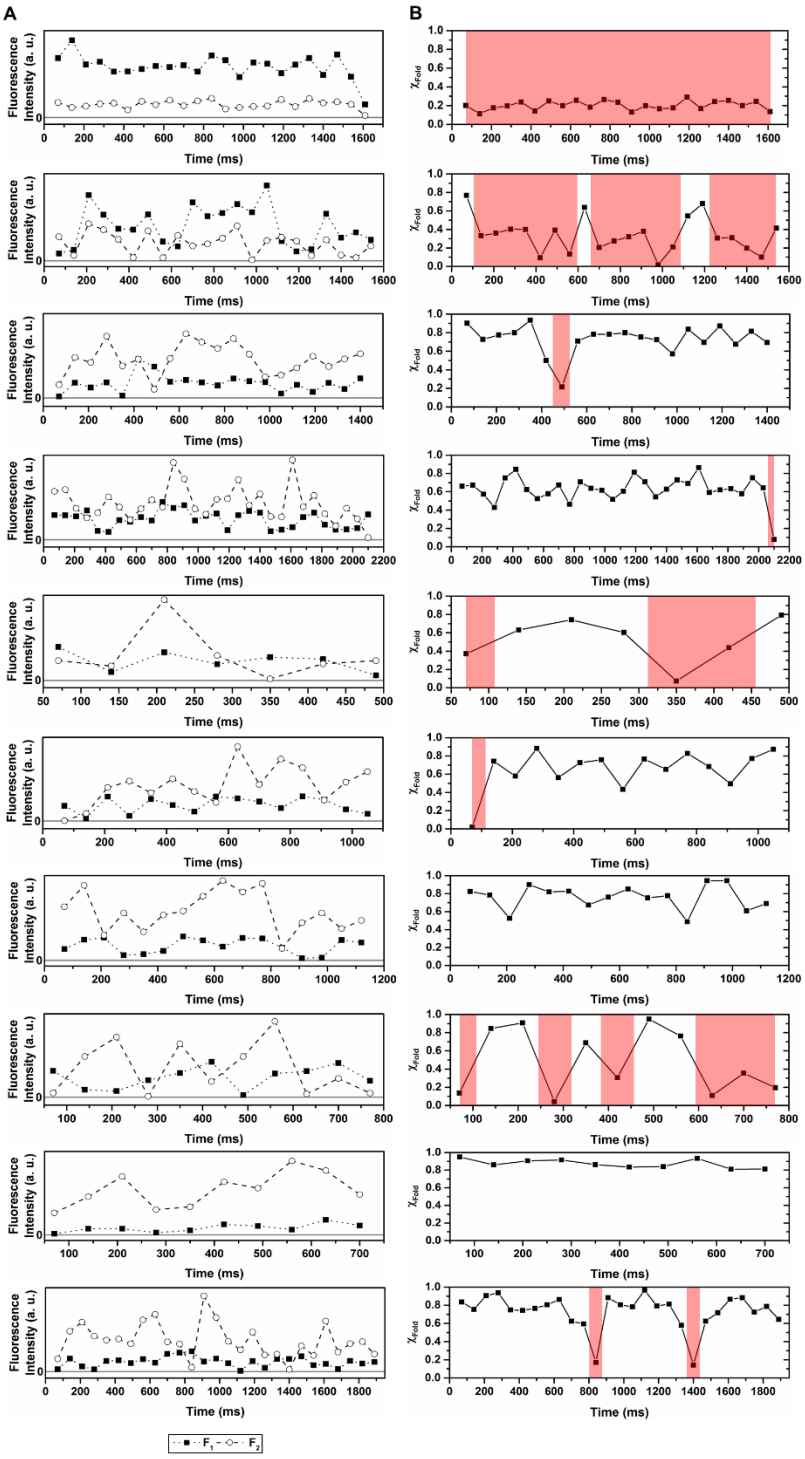


**Figure C. 2.** Sample trajectories of the fluorescence intensity in the donor and acceptor channels (A) as well as changes in corresponding $\chi_{Fold}$ (B) from two-color SM-FRET experiments that monitor changes in $FN_{FRET}$ conformation. The areas shaded red in panel B illustrate segments of trajectories in which $FN_{FRET}$ is unfolded based on the value of $\chi_{Fold}$. In the representative raw trajectories, the fluorescence intensities of $F_1$ and $F_2$ were anti-correlated, which is characteristic of FRET.

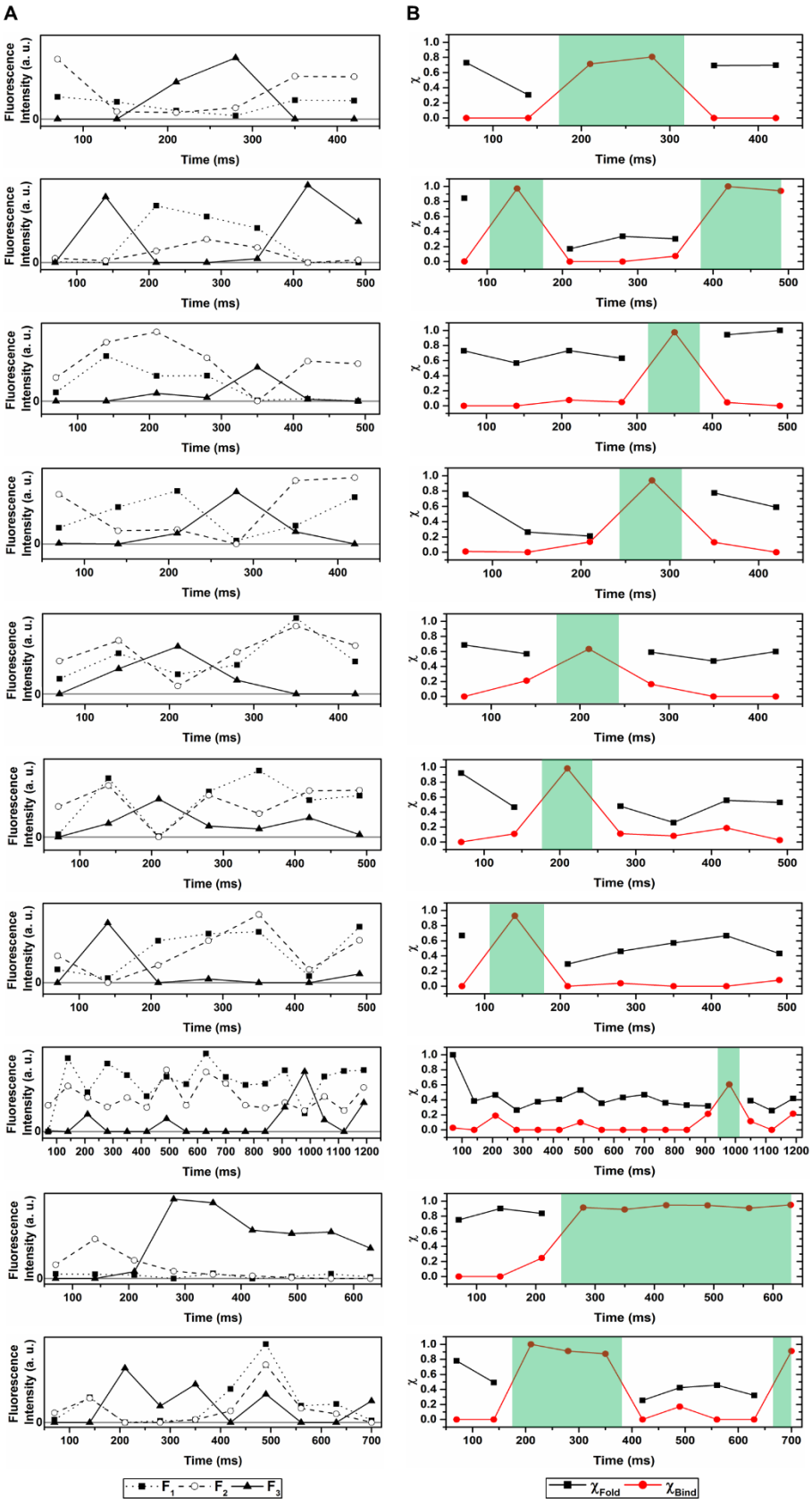
A
B
Fluorescence Intensity (a. u.)
Time (ms)
χ
F1
F2
F3
χFold
χBind

**Figure C. 3.** Additional sample trajectories in three-color single-molecule experiments. (A) Fluorescence intensity of donor ($F_1$) and acceptor ($F_2$, and $F_3$) labels plotted on the same scale and axis. (B) The corresponding $\chi$ values associated with $FN_{FRET}$ conformation ($\chi_{Fold}$) and integrin binding ($\chi_{Bind}$). The green-shaded regions in panel B represent segments of trajectories in which binding of the integrin to FN was identified. Due to the low signal-to-noise of the intensities of $F_1$ and $F_2$ during the binding events, the data points corresponding to $\chi_{Fold}$ during the bound state time intervals were not included in the $\chi$ plots.

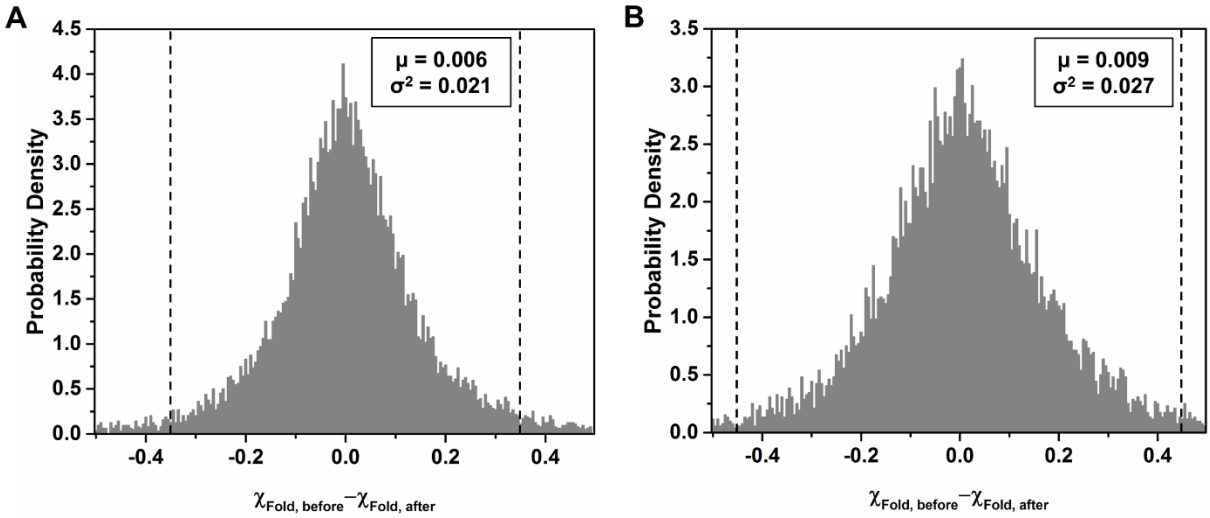


**Figure C. 4.** Probability density distribution of the difference in $\chi_{Fold}$ in the frames immediately before $\alpha_v\beta_3$ binding and immediately after $\alpha_v\beta_3$ dissociation on OEG (A) and TMS (B). The distributions on both surfaces had a mean close to zero, suggesting that the conformation of $FN_{FRET}$ during a binding event remained unchanged. The dashed lines correspond to the difference between $\chi_{Fold}$ for folded and unfolded $FN_{FRET}$ on OEG (0.35) and TMS (0.45) as determined from two-color FRET experiments. Accordingly, for a molecule to have been considered to have undergone an unfolding or refolding event during binding, the value of $\chi_{Fold, before}-\chi_{Fold, after}$ would be equal to this value or greater.

# Appendix D: Supporting Information for Chapter VI

## D.1 Supporting Tables

**Table D. 1.** Fitting parameters for integrated surface residence time distributions on p(SBMA$_x$-co-OEGMA$_y$) functionalized FS surfaces for folded and unfolded FN$_{FRET}$. The reported parameters were determined by fitting the cumulative residence time distributions for folded and unfolded FN$_{FRET}$ to an exponential mixture model with multiple populations. It was assumed that the desorption of each population could be described as a first-order process with $x_k$ and $\tau_k$ representing the relative fraction of each population and the characteristic surface residence time of each population, respectively. Additionally, $\langle\tau\rangle$ and $k_{des}$ represent the mean surface residence time and the mean characteristic desorption rate constant, respectively. The mean parameters $\langle\tau\rangle$ and $k_{des}$, which is equivalent to $\langle\tau\rangle^{-1}$, were determined from the weighted average of the individual population fractions times the population residence times. The numbers in parentheses correspond to the uncertainty in the least significant digit, and represent the standard error of the weighted fit values.

| Surface (State) | $\langle\tau\rangle$ (s) | $k_{des}$ (s$^{-1}$) | $x_k$ | $\tau_k$ (s) |
|---|---|---|---|---|
| **p(SBMA$_0$-co-OEGMA$_{100}$) (Folded)** | 0.22(1) | 4.6(2) | 0.661(6) | 0.108(2) |
| | | | 0.297(6) | 0.325(5) |
| | | | 0.042(9) | 1.11(1) |
| | | | 0.00045(2) | 8.0(3) |
| **p(SBMA$_0$-co-OEGMA$_{100}$) (Unfolded)** | 0.92(3) | 1.09(4) | 0.513(8) | 0.174(4) |
| | | | 0.373(7) | 0.62(1) |
| | | | 0.09(1) | 3.06(3) |
| | | | 0.0229(2) | 14.28(6) |
| **p(SBMA$_{25}$-co-OEGMA$_{75}$) (Folded)** | 0.221(8) | 4.5(2) | 0.765(4) | 0.111(1) |
| | | | 0.211(3) | 0.437(8) |
| | | | 0.022(5) | 1.53(4) |
| | | | 0.0017(1) | 6.3(2) |
| | 0.492(7) | 2.03(3) | 0.753(2) | 0.093(1) |

| | | | | |
|---|---|---|---|---|
| **p(SBMA$_{25}$-co-OEGMA$_{75}$) (Unfolded)** | | | 0.192(1) | 0.612(7) |
| | | | 0.044(2) | 3.06(3) |
| | | | 0.0106(1) | 16.05(8) |
| **p(SBMA$_{50}$-co-OEGMA$_{50}$) (Folded)** | 0.39(2) | 2.6(1) | 0.660(8) | 0.193(2) |
| | | | 0.300(6) | 0.60(1) |
| | | | 0.04(1) | 1.78(5) |
| | | | 0.0025(2) | 6.2(2) |
| **p(SBMA$_{50}$-co-OEGMA$_{50}$) (Unfolded)** | 0.46(2) | 2.2(1) | 0.725(4) | 0.134(2) |
| | | | 0.231(4) | 0.596(9) |
| | | | 0.037(6) | 2.98(5) |
| | | | 0.0078(1) | 14.2(1) |
| **p(SBMA$_{75}$-co-OEGMA$_{25}$) (Folded)** | 0.50(2) | 2.00(8) | 0.692(4) | 0.214(2) |
| | | | 0.278(4) | 0.82(1) |
| | | | 0.030(6) | 3.48(7) |
| | | | 0.0010(2) | 14(1) |
| **p(SBMA$_{75}$-co-OEGMA$_{25}$) (Unfolded)** | 0.256(9) | 3.9(1) | 0.831(2) | 0.088(1) |
| | | | 0.145(2) | 0.496(6) |
| | | | 0.020(3) | 2.75(4) |
| | | | 0.00370(6) | 15.0(1) |
| **p(SBMA$_{100}$-co-OEGMA$_{0}$) (Folded)** | 0.229(5) | 4.4(1) | 0.718(8) | 0.131(3) |
| | | | 0.266(8) | 0.427(8) |
| | | | 0.015(1) | 1.39(3) |
| **p(SBMA$_{100}$-co-OEGMA$_{0}$) (Unfolded)** | 1.05(3) | 0.95(3) | 0.53(1) | 0.189(5) |
| | | | 0.320(9) | 0.65(2) |

| | | |
|---|---|---|
| | 0.11(1) | 2.33(4) |
| | 0.0343(2) | 14.13(4) |

**Table D. 2.** Fitting parameters for integrated state dwell time distributions on p($SBMA_x$-co-$OEGMA_y$) functionalized FS surfaces for folded and unfolded $FN_{FRET}$. The reported parameters were determined by fitting the cumulative dwell time distributions for folded and unfolded $FN_{FRET}$ to an exponential mixture model with multiple populations. It was assumed that the conformational change of each population could be described as a first-order process with $x_k$ and $\tau_k$ representing the relative fraction of each population and the characteristic state dwell time of each population, respectively. Additionally, $\langle\tau\rangle$ and $k_{fold/unf}$ represent the mean state dwell time and the mean characteristic rate constant for folding or unfolding, respectively. The mean parameters $\langle\tau\rangle$ and $k_{fold/unf}$, which is equivalent to $\langle\tau\rangle^{-1}$, were determined from the weighted average of the individual population fractions times the population state dwell times. The numbers in parentheses correspond to the uncertainty in the least significant digit, and represent the standard error of the weighted fit values.

| **Surface, Dwell State (Conformational change)** | $\langle\tau\rangle$ **(s)** | $k_{fold/unf}$ **($s^{-1}$)** | $x_k$ | $\tau_k$ **(s)** |
|---|---|---|---|---|
| **p($SBMA_0$-co-$OEGMA_{100}$), Unfolded (Folding)** | 23.2(4) | 0.0431(7) | 0.481(3) | 0.159(5) |
| | | | 0.162(2) | 2.05(5) |
| | | | 0.357(4) | 63.9(7) |
| **p($SBMA_{25}$-co-$OEGMA_{75}$), Unfolded (Folding)** | 19.3(4) | 0.052(1) | 0.616(3) | 0.152(3) |
| | | | 0.128(2) | 2.20(5) |
| | | | 0.256(4) | 74(1) |
| **p($SBMA_{50}$-co-$OEGMA_{50}$), Unfolded (Folding)** | 12.4(4) | 0.081(3) | 0.682(3) | 0.166(5) |
| | | | 0.150(3) | 1.95(6) |
| | | | 0.169(4) | 71(2) |
| **p($SBMA_{75}$-co-$OEGMA_{25}$), Unfolded (Folding)** | 6.1(2) | 0.164(5) | 0.689(3) | 0.160(4) |
| | | | 0.167(3) | 1.70(4) |
| | | | 0.144(4) | 39.5(5) |

| | | | | |
|---|---|---|---|---|
| **p(SBMA$_{100}$-co-OEGMA$_0$), Unfolded (Folding)** | 11.6(2) | 0.086(2) | 0.480(4) | 0.152(5) |
| | | | 0.200(2) | 1.54(3) |
| | | | 0.319(5) | 35.0(2) |
| **p(SBMA$_0$-co-OEGMA$_{100}$), Folded (Unfolding)** | 0.31(3) | 3.2(3) | 0.848(7) | 0.094(6) |
| | | | 0.104(6) | 0.63(4) |
| | | | 0.048(9) | 3.36(3) |
| **p(SBMA$_{25}$-co-OEGMA$_{75}$), Folded (Unfolding)** | 0.73(6) | 1.4(1) | 0.823(4) | 0.228(7) |
| | | | 0.156(3) | 1.91(4) |
| | | | 0.021(5) | 11.4(2) |
| **p(SBMA$_{50}$-co-OEGMA$_{50}$), Folded (Unfolding)** | 1.2(1) | 0.83(7) | 0.739(9) | 0.31(2) |
| | | | 0.224(7) | 2.37(9) |
| | | | 0.04(1) | 9.7(4) |
| **p(SBMA$_{75}$-co-OEGMA$_{25}$), Folded (Unfolding)** | 2.1(2) | 0.48(5) | 0.729(4) | 0.230(8) |
| | | | 0.228(3) | 3.00(7) |
| | | | 0.043(5) | 30(2) |
| **p(SBMA$_{100}$-co-OEGMA$_0$), Folded (Unfolding)** | 0.18(1) | 5.6(3) | 0.869(5) | 0.078(3) |
| | | | 0.102(4) | 0.41(1) |
| | | | 0.029(6) | 2.26(2) |

**Table D. 3.** Fitting parameters for integrated surface association lifetime distributions on p(SBMA$_x$-co-OEGMA$_y$) functionalized FS surfaces for NBD-X. The reported parameters were determined by fitting the cumulative residence time distributions to an exponential mixture model with multiple populations. It was assumed that the deactivation of each population could be described as a first-order process with $x_k$ and $\tau_k$ representing the relative fraction of each population and the characteristic surface residence time of each population, respectively. Additionally, $\langle\tau\rangle$ and $k_{off}$ represent the mean surface association lifetime and the mean characteristic deactivation rate constant, respectively. The mean parameters $\langle\tau\rangle$ and $k_{off}$, which is equivalent to $\langle\tau\rangle^{-1}$, were determined from the weighted average of the individual population

fractions times the population lifetimes. The numbers in parentheses correspond to the uncertainty in the least significant digit, and represent the standard error of the weighted fit values.

| Surface | $\langle\tau\rangle$ (s) | $k_{off}$ ($s^{-1}$) | $x_k$ | $\tau_k$ (s) |
|---|---|---|---|---|
| **p(SBMA$_0$-co-OEGMA$_{100}$)** | 1.9(1) | 0.53(3) | 0.633(8) | 0.61(2) |
| | | | 0.306(8) | 2.65(4) |
| | | | 0.06(1) | 11.94(5) |
| **p(SBMA$_{25}$-co-OEGMA$_{75}$)** | 1.2(1) | 0.83(7) | 0.827(7) | 0.53(2) |
| | | | 0.142(7) | 2.63(8) |
| | | | 0.03(1) | 11.4(9) |
| **p(SBMA$_{50}$-co-OEGMA$_{50}$)** | 1.0(1) | 1.0(1) | 0.62(2) | 0.37(2) |
| | | | 0.29(2) | 1.21(6) |
| | | | 0.075(3) | 4.30(8) |
| | | | 0.01(1) | 12.9(1) |
| **p(SBMA$_{75}$-co-OEGMA$_{25}$)** | 0.86(7) | 1.2(1) | 0.75(2) | 0.38(3) |
| | | | 0.21(2) | 1.42(9) |
| | | | 0.036(2) | 5.6(2) |
| | | | 0.004(3) | 19(1) |
| **p(SBMA$_{100}$-co-OEGMA$_0$)** | 0.65(4) | 1.5(1) | 0.76(2) | 0.31(2) |
| | | | 0.20(2) | 1.09(5) |
| | | | 0.037(1) | 4.04(7) |
| | | | 0.003(2) | 15.7(2) |

## D.2 Supporting Figures

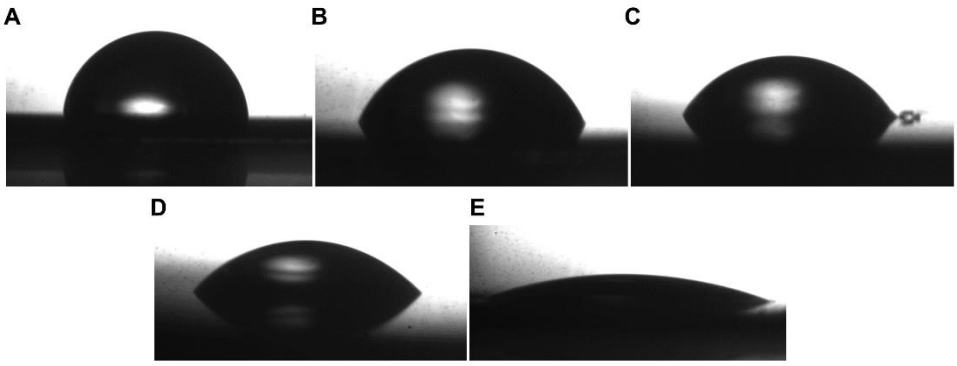


**Figure D. 1.** Representative water contact angle images for surfaces of different composition: CMPS initiator SAM (A), p(SBMA$_0$-co-OEGMA$_{100}$) (B), p(SBMA$_{25}$-co-OEGMA$_{75}$) (C), p(SBMA$_{50}$-co-OEGMA$_{50}$) (D), p(SBMA$_{75}$-co-OEGMA$_{25}$) (E), and p(SBMA$_0$-co-OEGMA$_{100}$) (F) FS functionalized surfaces.

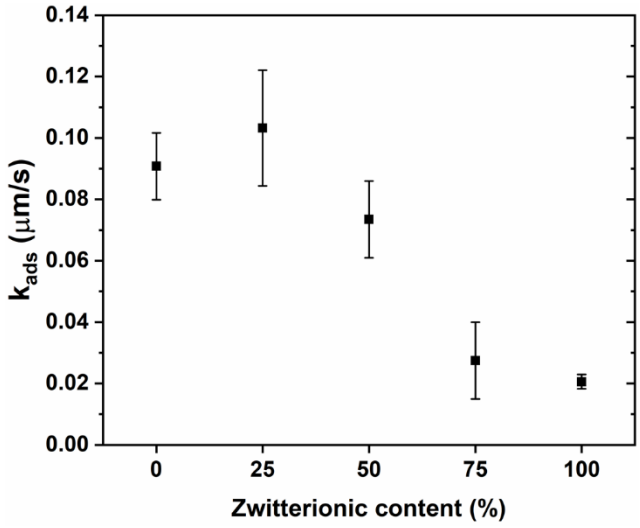


**Figure D. 2.** Adsorption rate constants of $FN_{FRET}$ at room temperature as a function of polymer brush composition. Error bars represent the standard deviation across 20 data sets for each experiment. Adsorption rate constant were measured in phosphate buffered saline (pH 7.4 and ionic strength 137 mM).

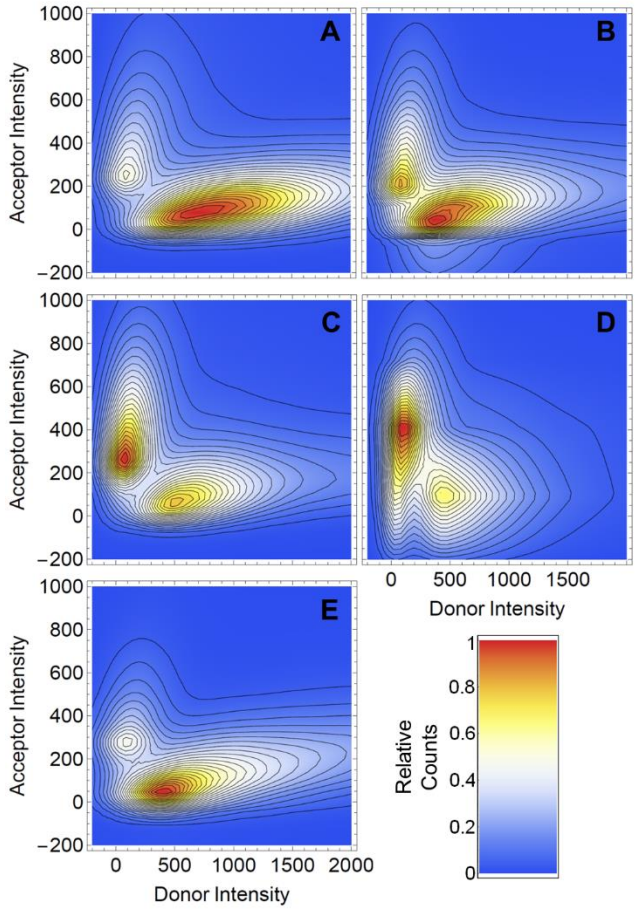


**Figure D. 3.** Heat map representation of binned acceptor and donor intensities of $FN_{FRET}$ on polymer brushes of different composition: p($SBMA_0$-co-$OEGMA_{100}$) (A), p($SBMA_{25}$-co-$OEGMA_{75}$) (B), p($SBMA_{50}$-co-$OEGMA_{50}$) (C), p($SBMA_{75}$-co-$OEGMA_{25}$) (D), and p($SBMA_0$-co-$OEGMA_{100}$) (E) FS functionalized surfaces. The plot shows two discrete population peaks corresponding to folded and unfolded populations.

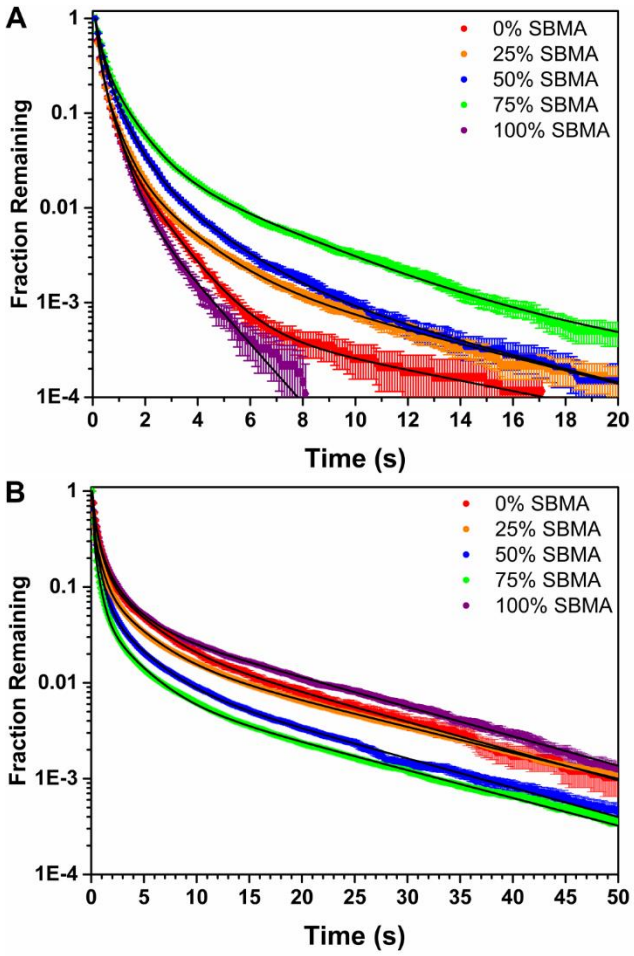


**Figure D. 4.** Complementary cumulative surface residence time distributions (CCSRTD) for $FN_{FRET}$ on FS functionalized with p($SBMA_0$-co-$OEGMA_{100}$) (red), p($SBMA_{25}$-co-$OEGMA_{75}$) (orange), p($SBMA_{50}$-co-$OEGMA_{50}$) (blue), p($SBMA_{75}$-co-$OEGMA_{25}$) (green), and p($SBMA_0$-co-$OEGMA_{100}$) (purple) as a function of folding state. CCSRTD for always folded and always unfolded $FN_{FRET}$ are represented in panels A) and B), respectively. The distributions were fit to an exponential mixture model (black line), which assumed a superposition of four first-order desorption processes. Based on the fitting parameters, the characteristic surface residence time for each sub-population of folded or unfolded molecules on each surface was determined. Error bars represent a 68% confidence interval based on a Poisson distribution for each data point. Each distribution was generated from ~$10^5$ molecular trajectories.

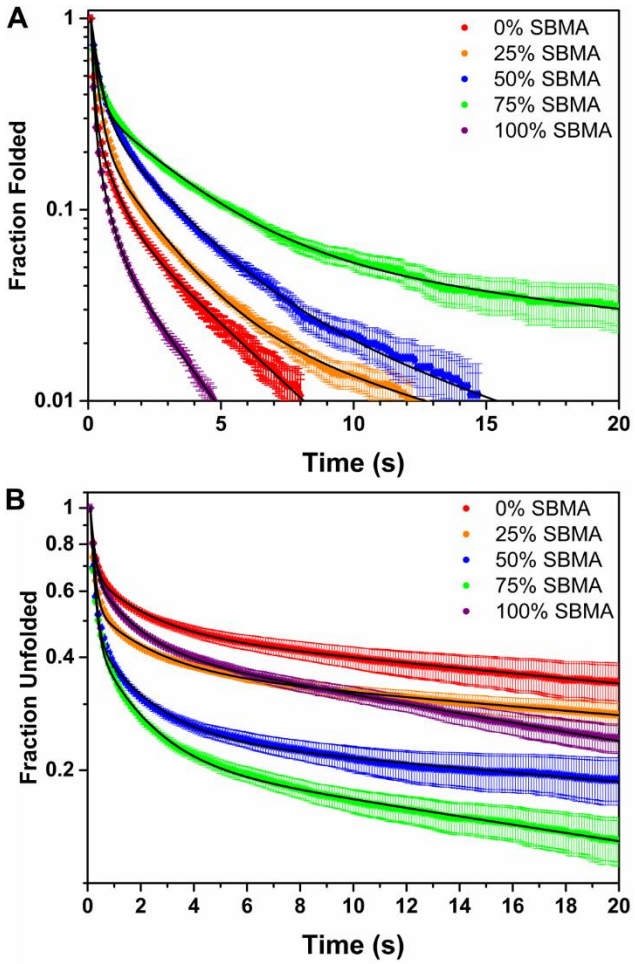


**Figure D. 5.** Complementary cumulative dwell time distributions (CCDTD) for folded (A) and unfolded (B) $FN_{FRET}$ on p($SBMA_0$-co-$OEGMA_{100}$) (red), p($SBMA_{25}$-co-$OEGMA_{75}$) (orange), p($SBMA_{50}$-co-$OEGMA_{50}$) (blue), p($SBMA_{75}$-co-$OEGMA_{25}$) (green), and p($SBMA_0$-co-$OEGMA_{100}$) (purple) FS functionalized surfaces. Each distribution was fit to an exponential mixture model (black line), which assumed a superposition of three first-order apparent high-to-low FRET or low-to-high FRET transitions. Analysis of the model fit yielded the relative fraction and characteristic time constants for each sub-population in each distribution. Error bars represent a 68% confidence interval based on a Poisson distribution for each data point. Each distribution was generated from ~$10^4$ molecular trajectories.

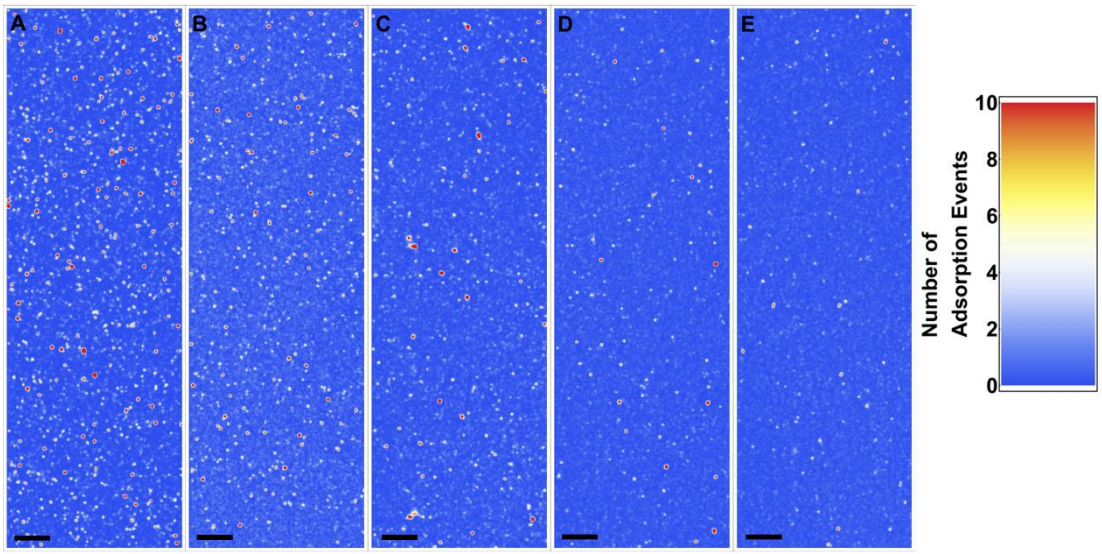


**Figure D. 6.** Super-resolution mapping of surface adsorption of NBD-X using mbPAINT, obtained from the accumulation of NBD-X trajectories on the polymer brushes for different chemical compositions: p(SBMA$_0$-co-OEGMA$_{100}$) (A), p(SBMA$_{25}$-co-OEGMA$_{75}$) (B), p(SBMA$_{50}$-co-OEGMA$_{50}$) (C), p(SBMA$_{75}$-co-OEGMA$_{25}$) (D), and p(SBMA$_0$-co-OEGMA$_{100}$) (E) FS functionalized surfaces. The numbers of adsorption events per pixel was counted and displayed in the form of a heat map. It can be observed that the number of strong adsorption sites systematically decreased as the content of SBMA increased on the brush surface.

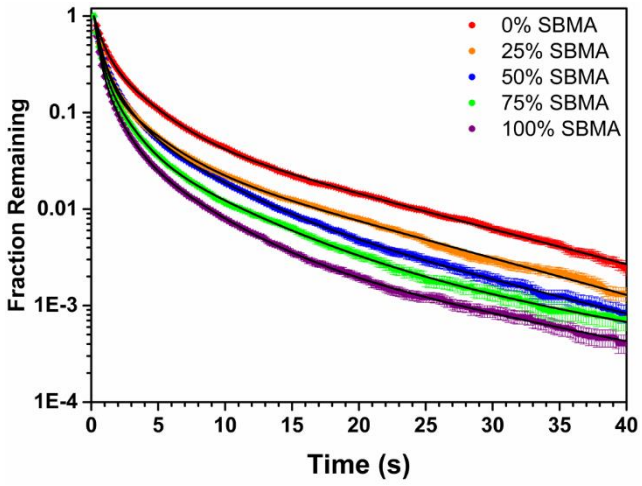


**Figure D.7.** Complementary cumulative surface association time distributions (analogous to CCSRTD) for NBD-X on FS functionalized with p(SBMA$_0$-co-TEGMA$_{100}$) (red), p(SBMA$_{25}$-co-TEGMA$_{75}$) (orange), p(SBMA$_{50}$-co-TEGMA$_{50}$) (blue), p(SBMA$_{75}$-co-TEGMA$_{25}$) (green), and p(SBMA$_0$-co-TEGMA$_{100}$) (purple) as a function of folding state. The distributions were fit to an exponential mixture model (black line), which assumed a superposition of three first-order deactivation (i.e., dissociation) processes. Based on the fitting parameters, the characteristic

surface deactivation time for each sub-population of NBD-X molecules on each surface was determined. Error bars represent a 68% confidence interval based on a Poisson distribution for each data point. Each distribution was generated from ~$10^5$ molecular trajectories.